Next Generation Integrated Vehicle Dynamics and Controls

By

Louis Filipozzi

Dissertation

Submitted in partial satisfaction of the requirements for the degree of

Doctor of Philosophy

in

Mechanical and Aerospace Engineering

in the

Office of Graduate Studies

of the

University *of* California

Davis

Approved:

Francis Assadian, Chair

Donald L. Margolis

Shima Nazari

Committee in Charge

2022

To my family.

Contents

List of Figures

List of Tables

Abstract

The increasing number of active chassis systems leads to a higher need for control integration: coordinating the vehicle actuators in a supervised way has the potential of enhancing the vehicle performance in terms of handling and power efficiency while addressing the possible conflicts between the different actuators, thus reducing implementation cost of active systems thanks to better reusability, ease of configuration and calibration. This research presents the development of a multi-layered control framework for vehicles equipped with an electric drivetrain, independent braking, and active steering actuators. The control architecture is decomposed into two parts: an abstract layer that defines controls at the wheel level and which does not require precise knowledge of the actuators equipped on the vehicle, and an application layer that coordinates the actuators to follow the wheel control requests. A simplified tire model is developed to model the coupling behavior between the longitudinal and lateral tire forces; the abstract layer utilizes multivariable control methods in conjunction with the simplified tire model to define optimal wheel controls. Similarly, a control allocation is implemented in the application layer to coordinate the brake and drivetrain actuators. The distribution of actuator commands is made invisible at the wheel torque level by cleverly using the Smith-McMillan decomposition of a redundant system, simplifying the controller design by dissociating the actuator allocation problem from the control problem while ensuring internal stability and good robustness properties. Simulations with a high-fidelity vehicle model validate the control framework. Several actuator configurations are considered to highlight the reusability of the control architecture. Results show that the control architecture provides a unified framework for the vehicle's longitudinal, lateral, and yaw control.

Acknowledgments

First and foremost, I would like to thank my thesis advisor, Prof. Francis Assadian. His experience in the automotive industry and controls has been incredibly insightful. In addition to his guidance for this work, he has always been there to provide valuable advice. We had many discussions about modeling and robust control throughout my research that laid the groundwork for this dissertation. It has been a pleasure working with him on this thesis.

I would like to thank Prof. Donald L. Margolis and Prof. Shima Nazari for serving on my thesis committee for their help, advice, and suggestions with this dissertation.

I am deeply grateful to Ford Motor Company for supporting this research through a University Research Project grant. I would like to offer my special thanks to Ming Kuang, Rajit Johri, José Velazquez Alcantar, and the Vehicle Control and System Engineering research group. Ming was responsible for making this University Research Project between UC Davis and Ford Motor Company possible. In addition to that, he helped refine the scope of the project during my summer internships at Ford Motor Company in Dearborn, MI, during which I have been lucky enough to work under the mentorship of Rajit and José. It has been a pleasure working with them and getting to know them professionally and personally.

To Miranda, thank you for being there and encouraging me throughout my PhD. To my parents, siblings, and family, you put up with me being away and missing many events. I am forever grateful for your patience and understanding, and I hope to have time to reconnect with each of you soon.

Nomenclature

Acronyms

k-NN k-Nearest Neighbors.

4WD Four Wheel Drive.

4WS Four Wheel Steering.

ABS Anti-lock Braking System.

ACC Adaptive Cruise Control.

ADAS Advanced Driver-Assistance Systems.

AEB Autonomous Emergency Braking.

AFS Active Front Steering.

ANN Artificial Neural Network.

ARC Active Roll Control.

ARS Active Rear Steering.

CAS Collision Avoidance System.

CDC Continuous Damping Control.

COO Controller Output Observer.

DoF Degree of Freedom.

DSC Dynamic Stability Control.

eAWD e-All Wheel Drive.

ECU Electronic Control Unit.

EHB Electro-Hydraulic Brakes.

EKBF Extended Kalman-Bucy Filter.

EKF Extended Kalman Filter.

eLSD e-Limited Slip Differential.

ePAS electric Power Assisted Steering.

ESC Extremum Seeking Control.

ESP Electronic Stability Program.

GCC Global Chassis control.

GPS Global Positioning System.

HCU Hydraulic Control Unit.

HEV Hybrid Electric Vehicles.

IVDC Integrated Vehicle Dynamics and Control.

IWEM In-Wheel Electric Motors.

LFT Linear Fractional Transformation.

LMI Linear Matrix Inequality.

LP Linear Programming.

LQR Linear Quadratic Regulator.

LTI Linear Time-Invariant.

LTV Linear Time-Varying.

LTVMPC Linear Time-Varying MPC.

MHE Moving Horizon Estimation.

MIMO Multiple Input Multiple Output.

MPC Model Predictive Control.

NLP Nonlinear Programming.

NMPC Nonlinear MPC.

OCP Optimal Control Problem.

PAS Power Assisted Steering.

PROMETHEUS PROgraM for a European Traffic with Highest Efficiency and Unprecedented Safety.

PSD Power Spectral Density.

PWM Pulse Width Modulation.

QP Quadratic Programming.

QPP Quadratic Programming Problem.

RGA Relative Gain Array.

RLS Recursive Least Square.

RMS Root Mean Square.

RMSE Root Mean Square Error.

RTI Real-Time Iteration.

SIMO Single Input Multiple Output.

SISO Single Input Single Output.

SQP Sequential Quadratic Programming.

TCS Traction Control System.

TV Torque Vectoring.

UKF Unscented Kalman Filter.

UMVF Unbiased Minimum Variance Filtering.

YCOO Youla Controller Output Observer.

Notation

δ_{dri} Driver steering angle at the wheel level.

δ_{ij} Steering angle of the ij wheel.

f_x Total longitudinal force applied on the chassis.

f_{xij} Longitudinal tire force of the ij wheel.

f_y Total lateral force applied on the chassis.

f_{yij} Lateral tire force of the wheel.

f_{zij} Vertical tire force of the wheel.

G_a Nullspace allocator transfer function matrix.

G_{mot} Motor gearing ratio.

h Height of the vehicle center of mass.

I_{zz} Yaw inertia.

J_w Wheel inertia.

K_a Matrix generated the right nullspace of an over-actuated multivariable system.

l Vehicle wheelbase.

l_i Distance from the vehicle center of mass to the axle i.

m Vehicle mass.

μ_{ij} Combined friction coefficient of the ij wheel.

μ_{ijx} Longitudinal friction coefficient of the ij wheel.

μ_{ijy} Lateral friction coefficient of the ij wheel.

m_z Yaw moment applied on the vehicle.

ω_{ij} Wheel angular velocity.

ω_x Roll angular velocity.

ω_y Pitch angular velocity.

ω_z Yaw angular velocity.

r_w Wheel radius.

s_{ij} Combined slip of the ij wheel.

s_{ijx} Longitudinal slip ratio of the ij wheel.

s_{ijy} Slip angle of the ij wheel.

τ_{ij} Torque applied on the ij wheel.

τ_{tot} Total wheel torque.

τ_{TV_i} Left-to-right torque vectoring applied on the axle i.

$\tau_{TV_{F/R}}$ Front-to-rear torque vectoring.

θ_{dri} Driver steering angle at the steering wheel.

v_x Longitudinal vehicle velocity.

v_y Lateral vehicle velocity.

v_z Vertical vehicle velocity.

w Vehicle track width.

w_j Distance from the vehicle center of mass to the side j.

Chapter 1

Introduction

1.1 Research Goal and Scope

Today's vehicles are already over-actuated; different control modules can impact the same physical variable. For instance, Electronic Stability Program (ESP), Torque Vectoring (TV), electric Power Assisted Steering (ePAS), and Active Front Steering (AFS) affect the yaw behavior of the vehicle either by creating a yaw moment from longitudinal tire forces or by modifying the wheel steering angle. Without any coordination between the different control modules, conflicts may arise, compromise the vehicle's stability, and threaten the passenger's safety. For instance, if a driver accelerates during cornering on a slippery road, both slip controls and ESP could be triggered. Since control modules have their local objectives and are usually designed to be mutually exclusive, a common way to avoid using controls simultaneously is subsystem prioritization. In the previous example, ESP would be given priority, and the vehicle would then use the friction brake to correct the vehicle yaw, decelerating the vehicle contrary to the driver's intention. Volvo classified chassis controls and coupling between different actuators according to the dynamic motion of the vehicle [1]. This classification is helpful to identify possible conflicts between control modules.

New features and actuators are being introduced to vehicles. For instance, Four Wheel Steering (4WS) allows rear-wheel steering; new electric drivetrains and Electro-Hydraulic Brakes (EHB) enable individual wheel torque distribution. Overall, vehicles are being increasingly more over-actuated. These actuators create new degrees of freedom that the driver cannot directly control, hence an increasing number of chassis modules. Increasing over-actuation promises to improve safety (due to actuator redundancy) and enhance dynamic performance (in terms of handling, comfort, or energy

efficiency); however, when the number of actuators and sensors increases, the number of possible conflicts increases too. It becomes more difficult to foresee all the conflicts that could happen, thus requiring more extensive testing. In addition to that, proper coordination between the vehicle actuators is necessary to fully exploit the potential of each subsystem and the couplings between the different domains they impact. The increased over-actuation leads to more complex control architectures that are difficult to maintain and cannot be easily modified to implement new actuators.

Finally, the control functions and electronic architectures of most production vehicles are based on the lowest bids of many supplier solutions [2]. Over many years, these solutions have resulted in costly and less than ideal software and hardware legacies which are incredibly difficult to calibrate and expensive to implement. On the other hand, most new vehicle attributes are increasingly becoming software-based. Control functional and electronic architectures have reached saturation levels, and without fundamental change to this area, the new vehicle features will become more and more challenging to implement. To illustrate this, one can consider the evolution of the number of Electronic Control Unit (ECU) in modern vehicles: modules have their own control logic, resulting in a high number of ECU. Indeed, modern cars can have up to 80 ECU which results in complex and costly electronic architecture [3]. Control integration promises to reduce vehicle costs by reducing the number of sensors and hardware control units.

For all these reasons, proper functional control and electronic control architectures, including an appropriate 'plug and play' optimization strategy for a fully centralized Integrated Vehicle Dynamics and Control (IVDC), also called Global Chassis control (GCC), have tremendous benefits for any vehicle and are magnified for electric cars. Kissai [2] describes attributes of an ideal architecture:

Adaptability: The vehicle is exposed to wide variation in operating conditions, either from the environment, the driver behavior and expectation, or the vehicle properties themselves. Dynamic reconfiguration is necessary to face these variations while maintaining suitable performance and safety.

Fault tolerance: The vehicle must be able to operate in degraded modes, for instance, after a component failure. The failure can be due to hardware (e.g., a fluid leakage, broken sensor) or software.

Extensibility: The architecture should be 'plug and play' to allow adding new features or technologies

without redesigning the entire control strategy.

Modularity: It allows manufacturers and suppliers to independently develop components of the architecture, thus reducing cost and implementation time and ensuring flexibility, extensibility, and reusability.

The goal of this project is to investigate control functionalities, electronic architectures, and various optimization approaches to design a pragmatic architecture and a centralized controller for the next-generation IVDC applicable to electric vehicles. The following questions should be answered to achieve this goal:

1. What is the optimal torque distribution to improve the vehicle dynamics without compromising energy efficiency, and what is the best optimization strategy to coordinate the drivetrain actuators?

2. How can active steering be used to improve vehicle handling in safety-critical situations?

3. What are the best low-level control strategies for propulsion, regenerative braking, torque vectoring, and steering to follow the desired targets?

4. What vehicle states (e.g., vehicle velocity) and environmental parameters (e.g., tire-road friction potential) are necessary to accomplish the desired control task. What are the most suitable estimation methods to observe these signals if direct measurements are not available?

5. If full control integration cannot be achieved, how will partial integration affect vehicle performance and safety?

The novelty of this research is to consider unique control approaches to design IVDC for electric vehicles.

1.2 Dissertation Outline

Chapter 1 conducts a literature review of control architecture and methodologies used in global chassis control.

Chapter 2 describes the modeling techniques used in this thesis. A complete full vehicle model is described. The model includes 6 Degree of Freedom (DoF) associated with the chassis, 4 DoF associated with the vehicle suspension, and 4 DoF associated with the wheel spin. Different tire models are described, and the tire coupling and saturation phenomena are discussed. Finally, models for active chassis systems are provided and analyzed.

Chapter 3 introduces the multi-layered control architecture proposed in this dissertation. This chapter also highlights different methodologies for combined optimization and control and investigates the effect of adding a control allocation in a feedback loop in terms of robustness.

Chapter 4 discusses the normal tire force estimation framework. Simulations with a full vehicle model show that the estimation strategy offers good and robust estimates. A review of the maximum friction coefficient estimation method is conducted, and a simple observer is proposed to estimate the maximum tire forces achievable.

Chapter 5 describes the high-level control strategy for the IVDC. It allocates controls at the wheel level in an actuator-agnostic way such that it can be reused for vehicles equipped with different sets of actuators. Several control implementations are proposed and investigated.

Chapter 6 proposes low-level controller to track the command of the high-level controller presented in Chapter 5. Control strategies are developed to integrate the electric motors with the friction brakes, including when the tire is saturating.

Chapter 7 presents simulation results of the entire control architecture combining the estimation framework, high-level and low-level controllers presented in Chapters 3 to 6.

1.3 Literature Review of Active Systems and Control Integration

1.3.1 Active Chassis Systems

Active safety systems have been gradually introduced in commercial vehicles since the late 70s, starting with Anti-lock Braking System (ABS). First introduced as an option, it is now a safety standard in passenger vehicles. ABS relaxes the brakes to prevent them from locking and improve braking distance, vehicle stability, and steerability. Similarly to ABS, Traction Control System

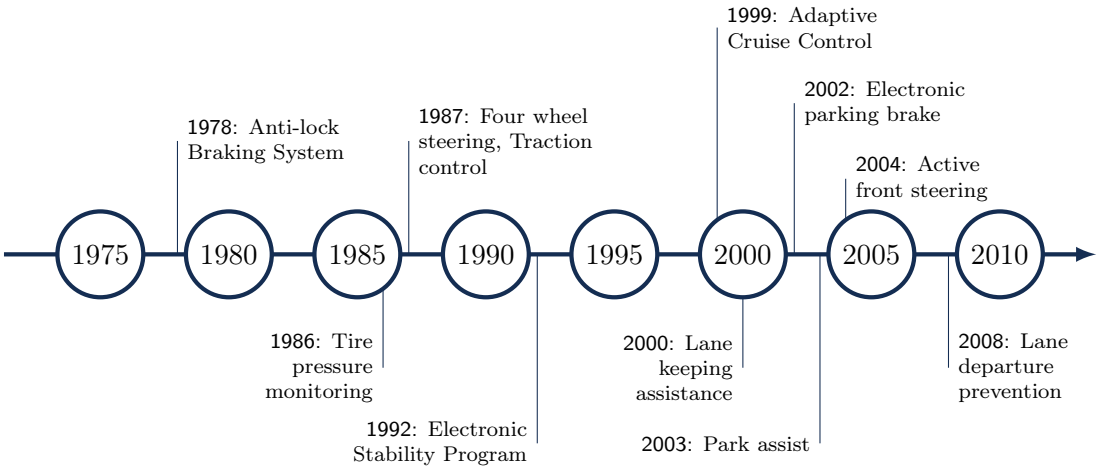

Figure 1.1: Timeline of deployment of active chassis control systems

(TCS) prevents loss of traction during acceleration by reducing the motor torque. ePAS applies a torque on the steering column to help the driver steer. Similarly, AFS altered the wheel steering angle; BMW proposes active steering to increase the gear ratio from the steering wheel to the wheel at low speed to help to park and improve maneuverability and decrease this ratio at high velocity in hazardous situations to improve directional stability [4]. At first, control integration was not necessary since each system mostly affected a single domain: systems based on longitudinal tire forces like ABS and TCS were used for longitudinal control, and systems affecting the lateral tire forces were used for lateral control. The introduction of ESP, also called Electronic Stability Control or Dynamic Stability Control, breaks this assumption. ESP applies a torque difference between the two wheels of the same axle by modulating the brake pressure independently on each side to generate a yaw moment on the vehicle. The torque difference applied by ESP stabilizes the car when it is losing directional stability, but it affects both the vehicle's longitudinal and lateral motions. TV can achieve the same effect but applies a torque difference using motors. Another system that combines different domains is Active Rollover Protection, which detects potential rollover events due to excessive speed during cornering and applies braking torque or reduces the engine torque to prevent the rollover from happening. Figure 1.1 shows a timeline of the deployment of active systems [5].

More and more features are being introduced to passenger vehicles to make them safer, more comfortable, and more power-efficient: Electronic Brake Distribution optimizes front to rear braking

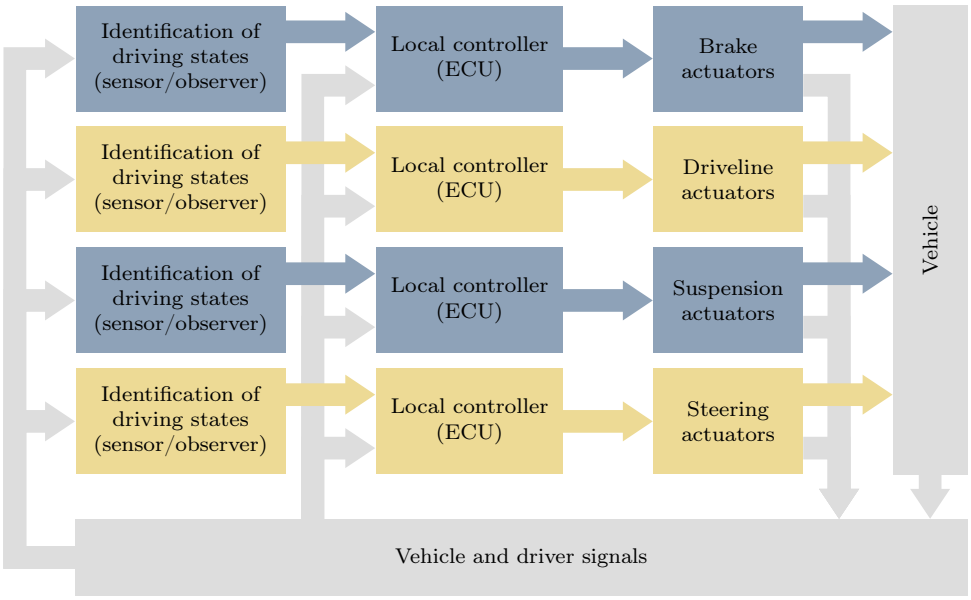

Figure 1.2: Decentralized (or parallel) architecture

torque distribution by modulating the rear brakes pressure; Systems such as Cruise Control and Hill Descent Control monitors the vehicle speed in specific situations; Active Roll Control modifies the roll behavior of the vehicle; Semi-Active Suspensions modifies the ride properties of the car to either improve passenger comfort or vehicle ride performance; Regenerative Braking uses electric machines as a generator to decrease the vehicle speed while recovering energy and reducing the vehicle carbon footprint. The introduction of Advanced Driver-Assistance Systems (ADAS) (e.g., Automatic Emergency Braking, Adaptive Cruise Control, Lane Keeping System), the use of new actuators (e.g., extra electric motors in Hybrid Electric Vehicles (HEV)), and the development of autonomous vehicles will only strengthen this trend.

1.3.2 Integrated Vehicle Control Architecture

Control architectures of GCC are classified in three categories: decentralized, centralized, and multi-layered [6]. With the decentralized architecture, the controls of the different subsystems are designed independently and have their ECU. Fig. 1.2 shows a representation of the decentralized architecture, the architecture has a parallel structure, and control modules are working simultaneously. Each module focuses on its local targets by using the vehicle actuators without supervision. Instead, integration is made downstream by allowing communication between the control modules. This

approach is easy to implement and has a reduced computational load compared to integrated schemes [7], but it does not take advantage of sharing the information of different sensors and actuators [6].

Control methodologies used to coordinate the actuators in decentralized architectures are based on system prioritization. For instance, *pure subsumption* assigns priority to the different control functional objectives. The actuators apply the control with the highest priority and subsume lower authority controls. Other methods can also be used to rank the control authority, e.g., *largest activation* applies the command with the highest modulus [8]. A single control functional dominates and takes over the actuator with both of these methods. It allows to switch between different control modes, and there is a danger of creating instabilities or undesirable transient responses. Other control methods such as Artificial Neural Network (ANN) or fuzzy logic can be used instead to ensure smooth transitions during conflicts.

The centralized architecture utilizes a unique controller for all the actuators of the vehicle (Fig. 1.3). It gathers all signals from the sensors, state estimators, and operation information to generate control signals, usually resulting from a multi-objective optimization. The centralized control architecture's implementation relies on predictive control and robust control methods such as $\mathcal{H}_\infty$ and sliding mode control. While this approach has all the benefits resulting from control integration, it suffers from a lack of flexibility and fail-safe redundancy.

Researchers, both in academia and in the industry, focus mainly on the multi-layered architecture as it offers a more modular, reusable, and extensible platform [9]. In the multi-layered architecture, an upper controller generates generalized forces that should be applied to the vehicle to follow the driver's motion request. A mid-level controller allocates these generalized efforts among the available actuators. Finally, low-level controllers execute their local control targets.

The high-level controller is usually designed with the same advanced Multiple Input Multiple Output (MIMO) control methods used by the centralized architecture. The mid-level control allocation can be formulated as an optimization problem to minimize secondary objectives such as power efficiency or tire wear while meeting high-level targets by using the additional degrees of freedom provided by the vehicle over-actuation. Control allocation can be formulate as more or less computational expensive problems: Linear Programming (LP), Quadratic Programming (QP), Nonlinear Programming (NLP). Computational load is a major concern and needs to be

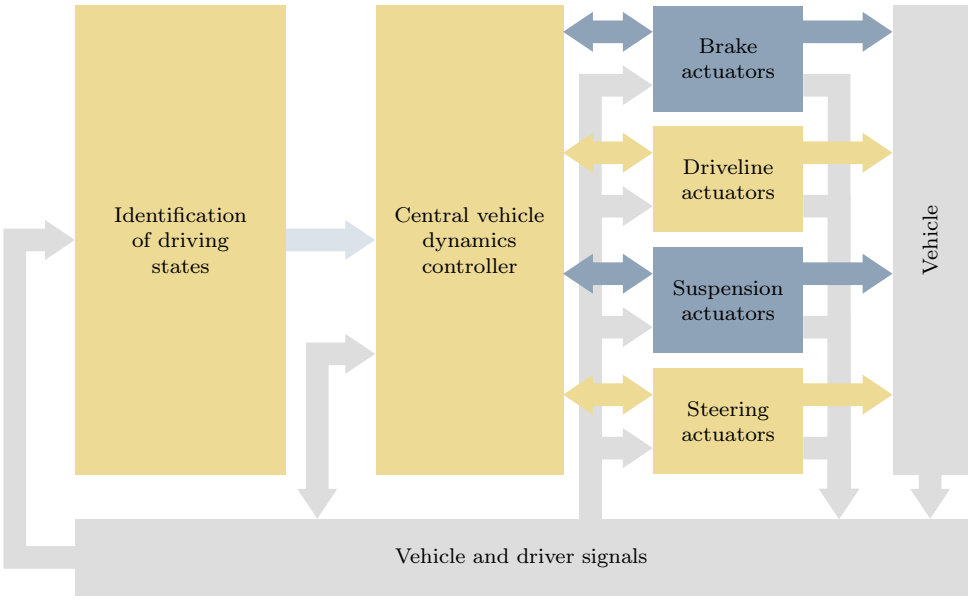

Figure 1.3: Centralized architecture

considered for real-time implementation. Several control allocation methods are well described theoretically, such as direct pseudo inverse based on the Moore-Penrose inversion, daisy-chain, and optimization-based allocation [10], [11]. Other benefits of control allocation include

- Actuator saturation and bandwidth: Constrained allocation problem allows for enforcing constraints on the actuator signals; this can be used to enforce magnitude and rate saturation. Moreover, one can also penalize the rate of change or the use of an actuator.

- Dynamic reconfiguration: It allows for modifying the priority of the actuators, including in case of an actuator failure, and the priority of the targets if all targets cannot be met at the same time. For instance, if the vehicle is near the handling limit, the control allocation can be modified to promote the tracking of lateral force and yaw moment target over the longitudinal force.

For these reasons, the multi-layer architecture offers a more modular and reusable platform for control integration than the centralized approach.

Soltani [11] propose a six-layer architecture (Figure 1.4). The first layer defines the motion target for the six degrees of freedom of the vehicle (longitudinal, lateral, bounce, roll, pitch, and yaw). Depending on the driving conditions, the goal of the integrated controls may change. The

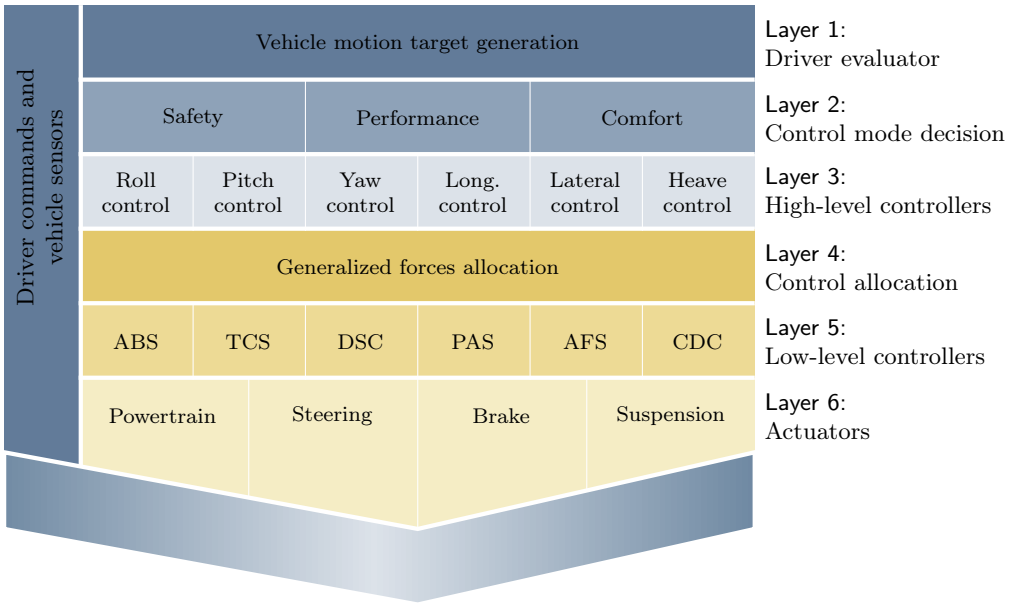

Figure 1.4: Multi-layered architecture of the IVDC control structure

second layer decides the control mode of the architecture (safety, performance, or comfort) based on estimates of the vehicle and environmental states (i.e., vehicle velocities, road friction potential). The third layer generates forces and moments associated with each degree of freedom of the vehicle to follow the vehicle's motion targets. Then, the fourth layer allocates the forces and moments to the actuator. Finally, low-level vehicle dynamic controls (layer 5) such as ABS, TCS, or Continuous Damping Control (CDC) compute control to apply on the smart actuators which correspond to the sixth layer.

Kissai [2], [9] proposes another classification for GCC architectures: *upstream* and *downstream* architectures. Instead of defining the architecture from its control and electronic structure, the definition distinguishes different control architectures by the position of the layer responsible for coordinating the control signal with respect to the control flow. The downstream coordination approach lets the different control modules work independently; the coordination between the actuators is ad hoc and downstream. This approach corresponds to the decentralized architecture. The upstream approach gathers the centralized and multi-layered architectures; it defines signals to command the lower-level subsystems and actuators to achieve multiple objectives. The downstream approach is usually less complex but limited to a single objective, whereas the upstream approach uses more complex control methodologies to achieve multiple objectives.

1.3.3 Control Methodologies for IVDC

Vivas-Lopez [12] implements a centralized architecture to integrate a large set of actuators: ABS-based ESP, semi-active suspensions using CDC, and AFS. The author claims to use a hierarchical control architecture; however, the architecture does not follow the structure of the multi-layered architecture shown in Figure 1.4. Indeed, it lacks the control allocation layer, which outputs low-level control signals from high-level generalized forces and considers couplings between the different domains. Instead, it follows more closely the centralized architecture presented in Figure 1.3 where a central controller directly defines command for lower-level systems and actuators. A decision layer, which combines the 'Identification of driving states' and 'Central vehicle dynamics controller' blocks of Figure 1.3, identifies the driving situation by using the k-Nearest Neighbors (k-NN) classification algorithm. Once the driving situation has been identified, a set of heuristic rules defines whether the driving situation is critical and whether the operating mode should be modified. The decision layer outputs three signals which correspond to the trade-off between ride and comfort for suspension, the use of active steering, and the generation of a brake-based yaw moment for ESP. The active suspension uses a weighted sky-hook and ground-hook control law, and the ESP and active steering are controlled by fuzzy-logic controllers, which define the brake-based yaw moment and the active steering angle to be applied. A rule-based algorithm allocates the brake-based yaw moment to the four wheels. Finally, low-level controllers are implemented by proportional linear Single Input Single Output (SISO) controllers.

He et al. [13] investigate the integration of semi-active suspension using CDC with ESP to improve the vehicle stability and handling in emergency situations. A rule-based centralized controller is used to supervise both ESP controller and CDC actuators. Based on the vehicle sideslip angle and yaw rate, the vehicle is considered to be in stable or unstable conditions. In unstable conditions, the CDC actuator is controlled to follow a sky-hook model to improve the tire load and braking performance; in stable conditions, the CDC controller aims to improve the ride performance.

Falcone et al. [14] proposed to use an Model Predictive Control (MPC) to combine braking and steering in autonomous vehicles, thus implementing a centralized control architecture. The controller sets the steering angle and the longitudinal slip at each wheel to follow a predefined trajectory while minimizing the actuation effort and enforcing physical constraints on the wheel slip to maintain

the vehicle stability. The internal model used by the MPC is linearized at each timestep to reduce the complexity associated with solving the optimization problem. Low-level slip controllers convert the slip request of the high-level controller to a braking torque independently at each wheel. In reference [15], they compare the performance of the MPC whose model is linearized at each timestep with a nonlinear MPC. The linear MPC can perform close to the nonlinear MPC while limiting the computational burden by enforcing an additional constraint on the slip angle. Falcone's work is extended to comprise active differential and fit in the context of IVDC in [16]. The architecture from the latter work yields a multi-layered IVDC architecture where the high-level MPC defines the steering angle and slip ratios at the four wheels. Low-level slip controllers ensure good tracking of the MPC slip targets and coordinate the active brake and active differential actuators; however, few details are given on the design of the slip controllers and their dynamics are neglected.

Varhagen [17] proposed a GCC for vehicles equipped with In-Wheel Electric Motors (IWEM). The proposed architecture takes advantage of the properties of electric motors, namely, IWEM allows generating a yaw moment on the vehicle by using both traction and braking torque contrary to brake-based ESP. Electric motors also have higher bandwidth than EHB, and IWEM allow to estimate both the torque and wheel slip with high accuracy. The last property motivates Varhagen to build a multi-layered architecture centered around the individual wheel slip: high-level controllers define the generalized forces to follow an acceleration and yaw rate request; a control allocation formulated as a Quadratic Programming Problem (QPP) defines low-level longitudinal slip target to meet the high-level target, the control allocation is designed based on a linearized tire model and fuzzy logic is used to retrieve the tire saturation phenomenon; PI slip controllers with Controller Output Observer (COO) disturbance rejection command the electric motor torque; observer and state estimators compute the signal necessary for the controllers to operate. Velazquez [18], [19] propose an analogous architecture for HEV which uses longitudinal wheel force as interfaces for the low-level controllers instead of slip ratios in Varhagen's architecture. The architecture implements gain-scheduled $\mathcal{H}_\infty$ high-level controllers, Youla parameterized low-level controllers to control the actuators, and COO to estimate the longitudinal tire forces. Velazquez compares the slip-based control architecture of Varhagen with his force-based control architecture and a benchmark MPC centralized architecture with idealized assumptions such as access to perfect measurements and information on the road surface friction coefficient. Velazquez concludes that all methods can

successfully stabilize a Four Wheel Drive (4WD) electric vehicle during low-μ launch and high-speed double lane change; the tire force and slip control architecture achieve relatively similar tracking performance to the benchmark MPC architecture. However, the idealized MPC framework provides better power consumption than the other architectures. The work of Varhagen and Velazquez provides complete architectures, including observers and controllers, for an electric 4WD vehicle; however, it is not clear how to modify the architecture to accommodate other actuators such as active steering and suspension. Kissai et al. [20], [21] implement a multi-layer architecture with an $\mathcal{H}_\infty$ filter as a high-level controller, a least square control allocation to distribute the forces to the different wheels, and low-level controllers to control the actuators. Nigicser et al. [22] proposes a MPC scheme to apply a yaw moment on the vehicle body to reduce the risk of secondary collisions after an impact; the yaw moment is allocated to the different wheels by a rule-based controller. They plan to integrate active steering into the control architecture in the future.

Although robust control and optimization-based control have been widely used to implement hierarchical GCC architectures, the literature is rich with other ideas. The following paragraphs list a few manuscripts proposing more esoteric control schemes.

Mousavinejad [23] proposes to use nonlinear control methods to integrate AFS with brake-based ESP. Independent sliding mode controllers are designed for AFS and ESP to follow yaw rate and sideslip angle targets generated by a nonlinear vehicle model. The coordination between the different systems is based on adaption gains that define each subsystem's contribution toward achieving the goal. A metric based on the sideslip angle allows for identifying stable and unstable conditions: in the stable region, only AFS is used to follow the target since the brake-based yaw moment control would reduce the vehicle speed; in the unstable region, both AFS and ESP are used to follow the target and ensure vehicle stability. While the approach is simple, robust, and effective, the proposed architecture is not flexible and extensive to new actuators; moreover, actuator saturation is not considered in the metric distinguishing stable and unstable conditions. Yim [24] coordinates AFS with 4WD and Active Roll Control (ARC) by using a sliding mode high-level controller designed from a bicycle model; the sliding mode controller defines a yaw moment that is then allocated to the vehicle actuators by a weighted least square optimization. Shyrokau [25] implements a multi-layer control system to integrate a wide variety of actuators: frictions brakes, in-wheel electric motors, steering and camber angle actuators, dynamic tire pressure system, and active suspension. The

objective of the proposed integration strategy is mainly to improve the vehicle's energy efficiency. Shyrokau uses a second-order sliding mode controller as the upper controller. The control allocation is formulated as QPP.

Zengin [26] aims to address uncertainties in operating condition and tire forces by using multiple model adaptive control. Robust control guarantees stability and robustness against uncertainties within a certain range; larger uncertainties (e.g., resulting from variation in operating conditions, component aging, or failure) could result in degraded performance or instabilities. Multiple models adaptive control aims to expand the range of uncertainties the system can face without losing performance and stability. Zengin designs a MPC based multiple model adaptive controller to integrate AFS and TV, he concludes that the proposed MPC outperforms other nonadaptive MPC controller in terms of tracking and stability.

Andreasson [27] uses an inverse dynamic model with a $\mathcal{Q}$-loop for high gain feedback to generate the generalized forces to apply on the chassis, which are then allocated to each wheel as torque, steering angle, and tire load by a constrained weighted-least square. The mapping from wheel torque, steering angle, and normal force to generalized force and moment is nonlinear; the mapping is linearized around the current operating point. The linearization simplifies the control allocation and avoids using a nonlinear solver; instead, the allocation is formulated as a linear least-square optimization problem.

Yin [28] notices that the Udwadia-Kabala method is more suitable than the Newtonian and Lagrangian methods for systems with holonomic and nonholonomic equality constraints. Indeed, dealing with rotating motion is difficult in Newtonian mechanics, and contrary to the Udwadia-Kabala method, Lagrangian mechanics require introducing Lagrangian multipliers to address constraints. For these reasons, the author claims that the Udwadia-Kabala method is more suitable for handling systems involving holonomic and nonholonomic constraints with many degrees of freedom. Hence, this procedure applies to a vehicle's lateral and handling motion controller with independent front and active rear steering. In addition, Yin uses a diffeomorphism to convert inequality constraints on the tracking error to equality constraints, allowing the use of the Udwadia-Kabala method even in the presence of inequality constraints. It is worth noting that the work demonstrated by the author relies heavily on nonlinear mapping and does not take into account uncertainties.

1.3.4 Summary of Control Architecture and Methodologies for IVDC

Table 1.1 summarizes the articles reviewed and lists the control methodologies used by the centralized and multi-layered architectures for IVDC. From this literature review, we can conclude that IVDC has enormous potential to improve the performance and safety of hybrid electric vehicles by integrating different actuators and expanding their operating range (for instance, by using electric motors during slip events to take advantage of their improved bandwidth and power efficiency) and taking into account actuator coupling. It also promises to reduce implementation costs of active onboard systems due to better reusability and ease of configuration and calibration. However, many questions stay unanswered, research is still active, and a pragmatic GCC architecture is yet to be developed.

The vehicle must face a wide range of operating conditions and many uncertainties, especially in the interaction between the road and the tire. Designing a control architecture for IVDC also involves enforcing constraints on physical quantities, e.g., on actuators to satisfy the feasibility of the command or on physical quantities such as sideslip to ensure stability. As Andreasson's, Yin's, and Zengin's work illustrates, systematic and efficient approaches to address these challenges (wide range of operating conditions, uncertainties, physical constraints) are still being developed.

The multi-layered architecture seems to be the most promising and practical implementation as it offers more flexibility and reusability while integrating the different controls in a centralized manner. In terms of control implementation, it relies heavily on MIMO robust control methods and numerical optimization methods for control allocation. However, the architecture could be made more flexible and modular. For instance, for a vehicle platform used by several vehicles equipped with different actuators, the entire control allocation of the multi-layered architecture must be redesigned for each set of actuators. The goal of the control allocation is to allocate the actuator commands to minimize secondary objectives (e.g., power efficiency); this *in fine* allocates the forces at the wheel level and should be subject to physical constraints to enforce vehicle stability. Assuming precise knowledge of the actuators is not necessary to allocate the forces at the tire level, the allocation could be divided into two steps: first at the wheel level and then at the actuator level. This abstraction would provide more flexibility and modularity: only the second step would be modified if the set of actuator changes and stability were preserved since the first step would enforce it. Obviously, the first step is not entirely actuator independent, but precise knowledge of the actuators is unnecessary;

actuation saturation limits and bandwidth information should suffice.

Finally, modifying the vehicle control architecture to use a central controller implies modifying the underlying electronic architecture. For instance, brake-based ESP can be implemented in the same ECU as the brake control module. If that feature were implemented in a different control module, the control strategy might suffer from communication delay. Technical specifications, such as computational power or communication bandwidth, should be defined to ensure the feasibility of the architecture.

Table 1.1: Summary of the reviewed control architectures and control methodologies

Author	Actuators	Control methods
	Centralized architecture	
Falcone [14], [15]	EHB, steering	MPC controlling steering angles and wheel slip ratios of an autonomous vehicle. Low-level slip control to convert slip request to a braking torque request.
He [13]	ESP, CDC	Rule-based central controller.
Mousavinejad [23]	EHB, ESP, AFS	Independent sliding mode controllers for ESP and AFS; integration is done via adaption gains.
Vivas-Lopez [12]	CDC, AFS, EHB	k-NN classification with fuzzy logic controller. Rule-based allocation between the four EHB.
Velazquez [19]	4WD	MPC outputting longitudinal tire force from total torque and yaw rate requests.
Yin [28]	AFS, ARS	Control law based on the Udwadia-Kubala approach
Zengin [26]	AFS, TV	MPC-based multiple model adaptive control.
	Multi-layered architecture	
Falcone [16]	EHB, AFS, active differential	MPC controlling steering angles and wheel slip ratios. Slip control to convert slip request to a braking torque request. Downstream coordination between the EHB and active differential actuators.

Table continues on next page

Table 1.1 – continued from previous page

Author	Actuators	Control methods
Andreasson [27]	CDC, EHB, AFS, ARS	Inverse dynamic with $\mathcal{Q}$-loop; constrained weighted least square control allocation.
Kissai [20], [21]	ARS, rear-axle TV, EHB	Gain-scheduled $\mathcal{H}_\infty$ high-level controller generating generalized forces targets; weighted least-square control allocation maps generalized high-level target to long. tire force; low-level controller based on tire map.
Nigicser [22]	4WD	MPC; rule-based control allocation.
Shyrokau [25]	EHB, IWEM, AFS, ARS, CDC	Second-order sliding mode as high-level controller, QP-based control allocation.
Soltani [11]	ePAS, AFS, ESP	Youla parameterized high-level controllers; daisy-chain control allocation.
Varhagen [17]	4WD	PI high-level controllers define generalized forces; constrained QP control allocation of slip ratios; PI controller with COO disturbance rejection as low-level slip controller.
Velazquez [18], [19]	4WD	Gain-scheduled $\mathcal{H}_\infty$ high-level controllers define generalized forces; unconstrained QP control allocation of wheel torques; low-level slip and torque controllers designed with Youla parameterization.

Chapter 2

System Modeling

The first step to design controls is to develop system models. These models can then be used to analyze the systems and better grasp their dynamics, develop model-based controls, and represent the systems in simulation. The model should accurately represent the plant dynamics, but it should also remain simple enough to design control strategy. First, a full-chassis model is derived, which includes the six DoF of the chassis. Second, a simplified planar vehicle model is derived and used to derive vehicle controls. Finally, the vehicle system models are derived with the bond graph modeling technique as it is a powerful modeling method for mechatronic systems which span over multiple energy domains (e.g., mechanical, electrical, hydraulic) [29].

2.1 Chassis Model

The main assumptions used in this model are as follows. The sprung mass is modeled as a rigid body with six DoF. The unsprung masses are attached at the corners of the sprung mass as shown in Figure 2.1. Each unsprung mass can only move in the vertical direction relative to the sprung mass; there are no DoF in the longitudinal and lateral direction between the sprung and unsprung masses. The tire deflection is always normal to the ground. The suspension kinematics and its effect on the suspension forces are ignored. The roll motion of the chassis is constrained to a preset roll axis which represent the axis around which the chassis rolls. The roll axis is defined as the axis going through the front and rear roll centers, these roll centers are assumed to be at a fixed distance below the sprung mass center of mass, and they are the point of application of the forces transmitted to the sprung mass through the suspension links. The chassis model does not include anti-roll bars; thus, it

neglects the coupling between the left and right sides at each axle and the additional roll stiffness introduced by the anti-roll bar. This model possesses eighteen DoF: six DoF are associated with the longitudinal, lateral, heave, pitch, roll, and yaw dynamics of the sprung mass, four additional DoF are associated with the suspension deflection or additional degree of freedom of the unsprung masses, four DoF are associated to the tire deflection, and the last four DoF are associated to the four-wheel spins.

In order to easily describe the motion and dynamics of the vehicle, several reference frames are introduced. A body-fixed coordinate $\mathcal{R}_c$ is attached to the sprung mass at the center of gravity; its axes correspond to the principal directions of the chassis. In addition to this frame, another frame $\mathcal{R}_g$ is defined for each tire. It is attached to the center of the tire contact patch. This frame is obtained by rotating the inertial frame $\mathcal{R}_*$ by the vehicle yaw angle around its z-axis. For steered wheels, it is useful to define the tire frame $\mathcal{R}_t$ which is obtained by rotating $\mathcal{R}_g$ by the wheel steering angle around its z-axis. Finally, $\mathcal{R}_*$ denotes a fixed inertial frame.

The matrix $\underline{\boldsymbol{R}}_{\mathcal{R}_*\to\mathcal{R}_c} = \underline{\boldsymbol{R}}_\phi \underline{\boldsymbol{R}}_\theta \underline{\boldsymbol{R}}_\psi$ represents the transformation from the chassis frame to the inertial frame. The roll, pitch, and yaw rotation matrices $\underline{\boldsymbol{R}}_\phi$, $\underline{\boldsymbol{R}}_\theta$, and $\underline{\boldsymbol{R}}_\psi$ are defined as

$$\underline{\boldsymbol{R}}_\phi = \begin{bmatrix} 1 & 0 & 0 \\ 0 & \cos\phi & \sin\phi \\ 0 & -\sin\phi & \cos\phi \end{bmatrix}, \; \underline{\boldsymbol{R}}_\theta = \begin{bmatrix} \cos\theta & 0 & -\sin\theta \\ 0 & 1 & 0 \\ \sin\theta & 0 & \cos\theta \end{bmatrix}, \; \underline{\boldsymbol{R}}_\psi = \begin{bmatrix} \cos\psi & \sin\psi & 0 \\ -\sin\psi & \cos\psi & 0 \\ 0 & 0 & 1 \end{bmatrix} \tag{2.1}$$

Similarly, the rotation matrix used to convert from the ground frame $\mathcal{R}_g$ to the tire frame $\mathcal{R}_t$ is

$$\underline{\boldsymbol{R}}_{\delta_{ij}} = \begin{bmatrix} \cos\delta_{ij} & \sin\delta_{ij} & 0 \\ -\sin\delta_{ij} & \cos\delta_{ij} & 0 \\ 0 & 0 & 1 \end{bmatrix} \tag{2.2}$$

Notations The following notations are used to define position, velocity, acceleration, force and moment vectors. The position vector $\boldsymbol{l}_{A\to B,\mathcal{R}}$ indicates the vector from point A to point B expressed in the frame $\mathcal{R}$. The velocity vector $\boldsymbol{v}_{A,\mathcal{R}}$ corresponds to the velocity of point A in the frame $\mathcal{R}$, similarly $\boldsymbol{a}_{A,\mathcal{R}}$ corresponds to its acceleration. The angular velocity of a frame is denoted as $\boldsymbol{\omega}_{\mathcal{R}}$. Forces and moments exerted by a body B_1 on B_2 and expressed in the frame $\mathcal{R}$ are noted respectively

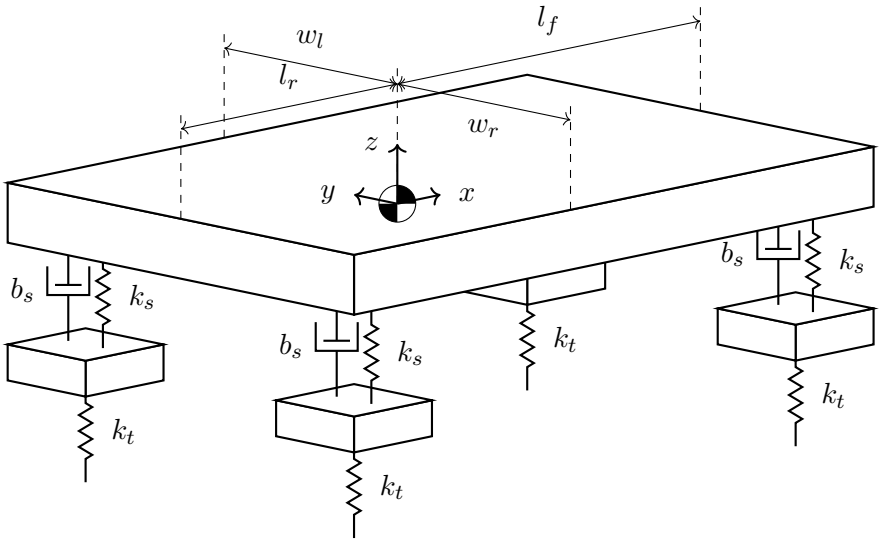

Figure 2.1: Full vehicle model

as $\boldsymbol{F}_{B_1 \to B_2, \mathcal{R}}$ and $\boldsymbol{M}_{B_1 \to B_2, \mathcal{R}}$.

The point CG denotes the center of gravity of the sprung mass, s_{ij} denotes the four corners of the sprung mass where $(i, j) \in \{F, R\} \times \{R, L\}$, u_{ij} denotes the four unsprung masses, and g_{ij} denotes the center of contact patch for the ij wheel. Moreover, the vehicle model consists of the following rigid bodies: the sprung mass S, the unsprung masses U_{ij}, and the ground G.

Given a vector $\boldsymbol{A}$ defined in a body-fixed frame $\mathcal{R}$, the notation $\dot{\boldsymbol{A}}|_{\mathcal{R}}$ is used to denote the vector obtained by differentiating the individual components of the vector $\boldsymbol{A}$. Moreover, A^x correspond to the component of the vector $\boldsymbol{A}$ along the x-axis of the frame in which the vector is expressed. Vectors $\boldsymbol{x}_{\mathcal{R}}$, $\boldsymbol{y}_{\mathcal{R}}$, and $\boldsymbol{z}_{\mathcal{R}}$ correspond to the x, y, and z axes of the frame $\mathcal{R}$.

Using these notations, the states of the vehicle model are the center of gravity velocity $\boldsymbol{v}_{CG,\mathcal{R}_c}$, the sprung mass rotational velocity $\boldsymbol{\omega}_{\mathcal{R}_c}$, the unsprung mass velocities $v^z_{u_{ij},\mathcal{R}_c}$, the suspension length $l^z_{s_{ij} \to u_{ij}, \mathcal{R}_c}$, the laden wheel radius $l^z_{u_{ij} \to g_{ij}, \mathcal{R}_g}$. Additionally, the roll, pitch, and yaw chassis angles are denoted as ϕ, θ, and ψ respectively.

Velocities The velocities at the corners of the chassis are defined from the vehicle geometry, and the sprung mass states $\boldsymbol{v}_{CG,\mathcal{R}_c}$, and $\boldsymbol{\omega}_{\mathcal{R}_c}$.

$$\boldsymbol{v}_{s_{ij},\mathcal{R}_c} = \boldsymbol{v}_{CG,\mathcal{R}_c} + \boldsymbol{\omega}_{\mathcal{R}_c} \times \boldsymbol{l}_{CG \to s_{ij},\mathcal{R}_c} \tag{2.3}$$

The lateral and longitudinal compliances between the sprung mass and unsprung masses are neglected, thus, there is no relative velocity between the center of mass of the chassis and the unsprung masses on the $\boldsymbol{x}_{\mathcal{R}_c}$ and $\boldsymbol{y}_{\mathcal{R}_c}$ directions. The vertical component of the velocity of the unsprung masses $v^z_{u_{ij},\mathcal{R}_c}$ is dictated by the vertical velocity of the point s_{ij} and by the suspension relative velocity. The velocities of the unsprung masses in the chassis frame along is

$$\boldsymbol{v}_{u_{ij},\mathcal{R}_c} = \begin{bmatrix} v^x_{u_{ij},\mathcal{R}_c} \\ v^y_{u_{ij},\mathcal{R}_c} \\ v^z_{u_{ij},\mathcal{R}_c} \end{bmatrix} = \boldsymbol{v}_{s_{ij},\mathcal{R}_c} + \boldsymbol{\omega}_{\mathcal{R}_c} \times \boldsymbol{l}_{s_{ij}\to u_{ij},\mathcal{R}_c} + \begin{bmatrix} 0 \\ 0 \\ \dot{l}^z_{s_{ij}\to u_{ij},\mathcal{R}_c} \end{bmatrix} \tag{2.4}$$

The velocities of the unsprung masses must first be converted to the ground frame $\mathcal{R}_g$ as follows $\boldsymbol{v}_{s_{ij},\mathcal{R}_g} = \underline{\boldsymbol{R}}^T_\theta \underline{\boldsymbol{R}}^T_\phi \boldsymbol{v}_{s_{ij},\mathcal{R}_c}$ to compute the velocities of the contact patch. Finally, the velocities of the contact patch g_{ij} is defined by the velocity of the sprung mass s_{ij} and by the tire deflection relative velocity as follows,

$$\boldsymbol{v}_{g_{ij},\mathcal{R}_g} = \boldsymbol{v}_{u_{ij},\mathcal{R}_g} + \boldsymbol{\omega}_{\mathcal{R}_g} \times \boldsymbol{l}_{u_{ij}\to g_{ij},\mathcal{R}_g} + \begin{bmatrix} 0 \\ 0 \\ \dot{l}^z_{u_{ij}\to g_{ij},\mathcal{R}_g} \end{bmatrix} \tag{2.5}$$

Tire Forces The lateral and longitudinal velocities of the contact patch can be used to compute the wheel's longitudinal and lateral slips. From this values, an empirical model like the Magic Formula described in Section 2.2.1 can be used to compute the longitudinal and lateral tire forces $F^x_{G\to U_{ij},\mathcal{R}_t}$ and $F^y_{G\to U_{ij},\mathcal{R}_t}$. The tire model allows computing the tire forces in the tire frame $\mathcal{R}_t$. Thus, for steered wheels, it is necessary to convert the forces from the tire frame $\mathcal{R}_t$ to the frame $\mathcal{R}_g$.

The tire normal forces is defined by the tire deflection in the $\boldsymbol{z}_{\mathcal{R}_t} = \boldsymbol{z}_{\mathcal{R}_g}$ direction. In the case of wheel lift-off, the tire deflection must be saturated so that the wheel radius does not exceed the unladen wheel radius. A linear relation is assumed between the tire normal deflection and the tire normal force,

$$F^z_{G\to U_{ij},\mathcal{R}_g} = F^z_{G\to U_{ij},\mathcal{R}_t} = k_t(r_{ijw} - r_{unladen}) \tag{2.6}$$

$$r_{ijw} = \min(r_{unladen}, l^z_{g_{ij}\to u_{ij},\mathcal{R}_g}) \tag{2.7}$$

Suspension Forces Neglecting the lateral and longitudinal compliance between the sprung and unsprung masses would require computing the derivative of the longitudinal and lateral acceleration of the unsprung masses in the vehicle frame $\mathcal{R}_c$. Differentiating the velocities is possible but is not desirable in simulation. Instead, Shim [30] proposes to neglect the inertia forces of the unsprung mass in the longitudinal and lateral directions. Shim shows that this simplification does not significantly impact the roll response in a step steer scenario, even during vehicle roll-over and wheel lift-off. Using this simplification, the lateral and longitudinal forces transmitted to the sprung mass by the suspension become:

$$F^x_{U_{ij}\to S,\mathcal{R}_g} = -F^x_{S\to U_{ij},\mathcal{R}_g} = F^x_{G\to U_{ij},\mathcal{R}_g} + F^x_{grav\to U_{ij},\mathcal{R}_g} \tag{2.8}$$

$$F^y_{U_{ij}\to S,\mathcal{R}_g} = -F^y_{S\to U_{ij},\mathcal{R}_g} = F^y_{G\to U_{ij},\mathcal{R}_g} + F^y_{grav\to U_{ij},\mathcal{R}_g} \tag{2.9}$$

Each suspension is modeled by a spring and damper mounted in parallel. The suspension stiffness and the damper are nonlinear and represented by the functions $k(\cdot)$ and $b(\cdot)$ respectively. The total force applied by the strut to the sprung mass in the $\boldsymbol{z}_{\mathcal{R}_c}$ is

$$F^z_{U_{ij}\to S,\mathcal{R}_c} = k(l^z_{s_{ij}\to u_{ij},\mathcal{R}_c}) + b(\dot{l}^z_{s_{ij}\to u_{ij},\mathcal{R}_c}) \tag{2.10}$$

Finally, the force applied by the unsprung mass on the chassis in the chassis frame can be obtained using rotation matrices $\boldsymbol{F}_{U_{ij}\to S,\mathcal{R}_c} = \underline{\boldsymbol{R}}_\phi \underline{\boldsymbol{R}}_\theta \boldsymbol{F}_{U_{ij}\to S,\mathcal{R}_g}$.

Sprung Mass Equations of Motion The vehicle is assumed to have a roll axis on which the lateral force $F^z_{U_{ij}\to S,\mathcal{R}_c}$ applied by the unsprung masses acts. The inclusion of this roll axis reduces the total roll moment transferred to the sprung mass by the suspension since it reduces the level arm of the lateral forces acting on the sprung mass. Instead of higher roll moments, the roll axis introduces a load transfer between the wheels through the suspension links [30]. The load transfer is described by jacking forces $F_{jack,i}$ which transfers the load on the axle i from the left wheel to the right wheel. The moment applied by the jacking forces around the roll axis is $t_i \cdot F_{jack,i}$ where t_i is the track width of the axle i and this moment must compensate for the reduction of the roll moment due to t

the presence of a roll axis. Thus, the jacking forces are

$$t_i \cdot F_{jack,i} = M_{no\ roll,i} - M_{roll,i} \tag{2.11}$$

$$M_{no\ roll,i} = \sum_i F^y_{G\to U_{ij},\mathcal{R}_g} \cdot l^z_{g_{ij}\to u_{ij},\mathcal{R}_g} + F^y_{U_{ij}\to S,\mathcal{R}_c} \cdot l^z_{u_{ij}\to s_{ij},\mathcal{R}_g} \tag{2.12}$$

$$M_{roll,i} = \sum_i h_{ri} \cdot F^y_{U_{ij}\to S,\mathcal{R}_g} \tag{2.13}$$

where h_{ri} is the distance of the roll center of the axis i from the sprung mass. $M_{no\ roll,i}$ would be the roll moment applied by the lateral force of the axle i on the sprung mass in the absence of a roll, and $M_{roll,i}$ is the roll moment applied by the axle when considering the roll axis. Finally, we define the vector $\boldsymbol{F}_{\Delta ij,\mathcal{R}_c}$ as follows to describe the load transfer.

$$\boldsymbol{F}_{\Delta ij,\mathcal{R}_c} = \begin{cases} \begin{bmatrix} 0 & 0 & +F_{jack,i} \end{bmatrix}^T, & \text{if } j = R \\ \begin{bmatrix} 0 & 0 & -F_{jack,i} \end{bmatrix}^T, & \text{if } j = L \end{cases} \tag{2.14}$$

Let $\boldsymbol{F}_{\overline{S}\to S,\mathcal{R}_c}$ and $\boldsymbol{M}_{\overline{S}\to S,\mathcal{R}_c}$ be the sum of the external forces and moments, respectively, acting on the sprung mass. The equations of motion of the chassis are given by

$$\left.\frac{\mathrm{d}\boldsymbol{v}_{CG,\mathcal{R}_c}}{\mathrm{d}t}\right|_{\mathcal{R}_c} = \frac{1}{m_s}\boldsymbol{F}_{\overline{S}\to S,\mathcal{R}_c} - \boldsymbol{\omega}_{\mathcal{R}_c} \times \boldsymbol{v}_{CG,\mathcal{R}_c} \tag{2.15}$$

$$\left.\frac{\mathrm{d}\boldsymbol{\omega}_{\mathcal{R}_c}}{\mathrm{d}t}\right|_{\mathcal{R}_c} = \underline{\boldsymbol{I}}^{-1}\boldsymbol{M}_{\overline{S}\to S,\mathcal{R}_c} \tag{2.16}$$

The external forces acting on the chassis are the force of gravity $\boldsymbol{F}_{grav\to S,\mathcal{R}_c}$, the force exerted by the suspension (in the vertical direction), and unsprung masses (in the lateral and longitudinal direction) $\boldsymbol{F}_{U_{ij}\to s,\mathcal{R}_c}$, and the jacking force due to the presence of the roll axis $\boldsymbol{F}_{\Delta ij,\mathcal{R}_c}$. Hence,

$$\boldsymbol{F}_{\overline{S}\to S,\mathcal{R}_c} = \boldsymbol{F}_{grav\to S,\mathcal{R}_c} + \sum_{ij} \boldsymbol{F}_{U_{ij}\to S,\mathcal{R}_c} + \boldsymbol{F}_{\Delta ij,\mathcal{R}_c} \tag{2.17}$$

As explained previously, the presence of a roll axis decreases the roll moment applied to the chassis by the lateral forces. The roll moment is generated by the imbalance of lateral and vertical forces around the roll axis. The pitch and yaw moment applied on the chassis are defined from the y and z components of the cross-product $\boldsymbol{l}_{CG\to s_{ij},\mathcal{R}_c} \times \boldsymbol{F}_{U_{ij}\to S,\mathcal{R}_c}$.

Thus, the roll, pitch, and yaw moments applied on the chassis are given by

$$M^x_{\overline{S}\to S,\mathcal{R}_c} = \sum_{ij} h_{ri} \cdot F^y_{U_{ij}\to S,\mathcal{R}_g} + \sum_i \frac{t_i \cdot (F^z_{U_{iL}\to S,\mathcal{R}_g} - F^z_{U_{iR}\to S,\mathcal{R}_g})}{2} \tag{2.18}$$

$$M^y_{\overline{S}\to S,\mathcal{R}_c} = \sum_{ij} l^z_{g_{ij}\to CG,\mathcal{R}_c} \cdot F^x_{G\to U_{ij},\mathcal{R}_c} + \sum_{ij} l^z_{u_{ij}\to s_{ij},\mathcal{R}_c} \cdot F^x_{U_{ij}\to S,\mathcal{R}_c} \tag{2.19}$$

$$- \sum_{ij} l^x_{u_{ij}\to s_{ij},\mathcal{R}_c} \cdot F^z_{U_{ij}\to S,\mathcal{R}_c} \tag{2.20}$$

$$M^z_{\overline{S}\to S,\mathcal{R}_c} = \sum_{ij} l^x_{u_{ij}\to s_{ij},\mathcal{R}_c} \cdot F^y_{U_{ij}\to S,\mathcal{R}_c} - \sum_{ij} l^y_{u_{ij}\to s_{ij},\mathcal{R}_c} \cdot F^x_{U_{ij}\to S,\mathcal{R}_c} \tag{2.21}$$

The first term of the roll moment corresponds to the roll moment produced by the lateral forces around the roll axis; the second term corresponds to the roll moment produced by vertical forces. The first term of the pitch moment corresponds to the moment produced around the axis $\boldsymbol{y}_{\mathcal{R}_g}$ by the longitudinal tire forces, which are transmitted to the sprung mass through the suspension. The second and third terms correspond to the cross product of the longitudinal and vertical forces acting on the sprung mass, respectively. Finally, the yaw moment is defined from the cross product of the longitudinal and lateral forces acting on the sprung mass.

The angular velocities of the sprung mass are given as follows,

$$\omega_x = \dot{\phi} - \dot{\psi}\sin\theta \tag{2.22}$$

$$\omega_y = \dot{\theta}\cos\phi + \dot{\psi}\cos\theta\sin\phi \tag{2.23}$$

$$\omega_z = -\dot{\theta}\sin\phi + \dot{\psi}\cos\theta\cos\phi \tag{2.24}$$

Thus, the Cardan angle should be integrated as follows,

$$\dot{\phi} = \omega_x + \sin\phi\tan\theta\ \omega_y + \cos\phi\tan\theta\ \omega_z \tag{2.25}$$

$$\dot{\theta} = \cos\phi\ \omega_y - \sin\phi\ \omega_z \tag{2.26}$$

$$\dot{\psi} = \frac{\sin\phi}{\cos\theta}\ \omega_y + \frac{\cos\phi}{\cos\theta}\ \omega_z \tag{2.27}$$

Unsprung Mass Equations of Motion Only the state associated with the vertical movement of the unsprung mass is updated since we assume that there is no lateral and longitudinal deflection

between the chassis and the unsprung masses. The update equation is given as follows,

$$\dot{v}^z_{u_{ij},\mathcal{R}_c} = \frac{1}{m_{us}}\Big(F_{grav\to U_{ij},\mathcal{R}_c} + F_{G\to U_{ij},\mathcal{R}_c} - F_{U_{ij}\to S,\mathcal{R}_c} - F_{\Delta ij,\mathcal{R}_c}\Big) - \omega^x_{\mathcal{R}_c} v^y_{u_{ij},\mathcal{R}_c} + \omega^y_{\mathcal{R}_c} v^x_{u_{ij},\mathcal{R}_c} \quad (2.28)$$

Suspension and Tire Deflection Equations of Motion The equation of motion of the DoF associated to the suspension deflection is defined as follows

$$\dot{l}_{s_{ij}\to u_{ij}} = v^z_{u_{ij},\mathcal{R}_c} - v^z_{s_{ij},\mathcal{R}_c} \quad (2.29)$$

The tire normal deflection is assumed to be normal to the ground, thus, its equation of motion is

$$\dot{l}_{uij\to gij} = v^z_{gij,\mathcal{R}_g} - v^z_{uij,\mathcal{R}_g} \quad (2.30)$$

$$= v^z_{gij,\mathcal{R}_g} - (\underline{\boldsymbol{R}}^T_\theta \underline{\boldsymbol{R}}^T_\phi \boldsymbol{v}_{uij,\mathcal{R}_c}).\boldsymbol{z}_{\mathcal{R}_g} \quad (2.31)$$

where the normal velocity $v^z_{gij,\mathcal{R}_g}$ is an input of the system defined from the road profile. Road models are usually formulated as functions that define the height and the normal to the ground at any point. Road models can be divided into two categories: deterministic and stochastic models. *Deterministic* profiles can be defined as simple mathematical expressions or, more generally, as a heightmap that stores the measurement of a road profile. OpenCRG defines an open file format to store the profile of road surfaces. *Stochastic* profiles are defined from the statistical properties of the road, namely from its Power Spectral Density (PSD). Several expressions exist for the PSD of the road and usually rely on a few parameters such as the road roughness coefficient and its waviness exponent [31].

Wheel Spin Equation of Motion Each wheel has a degree of freedom corresponding to its wheel spin. The equation of motion for that degree of freedom is

$$J_w \dot{\omega}_{ij} = \tau - r_{ijw} f_{ijx} \quad (2.32)$$

where ω_{ij} is the wheel angular velocity, J_w is its inertia around its rotation axis, τ is the cumulative torque applied by the friction brakes and the drivetrain, r_{ijw} is the wheel radius defined in (2.7),

and $f_{ijxt} = F^x_{G\to U_{ij},\mathcal{R}_t}$ is the longitudinal tire force in the tire frame.

2.2 Tire Modeling

The force generated by the tire results from the visco-elasticity of the tire material [32]: when subjected to wheel slip, the tire deforms itself and generates a force. The longitudinal slip ratio and the velocity in the tire frame $\mathcal{R}_t$ are defined by:

$$\boldsymbol{v}_{gij,\mathcal{R}_t} = \underline{\boldsymbol{R}}_{\delta_{ij}} \boldsymbol{v}_{gij,\mathcal{R}_g}, \quad s_{ijx} = \frac{r_{ij}\omega_{ij} - v^x_{gij,\mathcal{R}_t}}{|v^x_{gij,\mathcal{R}_t}|} \tag{2.33}$$

The slip angle can be obtained from the velocity at the contact patch in the chassis frame $\mathcal{R}_c$.

$$s_{ijy} = \delta_{ij} - \tan^{-1}\left(\frac{v^y_{gij,\mathcal{R}_c}}{v^x_{gij,\mathcal{R}_c}}\right) \tag{2.34}$$

The tire normal force results from the compression of the tire normal stiffness. In the model of the vehicle, the tire compliance is assumed to be normal to the ground; therefore, the tire normal force is given by the following equation

$$F^z_{ground\to uij,\mathcal{R}_g} = \max(0, k_t q_{tij}) \tag{2.35}$$

where k_t is the tire stiffness and q_{tij} is the tire deflection.

The longitudinal and lateral tire forces $F^x_{ground\to uij,\mathcal{R}_g}$ and $F^y_{ground\to uij,\mathcal{R}_g}$ are defined by a tire model which maps the slip ratio and slip angle[1] to the longitudinal and lateral tire forces. Writing the longitudinal, lateral, and normal force in a vector form yield the vector $\boldsymbol{F}_{ground\to uij,\mathcal{R}_t}$. The forces are then expressed in the chassis frame.

$$\boldsymbol{F}_{ground\to uij,\mathcal{R}_c} = \underline{\boldsymbol{R}}_\phi \underline{\boldsymbol{R}}_\theta \boldsymbol{F}_{ground\to uij,\mathcal{R}_g} \tag{2.36}$$

$$= \underline{\boldsymbol{R}}_\phi \underline{\boldsymbol{R}}_\theta \underline{\boldsymbol{R}}^T_{\delta_{ij}} \boldsymbol{F}_{ground\to uij,\mathcal{R}_t} \tag{2.37}$$

[1] Depending on the tire model used and its complexity, other quantities can be needed to compute the tire force, e.g., the camber angle, the normal tire force.

2.2.1 Magic Formula Tire Model

The Magic Formula [33] is one of the most well-known semi-empirical tire models used in vehicle dynamics. Several versions of the Pacejka tire model exist; a simplified Magic Formula is presented in this section; it considers combined longitudinal slip and cornering, neglects the nonlinear relation between the wheel load and the tire force, and assumes a linear relation instead. The model defines a combined slip quantity $s = \sqrt{s_x^2 + s_y^2}$ which is converted to a combined friction coefficient:

$$\mu(s) = \mathrm{MF}\,(s) = D \sin\Big(C \tan^{-1}\left(Bs - E(Bs - \tan^{-1} Bs)\right)\Big) \tag{2.38}$$

The longitudinal and lateral tire friction coefficients are then calculated as follows by assuming a friction circle. Finally, since the model neglects the load sensitivity, the longitudinal and lateral tire forces are proportional to the normal force.

$$\mu_i = \frac{s_i}{s}\mu(s) \quad i \in \{x, y\} \tag{2.39}$$

$$f_i = \mu_i f_z \quad i \in \{x, y\} \tag{2.40}$$

2.2.2 LuGre Tire Model

Pacejka's tire model gives a simple representation of the tire. However, it only captures the steady-state operation of the tire and cannot be used to study the transient properties of the tire, e.g., for abrupt transient or μ-jump. Finally, it does not provide a physical interpretation of the tire force generation mechanism. Distributed tire friction models are a family of tire models that addresses these shortcomings. It models the tire as a rigid carcass on which flexible microscopic bristles are attached. The friction forces are generated through the interaction of the bristles with the road surface at the tire contact patch (Figure 2.2). This family includes tire models such as the brush tire model [33], Dahl [34], and LuGre [35] tire models.

The bristle deflection along the longitudinal and lateral axes is denoted as $z_x(\zeta, t)$ and $z_y(\zeta, t)$ where ζ defines the position of the bristle at the contact patch. The bristle deflection is determined by the relative velocity between the road and the tire defined in the longitudinal direction as $v_{rx} = r\omega - v\cos\alpha$ and in the lateral direction as $v_{ry} = -v\sin\alpha$. The bristle deflection dynamics is

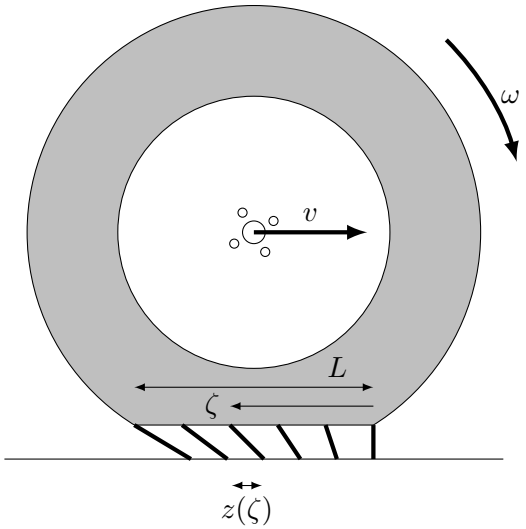

Figure 2.2: Brush representation of the tire

described by the following partial differential equation

$$\frac{\mathrm{d}z_i(\zeta,t)}{\mathrm{d}t} = \frac{\partial z_i(\zeta,t)}{\partial t} + r|\omega|\frac{\partial z_i(\zeta,t)}{\partial \zeta} = \Phi_i(v_r, z) \tag{2.41}$$

The friction generated by a single bristle at position ζ is

$$\mu_i(\zeta,t) = \sigma_{0i} z(\zeta,t) + \sigma_{1i}\frac{\partial z(\zeta,t)}{\partial t} + \sigma_{2i} v_{ri} \tag{2.42}$$

where σ_{0i} is the bristle longitudinal stiffness, σ_{1i} is the bristle damping coefficient, and σ_{2i} is the viscous friction.

The friction forces and moments are computed by summing the contribution of all the tire bristle over the contact patch. Hence the longitudinal, lateral tire forces and self aligning moment

$$f_i(t) = \int_0^L \mu_i(\zeta,t) f_z(\zeta)\,\mathrm{d}\zeta, \quad m_z(t) = \int_0^L \mu_y(\zeta,t) f_z(\zeta)\Big(\frac{L}{2} - \zeta\Big)\,\mathrm{d}\zeta \tag{2.43}$$

The LuGre tire model assumes that the friction is proportional to the bristle deflection. When the friction reaches the friction potential, the bristle tip starts to slip over the road surface, the bristle deflection becomes constant and the friction force is saturating. Assuming a Stribeck friction for the

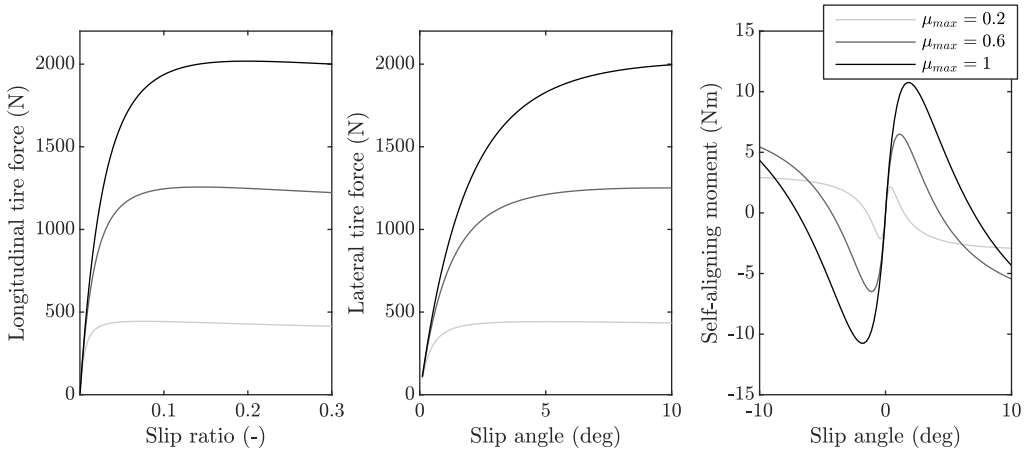

Figure 2.3: Steady-state tire forces and moments with different coefficient of friction. Assuming a friction circle (i.e. $\mu_{max,x} = \mu_{max,y}$) and a fixed constant static to kinetic friction ratio (i.e. $\mu_{sx} = 1.2\mu_{kx}$ and $\mu_{sx} = 1.2\mu_{kx}$).

friction potential, we have

$$g(v_r) = \mu_k(v_r) + \big(\mu_s(v_r) - \mu_k(v_r)\big)e^{-\left(\frac{\|v_r\|}{v_s}\right)^{\delta}} \tag{2.44}$$

where $\mu_k(v_r)$ is the kinetic friction and μ_s is the static friction. Assuming a tire friction circle, the stiction dynamics function Φ of a LuGre tire model is given by

$$\Phi_i(v_r, z) = v_{ri} - \frac{\sigma_{0i}\,\|v_r\|}{g(v_r)}z \tag{2.45}$$

Steady-state longitudinal and lateral tire forces, and self-aligning moment for different road friction potentials are shown in Figure 2.3. A trapezoidal normal force distribution is used when computing the tire forces and moments. According to the LuGre tire model, the road friction potential does not impact the tire forces at low slip. It only has an impact when the tire is saturating.

The distributed LuGre tire model can be transformed into a lumped model by using the average lateral and longitudinal bristle deflection as its only states

$$\bar{z}_i(t) = \frac{1}{f_z}\int_0^L z_i(\zeta, t)f_z(\zeta)\,\mathrm{d}\zeta \quad \text{where } f_z = \int_0^L f_z(\zeta)\,\mathrm{d}\zeta \tag{2.46}$$

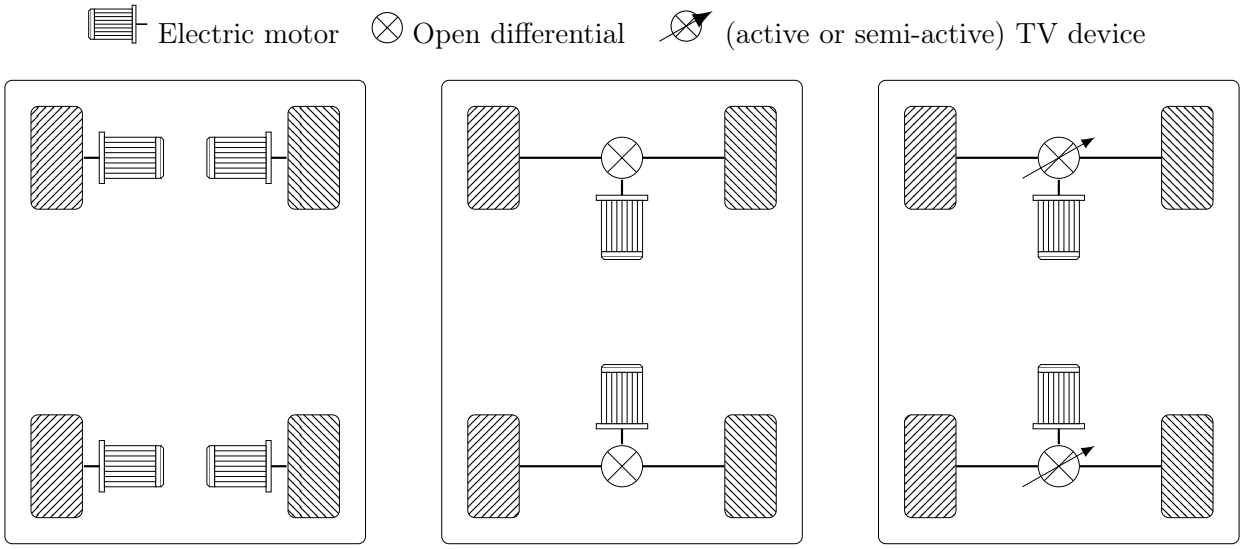

(a) Quad-motor drivetrain

(b) Dual-motor drivetrain with open differential

(c) eAWD drivetrain with left-to-right TV device

Figure 2.4: Electric drivetrain topologies.

2.3 Chassis System Model

2.3.1 Drivetrain Model

Drivetrain topologies of electric vehicles offer more flexibility than conventional vehicles due to the possibility of using several motors to control the wheels independently. Addressing these different topologies is one of the challenges a reusable control architecture must address. Several drivetrain topologies are considered in this work to evaluate the reusability of the control architecture (Figure 2.4): a quad-motor topology with one electric motor at each wheel; a dual-motor topology with one electric motor per axle, and an open differential to split the torque between the two wheels; an e-All Wheel Drive (eAWD) drivetrain with a traction motor at each axle and an active or semi-active TV device to create a torque difference between the left and right wheels. For all topologies, we assume the vehicle is equipped with EHB. Contrary to conventional hydraulic brakes, EHB allows applying different pressure at each brake; thus, we have control of individual friction braking torque.

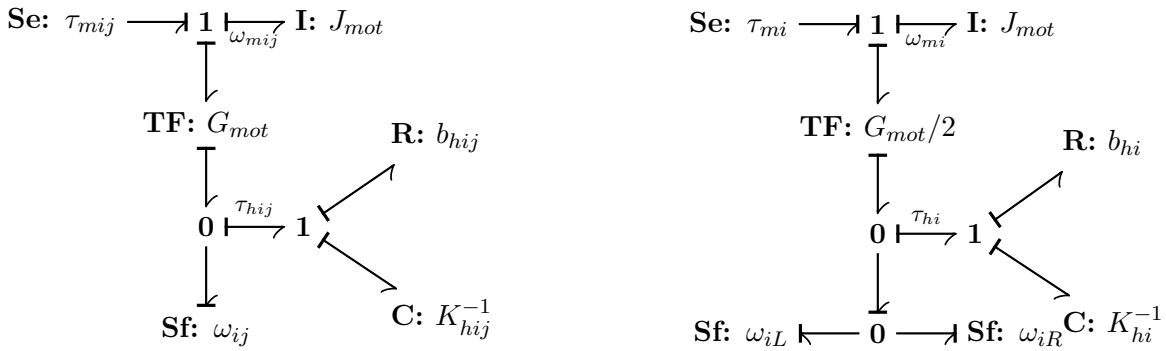

(a) Quad-motor drivetrain **(b)** Dual-motor drivetrain

Figure 2.5: Bond graph diagram of the quad and dual-motor drivetrain topologies.

Quad-Motor Model

The quad-motor topology (Figure 2.4a) has one motor per wheel. De Novellis [36] shows that this configuration provides the best performance in terms of handling and maneuverability when compared to other drivetrain topologies that cannot achieve left-to-right TV on each axle. This configuration allows applying wheel torque independently at each wheel. It improves power efficiency as regenerative braking can be used independently at each wheel. Moreover, compared to conventional vehicles, it eliminates the power losses associated with the transmission. The individual wheel torque distribution also has a considerable potential to improve the slip control of the wheels. However, if one motor becomes inoperable, the axle with the faulty motor cannot produce propulsion/braking torque without generating left-to-right torque vectoring.

Since there is no mechanical connection between the four wheels, each corner of the car can be modeled independently. The major assumptions used by this model are: the major dynamic modes of the system are defined by the electric motor inertia and shaft compliance [37], the gear lash and shaft inertia are neglected. The bond graph model is shown in Figure 2.5a

$$\tau_{hij} = K_{hij}\theta_{hij} + b_{hij}\dot{\theta}_{hij} \tag{2.47}$$

$$J_{mot}\dot{\omega}_{mij} = \tau_{mij} - \frac{\tau_{hij}}{G_{mot}} \tag{2.48}$$

$$\dot{\theta}_{hij} = \frac{\omega_{mij}}{G_{mot}} - \omega_{ij} \tag{2.49}$$

where τ_{hij} is the torque applied by the halfshaft on the wheel, τ_{mij} is the motor torque, K_{hij} and

b_{hij} are the halfshaft stiffness and damping, J_{mot} is the motor inertia, G_{mot} is the gear ratio, θ_{hij} is the halfshaft deflection, ω_{mij} is the motor speed, and ω_{ij} is the wheel speed.

Dual-Motor Model

The dual-motor topology (Figure 2.4b) uses two electric motors, one at each axle. The open differential splits in half the axle torque between the two wheels. Contrary to the quad motor topology, this configuration cannot achieve left-to-right TV. However, front-to-rear TV can still improve the handling behavior of a vehicle [19]. Figure 2.4c shows the last topology considered in this project. It is a variation of the dual-motor topology with left-to-right TV capabilities. It uses an electric motor on the front axle to apply active left-to-right torque vectoring and an e-Limited Slip Differential (eLSD) on the rear axle to apply semi-active TV from the wheel with high-angular velocity to the wheel with low-angular velocity.

The model of the dual-motor is based on the same assumptions as the one used by the quad-motor drivetrain, the bond graph diagram is shown in Figure 2.5b. Since each axle uses an open differential, the two halfshafts connecting the wheels to the differential are lumped into an equivalent halfshaft of stiffness K_{hi} and damping b_{hi}.

$$\tau_{hi} = K_{hi}\theta_{hi} + b_{hi}\dot{\theta}_{hi} \tag{2.50}$$

$$J_{mot}\dot{\omega}_{mi} = \tau_{mi} - \frac{2\tau_{si}}{G_{mot}} \tag{2.51}$$

$$\dot{\theta}_{hi} = \frac{2\omega_{mot}}{G_{mot}} - (\omega_{iL} + \omega_{iR}) \tag{2.52}$$

where τ_{hi} is the torque applied by the motor on the open differential, τ_{mi} is the motor torque, ω_{mi} is the motor speed, and ω_{iL} and ω_{iR} are the wheel speeds.

eAWD Model

Figure 2.6 shows the eAWD drivetrain layout. There is no mechanical connection between the front and rear axles. Thus, each axle can be modeled and controlled independently. This drivetrain provides the same capabilities as the quad-motor topology, i.e., the torque at each wheel can be controlled independently but with less flexibility, since it requires coordination between the left and right wheels of each axle.

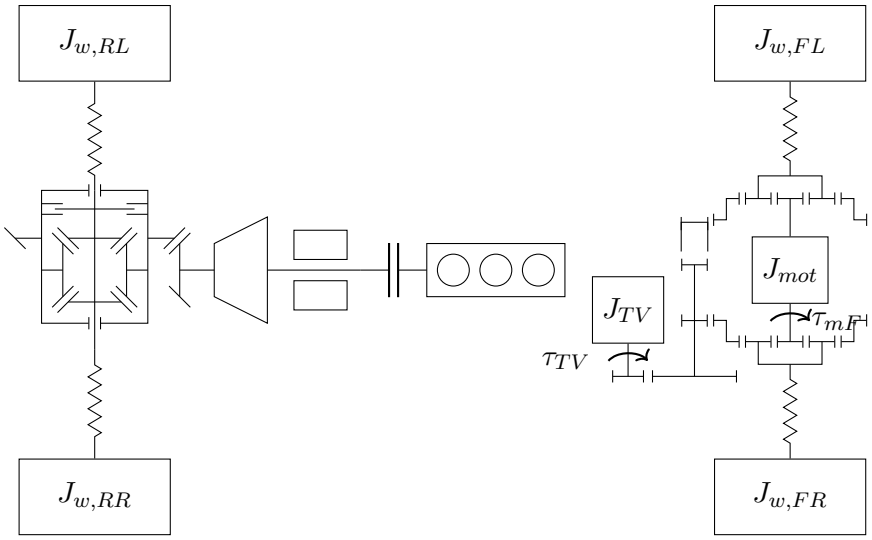

Figure 2.6: eAWD drivetrain schematic

Two electric motors power the front axle: the main motor, placed between two planetary gears and connected to the sun gears, provides traction force to the two front wheels; a smaller TV motor actively creates a torque difference between the two front wheels, it is connected to the ring gear and an idler gear which changes the direction of rotation on one side of the axle; The wheel shafts are connected to the carriers of the planetary gear. The left and right wheels rotate at the same speed during straight-line driving.

The rear axle is powered by an electric motor which transmits torque to an eLSD. The eLSD can be controlled to apply a torque difference between the left and right wheel if one wheel is rotating faster than the other. Contrary to the front axle, it is only possible to apply a torque difference from the fast-spinning wheel to the low-spinning wheel. The dynamic of the electric motor connected to the eLSD is not shown in Figure 2.6.

Figure 2.7 shows the bond graph diagram of the front axle of the eAWD drivetrain. The wheel shaft compliances are modeled by the compliances of stiffness K_{hFL} and K_{hFR} since they represent the dominant dynamic modes in the drivetrain [37]. The model ignores the inertia of the gears and shaft, which are negligible compared to the inertia of the wheels and the electric machines; it also neglects gear lash. From the bond graph diagrams, one can derive the state equations.

$$\dot{\omega}_{mF} = \frac{1}{J_{mF}}\Big[\tau_{mF} - \frac{\rho}{1+\rho}(\tau_{hFL} + \tau_{hFR})\Big] \tag{2.53}$$

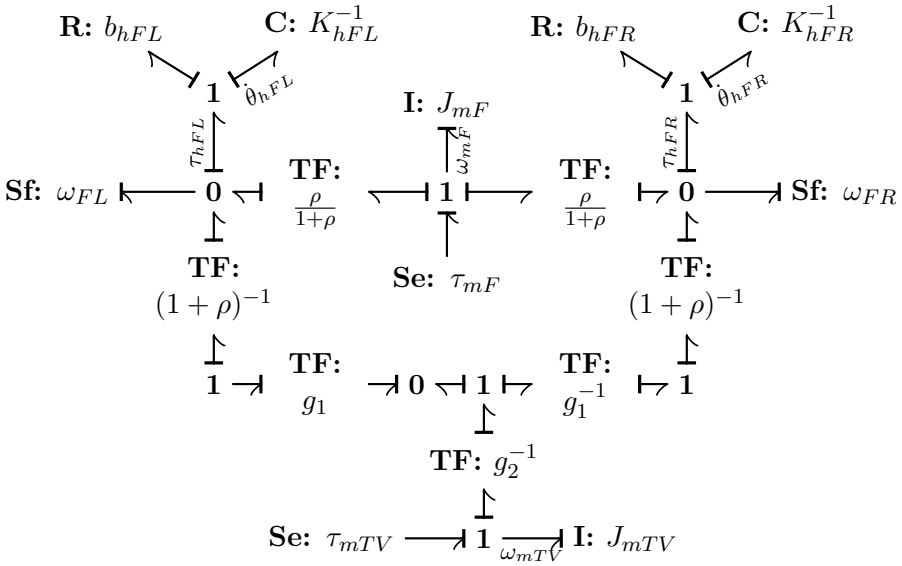

Figure 2.7: Bond graph of the front axle of the eAWD drivetrain

$$\dot{\omega}_{mTV} = \frac{1}{J_{mTV}}\Big[\tau_{mTV} - \frac{1}{g_1 g_2(1+\rho)}(\tau_{hFR} - \tau_{hFL})\Big] \tag{2.54}$$

$$\dot{\theta}_{hFL} = \frac{\rho}{1+\rho}\omega_{mF} - \frac{1}{g_1 g_2(1+\rho)}\omega_{mTV} - \omega_{FL} \tag{2.55}$$

$$\dot{\theta}_{hFR} = \frac{\rho}{1+\rho}\omega_{mF} + \frac{1}{g_1 g_2(1+\rho)}\omega_{mTV} - \omega_{FR} \tag{2.56}$$

with the wheel shaft torques

$$\tau_{hFL} = K_{hFL}\theta_{hFL} + b_{hFL}\Big(\frac{\rho}{1+\rho}\omega_{mF} - \frac{1}{g_1 g_2(1+\rho)}\omega_{mTV} - \omega_{FL}\Big) \tag{2.57}$$

$$\tau_{hFR} = K_{hFR}\theta_{hFR} + b_{hFR}\Big(\frac{\rho}{1+\rho}\omega_{mF} + \frac{1}{g_1 g_2(1+\rho)}\omega_{mTV} - \omega_{FR}\Big) \tag{2.58}$$

Figure 2.8 shows the bond graph diagram of the eAWD rear axle. We rely on the same assumptions as the ones used for the model of the eAWD front axle, namely, the dominant dynamic mode is due to the shaft compliance and the inertia of electric machines, neglected gear lash. In addition to these assumptions, two small inertias representing the shaft connecting the wheel to the eLSD are added. Although their inertias are small, they are necessary to prevent an algebraic loop in the model. Moreover, the compliance of the shaft connecting the traction motor to the eLSD is included to avoid derivative causality in the electric motor inertia. These modifications yield a model with integral causality at the expense of three additional states. Finally, the eLSD electric motor is

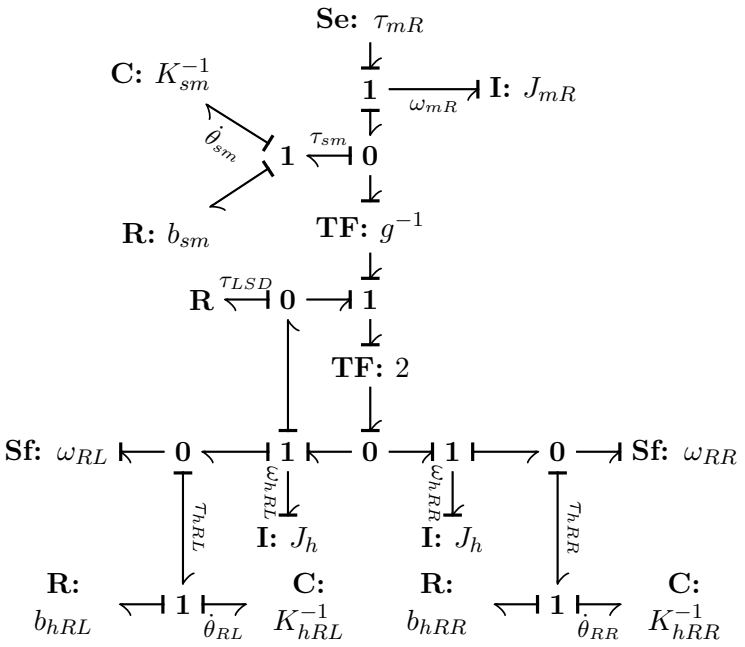

Figure 2.8: Bond graph of the rear axle of the eAWD drivetrain

considered as a perfect actuator applying a torque τ_{LSD} on the eLSD. The equations of motion for the rear axle are:

$$\dot{\omega}_{mR} = \frac{1}{J_{mR}}\Big[\tau_{mR} - \tau_{sm}\Big] \tag{2.59}$$

$$\dot{\omega}_{hRL} = \frac{1}{J_h}\Big[\frac{g\tau_{sm}}{2} - \frac{1}{2}\tau_{LSD} - \tau_{hRL}\Big)\Big] \tag{2.60}$$

$$\dot{\omega}_{hRR} = \frac{1}{J_h}\Big[\frac{g\tau_{sm}}{2} + \frac{1}{2}\tau_{LSD} - \tau_{hRR}\Big)\Big] \tag{2.61}$$

$$\dot{\theta}_{sm} = \omega_{mR} - \frac{g}{2}\Big(\omega_{hRL} + \omega_{hRR}\Big) \tag{2.62}$$

$$\dot{\theta}_{Rj} = \omega_{hRj} - \omega_{Rj} \tag{2.63}$$

with the wheel shaft and motor shaft torques

$$\tau_{sm} = K_{sm}\theta_{sm} + b_{sm}\dot{\theta}_{sm} \tag{2.64}$$

$$\tau_{hRj} = K_{hRj}\theta_{Rj} + b_{hRj}\dot{\theta}_{Rj} \tag{2.65}$$

The eLSD device is represented a resistive element which defines a torque τ_{LSD} from a speed difference $\omega_{cl} = \frac{1}{2}(\omega_{hRL} - \omega_{hRR})$. The torque τ_{LSD} applied by the limited-slip differential is computed

using the Karnopp friction model [38]. This model provides an adequate description for zero velocity; it was developed to overcome zero-velocity detection problems and avoid the need to switch between different state equations for sticking and sliding. Moreover, it does not need to change the causality signs in the bond graph diagrams and therefore does not require switching between different drivetrain models. When the velocity is large enough ($|\omega_{cl}| \geq DV$), the clutch torque τ_{sl} arises from the Coulomb and viscous friction force. When the velocity is small ($|\omega_{cl}| \leq DV$), i.e., when the clutch is locked, the clutch torque depends on external forces so that the clutch remains locked until the maximum static friction torque $\tau_{st,max}$ is reached. It is necessary to find an analytical expression of the clutch torque required to lock the clutch.

The motor velocity is related to the wheel halfshaft velocities via the following kinematic relation:

$$\omega_{mR} = \frac{g}{2}(\omega_{hRL} + \omega_{hRR})$$

Plugging the time derivative of this equation in (2.59) yields the shaft torque:

$$\tau_{sm} = \tau_{mR} - \frac{gJ_{mR}}{2}(\dot{\omega}_{hRL} + \dot{\omega}_{hRR})$$

Inserting this torque in the rear halfshaft dynamics equations (2.60) and (2.61) gives the following system of two equations:

$$\Big(J_h + \frac{g^2}{4}J_{mR}\Big)\dot{\omega}_{hRL} + \frac{g^2}{4}J_{mR}\dot{\omega}_{hRR} = \frac{g}{2}\tau_{mR} - \frac{1}{2}\tau_{LSD} - \tau_{hRL} \tag{2.66}$$

$$\frac{g^2}{4}J_{mR}\dot{\omega}_{hRL} + \Big(J_h + \frac{g^2}{4}J_{mR}\Big)\dot{\omega}_{hRR} = \frac{g}{2}\tau_{mR} + \frac{1}{2}\tau_{LSD} - \tau_{hRR} \tag{2.67}$$

The relative velocity of the clutch is defined as:

$$\omega_{cl} = \frac{1}{2}(\omega_{hRL} - \omega_{hRR}) \tag{2.68}$$

When the clutch is locked, the relative acceleration of the clutch is null, therefore $\dot{\omega}_{hRl} = \dot{\omega}_{hRR}$. Subtracting Equation (2.66) to Equation (2.67), one can find the torque τ_{lock} required to maintain the clutch locked:

$$\tau_{lock} = \tau_{hRR} - \tau_{hRL}$$

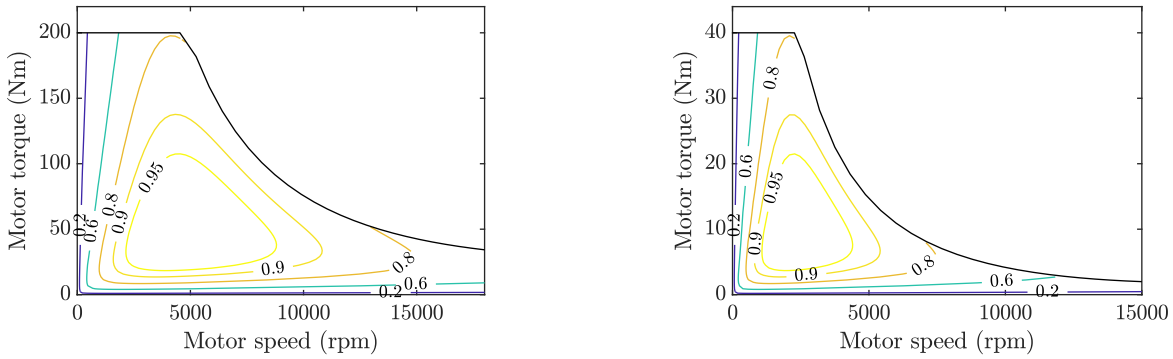

(a) Map propulsion motors

(b) Map of TV motor

Figure 2.9: Motor torque and efficiency map

The maximum static friction is expressed as a function of the clutch torque capacity τ_h and the static friction coefficient μ_{st}: $\tau_{st,max} = \mu_{st}\tau_h$. When the clutch is not locked, the clutch torque is given by the Coulomb friction model with the sliding friction coefficient μ_{sl}: $\tau_{sl} = \mu_{sl}\tau_h$. Finally, the clutch torque is given by:

$$\tau_{LSD} = \begin{cases} \min(|\tau_{lock}|, |\tau_{st,max}|) \times \text{sign}(\tau_{lock}) & \text{if } |\omega_{cl}| \leq DV \\ \tau_{sl} & \text{if } |\omega_{cl}| > DV \end{cases}$$

Electric Motor Torque and Efficiency Map

The torque generated by the electric motor is saturated by the base torque τ_b when the motor speed is smaller than the base speed ω_b. If the motor speed is faster than the base speed, the motor is saturated in power , i.e. the torque generated by the motor satisfies $|\tau_{mot}| \leq \frac{\tau_b \omega_b}{\omega_{mot}}$ where τ_{mot} and ω_{mot} are the motor torque and angular velocities. For a given motor torque τ_{mot} and speed ω_{mot}, the power loss is approximated by the following sum [39],

$$\mathcal{P}_{loss}(\tau_{mot}, \omega_{mot}) = \sum_{(m,n)\in[\![0,3]\!]^2} k_{mn} \left(\frac{\tau_{mot}}{\tau_b}\right)^m \left(\frac{\omega_{mot}}{\omega_b}\right)^n \tag{2.69}$$

where k_{mn} are parameters defining the power loss. Figure 2.9 shows the motor speed-torque map and efficiency map of the electric motors used in this dissertation.

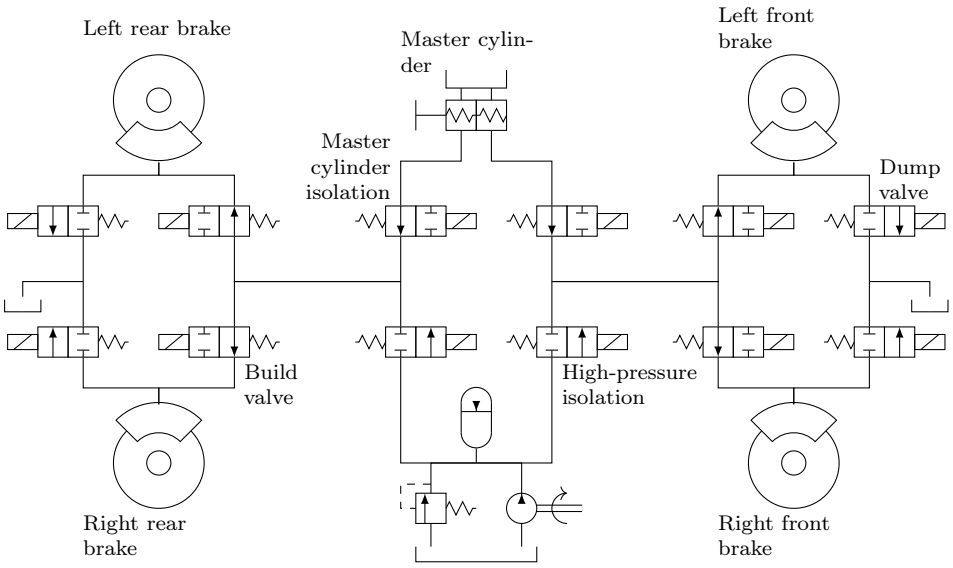

Figure 2.10: Hydraulic braking system

2.3.2 Brake Model

We assume that the vehicle uses EHB. Newer electric brake-by-wire actuators could be used, they allow for higher bandwidth and they are easier to control compared to hydraulic brakes [40].

The structure of the EHB is shown in Figure 2.10; it is composed of a Hydraulic Control Unit (HCU) and a pedal feel simulator (not shown in the figure). The HCU is controlled electronically and modifies the wheel brake line pressure independently at each wheel. The independent actuation at each wheel can be used to regulate the tire slip during traction and braking or regulate the vehicle sideslip by applying a brake torque difference during cornering on slippery surface [41]. When the brake pedal is pressed and if the EHB is working normally, the brake fluid is compressed in the pedal feel simulator, and a pressure source drives the brake fluid from the accumulator to the wheel cylinders [42].

The entire hydraulic circuit is not modeled in this thesis; for more information, the reader can refer to [43]. Only the pressure applied at each wheel is modeled; it is regulated with Pulse Width Modulation (PWM) on the solenoid build and dump valves. The brake pressure control is a discrete process with three states: increase, hold, and decrease the brake pressure. To represent the on and off behavior of the valves, the brake line pressure dynamic is described as follows:

$$\dot{P}_{in} = \frac{C_d S_b \beta_{hf}}{V_{hf}} u_b \Big(P_{high} - P_{in} \Big)^{\phi_b} - \frac{C_d S_d \beta_{hf}}{V_{hf}} u_d \Big(P_{in} - P_{low} \Big)^{\phi_d} \tag{2.70}$$

where P_{in} is the brake line pressure, P_{high} is the pressure applied by the pump, $P_{low} = 0$ is the pressure of the reservoir, C_d is the flow coefficient of the valves, V_{hf} is the brake oil volume, β_{hf} is the bulk modulus of the hydraulic fluid, S_b and S_d are the cross-section area of the build and dump valves, and ϕ_b and ϕ_d are coefficients for increased and decreased pressure. This equation also neglects some nonlinearity, such as the opening delays of the valves. In increase mode, $u_b = 1$ and $u_d = 0$ and the pressure P_{in} increases progressively towards P_{high}; in decrease mode, $u_b = 0$ and $u_d = 1$ and the pressure decreases towards P_{low}; in hold mode, $u_b = 0$ and $u_d = 0$ and the pressure P_{in} remains constant [44]. Because of the PWM of the valves, the pressure is usually not constant; instead, it oscillates between the values of the high and low-pressure sources. The amplitude of the oscillations depends on the frequency and type of carrier signal used by the PWM and on the duty-cycle. The controller defines the PWM duty-cycle to regulate the tire pressure and a PWM modulator generates the signals u_b and u_d to control the valve. Zhao [45] implements a backstepping controller whose outputs are the PWM duty-cycle of the build and dump valves to stabilize the brake pressure of the EHB. In this work, a PID controller is used.

Figure 2.11 shows the schematic of an EHB actuator. A hydraulic pipe conveys the brake fluid under pressure P_{in} to the cylinder chamber. The pressure applied by the chamber on the piston moves the brake pad and applies friction on the braking disk. The actuator is modeled using the bond graph modeling technique [29] as follows, the hydraulic line possesses hydraulic resistance and inertia, the chamber is modeled as a compliance C_{cyl}, and the piston is modeled by a linear transformer. The equations of motion are given as follows,

$$\dot{p}_l = P_{in} - \frac{R_l}{I_l} p_l - \frac{\beta_{hf}}{V_{cyl}} q_l \tag{2.71}$$

$$\dot{q}_l = \frac{1}{I_l} p_l - \frac{S_p}{m_p} p_p \tag{2.72}$$

$$\dot{p}_p = \frac{S_p \beta_{hf}}{V_{cyl}} q_l - b_p \dot{x}_{cal} - k_{cal} \max(x_{cal} - x_0, 0) \tag{2.73}$$

$$\dot{x}_{cal} = \frac{1}{m_p} p_p \tag{2.74}$$

where R_l is the line hydraulic resistance, p_l is the line fluid momentum, I_l is the hydraulic line inertia, V_{cyl} is the volume of the cylinder chamber, S_p is the surface area of the piston, p_p is the piston momentum, q_l is line volumetric flow rate, x_{cal} brake pad position, x_0 is the brake clearance,

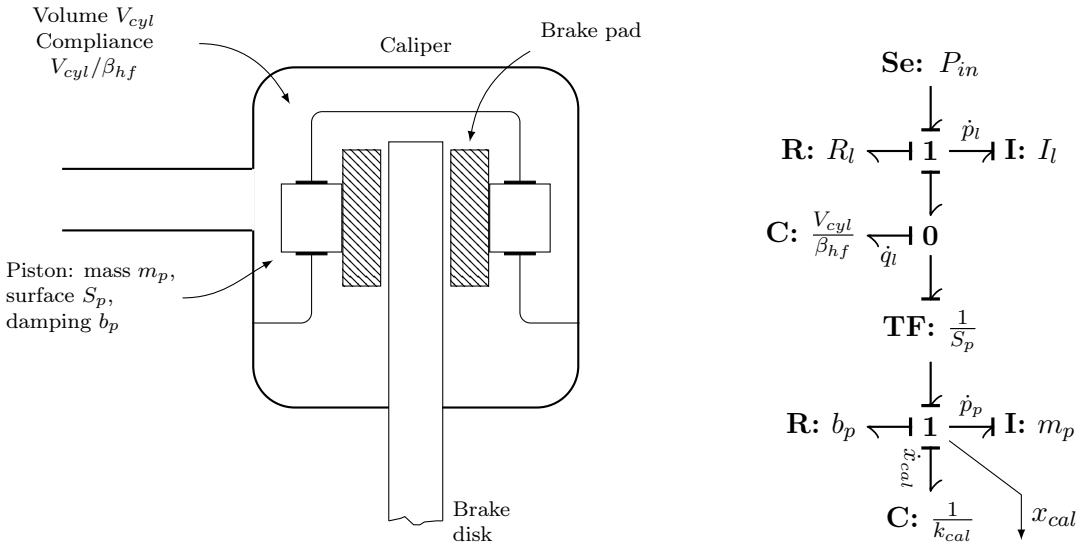

Figure 2.11: Schematic and bond graph model of a single-channel Electro-Hydraulic Brake

and k_{cal} is the caliper stiffness. Note that the pressure is offset such that $p = 0$ corresponds to the reservoir pressure. The brake torque is calculated as follows,

$$\tau_b = 2\mu_{cal} r_{eff} k_{cal} \max(x_{cal} - x_0, 0) \tag{2.75}$$

where μ_{cal} is the friction coefficient between the brake pad and disk, and r_{eff} is the brake pad effective radius. The brake torque τ_b must be modified as described in (2.76) to ensure that the brake only dissipates energy. This equation applies a torque τ_b opposite to the wheel spin ω such that the brake only dissipates power. Moreover, Karnopp friction is used to define the braking torque applied when the wheel is locked, τ_d is the torque applied on the wheel by the driveline, and $r_w f_x$ is the torque applied by the longitudinal tire force,

$$\tau_b \leftarrow \begin{cases} -\operatorname{sign}(\omega)\ |\tau_b|, & \text{if } |\omega| > \epsilon \\ \min\{|\tau_d - r_w f_x|, |\tau_b|\} \cdot \operatorname{sign}(\tau_b), & \text{otherwise} \end{cases} \tag{2.76}$$

The transfer function from the pressure input to the torque output can be obtained from the equation of motion of the EHB and the torque equation (2.75), assuming that $x_{cal} \geq x_0$ and $\tau_b \omega \leq 0$. The brake model is fourth-order system, however, this brake model can be simplified for control synthesis. By neglecting the fluid compliance in the chamber and by lumping the fluid inertia and

resistance to an equivalent mass $m_{eq} = m_p + S_p^2 I_l$ and an equivalent resistance $b_{eq} = b_p + S_p^2 I_l$. The following equation describes the simplified second-order transfer function from the pressure input P_{in} to the brake torque τ_b,

$$G_{EHB} = \frac{\tau_b}{P_{in}} = \frac{2\mu_{cal} r_{eff} k_{cal} S_p}{m_{eq} s^2 + b_{eq} s + k_{cal}} \tag{2.77}$$

2.3.3 Steering System Model

In this thesis, we consider several steering configurations: no active steering, AFS, Active Rear Steering (ARS), and 4WS which combines AFS and ARS. The steering at the front axle is based on a rack-pinion steering system for all configurations. This section provides a model of the rack-pinion steering system at the front axle equipped with AFS. For such a system, the steering angle at the wheel is a function of the steering angle applied by the driver and the steering angle applied by active steering.

The driver steering angle is transmitted to the rack and pinion mechanism by the steering column; linear compliance and damping are assumed to model the steering column. An epicyclic gear mounted at the base of the steering column combines the steering angle applied by the driver and the active steering. The rack and pinion mechanism is modeled by a linear transformer which converts the rotational displacement of the output shaft of the epicyclic gear to a linear displacement of the rack. The rack displacement can then be mapped to a wheel steering angle. We assume a linear relationship between the rack displacement and the wheel steering angle. In addition to that, the impact of the suspension geometry on the steering angle is also represented by a linear relation.

If the steering system is equipped with ePAS, the assistance torque can be modeled by a force F_{ePAS} acting on the rack. Additionally, the forces and moments generated by the tire-road interaction apply an effort F_{rack} that is transmitted to the driver by the steering rack and the steering column. The forces F_{rack} and F_{ePAS} are transmitted to the driver and constitute the steering feel of the vehicle. Active Left-to-Right TV with a mechanically connected steering column as presented here can modify that steering feels as discussed in [46].

Figure 2.12 shows the schematic and bond graph of the steering system. The only state of the system is the steering column compliance θ_{col}; g_1 and g_2 are the ratios of the epicyclic gear, r is the ratio of the rack-pinion mechanism, K_{col} and C_{col} are respectively the stiffness and damping of the steering column, θ_{dri} is the steering angle applied by the driver on the steering wheel, θ_{AFS} is the

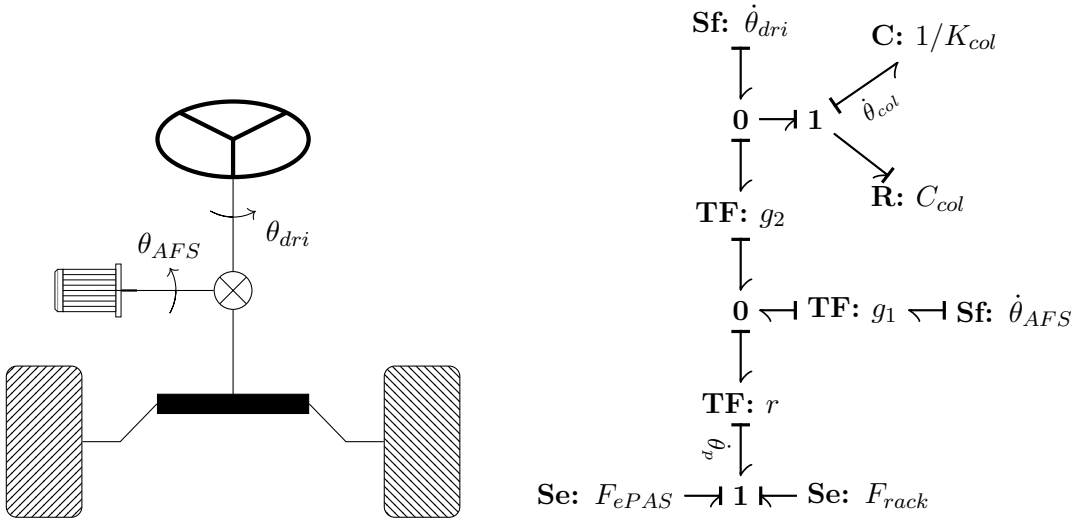

Figure 2.12: Schematic and bond graph model of an Active Front Steering System

steering angle applied by AFS, θ_p is the pinion position, and d is the displacement of the rack. The equations modeling the system are:

$$\dot{\theta}_{col} = -\frac{1}{C_{col}} \times \Big(K_{col}\theta_{col} + g_2 r(F_{rack} + F_{hyd}) \Big) \tag{2.78}$$

$$d = r\theta_p \tag{2.79}$$

$$\theta_p = g_1\theta_{AFS} + g_2(\theta_{dri} - \theta_{col}) \tag{2.80}$$

2.3.4 Chassis Systems and Vehicle Model Integration in MATLAB/Simulink

The vehicle model is implemented in MATLAB/Simulink. The bond graph modeling approach used to derive models for the different subsystems facilitates the decomposition of the vehicle model into block diagrams, Figure 2.13 shows how the chassis model interacts with the vehicle model; this structure allows to quickly replace a subsystem of the vehicle. The chassis block describes the chassis model with the wheel, tire, and suspension dynamics, see Section 2.1). The driveline, brake, and steering blocks implement the model derived in the previous sections. In the chassis model, the torque applied at each wheel is $\tau_{ij} = \tau_{hij} + \tau bij$, where τ_{hij} is the torque applied by the drivetrain and τ_{bij} is the torque applied by the brake. The environment block defines the interaction between the vehicle and the environment, i.e., the friction potential at each wheel and the road input velocity. The driver block represents the driver interacting with the vehicle through the steering wheel and

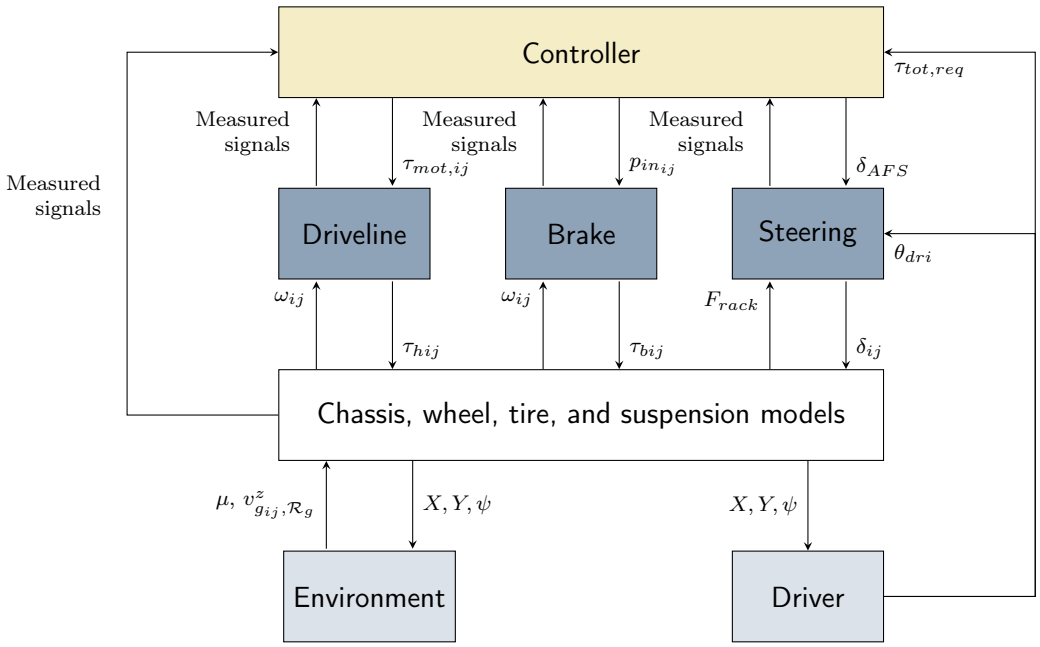

Figure 2.13: Interactions between the chassis systems, vehicle models, and the global chassis controller

gas and throttle pedals. Finally, the controller block implements the control strategies proposed in this dissertation.

2.4 Planar Vehicle Model

2.4.1 Model Derivation

The model developed in the previous section provides a good representation of the vehicle. However, it is too complex to be used to analyze the vehicle and develop control systems. A simplified double-track control-oriented model with seven degree-of-freedom is derived. The model schematics is shown in Figure 2.14. With such a model, the effects of lateral load transfer are considered. The degrees of freedom are the yaw motion, the lateral and longitudinal translation, and the rotation of the wheels. The model assumes steering on the front and rear axle with the same steering angle on the left and right tires, neglecting Ackerman steering geometry. The following equations describe the motion of the car:

$$m(\dot{v}_x - v_y\omega_z) = (f_{FLx} + f_{FRx})\cos(\delta_F) - (f_{FLy} + f_{FRy})\sin(\delta_F)$$

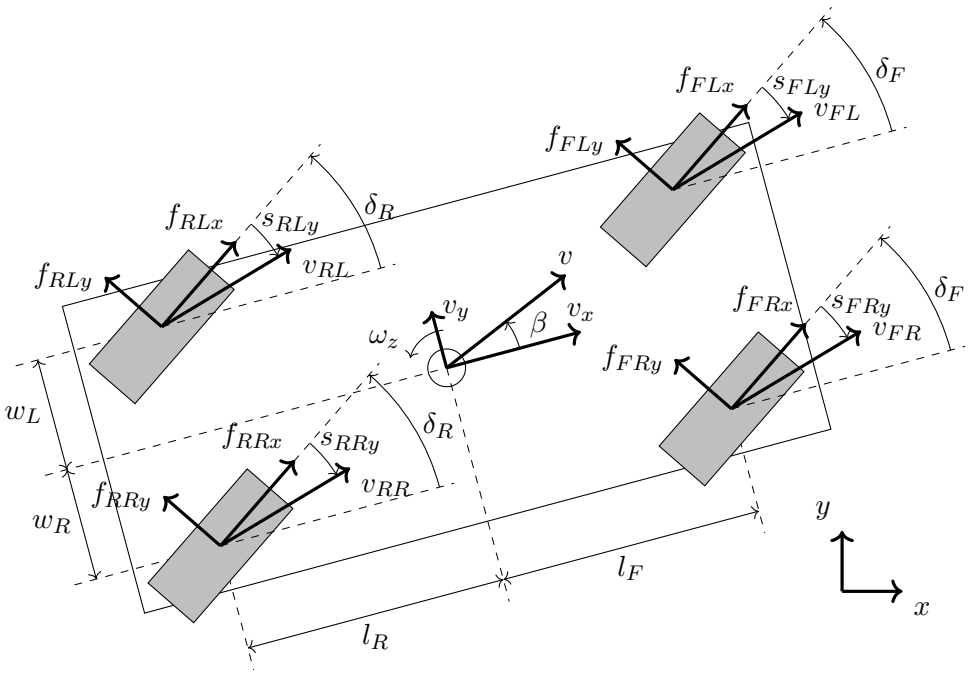

Figure 2.14: Double-track model of the chassis

$$+ (f_{RLx} + f_{RRx})\cos(\delta_R) - (f_{RLy} + f_{RRy})\sin(\delta_R) \tag{2.81}$$

$$\begin{aligned} m(\dot{v}_y + v_x\omega_z) &= (f_{FLx} + f_{FRx})\sin(\delta_F) + (f_{FLy} + f_{FRy})\cos(\delta_F) \\ &+ (f_{RLx} + f_{RRx})\sin(\delta_R) + (f_{RLy} + f_{RRy})\cos(\delta_R) \end{aligned} \tag{2.82}$$

$$\begin{aligned} I_{zz}\dot{\omega}_z &= l_F[(f_{FLy} + f_{FRy})\cos\delta_F + (f_{FLx} + f_{FRx})\sin\delta_F] \\ &- l_R[(f_{RLy} + f_{RRy})\cos\delta_R + (f_{RLx} + f_{RRx})\sin\delta_R] \\ &- w_L(f_{FLx}\cos\delta_F - f_{FLy}\sin\delta_F + f_{RLx}\cos\delta_R - f_{RLy}\sin\delta_R) \\ &+ w_R(f_{FRx}\cos\delta_F - f_{FRy}\sin\delta_F + f_{RRx}\cos\delta_R - f_{RRy}\sin\delta_R) \end{aligned} \tag{2.83}$$

$$J_w\dot{\omega}_{ij} = \tau_{ij} - f_{ijx}r, \quad i = F, R, j = L, R \tag{2.84}$$

where v_x and v_y are the longitudinal and lateral vehicle speed, the vehicle sideslip is defined as $\beta = \tan^{-1}\frac{v_y}{v_x}$, ω_{ij} denotes the wheel speeds, m is the vehicle mass, l_F, l_R, w_L, and w_R define the distance from the wheels to the center of mass, I_{zz} is the moment inertia about the vertical axis, J_w is the moment of inertia of a wheel about its axis of rotation, r is the wheel radius, and τ_{ij} is the torque applied on the wheel.

The planar vehicle model uses algebraic expressions to represent the weight transfer due to lateral

and longitudinal acceleration. Let f^0_{ijz} be the static normal load at wheel ij, Δm^x_j and Δm^y_i the longitudinal and lateral mass transfer, respectively. The normal load is expressed as follow:[2]

$$\begin{aligned} f_{FLz} &= f^0_{FLz} - \Delta m^x_L a_x - \Delta m^y_F a_y, \qquad f_{FRz} = f^0_{FRz} - \Delta m^x_R a_x + \Delta m^y_F a_y, \\ f_{RLz} &= f^0_{RLz} + \Delta m^x_L a_x - \Delta m^y_R a_y, \qquad f_{RRz} = f^0_{RRz} + \Delta m^x_R a_x + \Delta m^y_R a_y, \end{aligned} \tag{2.85}$$

$$\begin{aligned} f^0_{FLz} &= \frac{mgl_R w_R}{(l_F + l_R)(w_L + w_R)}, \qquad f^0_{FRz} = \frac{mgl_R w_L}{(l_F + l_R)(w_L + w_R)}, \\ f^0_{RLz} &= \frac{mgl_F w_R}{(l_F + l_R)(w_L + w_R)}, \qquad f^0_{RRz} = \frac{mgl_F w_L}{(l_F + l_R)(w_L + w_R)}, \end{aligned} \tag{2.86}$$

$$\begin{aligned} \Delta m^x_L &= \frac{mhw_R}{(l_F + l_R)(w_L + w_R)}, \quad \Delta m^x_R = \frac{mhw_L}{(l_F + l_R)(w_L + w_R)}, \\ \Delta m^y_F &= \frac{mhl_R}{(l_F + l_R)(w_L + w_R)}, \quad \Delta m^y_R = \frac{mhl_F}{(l_F + l_R)(w_L + w_R)} \end{aligned} \tag{2.87}$$

Note that this algebraic expression for the normal force leads to an algebraic loop in the expression of the planar vehicle model. Indeed, Equations (2.85) to (2.87) requires to know the accelerations $a_x = \dot{v}_x - v_y\omega_z$ and $a_y = \dot{v}_y + v_x\omega_z$ which depends on the sum of longitudinal and lateral forces applied on the chassis, however, the tire model also needs the vertical force to express the longitudinal and lateral tire forces. An algebraic loop forces to express the model as an implicit system of differential equation $f(\dot{x}, x, u) = 0$ which can cause difficulties when analysing the model or designing control. Fortunately, the algebraic loop can be broken and the system can be expressed as an explicit set of ordinary differential equation $\dot{x} = f(x, u)$. After substituting $\dot{v}_x - v_y\omega_z$ by a_x and $\dot{v}_y + v_x\omega_z$ by a_y in Equations (2.81) and (2.82), the longitudinal and lateral dynamic of the vehicle model can be rewritten as:

$$ma_x = \sum_{ij} \mu_{ijxc} f_{ijz}, \quad ma_y = \sum_{ij} \mu_{ijyc} f_{ijz} \tag{2.88}$$

where $\mu_{ijxc} = \mu_{ijx}\cos\delta_i - \mu_{ijy}\sin\delta_i$ and $\mu_{ijyc} = \mu_{ijx}\sin\delta_i + \mu_{ijy}\cos\delta_i$ are the friction coefficients in

[2] Recall that the chassis posses an anti-roll bar, hence it does not show the effect of roll stiffness difference between the front and rear axles. Adding the term $\pm k_{\phi_i}(\phi - \phi_i)$ to the algebraic normal force expression would represent the effects of an anti-roll bar on the load transfer, where k_{ϕ_i} denotes the rotational stiffness of the anti-roll bar at the axle i, $\phi - \phi_i$ is the displacement angle of the anti-roll bar at the axle i.

the vehicle longitudinal and lateral axes. Plugging Equation (2.85) leads to:

$$\Big[m + \sum_{j=L,R} \Delta m_j^x(\mu_{Fjxc} - \mu_{Rjxc})\Big]a_x + \Big[\sum_{i=F,R} \Delta m_i^y(\mu_{iLxc} - \mu_{iRxc})\Big]a_y = \sum_{ij} \mu_{ijxc} f_{ijz}^0 \tag{2.89a}$$

$$\Big[\sum_{j=L,R} \Delta m_j^x(\mu_{Fjyc} - \mu_{Rjyc})\Big]a_x + \Big[m + \sum_{i=F,R} \Delta m_i^y(\mu_{iLyc} - \mu_{iRyc})\Big]a_y = \sum_{ij} \mu_{ijyc} f_{ijz}^0 \tag{2.89b}$$

The previous equations define a linear system whose unknowns are the accelerations a_x and a_y; the linear system can easily be solved to determine the vehicle's longitudinal and lateral acceleration. Plugging the acceleration in the algebraic normal force expression yields the tire load distribution, breaking the algebraic loop.

Only the longitudinal and lateral forces of the tire are taken into account; the self-aligning moment, overturning moment, and rolling resistance are neglected. The forces exerted by the tires are found using the Magic Formula described in Section 2.2.1.

2.4.2 Model Analysis

The planar vehicle model is linearized and analyzed to understand the impact of the steering and the distribution of wheel torque on the vehicle's dynamics, especially on its yaw behavior. In this section, we will analyze the impact of front-to-rear TV, i.e., applying a torque difference between the two axles, and the left-to-rear TV, i.e., applying a torque difference within the same axle.

Planar Model Linearization

The planar model derived in Equations (2.81) to (2.87) is simplified before being linearized so that an analyses can be conducted. The wheel dynamics are neglected; hence the wheel force is proportional to the wheel torque $r_w f_{xij} = \tau_{ij}$. The forward velocity v_x is assumed constant; thus, the simplified model is a second-order model whose states are the lateral velocity v_y and the yaw rate ω_z. The small-angle approximation is used so that $\cos\delta_{ij} \sim 1$ and $\sin\delta_{ij} \sim \delta_{ij}$; assuming $|w_j\omega_z| \ll |v_x|$ with $j = R, L$ simplifies the expression of the slip angle. Using the small-angle approximation and ignoring the cross-terms $w_j\omega_z$ in the slip angle make the linearized model much simpler; however, the linearized model is only valid at a low slip angle during moderate cornering. The tire model

is also linearized; since the tire forces are a function of the longitudinal slip (itself dependant on the wheel torque), the longitudinal slip, and the tire load, the lateral tire force is approximated as follows:

$$f_{yij} = C_{xi} f_{xij} + \frac{1}{2} C_{yi} s_{yij} + C_{zi} f_{zij} \tag{2.90}$$

where C_{xi} is the sensitivity of the wheel lateral force with respect to the wheel longitudinal force, C_{yi} is the axle lateral stiffness, and C_{zi} is the wheel load sensitivity. The left and right tires of each axle are assigned the same parameters C_{xi}, C_{yi}, and C_{zi}. In practice, these coefficients depend on the operating condition of the tire and might differ between the left and right sides, for instance, due to load transfer during cornering. We assume that the discrepancies between the coefficients are minor and that the same value can be used between the two tires of the same axle.

The inputs of the model are the front and rear steering angle δ_F and δ_R, the total torque $\tau_{tot} = \sum_{ij} \tau_{ij}$, the torque difference between the front and rear axle $\tau_{TV_{F/R}} = \frac{1}{2}(\tau_{FL}+\tau_{FR}-\tau_{RL}-\tau_{RR})$, the front axle torque difference $\tau_{TV_F} = \frac{1}{2}(\tau_{FR} - \tau_{FL})$, and the rear axle torque difference $\tau_{TV_R} = \frac{1}{2}(\tau_{RR} - \tau_{RL})$. The state-space representation of the linearized model is as follows,

$$\begin{aligned}
\begin{bmatrix} \dot{v}_y \\ \dot{\omega}_z \end{bmatrix} = &\begin{bmatrix} -\frac{C_{yF}+C_{yR}}{m v_x} & -\left(v_x + \frac{l_F C_{yF} - l_R C_{yR}}{m v_x}\right) \\ -\frac{l_F C_{yF} - l_R C_{yR}}{I_{zz} v_x} & -\frac{l_F^2 C_{yF} + l_R^2 C_{yR}}{I_{zz} v_x} \end{bmatrix} \begin{bmatrix} v_y \\ \omega_z \end{bmatrix} + \begin{bmatrix} \frac{C_{yF}}{m} \\ \frac{l_F C_{yF}}{I_{zz}} \end{bmatrix} \delta_F + \begin{bmatrix} \frac{C_{yR}}{m} \\ -\frac{l_R C_{yR}}{I_{zz}} \end{bmatrix} \delta_R \\
&+ \begin{bmatrix} \frac{C_{xF}+C_{xR}}{2mr_w} - \frac{h(C_{zF}-C_{zR})}{mr_w(l_F+l_R)} \\ -\left(\frac{w_L - w_R - l_F C_{xF} + l_R C_{xR}}{2 I_{zz} r_w} + \frac{h(l_F C_{zF} + l_R C_{zR})}{I_{zz} r_w (l_F + l_R)}\right) \end{bmatrix} \tau_{tot} + \begin{bmatrix} \frac{C_{xF}-C_{xR}}{mr_w} \\ \frac{l_F C_{xF} + l_R C_{xR}}{I_{zz} r_w} \end{bmatrix} \tau_{TV_{F/R}} \\
&+ \begin{bmatrix} 0 \\ \frac{w_L + w_R}{I_{zz} r_w} \end{bmatrix} \tau_{TV_F} + \begin{bmatrix} 0 \\ \frac{w_L + w_R}{I_{zz} r_w} \end{bmatrix} \tau_{TV_R}
\end{aligned} \tag{2.91}$$

The linearized model is a second-order system whose natural frequency ω_0 and damping ratio ζ

$$\omega_0 = \sqrt{\frac{(l_F + l_R) C_{yF} C_{yR}}{m I_{zz} v_x^2} \left(l_F + l_R + K_U v_x^2\right)} \tag{2.92}$$

$$\zeta = \frac{1}{2\sqrt{m I_{zz}}} \frac{I_{zz}(C_{yF} + C_{yR}) + m(l_F^2 C_{yF} + l_R^2 C_{yR})}{\sqrt{(l_F + l_R) C_{yF} C_{yR} (l_F + l_R + K_U v_x^2)}} \tag{2.93}$$

Table 2.1: Gain $K_{u\omega_z}$ and numerator time constant $\tau_{u\omega_z}$ of the linearized model $G_{u\omega_z}$

Input u	Gain $K_{u\omega_z}$	Time constant $\tau_{u\omega_z}$
δ_F	$\frac{C_{yF}C_{yR}(l_F+l_R)}{I_{zz}v_x m}$	$\frac{v_x l_F m}{C_{yR}(l_F+l_R)}$
δ_R	$-\frac{C_{yF}C_{yR}(l_F+l_R)}{I_{zz}v_x m}$	$\frac{v_x l_R m}{C_{yF}(l_F+l_R)}$
τ_{tot}	$-\frac{\begin{array}{c}(C_{yF}+C_{yR})(w_L-w_R)+\\ 2h(C_{yF}C_{zR}+C_{yR}C_{zF})+\\ (C_{xR}C_{yF}-C_{xF}C_{yR})(l_F+l_R)\end{array}}{2I_{zz}v_x m r_w}$	$\frac{\begin{array}{r}v_x m(w_L-w_R+l_R C_{xR}-l_F C_{xF}+\\ 2h(C_{zF}+C_{zR}))\end{array}}{\begin{array}{r}(C_{yF}+C_{yR})(w_L-w_R)+\\ (C_{xR}C_{yF}-C_{xF}C_{yR})(l_F+l_R)+\\ 2h(C_{yF}C_{zR}+C_{yR}C_{zF})\end{array}}$
$\tau_{TV_{F/R}}$	$\frac{(C_{xF}C_{yR}+C_{xR}C_{yF})(l_F+l_R)}{I_{zz}v_x m r_w}$	$\frac{v_x m(l_F C_{xF}+l_R C_{xR})}{(C_{xF}C_{yR}+C_{xR}C_{yF})(l_F+l_R)}$
τ_{TV_F} or τ_{TV_R}	$\frac{(w_L+w_R)(C_{yF}+C_{yR})}{I_{zz}v_x m r_w}$	$\frac{v_x m}{C_{yF}+C_{yR}}$

where K_U is the vehicle understeer gradient defined as:

$$K_U = \frac{m}{l_F+l_R}\Big(\frac{l_R}{C_{yF}} - \frac{l_F}{C_{yR}}\Big) \tag{2.94}$$

All the transfer functions mapping an input u of the model to a state x can be expressed as a transfer function formulated as:

$$G_{ux} = \frac{K_{ux}(\tau_{ux}s+1)}{s^2+2\zeta\omega_0 s+\omega_0^2} \tag{2.95}$$

where the coefficients K_{ux} and τ_{ux} can be found in Table 2.1 and Table 2.2, the coefficient for the input $u=\tau_{tot}$ are not shown for brevity. Assuming a vehicle such that $l_F \sim l_R \sim l$, $I_{zz} \sim ml^2$, $C_{xF} \sim C_{xR} \sim C_x$, $C_{yF} \sim C_{yR} \sim C_y$, and $C_{zF} \sim C_{zR} \sim C_z$, the time constants of the numerator of $G_{u\omega_z}$ are all similar to $\frac{v_x m}{2C_y}$, moreover the natural frequency and the damping factor are similar to:

$$\omega_0 \sim \frac{2C_y}{mv_x}\sqrt{1+\frac{K_U v_x^2}{2l}} \text{ and } \zeta \sim \Big(1+\frac{K_U v_x^2}{2l}\Big)^{-\frac{1}{2}} \tag{2.96}$$

Therefore, if the vehicle is a neutral steer, the transfer function is critically damped, and there is a zero-pole cancellation in the transfer function $G_{u\omega_z}$. Figure 2.15 shows the step response of the linearized model for an understeer vehicle. When the forward velocity increases, the system response becomes more oscillatory, as expected from Equation (2.96) for an understeer vehicle.

Table 2.2: Gain K_{uv_y} and numerator time constant τ_{uv_y} of the linearized model G_{uv_y}

Input u	Gain K_{uv_y}	Time constant τ_{uv_y}
δ_F	$\frac{C_{yF}(C_{yR}l_R(l_F+l_R)-l_F m v_x^2)}{I_{zz}v_x m}$	$\frac{I_{zz}v_x}{C_{yR}l_R(l_F+l_R)-l_F m v_x^2}$
δ_R	$\frac{C_{yR}(C_{yF}l_F(l_F+l_R)+l_R m v_x^2)}{I_{zz}v_x m}$	$\frac{I_{zz}v_x}{C_{yF}l_F(l_F+l_R)+l_R m v_x^2}$
$\tau_{TV_{F/R}}$	$\frac{m v_x^2(l_F C_{xF}+l_R C_{xR})+(l_F C_{xR}C_{yF}-l_R C_{xF}C_{yR})(l_F+l_R)}{-I_{zz}v_x m r_w}$	$\frac{-I_{zz}v_x(C_{xF}-C_{xR})}{m v_x^2(l_F C_{xF}+l_R C_{xR})+(l_F C_{xR}C_{yF}-l_R C_{xF}C_{yR})(l_F+l_R)}$
τ_{TV_F} or τ_{TV_R}	$-\frac{(w_L+w_R)(m v_x^2+l_F C_{yF}-l_R C_{yR})}{I_{zz}v_x m r_w}$	0

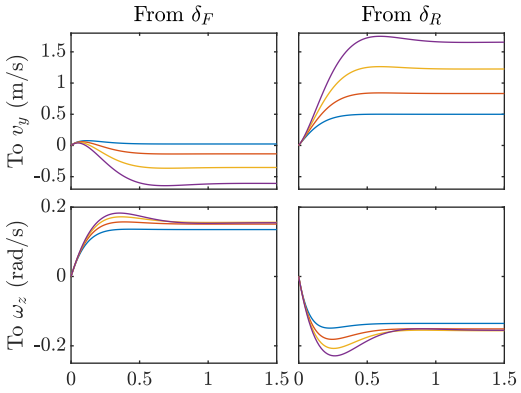

(a) Step response to a 2° input

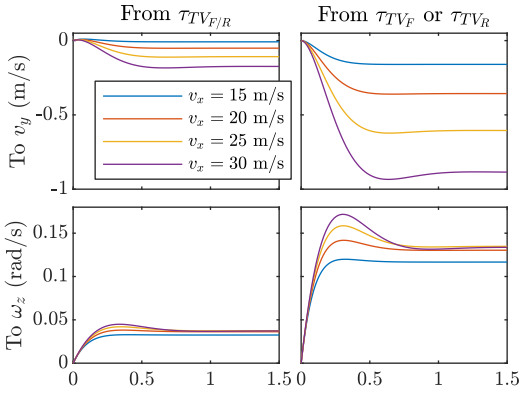

(b) Step response to a 1000 N m input

Figure 2.15: Step response of the linearized model at different speeds for an understeer vehicle.

Figure 2.15b shows the response of the linearized system to a step input of 1000 N m in $\tau_{TV_{F/R}}$, τ_{TV_F}, and τ_{TV_R}. Left-to-right torque vectoring provides higher gain than front-to-rear TV. The transfer functions from the front axle steering angle δ_F and the front-to-rear torque difference $\tau_{TV_{F/R}}$ to the lateral velocity v_y are characterized by a non-minimum phase zero. The inverse of the gain of the transfer function mapping front and rear steering angle to the lateral velocity and yaw rate is:

$$G_{[\delta_F \quad \delta_R]^T [v_y \quad \omega_z]^T}(s=0)^{-1} = v_x \begin{bmatrix} 1 & l_F + \frac{l_R m v_x^2}{C_{yF}(l_F+l_R)} \\ 1 & -l_R + \frac{l_F m v_x^2}{C_{yR}(l_F+l_R)} \end{bmatrix} \tag{2.97}$$

The same steering angle should be applied to the front and rear axles when solely tracking a constant lateral velocity target. On the other hand, different steering angles between the front and

rear axles should be used when solely tracking a constant yaw rate target; the difference depends on the vehicle wheelbase, cornering stiffness, and longitudinal vehicle speed: the steering angle should be opposite in sign at low-speed and have the same sign at high-speed.

Nonlinear Analysis of Front-to-Rear Torque Vectoring

The model linearization already gives some insights on the effect of front-to-rear TV on the vehicle yaw angular speed. The presence of the longitudinal and lateral tire stiffness in the coefficients $K_{\tau_{TV_{F/R}}\omega_z}$ and $\tau_{\tau_{TV_{F/R}}\omega_z}$ in Table 2.1 indicates that this effect is due to coupling between longitudinal and lateral tire force. Since this coupling is highly nonlinear, a nonlinear analysis must be conducted to understand the true potential of front-to-rear TV [47]. We assume that the same torque and steering angle are applied to the left and right wheels. The left and right wheels can be combined into a single wheel yielding the single-track bicycle model. The torque is distributed such that $f_{xF} = f_{xFL} + f_{xFR} = kf_x$ and $f_{xR} = f_{xRL} + f_{xRR} = (1-k)f_x$ where $f_x = f_{xF} + f_{xR}$ is the total longitudinal force. From Equations (2.34), (2.38) to (2.40) and (2.81) to (2.87), we can write the following system of equations which represents a single-track bicycle model with longitudinal load transfer and the Pacejka tire model described in Section 2.2.1.

$$ma_x = f_{xF}\cos\delta_F - f_{yF}\sin\delta_F + f_{xR}\cos\delta_R - f_{yR}\sin\delta_R \tag{2.98}$$

$$m_z = l_F(f_{xF}\sin\delta_F + f_{yF}\cos\delta_F) - l_R(f_{xR}\sin\delta_R + f_{yR}\cos\delta_R) \tag{2.99}$$

$$f_{xF} = kf_x,\ \ f_{xR} = (1-k)f_x \tag{2.100}$$

$$s_{yF} = \delta_F - \tan^{-1}\left(\frac{v_y + l_F\omega_z}{v_x}\right),\ \ s_{yR} = \delta_R - \tan^{-1}\left(\frac{v_y - l_R\omega_z}{v_x}\right) \tag{2.101}$$

$$s_F = \sqrt{s_{xF}^2 + s_{yF}^2},\ \ s_R = \sqrt{s_{xR}^2 + s_{yR}^2} \tag{2.102}$$

$$f_F = \frac{m(gl_R - ha_x)}{l_F + l_R}\,\mathrm{MF}\,(s_F),\ \ f_R = \frac{m(gl_R + ha_x)}{l_F + l_R}\,\mathrm{MF}\,(s_R) \tag{2.103}$$

$$f_{xi} = \frac{s_{xi}}{s_i}f_i,\ \ f_{yi} = \frac{s_{yi}}{s_i}f_i \quad i \in \{F, R\} \tag{2.104}$$

where f_F and f_R are the combined tire forces of the front and rear axles, f_{xF} and f_{xR} denote the longitudinal axle force, f_{yR} denote the lateral axle force, m_z is the yaw moment applied on the vehicle, MF is the Pacejka's magic formula introduced in Equation (2.38).

Solving this nonlinear system of equations for a given longitudinal acceleration a_x and torque

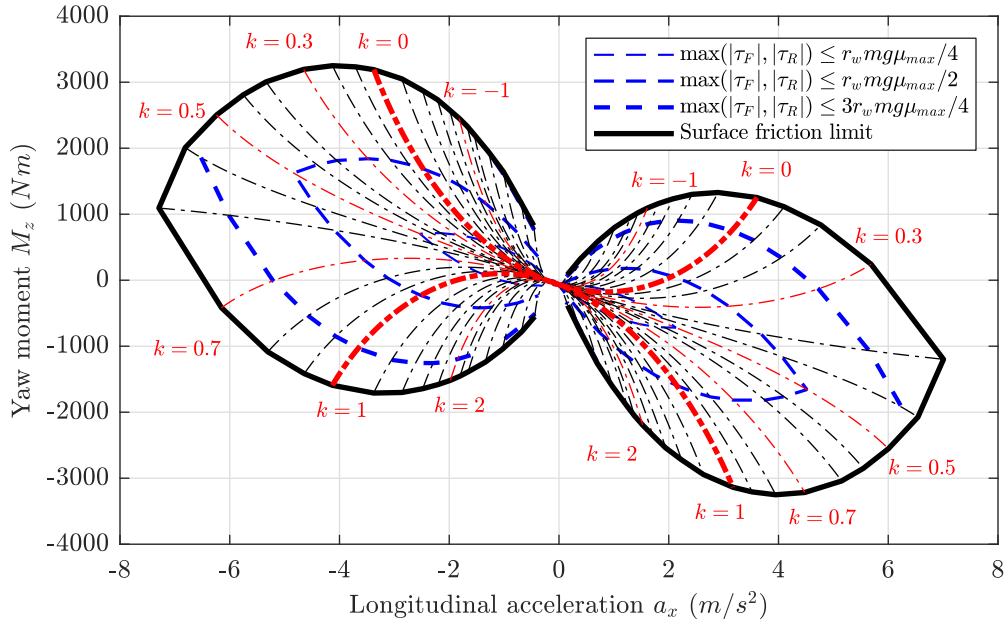

(a) Left turn (i.e. positive yaw rate). The plot was generated for the following conditions: velocity $v = 100\,\mathrm{km\,h^{-1}}$, sideslip angle $\beta = 2.8\,\mathrm{deg}$, and yaw rate $\omega_z = 30\,^\circ\,\mathrm{s^{-1}}$.

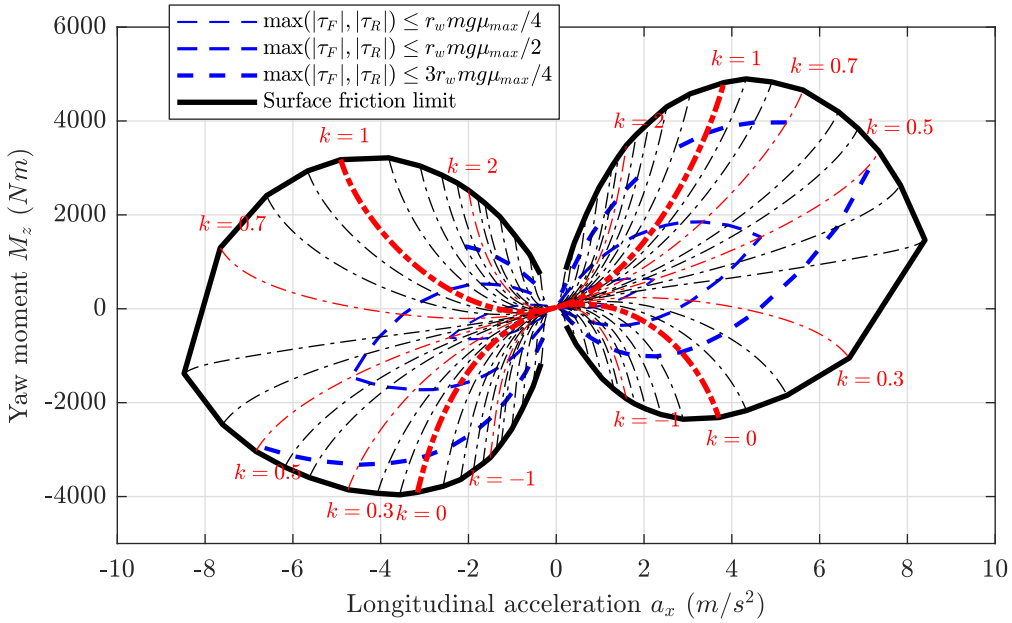

(b) Right turn (i.e. negative yaw rate). The plot was generated for the following conditions: velocity $v = 100\,\mathrm{km\,h^{-1}}$, sideslip angle $\beta = -1.6\,\mathrm{deg}$, and yaw rate $\omega_z = -20\,^\circ\,\mathrm{s^{-1}}$.

Figure 2.16: Yaw moment during front-to-rear TV. Increasing the front-to-rear torque ratio k leads to a larger yaw moment in the direction opposite to the yaw motion.

distribution k under given states (v, β, ω_z) yields the yaw moment m_z applied by the tire force on the vehicle. Doing so over a range of values for k and a_x allows to produce the graph shown in Figure 2.16. As can be seen from this graph, modifying the torque distribution between the front and rear axle modifies the yaw moment applied to the vehicle and affects the yaw behavior of the car.

Figure 2.16 shows that applying more torque on the front axle (i.e. increasing the ratio k) introduces a yaw moment in the opposite direction of the vehicle yaw motion, making the vehicle relatively more understeer. Reciprocally, more torque on the rear axle (i.e. decreasing the ratio k) makes the vehicle relatively more oversteer. The sensitivity of the yaw moment to the axle torque distribution is due to the coupling between longitudinal and lateral tire force. Indeed, during combined slip, increasing the longitudinal slip decreases the lateral cornering stiffness; thus, applying more torque on the front axle increases the front lateral cornering stiffness and decreases the rear lateral cornering stiffness, which increases the understeer gradient, see Equation (2.94), and changes the yaw behavior of the car.

Contrary to active left-to-right TV, front-to-right TV can only modify the yaw moment applied on the vehicle during combined longitudinal acceleration and cornering. Indeed, Figure 2.16 shows that under low longitudinal acceleration, the front-to-rear torque distribution does not have a significant impact on the vehicle yaw moment. Moreover, during pure straight driving, the lateral force would be zero; modifying the distribution of torque between the two axles would not affect the lateral force, and the yaw moment would stay unchanged. Finally, front-to-rear TV requires a large actuator authority over the ratio k, which is not always possible depending on the drivetrain topology. It also requires operating near the friction saturation limits of one of the axles to significantly alter the vehicle yaw moment, restricting the application of front-to-rear TV to powerful vehicles at least during traction.

2.5 System Coupling Mechanism

2.5.1 Tire Force Coupling

The longitudinal and lateral forces generated by the tire are nonlinear functions of the longitudinal slip, slip angle, and wheel load. The longitudinal and lateral tire forces are not independent of each

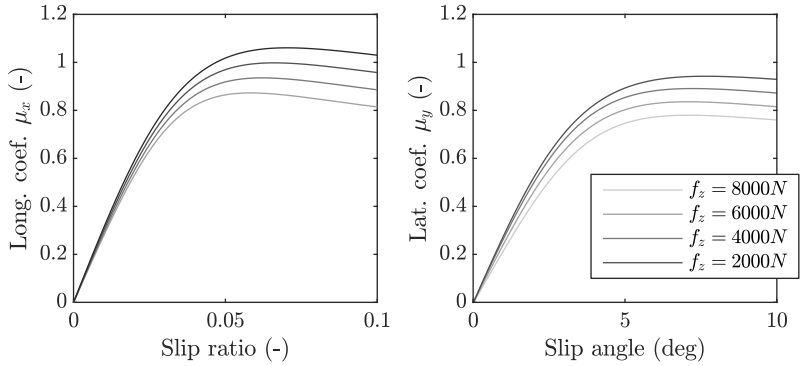

Figure 2.17: Tire load sensitivity of the friction coefficient with an MF94 Pacejka tire model

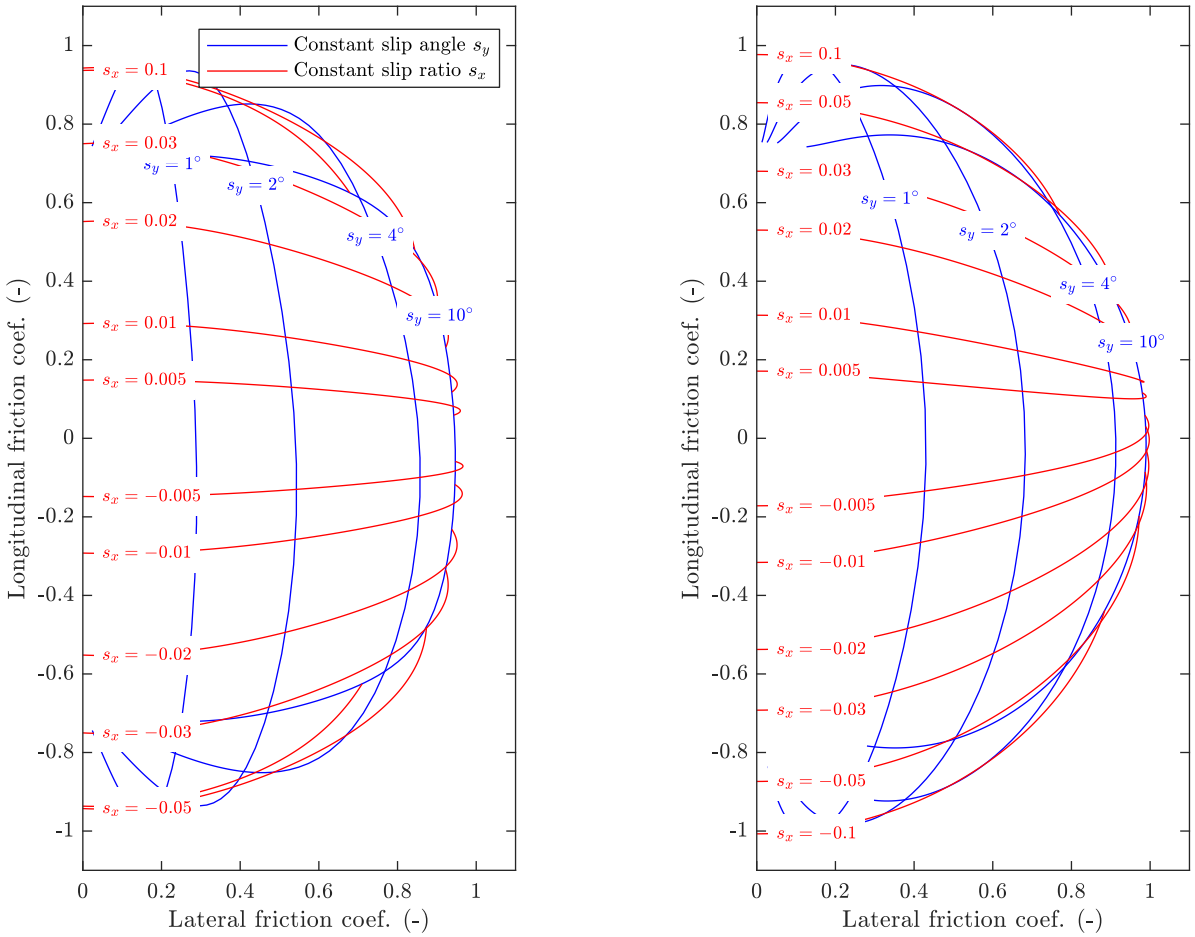

(a) MF94 Pacejka tire model

(b) Steady-state LuGre tire model

Figure 2.18: Steady-state friction coefficient for varying slip ratio and slip angle. Red curves correspond to fixed slip ratio, and blue curves to fixed slip angle.

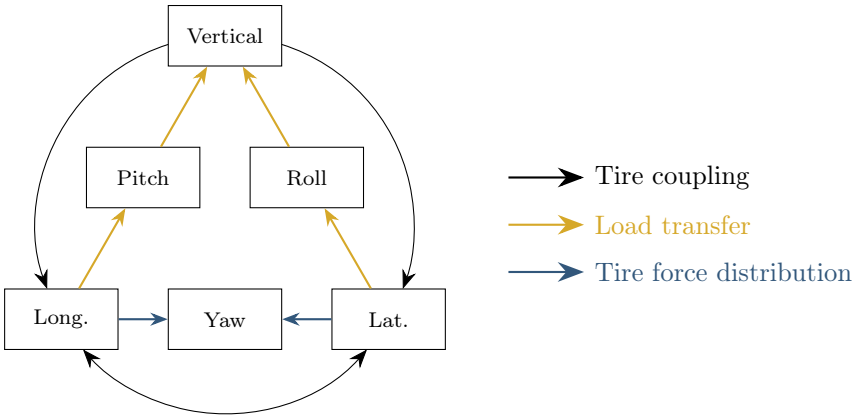

Figure 2.19: Summary of system coupling mechanism

other; they are constrained to evolve within a friction ellipse, usually simplified as a friction circle, by the friction potential between the tire rubber and the road. When the tire operates close to saturation, the longitudinal and lateral forces compete with each other, and peak longitudinal and lateral forces cannot be achieved simultaneously. Figure 2.18 shows the friction ellipse, constant slip ratio curves, and constant slip angle curves with two tire models.

The relation between the longitudinal or lateral force and the vertical force is not linear. Figure 2.17 shows the longitudinal and lateral friction coefficients for several tire loads. As can be seen, the friction coefficients μ_x and μ_y are not independent of the wheel load; instead, increasing the wheel load leads to reduced friction coefficients and also modifies the slip ratio and slip angle corresponding to peak friction. This sensitivity of friction coefficient to the wheel load and the load transfer that happens when the vehicle is subjected to acceleration decreases the maximum friction force the vehicle can produce. For instance, with the tire model used to generate Figure 2.17, the maximum lateral force during pure cornering under 2 kN, 4 kN, and 6 kN are respectively 1884 N, 3563 N, and 5015 N, so an axle where each wheel loads 4 kN should theoretically be able to provide $2 \times 3563 = 7126$ kN of lateral force, however, because of the weight transfer, the load will be redistributed. If the load is 2 kN on one wheel and 6 kN on the other, the axle can only provide up to $1884 + 5015 = 6899$ kN of lateral force.

2.5.2 Chassis Coupling

The longitudinal and lateral motions of the vehicle are coupled to the vertical motion; when the vehicle accelerates, decelerates, or turns, the vehicle pitches up or down and rolls; the pitch and roll compress or extend the suspensions and redistributes the wheel loads. The distribution of longitudinal and lateral tire forces can affect the yaw behavior of the vehicle. Left-to-right TV uses a torque imbalance between the left and right wheels to generate a moment around the yaw axis of the vehicle; front-to-right TV uses an imbalance between the front and rear axles to modify the understeer gradient of the vehicle during cornering. Finally, as discussed in Section 2.5.1, the lateral and longitudinal tire forces depend on the normal wheel load, and the friction ellipse constrains the lateral and longitudinal motions. Longitudinal, lateral, and vertical tire forces are not independent of each other, especially when the tire operates in the nonlinear and saturated regions. Figure 2.19 summarizes the different coupling mechanism.

Chapter 3

Architecture Overview and Control Allocation

3.1 Structure of the IVDC Architecture

This dissertation focuses on electric vehicles with and without active steering. Several electric motors can be used to propel the vehicle with different constraints: the dual-motor only allows front-to-rear TV while the quad-motor and eAWD allow for independent wheel torque control; EHB actuator are used allowing independent wheel braking. We also investigate the use of active steering with AFS, ARS, and 4WS. The architecture should be reusable between different configurations combining the aforementioned actuator sets. Actuators controlling the heave, pitch, and roll motions of the vehicle, such as CDC actuators and active anti-roll bar, are not considered. Therefore, we do not have direct control over the vehicle pitch, roll, and heave motions; the control architecture is intended for planar motion control and controls the following variables: the total longitudinal torque, the lateral vehicle velocity, and the vehicle yaw rate. In addition to restricting the motion covered by the control architecture, the nonlinear relation between the longitudinal and lateral tire force and the wheel load is ignored. Figure 3.1 shows the structure of the IVDC architecture.

Contrary to the multi-layer architecture shown in Figure 1.4, the proposed control architecture allocates controls at each wheel instead of using generalized forces. The wheel control signals are the wheel torques and steering angles. This research does not consider heave control, but it could be inserted into the architecture by regulating the wheel load.

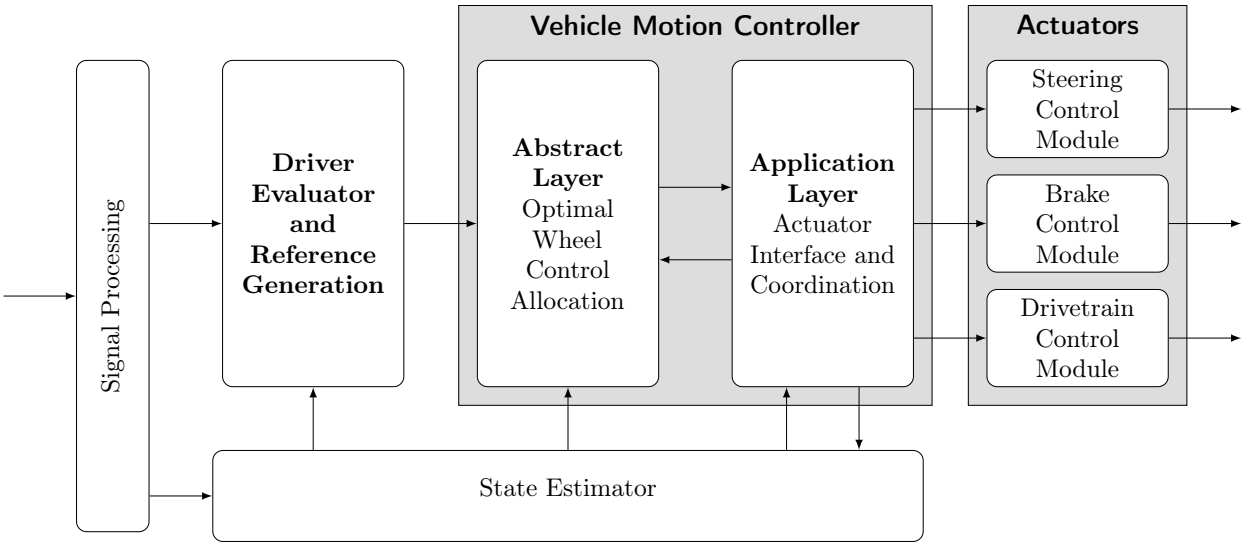

Figure 3.1: Overview of the Integrated Vehicle Dynamics and Control multi-layered control architecture

3.1.1 Estimation

All the forces applied on the vehicle, except for aerodynamic drag and gravity, result from the interaction of the tire and the road. Tire-road forces are limited in amplitude by the friction ellipse; trying to exceed the surface friction limit will lead to excessive slip and instabilities. Information on the road condition and the tire normal load distribution will help the control strategy evaluate the vehicle's maximum capabilities. Unfortunately, the friction potential and the tire normal forces cannot be measured directly with common vehicle sensors, and they must be estimated.

The algebraic expressions of the normal forces can provide a simple estimate of the tire normal load from the vehicle's longitudinal and lateral acceleration [48]. More elaborate observers using Extended Kalman Filter (EKF) or COO have also been implemented to estimate the tire normal force [49], [50]. However, these estimation schemes usually rely on algebraic expressions and do not capture the normal tire force dynamics. In Chapter 4, we propose observers to estimate the tire normal load distribution without relying on algebraic expressions.

The estimation of the friction potential is also a complex task [32]. First estimation schemes monitor the tire stiffness to infer the road conditions [51]. However, newer results question the underlying assumption used by these schemes [52]. Researchers also used model-based estimation techniques with commonly available sensors to estimate the tire-road friction potential. Ray [53]

estimates vehicle states and tire forces with an EKF, the friction potential is then inferred from the tire model using Bayesian selection. A common problem with model-based approaches is that they require high slip excitation to obtain accurate estimates. In Chapter 4, a simple strategy is developed to obtain the maximum friction coefficient when the tire operates near its saturation limits.

The control system also needs to estimate several vehicle states, such as the longitudinal velocity v_x and the lateral velocity v_y. The vehicle velocities v_x and v_y are needed to compute the wheel slips and slip angles to identify if the vehicle is stable. The slip controls developed in Chapter 6 use a disturbance rejection scheme and rely on an estimate of the longitudinal tire forces; observers developed by Velazquez [19], [54], [55] are used in this manuscript to estimate the vehicle state and longitudinal tire forces.

3.1.2 Driver Evaluator

A pedal map converts the pedal position to a longitudinal torque request. Concerning the lateral velocity and yaw rate targets, they must approximate the vehicle's handling performance. De Novellis [36] conducted experiments showing that in quasi-steady-state, the lateral acceleration of the vehicle can be described by a function, see Equation (3.1). This function is used in the reference model to imitate the vehicle's behavior. Below a predefined lateral acceleration threshold a_y^*, the lateral acceleration target is proportional to the driver steering angle at the wheel δ_{dri} to obtain a desired and tunable understeer gradient K_U. Above that threshold, the relation between lateral acceleration and steering angle becomes nonlinear to represent the understeering of the vehicle caused by tire saturation. The target yaw rate is computed from the target lateral acceleration assuming steady-state as $\omega_{z,ref} = \frac{a_{y,ref}}{v_x}$. Finally, the reference lateral velocity is computed from the steady-state yaw rate equation of a bicycle model with cornering stiffness C_F and C_R: $v_{y,ref} = \frac{l_F C_F}{l_F C_F - l_R C_R} v_x \delta_{dri} - \frac{l_F^2 C_F + l_R^2 C_R}{l_F C_F - l_R C_R} \omega_{z,ref}$, where the tunable understeer gradient K_U is utilized to tune the cornering stiffness C_F and C_R.

$$a_{y,ref} = \begin{cases} \delta_{dri}/K_U & \text{if } \delta < a_y^* K_U \\ a_{y,max} + (a_y^* - a_{y,max}) e^{\frac{a_y^* K_U - \delta_{dri}}{(a_{y,max} - a_y^*) K_U}} & \text{if } \delta \geq a_y^* K_U \end{cases} \tag{3.1}$$

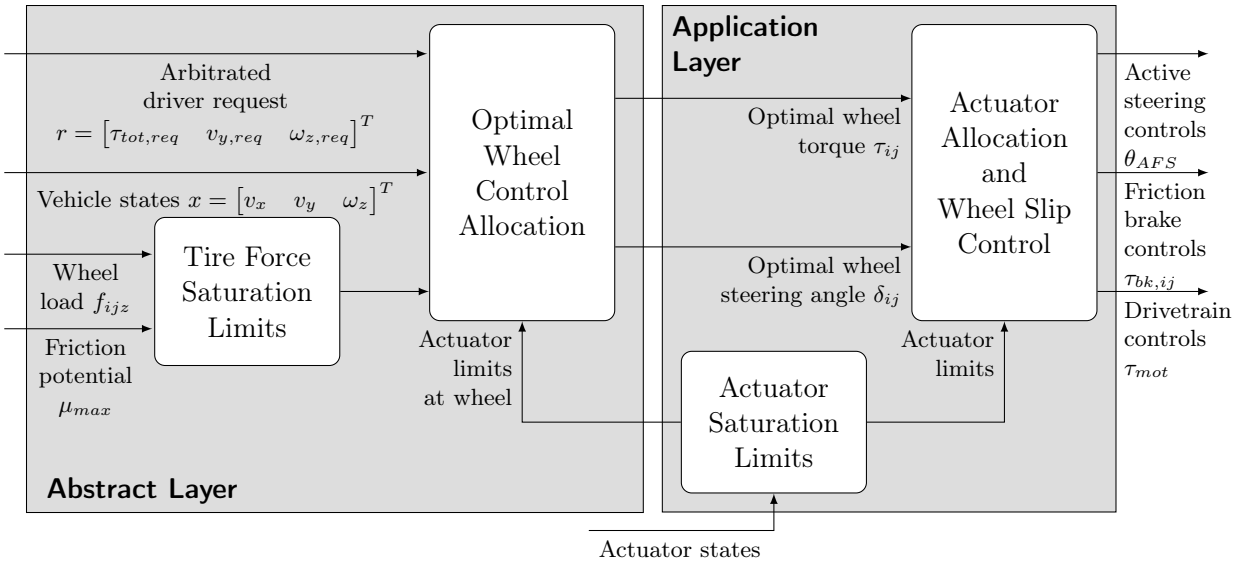

Figure 3.2: Structure of the Vehicle Motion Controller for planar motion control

3.1.3 Vehicle Motion Controller

The block labeled 'Vehicle Motion Controller' maps the motion request to the actuator commands, Figure 3.2 shows a more precise implementation of this component. The architecture is decomposed into two layers to improve the architecture reusability. The abstract layer converts the driver's request to commands for each wheel; it considers the vehicle's four wheels as actuators whose control signals are the wheel torques and steering angles. The application layer converts the wheel controls to actuator commands which are sent to the actuator layer. Using this approach reduces the calibration cost associated with designing the 'Generalized forces allocation' layer of the multi-layered architecture for different vehicles sharing the same platform but equipped with different actuator sets. Moreover, given an actuator configuration, deteriorated configuration sets can be created to easily disable faulty actuators, thus improving the architecture fault tolerance.

Abstract Layer

The 'Optimal Wheel Control Allocation' is the main component of the abstract layer. Its goal is:

- Allocate the wheel controls to track the driver requests. These controls must be feasible, i.e. the actuators must be able to apply the allocated wheel torque and steering angle controls. The abstract layer aims to be actuator-independent so that it does not need to be redesigned between different actuator sets. However, it still needs to be aware of the capabilities of

the actuators; this is illustrated by the signals feeding the actuator saturation limits to the 'Optimal Wheel Control Allocation' block.

- Enforce vehicle stability. The architecture assumes that information about the road condition is available in the form of a maximum friction coefficient; constraints limiting the tire forces within the friction circle are used to maintain vehicle stability.

Several implementations can be envisioned for the 'Optimal Wheel Control Allocation' block. One possible implementation is to define generalized forces to apply on the chassis and a control allocation mapping the generalized forces to the wheel controls; this would result in an architecture similar to the multi-layered architecture described in Figure 1.4 where the Layer 4 combines the control allocation mapping the generalized forces to the wheel controls and the application layer. Another possibility is to use optimization-based control to directly allocate wheel controls from the driver's request. Both approaches will be investigated in this dissertation.

Application Layer

The application layer's role is to allocate the actuator controls (motor torque for the drivetrain, brake torque for the friction brake, and motor angular displacement for the active steering) while enforcing actuator magnitude and rate saturation. It also needs to define actuator capabilities in terms of constraints, for instance, the dual-motor drivetrain cannot apply a yaw moment without resorting to brake-based torque vectoring, so the application layer must define the following constraint $\tau_{iL} - \tau_{iR} = 0$ if brake-based TV is not allowed, and $|\tau_{iL} - \tau_{iR}| \leq |\tau_f|$ where τ_f is the maximum torque the brake can applied if brake-based TV is allowed.

Distributing the wheel controls to the actuators can be decomposed into two parts: one that maps the wheel steering controls to the active steering actuators, and one mapping the wheel torque to the brake and drivetrain actuators. In addition to coordinating the brake and drivetrain, the application layer must also ensure wheel stability in case the maximum friction coefficient is over-estimated.

3.2 Dynamic Control Allocation

The control architecture heavily uses control allocation to optimally distribute the controls to the different wheels and actuators. If the system has more actuators than controlled signals, the system

is over-actuated. Different inputs can yield the same steady-state output response for such a system. A control allocation aims to distribute the controls to achieve the desired target optimally.

A mathematical formulation of control allocation is given in this paragraph. A vector $\boldsymbol{y} \in \mathbb{R}^{n_y}$ defines the desired targets, for instance the generalized forces to apply on the vehicle; $\boldsymbol{u} \in \mathbb{R}^{n_u}$ defines the actuator commands; the mapping from actuator command to controlled signals is represented as $\boldsymbol{y} = f(\boldsymbol{u})$. The goal of control allocation is to find a vector $\boldsymbol{u}$ such that $\boldsymbol{y} = B\boldsymbol{u}$. Since it is not always possible to find a distribution that perfectly equals the target, this could be due to constraints on the actuators or infeasible target $\boldsymbol{y}$; it is usually preferable to minimize the error $\boldsymbol{y} - B\boldsymbol{u}$ between the requested targets and the achieved ones. Some prioritization is usually involved so that if the desired target cannot be achieved, the allocation will favor some control objectives (i.e., element of the vector $\boldsymbol{y}$) over others. Hence, one of the goal of the optimization can be formulated as minimizing a weighted cost of the tracking error $\|Q(\boldsymbol{y} - B\boldsymbol{u})\|$. The solution to this problem is not unique if the number of actuators n_u is greater than the number of targets n_y; in this situation, it is possible to specify secondary objectives $\mathcal{J}(u)$ to uniquely define the controls $\boldsymbol{u}$. Finally, constraints $g(\boldsymbol{u}) \leq 0$ on the system can be defined to limit the operating range of the actuators. To summarize, the control allocation can be formulated as the following optimization problem:

$$\boldsymbol{u} = \arg\min_{u} \|Q(\boldsymbol{y} - B\boldsymbol{u})\| + \mathcal{J}(\boldsymbol{u}) \tag{3.2a}$$

$$\text{subject to: } g(\boldsymbol{u}) \leq 0 \tag{3.2b}$$

3.2.1 Unconstrained Control Allocation

Assuming a linear map from controls to target $\boldsymbol{y} = f(\boldsymbol{u}) = B\boldsymbol{u}$ where B is a $n_y \times n_u$ matrix, an obvious solution if $n_u = n_y$ and B is not singular is $\boldsymbol{u} = B^{-1}\boldsymbol{y}$. The Moore-Penrose pseudo-inverse $B^\dagger$, defined as $B^\dagger = B^T(BB^T)^{-1}$ if B is non-singular and $n_y \leq n_u$, generalizes the previous result to the case of singular or non-square matrix B. Moreover, if the secondary cost is chosen as a quadratic cost of the error between the controls u and a desired allocation $\boldsymbol{u}_p$, i.e. $\mathcal{J}(\boldsymbol{u}) = \frac{1}{2}(\boldsymbol{u} - \boldsymbol{u}_p)^T W(\boldsymbol{u} - \boldsymbol{u}_p) = \frac{1}{2}\|\boldsymbol{u} - \boldsymbol{u}_p\|_W^2$ where W is a positive definite symmetric matrix, the solution of the optimization problem is defined by the weighted pseudo-inverse $B^\sharp = W^{-1}B^T(BW^{-1}B^T)^{-1}$ and $\boldsymbol{u} = (I - B^\sharp)\boldsymbol{u}_p + B^\sharp\boldsymbol{y}$, which reduces to $\boldsymbol{u} = B^\sharp\boldsymbol{y}$ if $\boldsymbol{u}_p = 0$.

3.2.2 Constrained Control Allocation

The weighted pseudo-inverse method can be modified to accommodate actuator constraints, yielding the redistributed pseudo-inverse. This method uses the solution of the unconstrained weighted pseudo-inverse as an initial solution. If some control elements exceed their saturation limits, the vector of control is decomposed into elements that exceed their limits and elements that do not. The value of the control signals exceeding their limits is saturated to ensure feasibility, and the unsaturated controls are recomputed to include the error caused by the saturation. This process is repeated until an adequate solution is found or all the controls are saturated.

Daisy-chaining offers a similar approach. The actuators are ranked in a hierarchy (u_i) based on *a priori* knowledge of the system, the control target $\boldsymbol{y} = B\boldsymbol{u} = \sum_i B_i u_i$ is distributed first to the actuators that are higher in the hierarchy by a weighted pseudo-inverse $\hat{u}_i = B_i^{\sharp}(\boldsymbol{y} - \sum_{j<i} B_j u_j)$. If the value of $\hat{u}_i$ satisfies the actuator bounds, the actuator u_i is set to $\hat{u}_i$ and $\forall j > i, u_j = 0$. If the actuators cannot provide such command, the value of the control input is clipped to satisfy the actuator constraints and the process is repeated for the actuator u_{i+1}.

Both approaches only differ in how they deal with actuator saturation: the redistributed pseudo-inverse redistributes the target error due to saturation to all unsaturated actuators, whereas the daisy-chain method redistributes the control to the unsaturated actuator with the highest priority. These two approaches do not guarantee optimal results because they do not consider the entire attainable set of command signals. Finally, they only enforce bounds actuator constraints $\boldsymbol{u}_{min} \leq \boldsymbol{u} \leq \boldsymbol{u}_{max}$. To use more general constraints, the control allocation must be formulated by an optimization problem.

Three classes of optimization problems are presented: Linear Programming (LP), Quadratic Programming (QP), Nonlinear Programming (NLP).

LP minimizes a linear cost subject to polytopic constraints, the problem can be formulated as described in Equation (3.3) where the ℓ_1-norm of a vector is $\|\boldsymbol{x}\|_1 = \sum_i |x_i|$. LP problems can be solved with the simplex algorithm which proceeds by iteratively visiting the vertices of the polytope described by the constraints of the problem, each iteration provides an improved solution. To use the simplex algorithm, the problem must be transformed to a canonical LP problem defined as $\arg\min_u \boldsymbol{c}^T\boldsymbol{x}$ subject to $A\boldsymbol{x} \leq \boldsymbol{b}$ and $\boldsymbol{x} \geq 0$, where $\boldsymbol{x}$ are the optimization variables, this can be

achieved by introducing the variable $\boldsymbol{s} = Q(\boldsymbol{y} - B\boldsymbol{u})$ and $\boldsymbol{t} = W_u(\boldsymbol{u} - \boldsymbol{u}_p)$ and decompose them into positive and real parts such that $\boldsymbol{s} = \boldsymbol{s}^+ + \boldsymbol{s}^-$ and $\boldsymbol{t} = \boldsymbol{t}^+ + \boldsymbol{t}^-$ where $\boldsymbol{s}^+$ and $\boldsymbol{t}^+$ are positive and $\boldsymbol{s}^-$ and $\boldsymbol{t}^-$ are negative, the optimization variable is then the stacked vector of $\boldsymbol{s}^+$, $\boldsymbol{s}^-$, $\boldsymbol{t} = \boldsymbol{t}^+$, and $\boldsymbol{t}^-$. This illustrates one of the disadvantages of LP, even though the simplex algorithm is fairly efficient, formulating the control allocation of n_y signals to n_u allocated controls as a LP problem results in an optimization problem with $2(n_y + n_u)$ optimization variables. Moreover, solutions of LP problems are found at the vertices of the polytope defined by the constraints, this often result in solution where only a few actuators are used close to their saturation limits; on the contrary, QP and NLP problems yields solution which tends to use all actuators but to a smaller extent, this is usually a more suitable behavior.

$$\boldsymbol{u} = \arg\min_{u} \|Q(\boldsymbol{y} - B\boldsymbol{u})\|_1 + \|W_u(\boldsymbol{u} - \boldsymbol{u}_p)\|_1 \tag{3.3a}$$

$$\text{subject to: } A\boldsymbol{u} \leq \boldsymbol{b} \tag{3.3b}$$

QP solves problem with a quadratic cost and polytopic constraints defined in Equation (3.4), where $\|\boldsymbol{x}\|_2 = \left(\sum_i x_i^2\right)^{\frac{1}{2}}$ denotes the ℓ_2-norm of $\boldsymbol{x}$. Several classes of algorithms exist to solve such problems. Interior point solvers, such as HPIPM, convert the constrained problem to an unconstrained problem by introducing a barrier function that penalizes the constraints violation; the solution can then be obtained using Newton's method. Active set methods use another approach; they identify a subset of active inequality constraints to reduce the complexity of the search; examples of QP solver based on the active set method include qpOASES. QP has been widely used in the context of control allocation. A common cost function is to penalize a weighted sum of the quadratic tracking error and the actuator rate of change; it ensures perfect tracking if enough actuation is available and allows for tuning the bandwidth of the actuators.

$$\boldsymbol{u} = \arg\min_{u} \|Q(\boldsymbol{y} - B\boldsymbol{u})\|_2^2 + \|W_u(\boldsymbol{u} - \boldsymbol{u}_p)\|_2^2 \tag{3.4a}$$

$$\text{subject to: } A\boldsymbol{u} \leq \boldsymbol{b} \tag{3.4b}$$

NLP represents the most general class of optimization problems described in this manuscript; see Equation (3.5). NLP problems can be highly computationally intensive, Sequential Quadratic Programming (SQP) provides a method to solve such problem, it produces a sequence of solutions, each solution to a QP subproblem, which converge to a local minimum of the NLP problem. Given an estimate of the solution, it linearizes the NLP problem into a QP problem (using a second-order Taylor expansion of the NLP cost function and a first-order Taylor expansion of the NLP inequality constraints). The solution of the QP subproblem defines a search direction, and the estimate of the solution is updated using this direction; the process is repeated until an optimal enough solution is found.

$$\boldsymbol{u} = \arg\min_{u} \|Q(\boldsymbol{y} - B\boldsymbol{u})\| + \mathcal{J}(\boldsymbol{u}) \tag{3.5a}$$

$$\text{subject to: } g(\boldsymbol{u}) \leq 0 \tag{3.5b}$$

3.3 Stability and Robustness of Feedback System with Dynamic Control Allocation

The structure of the multi-layer control architecture is extensible, intuitive, and flexible. The high-level controllers are usually implemented as MIMO controller generating a desired generalized forces to be applied on the vehicle. The forces and moments are then allocated to the actuators by a control allocation usually formulated as an optimization problem. The control allocation is usually placed inside the feedback loop between the high-level controller and the low-level controls/smart-actuators; this approach was used in [11], [17], [19], [21] to implement multi-layered IVDC architectures. However, additional considerations must be taken when adding the control allocation inside the feedback loop: e.g., constrained allocations can cause windup issues; dynamic allocations include addition of different dynamics inside the feedback loop. The control allocation and control loop designs are not independent; neglecting these considerations can destabilize the control loop.

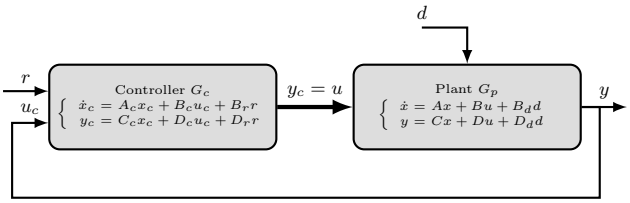

(a) Without control allocation and saturation

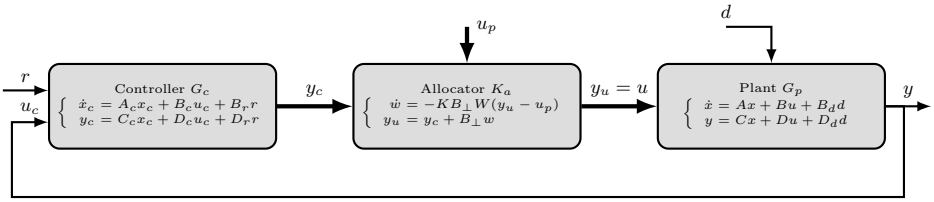

(b) With control allocation and without saturation

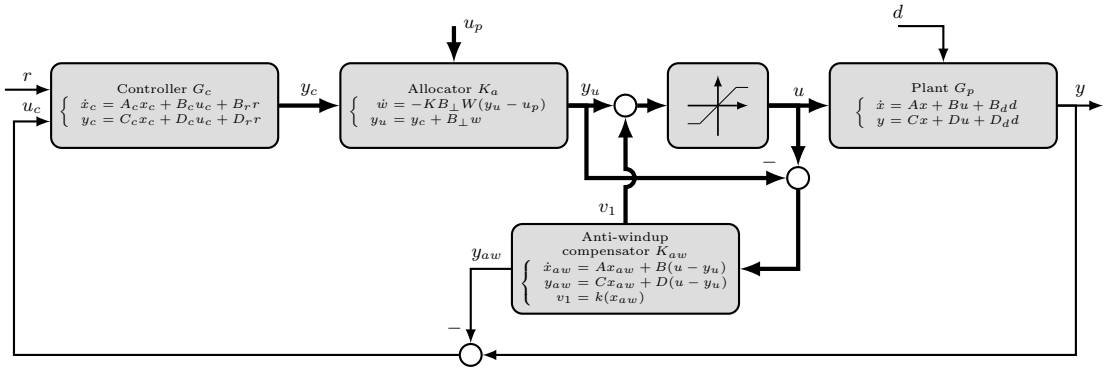

(c) With control allocation and saturation

Figure 3.3: Feedback loop with dynamic control allocation using the nullspace allocator [56]

3.3.1 Nullspace Allocator Framework

Zaccarian [56] proposes a framework for dynamic control allocation of over-actuated systems, which decouples the design of control allocation and feedback controller while guaranteeing internal stability, see Figure 3.3. Given a feedback loop with a controller G_c and a plant G_p (Figure 3.3a), Zaccarian shows that an allocator block K_a, whose design is independent of the controller, can be interconnected between the controller and the plant (Figure 3.3b) to modify the plant input without modifying its steady-state output while maintaining stability. The allocator block minimizes a quadratic cost between a fictitious control input u_p representing the desired input allocation and the input applied to the plant u, allowing to take advantage of the additional degree of freedom offered by the plant over-actuation.

A distinction is made in the design of the allocator between *strong* and *weak input redundancy*. Given a state-space (A, B, C, D) of the plant, if the right nullspace $\mathrm{Ker}(P^*)$ of the matrix $P^* =$

$\begin{bmatrix} B^T & D^T \end{bmatrix}^T$ is not empty, the plant is strongly-input redundant; if $G_p(s=0) = CA^{-1}B + D$ is a finite matrix and its right nullspace is not empty, the plant is weakly-input redundant and P^* is used to denote $G_p(s=0)$. The design of the nullspace allocator is based on the matrix $B_\perp$ whose column space $\mathrm{Im}(B_\perp)$ corresponds to the right nullspace of P^*:

$$\mathrm{Im}(B_\perp) = \mathrm{Ker}(P^*) \tag{3.6}$$

Zaccarian [57] shows that if the plant G_p is strongly input redundant, interconnecting the nullspace allocator K_a between the controller and the plant does not affect internal stability and that the system outputs of the controls loops with and without allocator are the same at any time, i.e., the allocation is invisible at the plant output. The guarantees are less strict if the system is weakly input redundant since Zaccarian shows that with weakly-input systems, the dynamic of the allocator must be made slow enough to guarantee stability; moreover, the allocation will be invisible at the plant output only during steady-state, but it will be visible during transient.

This framework can also be used in the presence of actuator magnitude and rate saturation; Figure 3.3c shows a feedback loop equipped with control allocation and magnitude saturation, an anti-windup compensator is used to guarantee closed-loop stability.

The nullspace allocator framework is convenient since it provides modularity and flexibility. The different components can be designed independently; in particular, the design of the allocator is independent of the controller and have their own goal: the controller stabilize the plant, the allocator modifies the distribution without losing stability to follow a desired distribution u_p, which can be defined by a control allocation, anti-windup compensator and magnitude, and rate saturation blocks ensure the feasibility of the command. However, the nullspace allocator framework also has some limitations. First, even though magnitude and rate constraints can be added with the anti-windup compensator and saturation blocks, the optimization problem solved by the actuator is unconstrained; Kolaric et al. [58] address that issue and impose actuator constraints directly in the optimization problem. Second, a distinction must be made between weakly and strongly-input redundant systems. Cristofaro [59] shows that this distinction can be waived for linear systems, generalizing the invisible property of strongly input-redundant systems to weakly input-redundant systems during transient and alleviating the need for slower allocator dynamics. Cristofaro [59] and

Serrani [60] propose to modify the dynamic allocation framework by decomposing the allocator into two components: an annihilator block which injects a signal to the plant input that is invisible at the plant output (thus providing new degrees of freedom to redistribute the plant inputs), a steady-state optimizer exploits these extra degrees of freedom to minimize a cost function. Third, the allocator only minimizes quadratic cost. Cocetti [61] uses the annihilator block with an optimizer formulated as a gradient flow of a cost function minimizing a ℓ_1, ℓ_2, or ℓ_∞-norm to generalize the nullspace allocator framework to other cost function. Finally, there is no robustness guarantee in the presence of uncertainties. Cocetti partially addresses that issue by showing that there exists a slow enough gradient flow optimizer that guarantees robust stability to parametric uncertainties.

3.3.2 Nullspace Allocator from the Smith-McMillan Form

In this section, we rederive the nullspace allocator proposed by Zaccarian in [57] but by using the properties of the Smith-McMillan form of the system instead of using a state-space representation. The Smith-McMillan-based nullspace allocator generalizes the properties of strongly-input redundant to the case of weakly-input redundant systems and facilitates the robustness analysis of the allocator framework.

The Smith-McMillan form generalizes the concept of poles and transmission zeros for MIMO systems. If the system is represented by a rational transfer function matrix $G_p(s)$ such that $\boldsymbol{y} = G_p(s)\boldsymbol{u}$, it can be decomposed[1] as follows [62], [63]

$$U_L G_p U_R = M_p = \begin{bmatrix} \operatorname{diag}(\frac{\eta_1}{\delta_1}, \ldots, \frac{\eta_r}{\delta_r}) & 0_{r\times(n_u-r)} \\ 0_{(n_y-r)\times r} & 0_{(n_y-r)\times(n_u-r)} \end{bmatrix} \tag{3.7}$$

where r is the rank of the system, U_L and U_R are unimodular matrices, the numerator η_k divides η_{k+1} and the denominator δ_k divides δ_{k-1}, and $\forall k$, $\frac{\eta_k}{\delta_k}$ is irreducible. The transmission zero of the system are the the value of s which would decrease the rank of the matrix G_p, i.e. the roots of the

[1] The most straightforward way to obtain the Smith-McMillan form is to decompose the rational matrix G_p into a numerator polynomial matrix P and a denominator polynomial function δ such that $G_p = P/\delta$, and to compute the Smith normal form of the polynomial matrix P. Unfortunately, some software only allows computing the Smith normal form of a square matrix. This problem can be easily circumvented by first computing the column-style Hermite normal form H of P. Because the matrix H is wide and lower triangular if the system is over-actuated, a square matrix H_s can be extracted from the first columns of H such that $H = [H_s \quad 0]$. Finally, the Smith normal form of P is $[M_s \quad 0]$ where M_s is the Smith normal form of the square matrix H_s.

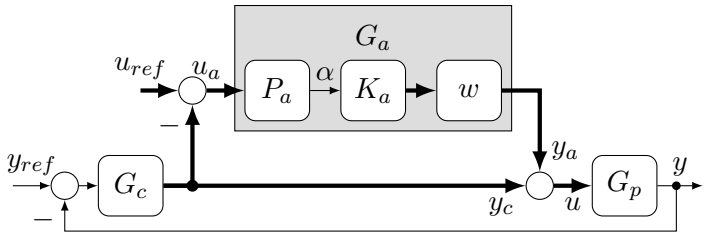

Figure 3.4: Dynamic control allocation with the Smith-McMillan-based allocator. $G_a = K_a P_a w(s)$ denotes the Smith-McMillan-based allocator where K_a is the polynomial matrix generating the right nullspace of G_p, P_a is a rational matrix defining the extra DoF α due to over-actuation, and $w(s)$ is a unit gain scalar transfer function.

numerators η_k; the poles of the systems are the value of s for which $G_p(s)$ is singular, i.e. the roots of the denominators δ_k.

If the system G_p has maximum rank and is over-actuated (i.e. $r = n_y$ and $n_u > n_y$), the last $n_a = n_u - r$ columns of the Smith-McMillan form are zeros, or similarly the last n_a columns of $G_p U_R = U_L^{-1} M_p$ are zeros, thus the last n_a columns of U_R generate the right nullspace of the rational matrix G_p. Let the last n_a column of U_R be denoted as K_a, such that $\mathrm{Im}(K_a) = \mathrm{Ker}(G_p)$. The matrix K_a generalizes Equation (3.6) for both weakly and strongly-input redundant systems by using dynamic rational transfer function instead of a static gain matrix.

With an over-actuated non-singular linear system, the dimension of the vector space generated by the plant output is rank $(G_p(s)) = n_y$; if a one degree-of-freedom linear controller is used (i.e., its input is the target error) the vector space generated by the plant input is also of dimension n_u. Therefore, a single one degree-of-freedom controller does not fully utilize the over-actuation since the controller does not use $n_a = n_u - n_y$ directions in the input space. The matrix K_a allows to inject a signal of dimension n_a and take advantage of the extra DoF offered by the over-actuation without modifying the plant output response.

Proposition 1 *Suppose the closed-loop connecting the controller G_c and the plant G_p is well-posed and the transfer function matrix verifies $G_p G_a = 0$. In that case, inter-connecting the allocator $(I - G_a)$ between the controller and the plant preserves the well-posedness of the control loop. Moreover, if the closed-loop without allocator is internally stable and the allocator G_a is stable, then the closed-loop with allocator is also internally stable.*

Proof. We can derive relations between the transfer function of the control loops with and without

allocator. Because of the invisibility property of the allocator, i.e. $G_p G_a = 0$, the allocator does not modify the output return ratio $L_y = G_p G_c$, the output sensitivity function $S_y = (I + L_y)^{-1}$, and the output closed-loop transfer function $T_y = L_y S_y$. However, the Youla transfer function, input return ratio $L_u = G_c G_p$, input sensitivity transfer function $S_u = (I + L_u)^{-1}$, and input closed-loop $T_u = L_u S_u$ are modified by the allocator. If Y, L_u, T_u, and S_u denote respectively the Youla transfer function, input closed-loop, input sensitivity transfer function without allocator, then with allocator they become respectively $Y^a = (I - G_a)Y$, $L_u^a = (I - G_a)L_u$, $T_u^a = (I - G_a)T_u$, and $S_u^a = (I + G_a L_u)S_u$.

A MIMO system is well-posed if and only if $(I + L_y(s))$ is invertible $\forall s$ [63]. Because the allocator does not modify the output return ratio, the closed-loop with allocator is well-posed if the original closed-loop without allocator is well-posed.

Moreover, the closed-loop system is internally stable if the transfer functions mapping all exogenous inputs to any signal are stable. All the transfer functions inside the control loop can be expressed in terms of Y, T_u, T_y, and $S_y G_p$ [63]. For the control loop shown in Figure 3.4, all transfer function can be expressed in terms of G_a and the Y, T_u, T_y, and $S_y G_p$ of the control loop without allocator. Therefore, if the closed-loop without allocator is internally stable and the allocator G_a is stable, then the closed-loop with allocator is internally stable. □

Proposition 2 *Let W be a symmetric matrix such that the polynomial matrix $K_a^T W K_a$ is invertible, let the filter $\bar{G}_a$ be defined as $\bar{G}_a = K_a(K_a^T W K_a)^{-1} K_a^T W$, and let G_a be defined as $G_a = \bar{G}_a w(s)$ where $w(s)$ is a scalar transfer function with unit gain. Then, injecting the signal $y_a = G_a(u_{ref} - y_c)$ to the controller output y_c such that the plant input is $u = y_c + y_a$ does not modify the plant output response and it guarantees that the signal u follows the signal u_{ref} in the least-square sense minimizing $\|u_{ref} - u\|_W^2 = \frac{1}{2}(u_{ref} - u)^T W (u_{ref} - u)$ at any time if $w(s) = 1$ and only during steady-state if $w(s) \neq 1$.*

Proof. The right nullspace of the plant G_p is generated by the transfer function matrix K_a; thus, injecting any output signals of K_a in the plant input will result in a zero plant output.

Let α be the input of the filter K_a, and let u_a and y_a be the input and output of the allocator $\bar{G}_a$ such that $u_{ref} - u = u_{ref} - y_c - K_a\alpha = u_a - K_a\alpha$ (see Figure 3.4 with $w(s) = 1$). The objective is

now to chose α such that the cost $\|u_{ref} - u\|_W^2$ is minimized:

$$\begin{aligned} \alpha &= \arg\min_{\alpha} \|u_{ref} - u\|_W^2 = \arg\min_{\alpha} \|u_a - K_a\alpha\|_W^2 \\ &= \arg\min_{\alpha} \left(\frac{1}{2}\alpha^T K_a^T W K_a \alpha - u_a^T W K_a \alpha + \frac{1}{2} u_a^T W u_a \right) \end{aligned} \tag{3.8}$$

This is an unconstrained QPP whose solution must satisfy $K_a^T W K_a \alpha = K_a^T W u_a$, since by assumption $(K_a^T W K_a)$ is invertible, the solution is $\alpha = (K_a^T W K_a)^{-1} K_a^T W u_a$ and using $u = y_c + \bar{G}_a u_a = y_c + \bar{G}_a(u_{ref} - y_c)$ guarantees that the input u minimizes the quadratic cost $\|u_{ref} - u\|_W^2$ at any time.

Finally, if the filter $w(s) \neq 1$, the same analysis can be done and the final value theorem yields that the steady-state of the signal u follows the constant signal u_{ref} by minimizing the cost $\|u_{ref} - u\|_W^2$. □

Interconnecting the allocator G_a as shown in Figure 3.4 is equivalent to modifying the controller transfer function G_c by $(I - G_a)G_c$ and adding a feedforward term G_a from u_{ref} to u. Proposition 1 shows that the allocator preserves the well-posedness of the control loop and that if the allocator is stable, internal stability is preserved too. Proposition 2 shows that the filter $\bar{G}_a$ allows modifying the input of the plant to follow the desired distribution without modifying the plant output response. However, the filter $\bar{G}_a$ is not guaranteed to be stable or even proper. If it is not, it must be multiplied by a scalar and unit gain transfer function $w(s)$ to obtain the stable and proper filter G_a. Canceling the unstable modes of the allocator $\bar{G}_a$ is permissible since the cancellation takes place inside the allocator block G_a. The transfer function $w(s)$ does not affect the invisibility property of the allocator; however, it only guarantees that the steady-state plant input u follows the input target u_{ref} in the least-square sense but not its transient. The allocator block is defined by:

$$G_a = \bar{G}_a w(s) = K_a (K_a^T W K_a)^{-1} K_a^T W w(s) \tag{3.9}$$

The matrix W defines the tracking priority of the different signals in the control distribution u_{ref} and the transfer function $w(s)$ defines the dynamic of the allocator.

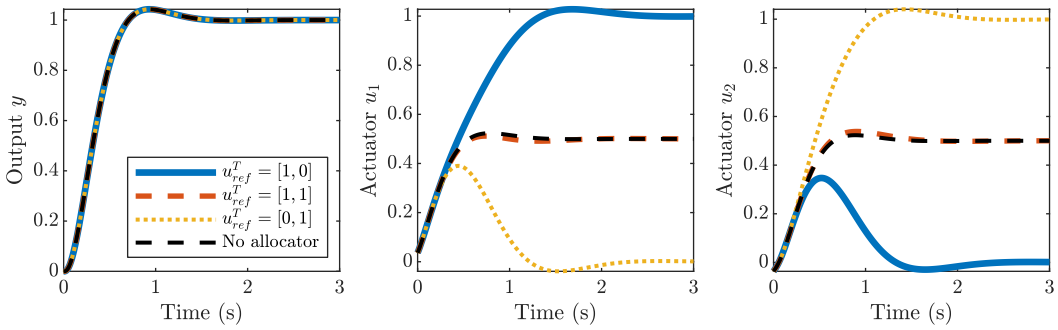

Figure 3.5: Step response of the input-delayed system with the Smith-McMillan-based allocator with $y_{ref} = 1$ and several u_{ref}. The time delays are $\tau_1 = 0.05\,\text{s}$ and $\tau_2 = 0.1\,\text{s}$, ω_0 is set to 4 Hz and the controller is design to have a closed-loop bandiwdth of 0.5 Hz.

Example with an Input-Delayed System To illustrate the design of the Smith-McMillan-based allocator, we consider a system with two identical actuators suffering from different communication delays, let the plant be written as $G_p = G_{p0}G_d = G_{p0}\begin{bmatrix} e^{-\tau_1 s} & e^{-\tau_2 s}\end{bmatrix}$ where $G_{p0}(s) \neq 0$ can be any transfer function. Since $G_{p0} \neq 0$, the right nullspace of G_p and the matrix K_a are set by the matrix G_d and are independent of G_{p0}. The allocator design requires a rational transfer function,[2] so the pure time delays are replaced by a first-order Padé approximation $\tilde{G}_d = \begin{bmatrix}\frac{2-\tau_1 s}{2+\tau_1 s} & \frac{2-\tau_2 s}{2+\tau_2 s}\end{bmatrix}$. The Smith-McMillan form M_P of the plant and the unimodular matrices U_L and U_R such that $M_P = U_L G_p U_R$ are:

$$M_P = \begin{bmatrix}\frac{1}{(2+\tau_1 s)(2+\tau_2 s)} & 0\end{bmatrix},\ U_L = 1,\ U_R = \begin{bmatrix}\frac{1}{8} - \frac{s\tau_1\tau_2}{16(\tau_1-\tau_2)} & (2+\tau_1 s)(2-\tau_2 s) \\ \frac{s\tau_1\tau_2}{16(\tau_1-\tau_2)} + \frac{1}{8} & -(2-\tau_1 s)(2+\tau_2 s)\end{bmatrix} \tag{3.10}$$

The matrix K_a can be obtained from the Smith-McMillan decomposition and is defined as $K_a^T = \begin{bmatrix}(2+\tau_1 s)(2-\tau_2 s) & -(2-\tau_1 s)(2+\tau_2 s)\end{bmatrix}$. Then, with $W = I$:

$$\bar{G}_a = \frac{1}{(\tau_1 s-2)^2(\tau_2 s+2)^2 + (\tau_1 s+2)^2(\tau_2 s-2)^2} \begin{bmatrix}(\tau_1 s+2)^2(\tau_2 s-2)^2 & -(\tau_1^2 s^2-4)(\tau_2^2 s^2-4) \\ -(\tau_1^2 s^2-4)(\tau_2^2 s^2-4) & (\tau_1 s-2)^2(\tau_2 s+2)^2\end{bmatrix} \tag{3.11}$$

[2] For this system, the right nullspace is generated by the causal matrix $K_a^T = e^{-\max(\tau_1,\tau_2)s}\begin{bmatrix}e^{\tau_1 s} & -e^{\tau_2 s}\end{bmatrix}$. The allocator could be designed based on the previous matrix K_a, however, the pure delays are approximated by rational functions to illustrate the design of the allocator for a rational transfer function.

This transfer function matrix is proper but it might be unstable, it is multiplied by the following unit-gain transfer function to cancel unstable poles:

$$w(s) = \frac{\omega_0^4}{32} \frac{(\tau_1 s - 2)^2(\tau_2 s + 2)^2 + (\tau_1 s + 2)^2(\tau_2 s - 2)^2}{(s^2 + 2\zeta\omega_0 s + \omega_0^2)^2} \tag{3.12}$$

Since the transfer function has a unit gain, it still guarantees optimal steady-state least-square tracking of the desired control input u_{ref}. Any value for ω_0 should guarantee stability; however, choosing ω_0 such that $\omega_0^2\tau_1\tau_2 \geq 1$ would increase the gain of the allocator at high frequencies, increasing the gain of the Youla transfer function at high frequencies. We will show in the following sections that it would also deteriorate the robustness properties of the system. Figure 3.5 shows the step response of the feedback loop with and without allocator to several inputs u_{ref} with the same feedback controller G_c. The controller G_c used to generate the plot was designed with a bandwidth of 0.5 Hz such that the closed-loop is a second-order Butterworth filter. The figure shows that the allocator allows modifying the distribution of inputs without modifying the output response of the plant, despite approximating the system as a rational transfer function matrix.

3.3.3 Robust Stability and Performance and the Linear Fractional Transform Framework

Nominal stability and nominal performance respectively guarantee that the system is stable and the performance metrics are satisfied for the nominal system G_p. Robust stability and robust performance extend this definition to any uncertain system in a set of perturbed plants derived from G_p; both robust stability and performance assume nominal stability as a prerequisite.

Uncertainties may have several origins: parameters in the model can be wrong or vary because of changes in the operating conditions; for a closed-loop system, there might be a mismatch between the synthesized controller and the one that is implemented (e.g., due to the balanced reduction to obtain a lower order controller or due to time discretization), the sensor might also differ from its model (e.g., neglecting the signal quantization and time discretization for digital sensors); higher-order model dynamics might be ignored. Uncertainties are often categorized in parametric uncertainties, where the order of the model is unchanged, and the exact value of some parameters is unknown but usually bounded, and unmodelled dynamics, where some dynamics would increase the system order

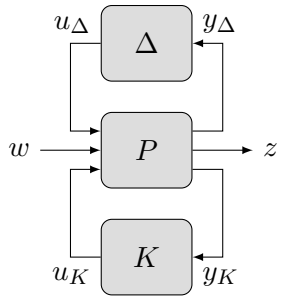

(a) $P - K - \Delta$ framework for controller synthesis.

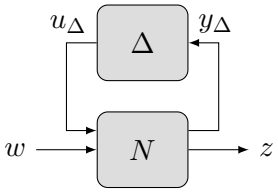

(b) $N - \Delta$ framework for robust performance analysis. N is defined as $N = F_l(P, K)$.

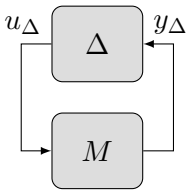

(c) $M - \Delta$ framework for robust stability analysis. M is defined as the upper left sub-block N_{11} of $N = F_l(P, K)$.

Figure 3.6: General framework for robustness analysis and robust controller synthesis

is missing.

The framework shown in Figure 3.6 generalizes the analysis for robust stability and robust performance and synthesis of the robust controller. The uncertainties are gathered in a block Δ, P represents an augmented plant, and K is the controller. The signal w stacks the exogenous input of the system, z are the regulated outputs, y_K are measured signals fed to the controller, u_K are the plant inputs defined by the controller, y_Δ and u_Δ are fictitious signals representing the inputs and outputs of the uncertainty block Δ. This framework makes extensive use of Linear Fractional Transformation (LFT), the lower and upper fractional transforms are respectively defined as follows,

$$F_l(P, K) = F_l(\begin{bmatrix} P_{11} & P_{12} \\ P_{21} & P_{22} \end{bmatrix}, K) = P_{11} + P_{12}(I - P_{22}K)^{-1}P_{21} \tag{3.13}$$

$$F_u(P, \Delta) = F_u(\begin{bmatrix} P_{11} & P_{12} \\ P_{21} & P_{22} \end{bmatrix}, \Delta) = P_{22} + P_{21}(I - P_{11}\Delta)^{-1}P_{12} \tag{3.14}$$

where the matrix P is decomposed into sub-blocks P_{11}, P_{12}, P_{21}, P_{22} of the appropriate size. Given a plant P and a controller K, the closed-loop mapping the fictitious signal u_Δ and exogenous inputs w to the fictitious signal y_Δ and regulated outputs z is denoted N and computed from the lower fractional transform $F_l(P, K)$. Similarly, given Δ an admissible uncertainty, a sampled uncertain augmented plant can be obtained from the upper fractional transform $F_u(P, \Delta)$. The set of admissible uncertainties is usually restricted to stable transfer functions with a unit $\mathcal{H}_\infty$-norm, this is without loss of generality because one can define filters in the augmented plant P so that the uncertainties satisfy $\|\Delta\|_\infty \leq 1$ and the assumption about Δ being stable may be relaxed [7, p. 311]. Therefore,

with the LFT framework robust stability of the closed-loop N can be defined as $F_u(N, \Delta)$ is stable $\forall\Delta$ such that $\|\Delta\|_\infty \leq 1$ and N is nominally stable. If N is nominally stable, the only possible way $F_u(N, \Delta)$ would be unstable is if $(I - N_{11}\Delta)^{-1}$ were not invertible, i.e. if one of the eigenvalues $\lambda_i(N_{11}\Delta)$ of $N_{11}\Delta$ would be equal to 1. The LFT framework reduces the robust stability of N to a criterion on $M = N_{11}$.

Moreover, regulated outputs are usually weighted by filters to define the requested performance of the system in the frequency domain by $\|F_l(P, K)\|_\infty \leq 1$. Therefore, with the LFT framework, robust stability of the closed-loop M can be defined as $F_u(M, \Delta)$ is stable $\forall\Delta$ such that $\|\Delta\|_\infty \leq 1$ and N is nominally stable. Similarly, robust performance of N is defined as $\|F_u(N, \Delta)\|_\infty \leq 1$ $\forall\Delta$ such that $\|\Delta\|_\infty \leq 1$ and N is nominally stable.

The uncertainty block Δ is qualified as structured if it can be written as a block diagonal matrix $\Delta = \text{blockdiag}(\Delta_1, \cdots, \Delta_i)$; if Δ is a full matrix, it is qualified as unstructured. The distinction between structured and unstructured uncertainties is important because the structure uncertainties define stricter constraints on the uncertainty which lead to better guarantees in terms of robustness. Indeed, for unstructured uncertainties, robust stability of M is ensured if and only if $\forall\omega, \forall\Delta$ the determinant $\det I_m\Delta(j\omega) \neq 0$ [7, p. 324], or equivalently $\lambda_i(M\Delta) \neq 1$ $\forall\Delta$ such that $\|\Delta\|_\infty \leq 1$. Therefore, for unstructured uncertainties, robust stability is equivalent to $\|M\|_\infty \leq 1$. For structure uncertainties, $\|M\|_\infty \leq 1$ is only a sufficient condition for robust stability, in fact a better sufficient condition for robust stability can be found: given an structured uncertainty Δ, if M is nominally stable and

$$\min_{D \in \mathcal{D}_\Delta} \left\|DMD^{-1}\right\|_\infty \leq 1 \text{ where } \mathcal{D}_\Delta = \{D \mid D\Delta = \Delta D\} \tag{3.15}$$

then the closed-loop M is robustly stable. This condition is stronger because $\left\|DMD^{-1}\right\|_\infty$ may be significantly smaller than $\|M\|_\infty$. It is convenient to introduce the following set defining all the matrices with the same structure as Δ:

$$S_\Delta = \{\Xi \mid \Xi \text{ stable with the same structure as } \Delta \text{ and } \|\Xi\|_\infty \leq 1\} \tag{3.16}$$

The structured singular value provides a way to quantify the robust stability and robust performance of a system by generalizing the concept of singular values. Given a structure for the uncertainty Δ,

it is defined as follows,

$$\mu_{\Delta}(M) = \begin{cases} 0 & \text{if } \{k_m \mid \det(I - Mk_mD) = 0, D \in S_{\Delta}\} = \emptyset \\ \frac{1}{\min\{k_m \mid \det(I - Mk_mD) = 0, D \in S_{\Delta}\}} & \text{otherwise} \end{cases} \tag{3.17}$$

The structured singular value corresponds to the inverse of the smallest factor k_m for which the uncertainty $k_m\Delta$ with $\|\Delta\|_{\infty}$ destabilizes the system M. A small structured singular value indicates good robustness since a larger disturbance is necessary to destabilize the system. If the uncertainty is a full matrix Δ_P, the structured singular value $\mu_{\Delta}(M)$ reduces to the maximum singular value of M denoted as $\overline{\sigma}(M)$. If Δ is a structured uncertainty, an upper bound on the structured singular value can be found:

$$\mu_{\Delta}(M(j\omega)) \leq \min_{D(j\omega) \in \mathcal{D}_{\Delta}} \overline{\sigma}(D(j\omega)M(j\omega)D(j\omega)^{-1}) \tag{3.18}$$

Another property of the structured singular value with uncertainty Δ is

$$\mu_{\Delta}(AB) \leq \overline{\sigma}(A)\mu_{\Delta A}(B) \text{ and } \mu_{\Delta}(AB) \leq \overline{\sigma}(B)\mu_{B\Delta}(A) \tag{3.19}$$

where $\mu_{\Delta A}$ denotes the structured singular value to uncertainties with structure similar to ΔA. Therefore, if Δ as the same structure as A (resp. B), the previous inequality yields $\mu_{\Delta}(AB) \leq \overline{\sigma}(A)\mu_{\Delta}(B)$ (resp. $\mu_{\Delta}(AB) \leq \overline{\sigma}(B)\mu_{\Delta}(A)$).

The following theorems define the notions of robust stability and robust performance in terms of conditions on the structured singular value and using the LFT framework [7].

Theorem 1 (Robust stability to structured uncertainty Δ [7, p. 331]) *Let M be a stable nominal system and Δ be a stable uncertainty, then any uncertain system $F_u(M, D)$ with $D \in S_{\Delta}$ are stable if and only if $\forall\omega, \mu_{\Delta}(M(j\omega)) \leq 1$.*

Theorem 2 (Robust performance to structured uncertainty Δ [7, p. 343]) *Let N be a stable nominal system and Δ be a stable uncertainty, $\forall D \in S_{\Delta}, \|F_u(N, D)\|_{\infty} \leq 1$ if and only if $\forall\omega, \mu_{\bar{\Delta}}(N(j\omega)) \leq 1$ where $\bar{\Delta} = \text{blockdiag}(\Delta, \Delta_P)$ and Δ_P is a full matrix such that $\|\Delta_P\|_{\infty} \leq 1$.*

3.3.4 μ-Analysis of the Smith-McMillan-Based Nullspace Allocator

This section analyses the robustness performance of the Smith-McMillan-based allocator to multiplicative input and output uncertainties.[3] For such uncertainties, the uncertain plant can be expressed as a function of the nominal plant G_p as follows,

$$G = (I + W_y \Delta_y) G_p (I + W_u \Delta_u) \tag{3.20}$$

where the uncertainty blocks Δ_u and Δ_y are assumed to be unstructured full-block complex perturbations, they are stacked in the uncertainty block $\Delta = \text{diag}(\Delta_u, \Delta_y)$. The filters W_u and W_y defines the range of the input and outputs uncertainties. To fit the LFT framework defined in Figure 3.6a, the controller is defined such that its inputs and outputs are respectively $y_K^T = \begin{bmatrix}(u_{ref} - y_c)^T & (y_{ref} - y)^T\end{bmatrix}$ and its output is $u_K^T = [y_a^T \quad y_c^T]$. The performance of the closed-loop is defined by the signal $z_\infty = W_p e = W_p(y_{ref} - y)$ and the tracking performance of the allocator is quantified by the signal $z_2 = W_a(u_{ref} - u)$ where W_p and W_a are tunable filters. These signals are stacked in the regulated output vector $z^T = [z_\infty \quad z_2]$. The augmented system P such that $\begin{bmatrix}y_\Delta & z & y_K\end{bmatrix}^T = P\begin{bmatrix}u_\Delta & w & u_K\end{bmatrix}^T$ is shown in Equation (3.21); the augmented closed-loop system N_{G_c}, obtained from the lower fractional transformation of P and G_c, is given in Equation (3.22).

$$P = \text{diag}(W_u, W_y, W_p, W_a, I, I) \left[\begin{array}{cc:cc:cc} 0 & 0 & 0 & 0 & I & I \\ G_p & 0 & 0 & 0 & G_p & G_p \\ \hdashline -G_p & -I & I & 0 & -G_p & -G_p \\ 0 & 0 & 0 & I & -I & -I \\ \hdashline 0 & 0 & 0 & I & 0 & -I \\ -G_p & -I & I & 0 & -G_p & -G_p \end{array}\right] \tag{3.21}$$

[3] Several type of uncertainties exist, multiplicative uncertainties are convenient to represent parametric uncertainties and higher frequency model mismatch. For multivariable systems, it is necessary to specify whether the perturbation is at the input or output of the plant, especially if the plant is ill-conditioned.

$$N_{G_c} = F_l(P, G_c) = \mathrm{diag}(W_u, W_y, W_p, W_a, I) \left[\begin{array}{cc:cc:c} -T_u & -G_cS_y & G_cS_y & 0 & S_u \\ S_yG_p & -T_y & T_y & 0 & S_yG_p \\ \hdashline -S_yG_p & -S_y & S_y & 0 & -G_pS_u \\ T_u & G_cS_y & -G_cS_y & I & -S_u \\ \hdashline T_u & G_cS_y & -G_cS_y & I & T_u \end{array}\right] \tag{3.22}$$

Finally, the closed-loop system with allocator N_{G_a,G_c} and the closed-loop system without allocator N_{0,G_c} can be obtained using another lower fractional transformation. Note that because the allocator has the property $G_pG_a = 0$, the following properties can be used to simplify the expression of the closed-loop N_{G_a,G_c}: $T_uG_a = 0$, $S_uG_a = G_a$.

$$N_{0,G_c} = F_l(N_{G_c}, 0_{n_u \times n_u}) = \mathrm{diag}(W_u, W_y, W_p, W_a) \left[\begin{array}{cc:cc} -T_u & -G_cS_y & G_cS_y & 0 \\ S_yG_p & -T_y & T_y & 0 \\ \hdashline -S_yG_p & -S_y & S_y & 0 \\ T_u & G_cS_y & -G_cS_y & I \end{array}\right] \tag{3.23}$$

$$N_{G_a,G_c} = F_l(N_{G_c}, G_a) = \mathrm{diag}(W_u, W_y, W_p, W_a(I - G_a)) \left[\begin{array}{cc:cc} -(I-G_a)T_u & -(I-G_a)G_cS_y & (I-G_a)G_cS_y & G_a \\ S_yG_p & -T_y & T_y & 0 \\ \hdashline -S_yG_p & -S_y & S_y & 0 \\ T_u & G_cS_y & -G_cS_y & I \end{array}\right] \tag{3.24}$$

As can be seen from Equation (3.24) and Equation (3.23), connecting the allocator to the feedback loop brings several modifications to the closed-loop transfer function. Connecting the allocator is equivalent to modifying the weighing filter W_a on the regulated output $z_2 = W_a(u_{ref} - u)$ by $W_a(I - G_a)$ without modifying the output z_∞ as should be expected since the allocator does not change the output response of the nominal system.

Theorems 1 and 2 shows that the μ value quantifies the robust performance and robust stability of the system, the following paragraphs derive bounds on the structured singular value. Let M_{G_a,G_c} and M_{0,G_c} be the transfer function from u_Δ to y_Δ of the closed-loop with and without allocator respectively. These matrices can be obtained by extracting the upper left sub-block from the N_{G_a,G_c}

and N_{0,G_c} matrices. Assuming that the filters W_u and W_y are invertible, the following relation exists between M_{0,G_c} and M_{G_a,G_c}: $M_{G_a,G_c} = W_\Delta M_{0,G_c}$ where $W_\Delta = \text{diag}(W_u(I - G_a)W_u^{-1}, I)$. Since the filter W_Δ has the same structure as the uncertainty block Δ, using (3.19) we have:

$$\forall \omega \in \mathbb{R},\ \underline{\sigma}(W_\Delta(j\omega))\mu_\Delta(M_{0,G_c}(j\omega)) \leq \mu_\Delta(M_{G_a,G_c}(j\omega)) \leq \overline{\sigma}(W_\Delta(j\omega))\mu_\Delta(M_{0,G_c}(j\omega)) \tag{3.25}$$

The previous inequality shows that the μ value quantifying the robust stability of the closed-loop with allocator is bounded by the robust stability μ value of the closed-loop without allocator and by a multiplicative factor defined by the allocator transfer function and the filter on the input uncertainty. The singular value $\overline{\sigma}(W_\Delta)$ is bounded by $1 \leq \overline{\sigma}(W_\Delta) \leq 1+\kappa(W_u)\overline{\sigma}(G_a)$ where κ denotes the condition of a matrix. Indeed, using the following properties of singular values: $\overline{\sigma}(\text{diag}(I, A)) = \max(1, \overline{\sigma}(A))$; $\overline{\sigma}(AB) \leq \overline{\sigma}(A)\overline{\sigma}(B)$; $\overline{\sigma}(I - A) \leq 1 + \overline{\sigma}(A)$; and $\overline{\sigma}(A^{-1}) = \underline{\sigma}(A)^{-1}$, we have:

$$\begin{aligned}
\overline{\sigma}(W_\Delta) &= \overline{\sigma}(\text{diag}(W_u(I - G_a)W_u^{-1}, I)) \\
&= \max(1, \overline{\sigma}(I - W_u G_a W_u^{-1})) \geq 1 \\
&\leq \max(1, 1 + \overline{\sigma}(W_u G_a W_u^{-1})) \\
&\leq 1 + \overline{\sigma}(W_u)\overline{\sigma}(G_a)\overline{\sigma}(W_u^{-1}) \\
&\leq 1 + \kappa(W_u)\overline{\sigma}(G_a)
\end{aligned}$$

Thus, Equation (3.25) shows that the robust stability μ value of the closed-loop without allocator is determined by the μ value associated with the robust stability of the closed-loop without allocator and by the singular values of the allocator. Increasing the $\mathcal{H}_\infty$ norm of the allocator would increase the upper bound on the μ value and deteriorate the robust stability of the system.

Similarly, we can derive bounds on the robust performance of the system with exogenous input $w = r$ and regulated output $z = z_\infty = W_p e$ with and without allocator. Let $N^\infty_{G_a,G_c}$ and N^∞_{0,G_c} be this closed-loop with and without allocator respectively, these matrices can be obtained by extracting the upper left sub-block from N_{G_a,G_c} and N_{0,G_c}.

$$\forall \omega \in \mathbb{R},\ \underline{\sigma}(W_{\bar{\Delta}}(j\omega))\mu_{\bar{\Delta}}(N^\infty_{0,G_c}(j\omega)) \leq \mu_{\bar{\Delta}}(N^\infty_{G_a,G_c}(j\omega)) \leq \overline{\sigma}(W_{\bar{\Delta}}(j\omega))\mu_{\bar{\Delta}}(N^\infty_{0,G_c}(j\omega)) \tag{3.26}$$

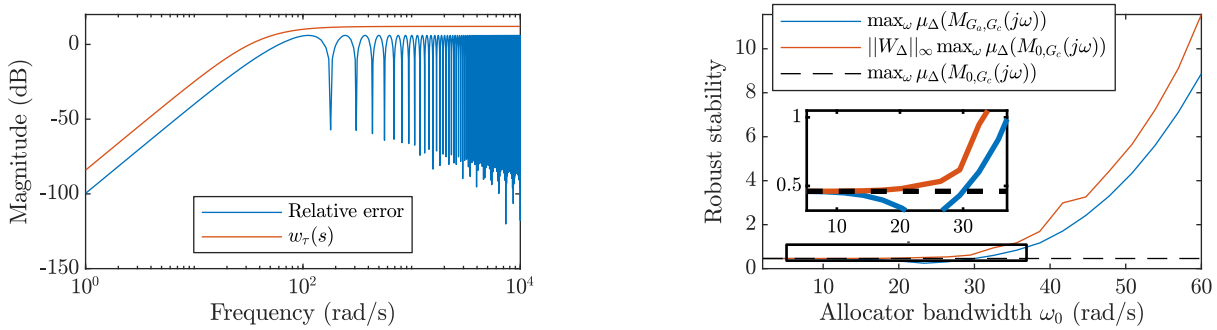

(a) Relative error between a pure time delay and its first-order Padé approximation

(b) Robust stability performance

Figure 3.7: Uncertainty of the input-delayed system and robust stability with different Smith-McMillan-based allocators

where $W_{\bar{\Delta}} = \text{diag}(W_u(I - G_a)W_u^{-1}, I, I)$ which can be bounded by $1 \leq \overline{\sigma}(W_{\bar{\Delta}}) \leq 1 + \kappa(W_u)\overline{\sigma}(G_a)$. So the same conclusion applies for robust performance as robust stability.

The filter W_y does not appear in the upper bound on the structured singular value for both robust stability and performance. Indeed, the allocator is not sensitive to multiplicative output uncertainties: if an uncertain plant has only multiplicative output uncertainty, it can be formulated as $G = (I + W_y\Delta_y)G_p$ where G_p is the nominal plant, Δ_y is an uncertain block such that $\|\Delta_y\|_\infty \leq 1$, and W_y is a filter that weights the uncertainty. Without allocator, i.e. with connection $u = y_c$, the plant output is given by $y_0 = Gu = (I + W_y\Delta_y)G_p y_c$. With allocator, i.e. with connection $u = y_c + G_a u_a$, the plant output is $y_1 = Gu = (I + W_y\Delta_y)G_p(y_c + G_a u_a) = (I + W_y\Delta_y)G_p y_c$ since by design $G_p G_a = 0$. The uncertainty can be moved from the input of the plant to the output by multiplying the uncertainty filter by the conditional number of the plant $\kappa(G_p)$ [7]; therefore, this analysis should guarantee robust stability and robust performance of the control-loop with allocator for systems that are well-conditioned.

Example with an Input-Delayed System Continuing with the same example as in Section 3.3.2, the relative error between a pure time delay τ_i and its first-order Padé approximation is upper bounded by the magnitude of the following filter at any frequency, see Figure 3.7a:

$$w_{\tau_i}(s) = \left(\frac{\tau_i s}{\frac{\tau_i}{2}s + 1}\right)^3 \text{ guarantees } \left|\frac{e^{-\tau_i s} - \frac{2-\tau_i s}{2+\tau_i s}}{\frac{2-\tau_i s}{2+\tau_i s}}\right| \leq |w_{\tau_i}(s)| \tag{3.27}$$

Therefore, the approximation of the pure time delay of the actuators can be represented by a

multiplicative input uncertainty Δ_u weighted by the filter $W_u = \text{diag}(w_{\tau_1}(s), w_{\tau_2}(s))$ such that $\|\Delta_u\|_\infty \leq 1$. Figure 3.7 shows the structured singular value for robust stability of the closed-loop system for several Smith-McMillan-based allocator designed with different bandwidths ω_0. As can be seen from the figure, the upper bound defined in Equation (3.25) correctly overestimates the structured singular value of the closed-loop with allocator. Moreover, the upper bound guarantees that robustness is not deteriorated after connecting the allocator for frequencies $\omega_0 \leq \frac{1}{\sqrt{\tau_1 \tau_2}} = 14.14\,\text{rad}\,\text{s}^{-1}$. With this example, robust stability is actually preserved for frequencies up to $30\,\text{rad}\,\text{s}^{-1}$, using a faster allocator deteriorates the robustness of the closed-loop.

3.3.5 Summary

The Smith-McMillan-based allocator allows the decoupling of the design of the controller and the control allocation by injecting a signal in the feedback loop that is invisible at the output, which lets us use the extra DoF provided by the plant over-actuation. Its design is independent of the controller design and only depends on the plant model. For the nominal system, the allocator guarantees to maintain internal stability. For an uncertain system with multiplicative uncertainties, the μ-values associated with the robust stability and performance of the closed-loop with allocator are bounded by the μ-values of the closed-loop without allocator if the filters weighting the uncertainties are invertible. However, the Smith-McMillan-based allocator does not always provide optimal results. For instance, if the gain of the allocator is high, the bound on the μ-values might be large; if the filter weighting the multiplicative uncertainty is not invertible, Equations (3.25) and (3.26) are not valid and another approach must be used. Appendix A proposes a more general method to consider these cases and synthesize an allocator for an ill-conditioned system. Contrary to the Smith-McMillan-based allocator, the approach proposed in appendix A does not allow to decouple the design of the controller and allocator. Moreover, the appendix A shows that the ill-conditioned system exhibit a trade-off between robust performance and control allocation.

The Smith-McMillan-based allocator is used in Chapter 6 when integrating wheel slip controls with regenerative braking and allocating wheel torque to the electric motors of the drivetrain and to the EHB.

Chapter 4

Vehicle State and Parameters Estimation

Information on the road surface limit can help improve the performance and safety of the vehicle. The maximum friction force the tire can apply is limited by the friction potential of the road surface and by the normal tire force. These signals cannot be directly measured with standard vehicle sensors; they must then be estimated.

In this chapter, we present methods to estimate the tire normal force using the Youla Controller Output Observer (YCOO) and the Unbiased Minimum Variance Filtering (UMVF). Both provide real-time estimates of the normal forces based on inertial sensors and suspension deflection sensors. The last part of this chapter conducts a literature review of tire-road friction estimation methods and proposes a simple algorithm to estimate the maximum friction coefficient.

4.1 Tire Normal Force Estimation

Some observers have already been developed to estimate wheel normal force. Doumiati et al. [64], [65] propose a cascaded observer to estimate the tire normal forces, the first step of the algorithm implements a linear Kalman filter to estimate the lateral load transfer from the suspension deflection and accelerometer measurements, the second step infers the tire normal force from the lateral load transfer by using an algebraic expression for normal force. Jiang [49] extended the application of this estimation framework by adding the vehicle pitch dynamics to take into account the road angle and the road irregularities. These estimation methods usually rely on algebraic expressions for normal forces and do not capture the suspension dynamic that generates the tire forces.

4.1.1 Estimation Model

The model presented in Section 2.1 is used to analyze the coupling between input and outputs pairs using the Relative Gain Array (RGA). Given a linear system $G(s)$, the RGA defines the matrix Λ whose elements are defined by $\Lambda_{ij} = (G(0))_{ij}(G^{-1}(0))_{ji}$, i.e. Λ is the result of the element wise product between the gain of the system $G(0)$ and the transpose of its inverse $(G^{-1}(0))^T$. The RGA measures the ratio of magnitude between input-output pairs to identify which input should be pair to some output and to identify the couplings in the system. Since the RGA is a linear analysis tool, its computation require to linearize the model, the operating point is chosen to be a steady-state cornering such that the vehicle velocity is $v_x = 90\,\mathrm{km\,h^{-1}}$ and the vehicle lateral acceleration is $a_y = 0.4\,\mathrm{g}$ (the vehicle lateral velocity is $v_y = 0.2\,\mathrm{m\,s^{-1}}$; the heave velocity is $v_z = 0\,\mathrm{m\,s^{-1}}$; and the roll, pitch, and roll angular velocities are $\omega_x = \omega_y = 0\,\mathrm{rad\,s^{-1}}$ and $\omega_z = 0.15\,\mathrm{rad\,s^{-1}}$). The following matrices shows the RGA of two models mapping the tire forces $[f_{FLz} \quad f_{FRz} \quad f_{RLz} \quad f_{RRz}]$ to the suspension deflection $[q_{FLs} \quad q_{FRs} \quad q_{RLs} \quad q_{RRs}]$, Λ_1 shows the RGA for a vehicle without anti-roll bar and Λ_2 shows the RGA for a vehicle whose rear axle is equipped with an anti-roll bar.

$$\Lambda_1 = \begin{bmatrix} \mathbf{0.956} & -0.052 & 0.047 & 0.049 \\ -0.052 & \mathbf{0.960} & 0.045 & 0.047 \\ 0.047 & 0.045 & \mathbf{0.949} & -0.042 \\ 0.049 & 0.047 & -0.042 & \mathbf{0.945} \end{bmatrix}, \; \Lambda_2 = \begin{bmatrix} \mathbf{0.956} & -0.052 & 0.047 & 0.049 \\ -0.052 & \mathbf{0.960} & 0.045 & 0.047 \\ 0.047 & 0.045 & \mathbf{1.211} & \mathbf{-0.305} \\ 0.048 & 0.046 & \mathbf{-0.304} & \mathbf{1.208} \end{bmatrix} \tag{4.1}$$

The matrix Λ_1 has all its diagonal elements near one and small off-diagonal elements. The RGA analysis shows that when there is no anti-roll bar, there is almost no coupling between the four suspensions, and the model can be simplified by considering only the input-output pair from f_{ijz} to q_{ijs}. However, if the rear axle is equipped with an anti-roll bar, the left and right sides are coupled together, and this effect should not be neglected. In the following, we assume that the vehicle is not equipped with anti-roll bars to simplify the design of the observer, allowing us to use a quarter car model to represent the system and neglecting the coupling between the four corners of the vehicle. To consider the coupling between the left and right sides and the presence of an anti-roll bar, the observers should be redesigned using a roll half-car model instead of the quarter car model.

The quarter-car model shown in Figure 4.1 is used to estimate the wheel load at each tire. The

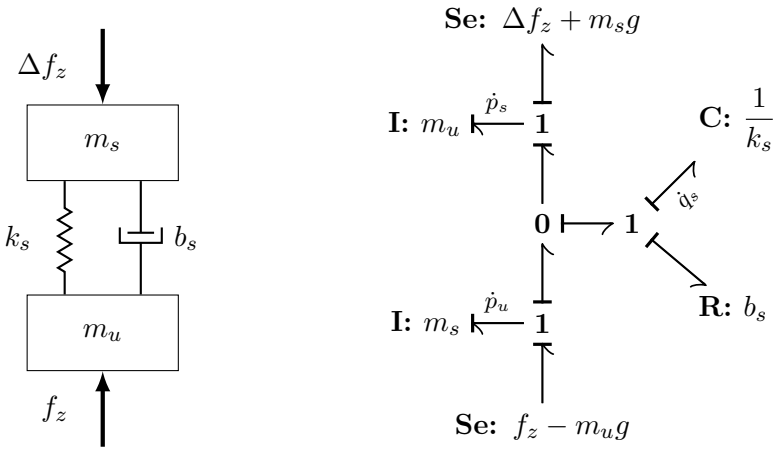

Figure 4.1: Quarter-car model of the suspension with wheel normal force and load transfer as inputs.

model has several inputs, a vertical force Δf_z applied to the sprung mass, representing the load transfer, and the normal tire force f_z. Inertias m_s and mu represent respectively the sprung mass and unsprung masses, k_s and b_s represent the suspension compliance and damping. The states of the model are the sprung mass and unsprung mass momentums p_s, and p_u, and the suspension deflection q_s. Measurement are the sprung mass heave acceleration $\frac{\dot{p}_s}{m_s}$ and the suspension deflection q_s. The equations of motion of the model are:

$$\dot{p}_s = k_s q_s + b_s \dot{q}_s - m_s g - \Delta f_z \tag{4.2}$$

$$\dot{p}_u = -k_s q_s - b_s \dot{q}_s - m_u g + f_z \tag{4.3}$$

$$\dot{q}_s = \frac{p_u}{m_u} - \frac{p_s}{m_s} \tag{4.4}$$

With this model, the tire normal force is an input to the model and not a function of a model state. In the traditional quarter-car model, an additional state representing the tire compliance q_t is present, its state derivative is given by $\dot{q}_s = v_{in} - \frac{p_u}{m_u}$ where v_{in} is the road input velocity. The traditional quarter-car model then computes the tire normal force as $f_z = k_t q_t$ with k_t the tire stiffness. Modifying the quarter-car model to consider f_z as an input requires to use observer capable of estimating unknown inputs instead of state estimation techniques (e.g., Kalman filtering), but using the traditional quarter-car model would necessitate knowing the road input velocity v_{in} and it would require to assume a parameter k_t to map the estimated tire compliance to the estimate of the normal force.

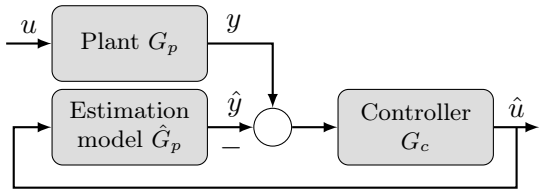

Figure 4.2: Block diagram of the YCOO estimation concept.

4.1.2 Youla Controller Output Observer

The YCOO is based on the COO framework and is developed using multi-variable Youla parameterization; it is a model-based estimation method that uses a controller to obtain the desired estimates by minimizing the error between the measurements and the virtual output of the estimation model. The YCOO block diagram is shown in Figure 4.2; this framework does not assume that all inputs of the estimation model are known, making it suitable for input estimation. Given some measurements y, the framework uses an estimation model mapping estimates $\hat{u}$ to estimated output $\hat{y}$, a controller that minimizes the error between these two measurements.

The transfer function from the the true input u to the estimated input $\hat{u}$ is given by $(I+L_u)^{-1}G_cG_p$ where $L_u = G_c\hat{G}_p$ is the return ratio. If the estimation model is a perfect representation of the system, i.e. $G_p = \hat{G}_p$, then this transfer function reduces to the closed-loop transfer function $T_u = L_u(I + L_u)^{-1}$. If the plant has multiplicative uncertainty such that $G_p = \hat{G}_p(I + \Delta)$, the relation becomes $\hat{u} = T_u(I + \Delta)u$. Thus, the YCOO relies on an accurate model of the system. The controller must be designed such that $T_u \approx I$ at low frequencies to guarantee good tracking of the measured quantities. Moreover, the Youla transfer function Y maps the sensor noise to the estimation error. Thanks to its loop shaping approach, the YCOO directly addresses the trade-off between noise rejection, bandwidth, and robustness to high-frequency multiplicative uncertainties. Indeed, a higher bandwidth would make the YCOO less robust to multiplicative uncertainties and make the estimation more sensitive to noise.

The quarter-car model from Figure 4.1 is used as the estimation model $\hat{G}_p$. The plant model can be written as a transfer function $\hat{G}_p = \frac{1}{\delta}P$ mapping the signals $\hat{u}$ to $\hat{y}$

$$\hat{G}_p = \begin{bmatrix} \frac{\dot{p}_s}{m_s f_z} & \frac{\dot{p}_s}{m_s \Delta f_z} \\ \frac{q_s}{f_z} & \frac{q_s}{\Delta f_z} \end{bmatrix} \tag{4.5}$$

$$= \frac{1}{m_s m_u s^2 + (m_s + m_u) b_s s + (m_s + m_u) k_s} \begin{bmatrix} k_s + b_s s & -(m_u s^2 + b_s s + k_s) \\ m_s & m_u \end{bmatrix} \tag{4.6}$$

The Smith-McMillan form M_P of the system and its unimodular matrices such that $M_P = U_L \hat{G}_p U_R$ are:

$$M_P = \begin{bmatrix} \frac{1}{m_s m_u s^2 + (m_s + m_u) b_s s + (m_s + m_u) k_s} & 0 \\ 0 & \frac{1}{m_s m_u} \end{bmatrix}, \tag{4.7}$$

$$U_L = \begin{bmatrix} 0 & 1 \\ m_u & m_u s^2 + b_s s + k_s \end{bmatrix}, \; U_R = \begin{bmatrix} 0 & \frac{1}{m_s m_u} \\ \frac{1}{m_u} & -\frac{1}{m_u^2} \end{bmatrix} \tag{4.8}$$

The controller is designed such that the closed-loop is a second-order Butterworth filter with unit gain $M_T = \frac{\omega_0^2}{s^2 + 2\zeta\omega_0 s + \omega_0^2} \frac{1}{(\tau s + 1)^2} I$, an additional pole must be added to the Butterworth filter to make the controller proper. The damping ratio ζ is set to $\frac{1}{\sqrt{2}}$. The closed-loop bandwidth must be high enough to provide good estimates, but a too high bandwidth will also lead to poor noise rejection. The natural frequencies of a quarter car model are the suspension frequency, approximately 1 Hz, and the wheel-hop frequency, approximately 10 Hz[66]. To provide a good estimate, the closed-loop bandwidth should be faster than the fastest dynamics of the system. Thus, the bandwidth of the closed-loop system is chosen 30 Hz. Singular values of the closed-loop transfer function and the controller are shown in Figure 4.3. At frequencies below the bandwidth, T_u is 0 dB and S_u has low gain, ensuring a good tracking. At higher frequencies, the gain of T_u decreases to reject sensor noise and make the estimate robust against high-frequencies model mismatch. The decoupled Youla transfer function is M_Y such that $M_T = M_Y M_P$, the closed-loop transfer function is $T_u = U_R M_T U_R^{-1}$ and the Youla transfer function is $Y = U_R M_Y U_L$. The controller is then obtained from $G_c = S_u^{-1} Y$ where $S_u = I - T_u$ is the input sensitivity function. This yields the following controller:

$$G_c = \frac{\omega_0^2}{(s^2 + 2\zeta\omega_0 s + \omega_0^2)(\tau s + 1)^2 - \omega_0^2} \begin{bmatrix} m_u & m_u s^2 + b_s s + k_s \\ -m_s & k_s + b_s s \end{bmatrix} \tag{4.9}$$

The transfer function which maps the measurements y to the input estimate $\hat{u}$ is the Youla transfer

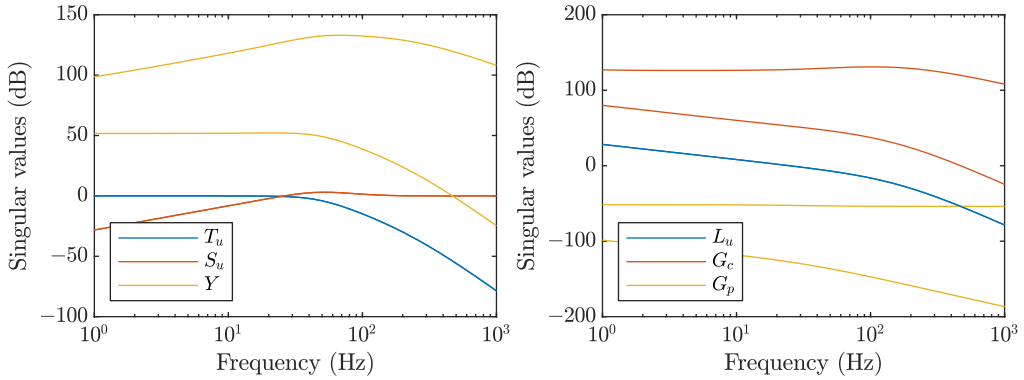

Figure 4.3: Singular values of the YCOO closed-loop transfer function T_u, S_u, and Y and of the return ratio L_u, controller G_c, and estimation plant G_p

function:

$$Y = \frac{\omega_0^2}{(\tau s+1)^2(s^2+2\zeta\omega_0 s+\omega_0^2)} \begin{bmatrix} m_u & m_u s^2 + b_s s + k_s \\ -m_s & b_s s + k_s \end{bmatrix} \tag{4.10}$$

Therefore, the estimate of the normal force is as follows,

$$\hat{f}_z(s) = \left[m_u s \times \left(\frac{p_s(s)}{m_s} + s q_s(s) \right) + b_s s q_s(s) + k_s q_s(s) \right] \frac{\omega_0^2}{(s^2+2\zeta\omega_0 s+\omega_0^2)(\tau s+1)^2} \tag{4.11}$$

4.1.3 Unbiased Minimum Variance Filtering

The UMVF is a variation of the Kalman filter for systems with unknown inputs. In addition to providing state estimates, it also computes an unbiased (i.e., with zero mean error) estimate of the unknown inputs [67]; the UMVF requires a stricter assumption than the Kalman filter; indeed, the model must be strongly observable. While observability guarantees that the sequence of states can be uniquely reconstructed from the measurements and knowledge of the inputs, a system is strongly observable if the sequence of both states and unknown inputs can be uniquely reconstructed from the measurements (and known inputs).

Considering a discrete-time Linear Time-Invariant (LTI) system defined by $x_{k+1} = Ax_k + Bu_k + He_k$ and $y_k = Cx_k + Du_k + Ge_k$ where x_k are the states, u_k are the known inputs, e_k are the unknown inputs, the LTI system is strongly observable if and only if the matrix Ψ has full column rank where G_d is the G matrix considering only feedthrough unknown inputs, i.e. with all zero-columns

removed [68].

$$\Psi = \begin{bmatrix} C & G & & & \\ CA & CH & \ddots & & \\ \vdots & \vdots & \ddots & G & \\ CA^{n-1} & CA^{n-2}H & \dots & CH & G_d \end{bmatrix} \tag{4.12}$$

The first column of the matrix Ψ corresponds to the observability matrix, thus observability and necessary for strong observability. The estimation model proposed in Equations (4.2) to (4.4) is not observable. Indeed, the state associated to $m_s p_s + m_u p_u$ does not produce an observable output. Similarity transformations are used to remove this unobservable state and obtain an observable model. Moreover, it is necessary to measure the suspension relative velocity $\dot{q}_s$ to make the system strongly observable. Suspension deflection sensors such as linear variable transformers can only measure the suspension suspension displacement [69], therefore measuring the signal $\dot{q}_s$ will require to differentiate the signal q_s. The strongly observable model is defined by the following matrices where the states are $x^T = [\frac{m_s p_u - m_u p_s}{m_s^2 + m_u^2} \quad q_s - \frac{m_s g}{k_s}]$, the unknown inputs are $e^T = [\Delta f_z \quad f_z - (m_s + m_u)g]$ and the outputs are $y^T = [\frac{\dot{p}_s}{m_s} \quad q_s \quad \dot{q}_s]$, note that the suspension deflection and the tire normal force are offset by their steady-state to zero input.

$$A = \begin{bmatrix} -\frac{b_s(m_s+m_u)}{m_s m_u} & -\frac{k_s(m_s+m_u)}{m_s^2+m_u^2} \\ \frac{m_s^2+m_u^2}{m_s m_u} & 0 \end{bmatrix}, \; H = \begin{bmatrix} \frac{m_u}{m_s^2+m_u^2} & \frac{m_s}{m_s^2+m_u^2} \\ 0 & 0 \end{bmatrix}, \tag{4.13}$$

$$C = \begin{bmatrix} \frac{(m_s^2+m_u^2)b_s}{m_s^2 m_u} & \frac{k_s}{m_s} \\ 0 & 1 \\ \frac{m_s^2+m_u^2}{m_s m_u} & 0 \end{bmatrix}, \; G = \begin{bmatrix} -\frac{1}{m_s} & 0 \\ 0 & 0 \\ 0 & 0 \end{bmatrix} \tag{4.14}$$

The UMVF filter assumes that the model can be described by the following discrete-time state-space system:

$$x_{k+1} = Ax_k + Bu_k + He_k + w_k \tag{4.15a}$$

$$y_k = Cx_k + Du_k + Ge_k + v_k \tag{4.15b}$$

where x_k are the states, u_k are the known inputs, e_k are the unknown inputs of the system, w_k is the process noise, and v_k are the sensor noise. The noises v_k and w_k are assumed to be Gaussian random variables with zero mean, independent over time and between them, and with covariance $E[w_k w_k^T] = Q_k$ and $E[v_k v_k^T] = R_k$.

Similarly to the Kalman filter, the UMVF algorithm works in two steps. The first step uses the plant model to propagate the estimation of the state and the error covariance matrix. The a priori estimates are:

$$\hat{x}_{k+1|k} = A\hat{x}_{k|k} + Bu_k \tag{4.16a}$$

$$P_{k+1|k} = AP_{k|k}A^T + Q_k \tag{4.16b}$$

The Kalman filter executes the measurement update defined by the following equations when a new sensor measurement is available. The gain L_{k+1} is computed to obtain the a posteriori state and covariance matrix.

$$\tilde{R}_{k+1} = CP_{k+1|k}C^T + R_{k+1} \tag{4.17a}$$

$$\Phi_{k+1} = \begin{bmatrix} -G & CH \end{bmatrix} \tag{4.17b}$$

$$\Omega_{k+1} = \begin{bmatrix} 0_{n\times p} & H \end{bmatrix} - P_{k+1|k}C^T\tilde{R}_{k+1}^{-1}\Phi_{k+1} \tag{4.17c}$$

$$L_{k+1} = P_{k+1|k}C^T\tilde{R}_{k+1}^{-1} - \Omega_{k+1}(\Phi_{k+1}^T\tilde{R}_{k+1}^{-1}\Phi_{k+1})^{-1}\Phi_{k+1}^T\tilde{R}_{k+1}^{-1} \tag{4.17d}$$

$$\hat{x}_{k+1|k+1} = \hat{x}_{k+1|k} + L_{k+1}(y_{k+1} - C\hat{x}_{k+1|k} - Du_{k+1}) \tag{4.17e}$$

$$P_{k+1|k+1} = L_{k+1}\tilde{R}_{k+1}L_{k+1}^T - P_{k+1|k}C^TL_{k+1}^T - L_{k+1}CP_{k+1|k}^T + P_{k+1|k} \tag{4.17f}$$

Palanthandalam-Madapusi [70] shows that $\hat{e}_k = H^\dagger L_{k+1}(y_{k+1} - C\hat{x}_{k+1|k} - Du_{k+1})$ and $\hat{e}_k = G^\dagger(y_k - C\hat{x}_{k|k} - Du_k)$ respectively guarantee that $E[\hat{e}_k] = G^\dagger GE[e_k]$ and $E[\hat{e}_k] = H^\dagger HE[e_k]$. Therefore, if H (resp. G) has full column rank the first equation (resp. the second equation) guarantees an unbiased estimate of the unknown input e_k, i.e. $E[\hat{e}_k - e_k] = 0$. The H and G matrices of the observable quarter-car model do not have full column rank, indeed rank $(H) =$ rank $(G) = 1$, however we can combine both equations to obtain an unbiased estimate of the unknown inputs. Let

V_H^T and V_G^T be the left eigenvectors of $H^\dagger H$ and $G^\dagger G$ associated to a non-zero eigenvalues,[1], then the unknown inputs is the solution of the linear system:

$$\begin{bmatrix} V_H^T \\ V_G^T \end{bmatrix} \hat{e}_k = \begin{bmatrix} V_H^T H^\dagger L_{k+1}(y_{k+1} - C\hat{x}_{k+1|k} - Du_{k+1}) \\ V_G^T G^\dagger (y_k - C\hat{x}_{k|k} - Du_k) \end{bmatrix} \tag{4.18}$$

From the previous equation, one can obtain an unbiased estimate of the unknown input e_k; indeed, taking the mean of the previous equation leads to:

$$\begin{bmatrix} V_H^T \\ V_G^T \end{bmatrix} E[\hat{e}_k] = \begin{bmatrix} V_H^T H^\dagger H \\ V_G^T G^\dagger G \end{bmatrix} E[e_k] = \begin{bmatrix} V_H^T \\ V_G^T \end{bmatrix} E[e_k] \tag{4.19}$$

Finally, the matrix $V^T = [V_H \quad V_G]^T$ has full column rank which guarantees that $E[\hat{e}_k] = E[e_k]$, $\hat{e}_k$ is an unbiased estimate of e_k. Multiplying Equation (4.18) on the left by $V^\dagger$ yields the value of the unbiased estimate $\hat{e}_k$.

4.1.4 Vehicle Mass Estimation

Both observers can estimate the transfer load Δf_z and the offset normal tire force $f_z - (m_s + m_u)g$ from the sprung mass acceleration and suspension displacement. However, the vehicle's mass must also be known to obtain the normal tire force f_z. This section proposes a calibration algorithm to obtain the static load at each wheel when the vehicle is at rest or during straight driving with constant speed.

Algebraic expression defined in Equations (2.85) to (2.87) gives the tire load during quasi-steady-state. When the vehicle is at rest or during straight driving at constant speed, the suspension force is given by $f_{ijz} = k_s q_{ijs}$, therefore $k_s q_{ijs} = f_{ijz}^0 \pm \Delta m_j^x a_x \pm \Delta m_i^y a_y$. Even though the vehicle is at rest, the acceleration a_x and a_y might not be zero since they correspond to the acceleration measured by the accelerometers in the vehicle x and y directions and include the acceleration of gravity if the vehicle roll and pitch are not zero. The variables f_{ijz}^0, Δm_j^x, and Δm_i^y depend on the value of distances w_L, w_R, l_F, l_R, the sprung mass m_s, and the height of the center of gravity h. Since the vehicle wheelbase $l_F + l_R$ and the vehicle width $w_L + w_R$ are known, this reduces to a system of four

[1] For any real matrix, the eigenvalues of $A^\dagger A$ and $AA^\dagger$ are either 0 or 1.

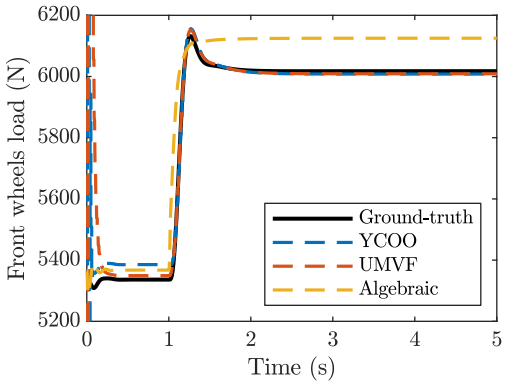

(a) Braking step of 3000 N m and wrong initial estimate.

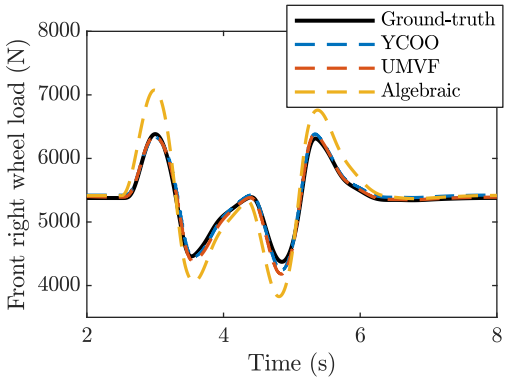

(b) Double lane change maneuver with 0.6 g maximum lateral acceleration.

Figure 4.4: Vertical tire force estimation on maneuvers with only longitudinal or lateral acceleration.

equations with four unknowns and can be solved to obtain the location of the center of gravity and the total sprung mass. Finally, the static load can be computed from Equation (2.86).

4.1.5 Simulation Results and Robustness Analysis

Both observers are tested on the full vehicle model derived in Chapter 2. Figure 4.4a shows the estimates during a braking step of 3000 N m at 1 s from an initial velocity of 90 km h^{-1}. The two observers are intentionally not initialized; both observers converge in approximately 0.1 s. The two observers provide better estimates than the algebraic expression, which suffers from a steady-state error. Figure 4.4b shows the estimate during a double lane change maneuver with a constant velocity of 90 km h^{-1} and with maximum lateral acceleration of 0.6 g. Both estimators provide a good estimate of the vertical tire force, whereas the estimation from algebraic expression does not capture the transient response. Figures 4.4a and 4.4b validate the two estimators for situations where the load transfer is due to longitudinal or lateral acceleration.

Figure 4.5 shows the estimate during a bounce sine sweep test. The vehicle velocity is maintained at 20 m s^{-1}. The road profile corresponds to sinusoidal bumps of decreasing wavelength with decreasing amplitude. The minimum wavelength is 1.6 m. Thus, the road excites the suspension over the frequency range 0 Hz to 3.5 Hz. The YCOO and the UMVF can estimate the wheel loads. Both observers reproduce the frequency response of the suspension: the wheel load amplitude increases when the road excitation gets closer to the suspension frequency (1 Hz obtained when $t \approx 13$ s) and remains constant at frequencies between the suspension and wheel-hop frequencies. Since the

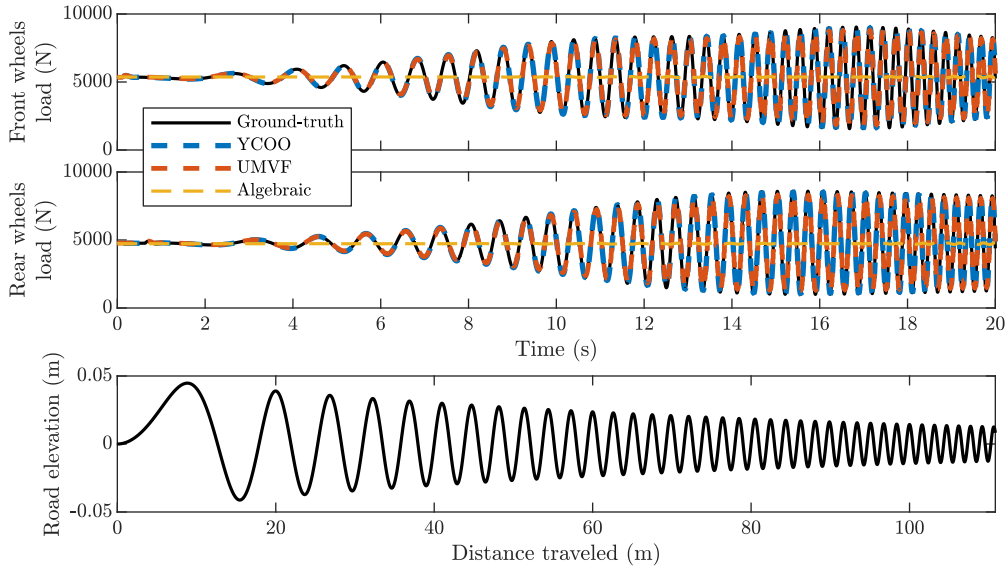

Figure 4.5: Vertical tire force estimation during a bounce sine sweep test. Vehicle speed is constant at 20 km h^{-1}. The minimum wavelength is 1.6 m at $t = 20$ s. The bottom figure shows the road profile.

longitudinal and lateral accelerations during this maneuver are almost zero, the algebraic expression cannot provide an accurate estimation of the wheel loads.

A robustness analysis investigates how robust the observers are to measurement noise and variation in the model parameters. Figure 4.6 evaluates the sensitivity of the wheel load estimation against the suspension stiffness. Uncertainties over this parameter result in an offset between the real and estimated wheel load due to the wrong calibration of the mass estimation strategy. The load transfer estimate also suffers from uncertainties in the suspension stiffness. Indeed, without any uncertainty, both observers yield a correct load transfer of 700 N, but with a SI50% stiffer suspension, the load transfer estimate is only 450 N. The robustness against the damping coefficient b_s is investigated in Figure 4.7a, the YCOO and the UMVF provide very close estimate, and only the estimate given by the UMVF is shown. The estimation is not robust against the damping coefficient in the transient, but it does not affect the steady-state estimation. Similarly, nonlinearities in the damper map affect the transient of the wheel load estimate when the suspension operates in the region approximated by the linear damper map. The linear and nonlinear damper maps are given in Figure 4.7b.

Figure 4.8 shows the estimated signals obtained with the YCOO and the UMVF when Gaussian white noise of time correlation 10 ms and power spectral density 10^{-4} and 10^{-9} are respectively added to the sprung mass vertical acceleration and to the suspension deflection measurements. The

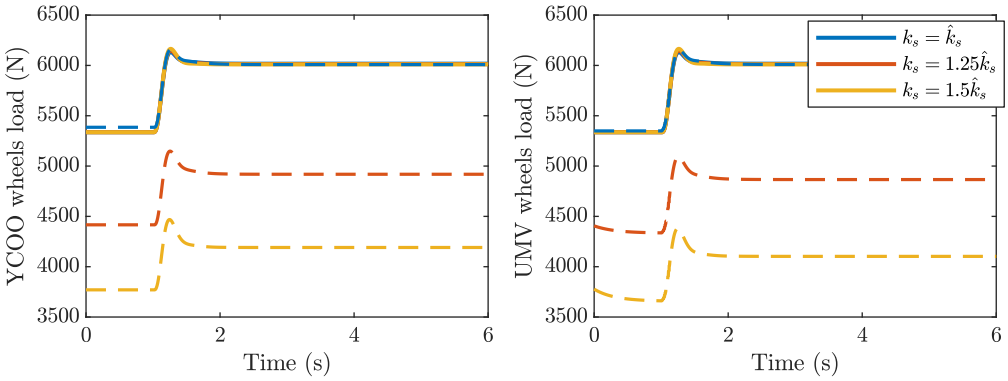

Figure 4.6: Robustness against suspension stiffness. Solid lines show the ground-truth signals and dashed lines show the estimated ones.

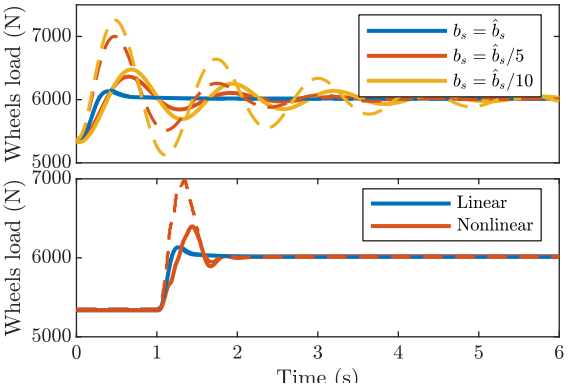

(a) Robustness against damping coefficient (**top**) and damping map (**bottom**).

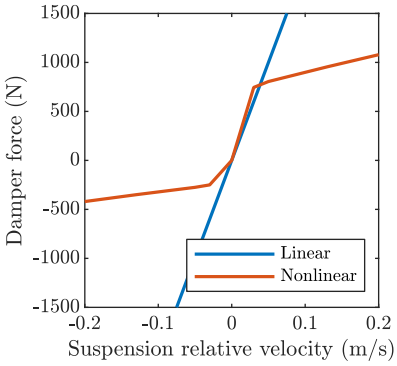

(b) Suspension linear and nonlinear damper map.

Figure 4.7: Robustness against uncertainties in the damping map during a braking maneuver. Solid lines show the ground-truth signals and dashed lines show the estimated ones.

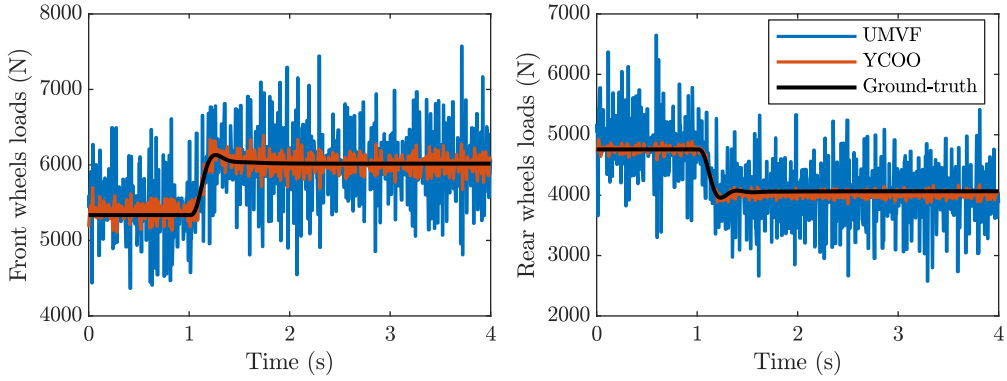

Figure 4.8: Normal force estimation with noisy measurements

YCOO offers better noise rejection than the UMVF.

4.2 Road Condition Identification

The tire forces are responsible for the stability and maneuverability of the vehicle [71]. Although describing the tire forces is complex, they are usually defined as a function of the wheel slip; these tire maps have a maximum that defines the tire friction potential. This value gives valuable information on the road condition in a compact way. The goal of active systems such as ABS and TCS is to maximize the tire forces by maintaining the wheel slip in a stable region. Knowledge of the road condition and the maximum friction coefficient can be used to improve the performance of these algorithms [72], [73]. Some systems rely strongly on a prediction of the road friction potential: e.g.Autonomous Emergency Braking (AEB) and Collision Avoidance System (CAS) monitor the distance between vehicles to ensure safe driving and use an estimate of the tire-road friction to compute a minimum distance between vehicles; Adaptive Cruise Control (ACC) can also benefit from information on the road condition to compute the vehicle maximum cornering velocity. Without a priori knowledge of the road grip, a conservative assumption must be taken, or it could lead to vehicle collision; this, however, could result in an unnecessary large safety margin or false intervention [74]. These new features will become even more critical with the predicted rise of fully autonomous vehicles. Indeed, to ensure safe driving, the vehicle should adapt its speed to the driving condition, and the friction potential would represent precious information.

Figure 4.9 illustrates a classification of different estimation concepts for the road grip potential. A distinction is made between approaches that rely on special sensors and model-based approaches that utilize a tire, vehicle, or powertrain model.

A possible classification of road friction estimation methods using special sensors is the cause-based versus effect-based methods. Cause-based approaches identify environmental causes that impact the maximum friction coefficient; this includes road lubricant properties and road textures. Conversely, effect-based approaches measure the effect of the tire-road friction, such as the noise emitted by the tire, the tire deformation, or the effect of the friction potential on the vehicle dynamics for the model-based approach.

The main drawback of effect-based methods is that they can only estimate the current grip

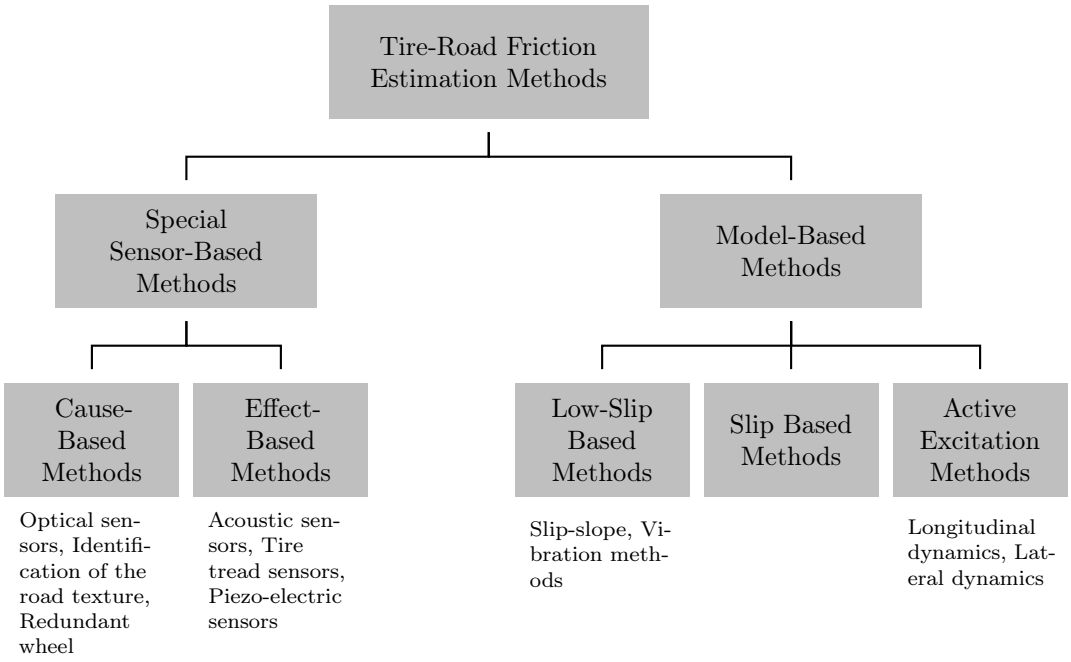

Figure 4.9: Classification of tire-road friction coefficient estimation methods

potential; on the contrary, a preview is possible with some cause-based methods, especially those using optical sensors. On the other hand, caused-based approaches strongly rely on databases of previous experiments. These methods do not estimate the friction coefficient directly but instead identify environmental or vehicle parameters known to be correlated with a given road surface. For instance, optical sensors can be used to identify the reflectivity of a road surface [75] to detect the presence of ice or water on the road and determine a maximum friction coefficient. It can still provide valuable information by narrowing the range of the maximum friction coefficient. However, this is only a rough estimation. Indeed, the friction coefficient is impacted by countless parameters, and two different tires can provide different grip potential on the same road surface [76]. This classification scheme is used extensively by sensor-based approaches but also by some model-based approaches such as the slip-slope method (see Section 4.2.2).

Some approaches do not require special sensors; instead, they implement a model-based estimation scheme that relies on standard vehicle sensors, three categories of model-based methods are listed. First, low-slip and slip-based methods estimate the impact of the road friction on the tire forces and moments. Low-slip-based methods aim to observe the road potential from the tire properties at low slip. These methods are based on the slip-slope assumption, which is described in Section 4.2.2.

Slip-based methods require higher slip values as the wheel has to operate in the nonlinear region of the tire. A certain degree of excitation is required for slip-based methods to work correctly. Finally, active excitation methods are a variation of the slip-based methods that can detect the maximum friction coefficient when the vehicle is driven at a constant speed.

4.2.1 Sensor-Based Approaches

The tire-road friction potential is dependent on many different factors. Vehicle speed, tire load, tire pressure, and environmental and road parameters (e.g., lubricant properties, temperature, the road micro, and macrotexture) influence the tire-road grip. Most of these parameters can be measured or estimated with sensors equipped on most commercial vehicles. However, road lubricant properties and road roughness have the most impact on the friction potential and are difficult or impossible to measure with standard sensors. The idea behind special sensor-based approaches is to use sensors not commonly found on commercial vehicles to measure signals correlated to the road's friction potential. These signals can result from the effect of the road-tire friction (effect-based) or relate to the friction generation mechanism (cause-based).

Optical sensors have been widely used to detect road surface properties correlated to the road friction potential. The main advantage of optical sensors is that they can provide predictive information on the friction potential by looking ahead of the contact patch. The use of optical sensors for friction detection started in the 1990s. The friction monitoring group of PROgraM for a European Traffic with Highest Efficiency and Unprecedented Safety (PROMETHEUS) uses the following three sensors [75]:

Water detection A 20 mW pulsating LED emits light on the road surface. A diode measures the reflected light to detect the presence of water on the road and to characterize the road by a wetness number. However, this sensor cannot estimate the water depth and thus the risk of aquaplaning. It is also not capable of detecting ice and snow.

Water depth measurement and ice detection This sensor addresses the limitation of the LED reflection sensor. A halogen lamp replaces the LED transmitter. The reflected light of different bands in the infrared 1 µm to 3 µm region depends on the water depth and the presence of ice.

Road texture detection A 30 mW laser diode is used to determine the road micro and macro texture

using optical triangulation, allowing to estimate the road roughness and identify the road surface.

The sensor signals are processed to obtain parameters such as a wetness number, water dept, and texture descriptors used to infer a friction potential. The prediction scheme was tested on a vehicle, and the error of maximum friction coefficient was found to be less than 0.1 for more than 90 % of the tested road surfaces.

Tuononen [77], [78] uses an optical sensor built inside the tire to measure the tire carcass deflection. While the main objective is to estimate the tire forces and moments, the combined measurement and estimation of the aligning torque and the slip angle allows one to estimate the friction potential during cornering. Indeed, the map from slip angle to self-aligning moment depends on the maximum friction coefficient (see Figure 2.3). Note that the self-aligning torque is more sensitive to the maximum friction coefficient at low slip angles than the longitudinal and lateral tire force, which should help provide a more reliable estimate of μ_{max}. The author also proposes to estimate the friction potential during free rolling from the estimated stress distribution along with the contact patch, which can be obtained from the tire carcass deflection.

Given the increasing interest in autonomous vehicles equipped with many optical sensors, researchers are taking the opportunity to use these new sensors and the enhanced processing power of embedded computers. Roychowdhury et al. [79] implement machine learning techniques for road surface condition identification and friction estimation from a front-headed camera. First, a convolutional neural network classifies the road surface into four categories (dry road, wet road, slush, and snow). Analyzing the hidden layers of the neural network shows that it uses information about the road texture, the sky, and the surroundings. Second, the road surface is divided into several patches (5 columns and three rows) to estimate the friction potential. Three levels of friction are possible: high, medium, and low. While other authors use different partitioning, Roychowdhury uses five columns for the two tracks of a vehicle and the three other lanes defined by the wheel tracks. A probability is associated with each patch, indicating the likelihood of being dry or snow, yielding a 5×3 matrix. A rule-based strategy identifies the friction state. If two columns are most likely dry surfaces in the proposed strategy, the friction potential is considered high. Otherwise, it may be medium or low. The authors report a road condition classification accuracy around 95 % and a road

friction estimation classification around 90 %.

4.2.2 Low-Slip Model-Based Approaches

Low-slip-based methods provide tire-road friction estimation based on the assumption that the longitudinal tire stiffness C_x depends on the friction potential; this property is called the *slip-slope* assumption. Experimental observations were first made by Dieckmann [80] and Ito [81]. They both reported that the tire stiffness, i.e., the slope of the tire force versus wheel slip curve in the low-slip region, is significantly lower for an icy road than for a dry or wet road. From these observations, researchers hypothesize that the road friction potential is a function of the tire stiffness properties so that μ_{max} could be observed by examining the tire stiffness properties.

According to tire modeling theory, the tire forces at low slip depends on the tire property only and is independent of the maximum friction coefficient. This is illustrated by the LuGre model (see Section 2.2.2 and Figure 2.3 which shows the steady-state tire forces and self-aligning moment with different friction potentials), indeed, assuming longitudinal slip only (i.e. $s_x v = r\omega - v = v_{rx}$ and $v_{ry} = 0$), a uniform normal force distribution, and neglecting the damping coefficient σ_{1x} and viscous friction σ_{2x} the longitudinal force of the lumped LuGre tire model is [82]

$$f_x(t) = \operatorname{sign}(v_{rx}) g(v_{rx}) \Big(1 - \frac{Z}{L}(1 - e^{-L/Z})\Big) \quad \text{where } Z = \Big|\frac{r_w \omega}{v_{rx}}\Big| \frac{g(v_{rx})}{\sigma_{0x}} \tag{4.20}$$

The tire longitudinal stiffness is given by

$$k = \frac{1}{f_z} \frac{\mathrm{d}f_x}{\mathrm{d}s_x}\bigg|_{s_x=0} \approx \frac{1}{2} \frac{L\sigma_{0x}}{f_z} \tag{4.21}$$

As can be seen from this equation, the longitudinal stiffness does not depend on the road friction properties but only on the contact patch length L, the tire normal force f_z, and the tire tread longitudinal stiffness σ_{0x}. Though this equation explains how aquaplaning and tire pressure can affect the longitudinal stiffness k. Indeed, an increase in tire pressure results in a decrease in the contact patch length L. Similarly, the tire is lifted during aquaplaning, and the length L decreases. Both situations are observed as a reduction of the longitudinal tire stiffness k.

Dieckmann [83] explains the slip-slope phenomenon by a specific longitudinal friction force

distribution at the contact patch during low-slip. The contact patch can be decomposed into two zones: a micro-sliding zone and a sticking zone [52]. Bristles in the sticking zone are not entirely stretched, and the end of the bristles is stuck to the ground. On the contrary, in the micro-sliding zone located at the trailing edge of the tire, the end of the bristles are sliding. Tire force measurements show that most of the friction forces are produced in the micro-sliding zone. If the road has a low friction potential, the peak of friction force at the trailing edge of the contact patch is saturated. Hence, a larger part of the contact patch must be used to provide the same amount of friction force which requires higher slip. Therefore, the slip-slope depends on the road friction potential. Dieckmann shows that this phenomenon occurs only for roads where $\mu_{max} \approx 0.3$, e.g., for icy and snowy roads.

Nevertheless, the slip-slope property has been challenged by newer experimental results performed by Andrieux et al. [52]. After conducting various braking tests on different road surfaces whose μ_{max} values ranged from 0.4 to 1.2, Andrieux denies the existence of a relationship between the friction potential and the slip-slope. Finally, authors like Dieckmann, Gustaffson, and Muller, who observe a slip-slope phenomenon, acknowledge that the longitudinal stiffness k is sensitive to other parameters such as tire pressure and tire wear.

Road-Condition Estimator Based on the Slip-Slope Property

Gustafsson [51], [84] proposed a road condition estimator based on the experimental evidence provided by Dieckmann. The estimator uses an EKF to estimate the longitudinal tire stiffness. He proposed a linear regression model where the slip-slope $k = \frac{C_x}{fz}$ and a bias δ are the unknown parameter to estimate. The regression model is

$$\lambda = \frac{1}{k}\mu + \delta + e \tag{4.22}$$

where μ is the under-the-tire friction coefficient $\mu = \frac{f_x}{f_z}$ and e is the measurement noise. The slip is computed by comparing the velocity of the driven and undriven wheels, while the longitudinal tire forces are estimated from measurements of the engine torque. The main reason invoked to use an EKF over other estimation methods like Recursive Least Square (RLS) is to track parameters with different speeds (e.g., fast-tracking for $\frac{1}{k}$ and slow for δ). Gustafsson performed tests on asphalt,

wet asphalt, gravel, snow, and ice road surfaces with different tires and driving styles. It was possible to distinguish asphalt roads from snowy or icy roads from the estimated slip-slope k. Gustaffson suggests a threshold $k_0 = 30$ to classify between asphalt and snow or ice in his article. The author remarks that this threshold should depend on the tire type (summer or winter tire), the tire pressure and wear, and other parameters. Hence, they provide a simple self-calibrating algorithm for the threshold. However, the slip-slope method is unable to distinguish between asphalt and gravel roads. Another parameter was introduced to fix this issue

$$\gamma = \mathrm{Var}[\omega_{driven} - \omega_{undriven}] \tag{4.23}$$

Gustafsson reported that the road condition could be identified using this new parameter. The maximum friction coefficient is then obtained from a database that relates the slip-slope to the friction coefficient from previous tests.

The estimator presented by Gustafsson suffers from some limitations. First, the estimator relies on an accurate wheel slip measurement, hence, an accurate vehicle speed measurement. Gustafsson used the rotational speed on undriven wheels to estimate the vehicle speed. Nevertheless, this cannot be implemented during braking or when all vehicle wheels are driven for Four-Wheel Drive vehicles. Second, the estimator is designed to work only at low-slip and does not produce accurate results during high-friction demands (e.g., ABS or TCS events). Third, cold tires lead to an overestimate of the slip-slope, and Gustafsson suggests that a 10 km drive is sufficient to obtain stationary and accurate road friction estimates. Finally, abnormal tire pressure corrupts the estimation results, but it can be detected by inspecting the estimated offset δ.

Müller [85] and Uchanski [86] extend the operating range of the estimator to moderate braking intervals by disconnecting the brakes of the rear axle, which allows for estimating the vehicle speed. In [85], the braking torque is estimated from the measured brake cylinder pressure. The same estimator proposed by Gustaffson is then applied to infer a maximum friction coefficient. Miller [87] suggests using Global Positioning System (GPS) signals to estimate the vehicle speed and improve the estimation of the wheel slip even during braking.

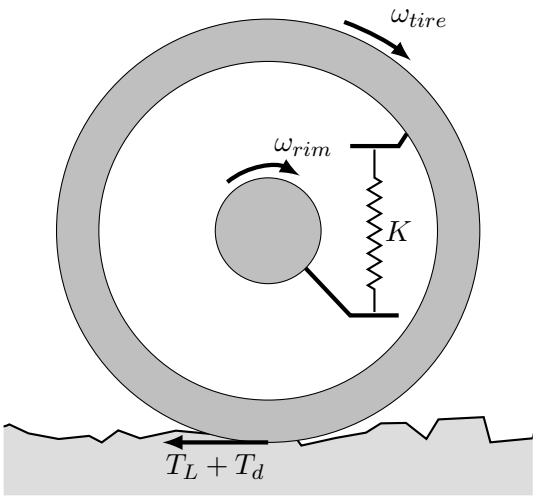

Figure 4.10: Tire vibration model

Road-Condition Estimator Based on the Vibration Methods

The vibration model-based methods are also based on the slip-slope assumption. However, instead of directly utilizing the slip-slope property, they focus on the frequency response of some vehicle subsystems (e.g., the spectrum of the wheel speed signal or the driveline frequency response).

Figure 4.10 shows the tire vibration models. It includes the tire sidewall compliance K whose deflection angle is θ_s. The system is excited by the longitudinal tire friction torque τ and a torque disturbance τ_d which arises from the unevenness of the road and which can be considered as a white noise. The tire sidewall compliance creates a resonance frequency at approximately 40 Hz. The tire pressure has an impact on the tire sidewall compliance, hence is also has an impact on the resonance frequency. Moreover, experiments have shown that the wheel speed signal frequency response is also affected by the road condition [88]. Equation of the tire vibration model are given by

$$J_{rim}\dot{\omega}_{rim} = -K\theta_s \tag{4.24}$$

$$J_{tire}\dot{\omega} = K\theta_s + \tau + \tau_d \tag{4.25}$$

$$\dot{\theta}_s = \omega_{rim} - \omega \tag{4.26}$$

The friction torque $\tau = r_w f_x$ is a non linear function of the wheel longitudinal slip. At low slip, its derivative is the slip slope, hence $\Delta\tau = \frac{\mathrm{d}\tau}{\mathrm{d}s_x} \times \Delta s_x = k r_w f_z \times \Delta s_x$. Assuming a constant vehicle speed v_x, the relation becomes $\Delta\tau = \frac{k r_w^2 f_z}{v_x}\Delta\omega$. Substituting τ in (4.25) and computing the transfer

function from the torque disturbance to the measured wheel speed yields

$$G(s) = \frac{\omega(s)}{\tau_d(s)} = \frac{K}{J_{rim}J_{tire}s^3 + J_{rim}\alpha r_w^2 s^2 + K(J_{rim} + J_{tire}) + K\alpha r_w^2} \quad \text{where } \alpha = \frac{kf_z}{v_x} = \frac{\mathrm{d}f_x}{\mathrm{d}v_{rx}}\Big|_{v_{rx}=0} \tag{4.27}$$

In the previous transfer function, the ter associated to the third degree in the polynomial can be neglected. After this simplification, the transfer function becomes a second order transfer function whose resonant frequency and damping ratio are

$$f_r = \frac{1}{2\pi}\sqrt{\frac{K}{J_{rim}}}, \quad \zeta = \pi f_r \frac{J_{rim} + J_{tire}}{\alpha r_w^2} \tag{4.28}$$

According to these equations, the slip-slope does not affect the resonant frequency of the wheel, which is mainly dictated by the tire sidewall compliance K. However, it affects the damping ratio, a smaller slip-slope results in more damped frequency response around the resonant frequency. Umeno [88] uses a band-pass filter to extract the torsional resonance frequency of the tire and use identification methods to obtain the damping ratio. First, a RLS approach is implemented, but due to the band-pass filter, the white noise assumption is no longer valid, and the RLS estimator fails to identify the parameters. Second, the instrumental variable method is used in place of the RLS. The second approach is finally tested on an actual vehicle; a clear distinction can be made between dry asphalt and icy road. Moreover, the observer can detect aquaplaning.

The main advantage of the vibrations methods is that they do not require the computation of the wheel slip, and thus there is no need to estimate the vehicle velocity. Only the wheel speed measurement is necessary. However, Ono et al. [89] notice that the 40 Hz resonance frequency disappears during braking because of the friction generated at the brake pad.

Low-slip-based methods aim to infer the friction potential of a road surface in the low-slip region; this would be extremely useful as the tire usually operates in this region. However, a controversy surrounding the impact of the friction potential in the low-slip region exists. Some experiments show that the road surface can be identified based on the slip-slope assumption. However, theoretical tire models and newer measurements by Andrieux fail to show a relationship between the grip potential and the slip-slope. Moreover, most of the low-slip-based methods require precise estimation of

the wheel slip, thus requiring the vehicle speed. Vibration methods alleviate this requirement by using the frequency response of the wheel speed signal at the expense of additional complexity in the hardware (sensor) and software (preprocessing). Finally, the low-slip estimation schemes do not estimate the friction potential directly; instead, they identify the slip-slope and correlate this parameter to a known road surface. However, the actual friction potential depends on the current tire-road surface combination. Therefore, it does not provide an estimate of the friction potential but only a (possibly large) range for μ_{max}.

4.2.3 Slip Model-Based Methods

Ray [53] proposed a Bayesian selection procedure to infer the most likely estimate of the maximum friction coefficient. An Extended Kalman-Bucy Filter (EKBF) estimates the vehicle state and tire forces. Given the estimate of the wheel slip and tire forces and a predefined tire model, the coefficient μ_{max} is inferred iteratively from the Bayesian rule. The estimation is validated experimentally with braking, cornering, and combined maneuvers. The estimation was adequate for braking and combined maneuvers with acceleration greater than 0.3 g. However, it was difficult to determine a reasonable estimate from maneuvers with steering only because of the proximity of lateral force versus slip angle for different μ_{max} at low slip.

Newer methods have been tested to estimate the road grip potential. Zanon [90] utilized Moving Horizon Estimation (MHE) to predict μ_{max}. MHE is an optimization-based approach that uses a series of measurements over a moving time window instead of measurements at a single timestep to determine the estimate. It can handle nonlinear systems and does not rely on a predefined error distribution contrary to the EKF. The vehicle is modeled as a double-track planar vehicle with a Pacejka tire model. The MHE defined the estimated by minimizing a cost function combining measurement errors and control inputs. The estimation scheme was tested in simulation. The observer can detect μ_{max} jump from wheel speed, vehicle acceleration, speed, and position measurements. The estimate is good during cornering but less accurate when the vehicle is driven in a straight line.

Excitation Problem for Slip Based Methods

A significant drawback of a slip-based approach is the need for high excitation to estimate the road maximum friction coefficient adequately. The level of excitation required varies widely, from 30 %

of grip utilization for model-based methods based on the tire self-aligning moment, up to 90 % for low-mu surfaces [32].

Wielitzka [91] et al. use an Unscented Kalman Filter (UKF) whose model is a two-track nonlinear vehicle model with both longitudinal and lateral dynamics. The model assumes a simplified magic formula as the tire model. Lateral forces are not static but assume a first-order dynamic; the dynamic behavior of longitudinal forces is neglected. Available measurements are the vehicle yaw rate, the longitudinal and lateral acceleration, and the four-wheel angular velocities. The vehicle is assumed to be front-driven; hence the rear wheel velocities can be used to measure the vehicle velocity. To avoid the drift of the estimated friction coefficient when the excitation is low, the authors stop estimating the coefficient when the sensitivity measure is below an empirically defined threshold. Moreover, the UKF does not directly estimate the friction coefficient $\hat{\mu}_{max}$ but a substitute parameter $\hat{\mu}_{sub}$. This is useful to maintain the estimated coefficient within predefined bounds μ_{lb} and μ_{ub} at the expense of additional nonlinearities. The relation between the substitute parameter and the estimated coefficient is

$$\hat{\mu}_{max} = \frac{\mu_{lb} + \mu_{ub}}{2} + \frac{\mu_{ub} - \mu_{lb}}{2} \tanh \hat{\mu}_{sub} \tag{4.29}$$

4.2.4 Active Force Excitation Methods

Active force excitation methods aim to address the excitation problem when estimating the friction coefficient during low-slip, especially when the vehicle is driven at a constant velocity, by applying a torque of opposite sign on the front and rear axles [92]. The front-to-rear torque difference generates high excitation allowing to estimate the friction potential while maintaining the vehicle speed constant: a ramp torque input is applied on the front axle while a controller adjusts the rear axle torque to maintain the vehicle speed. An obvious drawback of active force excitation methods is the power loss resulting from applying an opposite torque on the front and rear axle. Moreover, it assumes that a front-to-rear torque difference can be applied to the vehicle, requiring either independent braking for a front-wheel-drive vehicle or a dual-motor drivetrain topology. To estimate the friction coefficient, a decision must also be made on when to execute the active force excitation method. Finally, the effect of applying a torque difference between the front and rear axles on the vehicle handling should be considered (see Section 2.4.2).

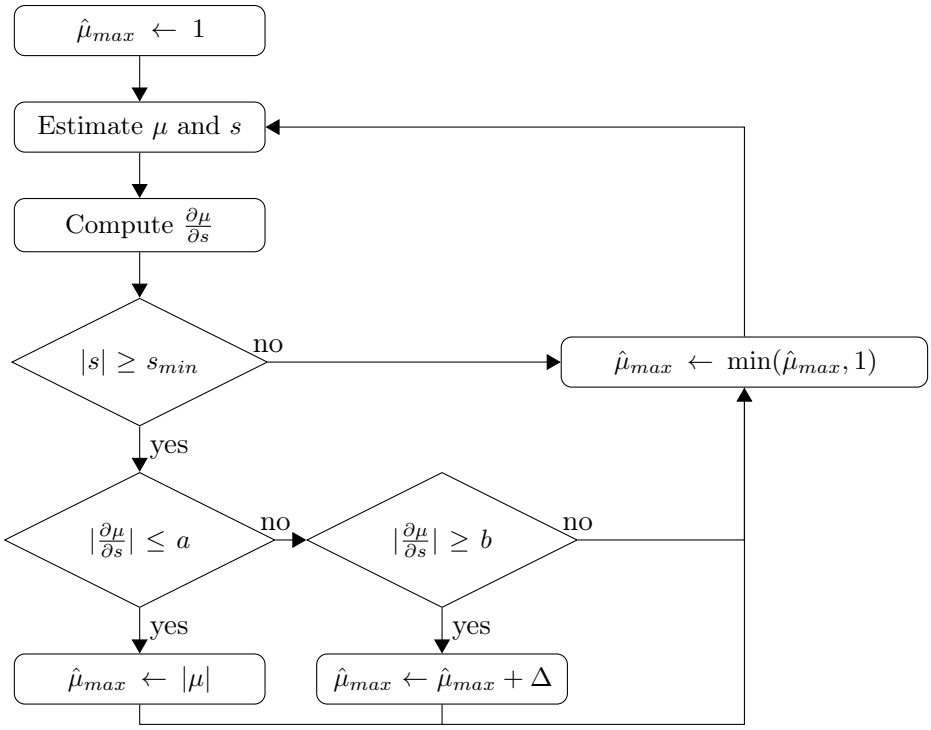

Figure 4.11: Friction potential algorithm estimation flowchart

4.2.5 Proposed Maximum Friction Coefficient Estimation Scheme

This dissertation uses a simple model-based approach to estimate the maximum friction coefficient when the wheel slip is high. The approach is described in Figure 4.11 and is based on the slope of the friction s–μ curve; the friction coefficient is obtained when the slope $\partial\mu/\partial s$ is smaller than a predefined threshold. An estimate of the slope $\partial\mu/\partial s$ is constructed by storing the last estimated values of the friction coefficient $\mu = \sqrt{f_x^2 + f_y^2}/f_z$ and the combined slip ratio s. An online linear regression with two parameters is used to compute the y-intercept and the slope of the line that best fits the data of the s–μ curve. It is then assumed that the value of this slope corresponds to the partial derivative $\frac{\partial \mu}{\partial s}$. Other methods can be used to obtain this partial derivative, notably the RLS algorithm.

If the absolute value of the current slip ratio is smaller than a predefined value s_{min}, the algorithm does not update the value of the maximum friction coefficient. If the longitudinal slip is large enough, the update rule of the maximum friction coefficient μ_{max} is:

- $\mu_{max} \leftarrow |\mu|$ if $\frac{\partial \mu}{\partial s} \leq a$ with a a small positive number, i.e. the new estimate of μ_{max} is the current estimate of μ. In this situation the wheel is assumed to be saturated or close to

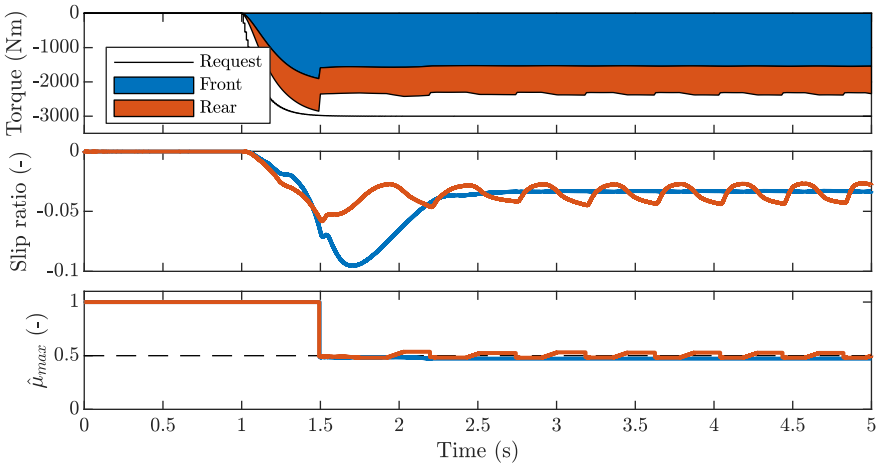

Figure 4.12: Simulation results for the friction potential estimation on a $\mu_{max} = 0.5$ surface during a 3500 N m step braking torque

saturation.

- $\mu_{max} \leftarrow \mu_{max} + \Delta$ if the value of the slope is higher than a threshold value b with $0 < a < b$, the estimate of μ_{max} is increased at a constant rate Δ. The wheel is assumed to be in the linear region in this situation. Since the wheel is not saturated, μ_{max} cannot be estimated; instead, it is increased until it reaches the maximum value possible (typically 1.0 or 1.2).

- $\mu_{max} \leftarrow \mu_{max}$ if the slope is between a and b.

The concept relies on the availability of different signals from the vehicle. First, an estimation of the slip ratio must be available; this is usually computed from the wheel speed sensors and the vehicle longitudinal speed estimation. Second, an estimation of the friction coefficient μ is needed; this can be computed from the estimation of the longitudinal and normal tire forces.

Simulation results

A simulation is used to demonstrate the effectiveness of the observer. The vehicle is driven on a straight line on a surface whose friction coefficient is $\mu_{max} = 0.5$; the driver requests a step braking torque of 3500 N m which exceeds the maximum torque the tire-road can provide (approximately 2000 N m), wheel torque controllers regulate the wheel torque applied at the wheel based on the estimate $\hat{\mu}_{max}$. Figure 4.12 shows the simulation results; the estimation scheme provides a reasonable estimate of

the maximum road-tire friction coefficient when the tire is close to saturation.

Chapter 5

Optimal Wheel Control Allocation

This chapter uses several control methodologies to implement the 'Optimal Wheel Controls Allocation' block of Figure 3.2 mapping the driver's requests to optimal wheel torque and steering angle: a multivariable control strategy defining generalized forces to apply on the chassis which are then distributed to the different wheels by a control allocation; model predictive controllers which directly allocate the wheel controls from the driver's request. Thus, this layer takes care of the front-to-rear and left-to-right torque split and the contribution of active steering. Constraints are also enforced to respect the surface friction limit and the actuator saturation and bandwidth.

All control methodologies used in this chapter are model-based strategies based on the vehicle planar model described by Equations (2.81) to (2.87). Inputs of this model are the wheel torque and steering angle which is compatible with the interface of the controller according to the control architecture defined in Figure 3.2. This planar vehicle model has seven states: the longitudinal and lateral velocities, yaw rate, and wheel speed; it would be beneficial in terms of computation and implementation to reduce the order of the model. The model is simplified to neglect the wheel inertia defined in Equation (2.84), thus removing the four states associated with the wheel spin in the vehicle model. Siampis [93] already used this assumption to simplify the design of a controller for TV on the rear axle near the handling limit. Note that since the wheel speeds are not states of the simplified model, it is impossible to define the wheel longitudinal slip ratio.

Neglecting the wheel inertia allows to directly map the wheel torque to the longitudinal tire force by $r_w f_{ijx} = \tau_{ij}$. Given the vehicle states (v_x, v_y, ω_z) and the wheel steering angle δ_{ij}, the wheel slip angle s_{ijy} can be computed from Equation (2.34). Using Pacejka's tire model presented in

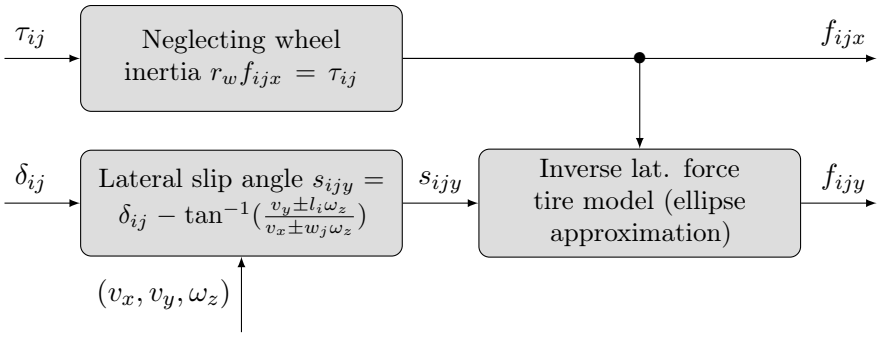

Figure 5.1: Computation of tire forces from wheel controls using the simplified tire model

Section 2.2.1, the computation of the lateral tire force requires the longitudinal slip ratio; however, as stated earlier, this is not possible. Thus, the tire model must be simplified in a way that preserves the coupling phenomenon between longitudinal and lateral tire forces but without relying on the longitudinal wheel slip; to accomplish that, the lateral tire force is computed by approximating the constant sip curves by ellipses, see Figure 5.1. The next section describes the approximation of the constant slip angle curves by ellipses, and it explains how to map the wheel controls, i.e., the wheel torque τ_{ij} and wheel steering angle δ_{ij}, to the generalized forces.

5.1 Tire Map from Wheel Controls to Tire Forces

Figure 5.2 shows the friction circle with friction curves for constant slip ratio and slip angle. The figure shows that ellipses can approximate the constant slip angle curve. The next section shows that the lateral friction coefficient can be computed using the ellipse from the current slip angle s_y and a desired longitudinal friction coefficient μ_x. The ellipse is defined as follows:

$$\frac{(\mu_x - \bar{\mu}_x)^2}{\Delta\mu_x^2} + \frac{(\mu_y - \bar{\mu}_y)^2}{\Delta\mu_y^2} = 1 \tag{5.1}$$

where $(\bar{\mu}_x, \bar{\mu}_y)$ define the ellipse center, and $\Delta\mu_x$ and $\Delta\mu_y$ are the ellipse semi axes.

5.1.1 Computation of the Ellipse Coefficients

The ellipse coefficients are computed by selecting four points on the constant slip angle curves so that the major and minor axes are aligned with the μ_x and μ_y axes. The first selected point is the origin $(\mu_x, \mu_y) = (0, 0)$ as it always belongs to the slip angle curves; indeed, with the simplified

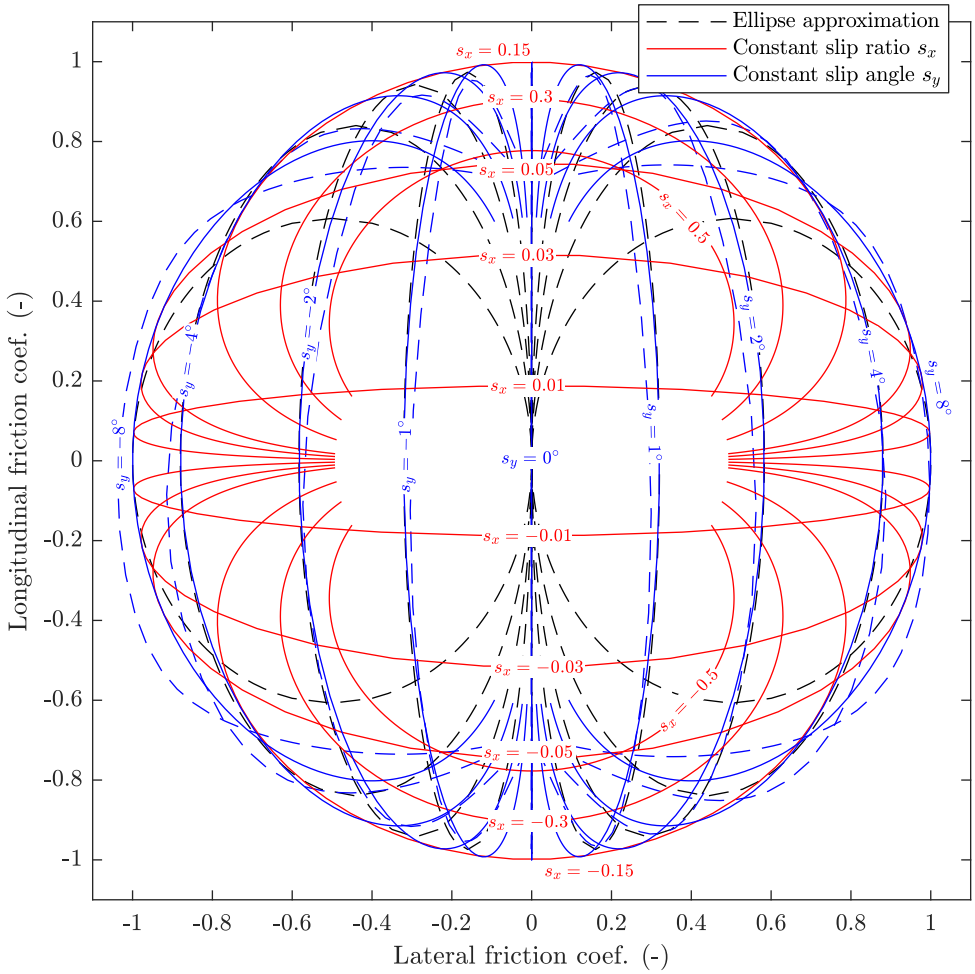

Figure 5.2: Constant slip angle curve with the tire ellipse simplification. Blue dashed curves are obtained with the MF94 Pacejka tire model used in the vehicle simulation model; solid blue curves show the constant slip curves for the simplified Pacejka model presented in Section 2.2.1 used in the model-based controls.

Pacejka tire model, the tire does not generate force when there is no slip. The second point is selected to correspond to maximum lateral force given a constant slip angle s_y, lateral force generation is maximized in pure cornering, i.e. when $s_x = 0$ and $s = s_y$, hence the second point $(\mu_x, \mu_y) = (0, \mu(s_y))$. The third and fourth points could be chosen to be the two points maximizing $|\mu_x|$ under a given slip angle s_y, unfortunately, this would require to solve the nonlinear equation $s\bar{\mu}_y = s_y\mu(s) = s_y \,\mathrm{MF}\,(s)$ for the unknown s, where MF denotes the Pacejka's magic formula. Since the approximation of the tire model by ellipse coefficients is aimed to be used online inside an optimization routine to generate optimal control allocation, it would be preferable to choose two points whose coordinates can be obtained from a simple analytical expression. Instead, the two last points are chosen such that the slip ratio is $s_x = \pm s_{max}$ where $s_{max} \approx \frac{1}{B}\tan\left(\frac{\pi}{2C}\right)$ is the slip providing the maximum friction according to the s–μ curve. Therefore, the third and fourth points are defined by the coordinates $(\pm\mu_x^*, \mu_y^*)$ where:

$$\mu_x^* = \frac{s_{max}}{\sqrt{s_{max}^2 + s_y^2}}\,\mathrm{MF}(\sqrt{s_{max}^2 + s_y^2}), \quad \mu_y^* = \frac{s_y}{\sqrt{s_{max}^2 + s_y^2}}\,\mathrm{MF}(\sqrt{s_{max}^2 + s_y^2}) \tag{5.2}$$

The two first point allows to compute the lateral friction offset $\bar{\mu}_y = \frac{\mathrm{MF}(s_y)}{2}$ and semi-axis of the lateral friction coefficient $\Delta\mu_y = \bar{\mu}_y$. The two last points set the value of the coefficients $\bar{\mu}_x$ and $\Delta\mu_x$. Assuming that the points $(\pm\mu_x^*, \mu_y^*)$ are on the major axis, we have $\bar{\mu}_x = 0$ and $\Delta\mu_x = \mu_x^*$. Hence the ellipse friction coefficients:

$$\bar{\mu}_y = \Delta\mu_y = \frac{\mathrm{MF}(s_y)}{2}, \bar{\mu}_x = 0, \Delta\mu_x = \frac{s_{max}}{\sqrt{s_{max}^2 + s_y^2}}\,\mathrm{MF}(\sqrt{s_{max}^2 + s_y^2}) \tag{5.3}$$

The friction circle can be scaled down by an estimate of the maximum friction coefficient to account for different road conditions; this can be achieved by multiplying the ellipse coefficients $\bar{\mu}_x$, $\bar{\mu}_y$, $\Delta\mu_x$, and $\Delta\mu_y$ by the maximum friction coefficients μ_{max} or by modifying the friction model $\mathrm{MF}(s)$ depending on the road condition.

Figure 5.2 shows the ellipse and constant slip angle curves for the Pacejka tire model used to represent the vehicle in simulation and the simplified Pacejka tire model described in Section 2.2.1 and used by the model-based controls. All curves are close to each other for a given slip angle; the ellipse adequately represents the coupling between longitudinal and lateral tire force. For low slip

angles, the ellipse gives a good approximation even in the nonlinear when the tire is saturating; for high slip angles, the ellipse gives a good approximation only when the longitudinal slip is small (i.e., on the side of the ellipse with larger μ_y in absolute value).

5.1.2 Mapping Wheel Controls to Generalized Forces

Given a torque τ_{ij} and a steering angle δ_{ijy}, the constant slip angle ellipses define the longitudinal and lateral tire forces while considering the coupling phenomena between them: neglecting the wheel inertia, the torque set the longitudinal tire force $f_{ijx} = \frac{\tau_{ij}}{r_w}$ and the longitudinal friction coefficient $\mu_x = \frac{f_x}{f_z}$; the steering angle sets the slip angle s_{ijy} using Equation (2.34). The coefficient of the ellipse for a given slip angle s_{ijy} is obtained from s_{ijy} itself and the parameters of the simplified Pacejka tire model using Equation (5.3). The lateral friction coefficient μ_{ijy} can be obtained from the ellipse given the current slip angle s_{ijy} and a desired longitudinal friction coefficient μ_{ijx} with Equation (5.4), and the lateral tire force can be obtained from Equation (5.5).

$$\mu_{ijy} = \frac{\Delta\mu_{ijy}}{\Delta\mu_{ijx}} \sqrt{\Delta\mu_{ijx}^2 - (\mu_{ijx} - \bar{\mu}_{ijx})^2} + \bar{\mu}_{ijy} \tag{5.4}$$

$$f_{ijy} = \mu_{ijy} f_{ijz} \tag{5.5}$$

Note that in the previous formula, μ_{ijx} must be constrained by $\bar{\mu}_{ijx} - \Delta\mu_{ijx} \leq \mu_{ijx} \leq \bar{\mu}_{ijx} + \Delta\mu_{ijx}$, doing so guarantees that the tire force is inside the friction circle. Moreover, Equation (5.4) only describes one-half of the ellipse, which corresponds to small slip ratios in amplitude as $\Delta\mu_{ijy}$ and $\bar{\mu}_{ijy}$ have the same sign.

Once the wheel controls τ_{ij} and δ_{ij} have been mapped to the longitudinal and lateral friction coefficients μ_{ijx} and μ_{ijy}, the longitudinal and lateral tire forces of the wheel ij in the chassis frame f_{ijxc} and f_{ijyc} can be obtained by multiplying the friction coefficient by the wheel load and using rotation transformation; the total longitudinal and lateral forces and the yaw moment applied on the chassis can be computed from f_{ijxc} and f_{ijyc} as follows,

$$f_{ijxc} = \mu_{ijx} f_{ijz} \cos\delta_{ij} - \mu_{ijy} f_{ijz} \sin\delta_{ij}, \quad f_{ijyc} = \mu_{ijx} f_{ijz} \sin\delta_{ij} + \mu_{ijy} f_{ijz} \cos\delta_{ij} \tag{5.6}$$

$$f_x = \sum_{ij} f_{ijxc}, \quad f_y = \sum_{ij} f_{ijyc}, \tag{5.7}$$

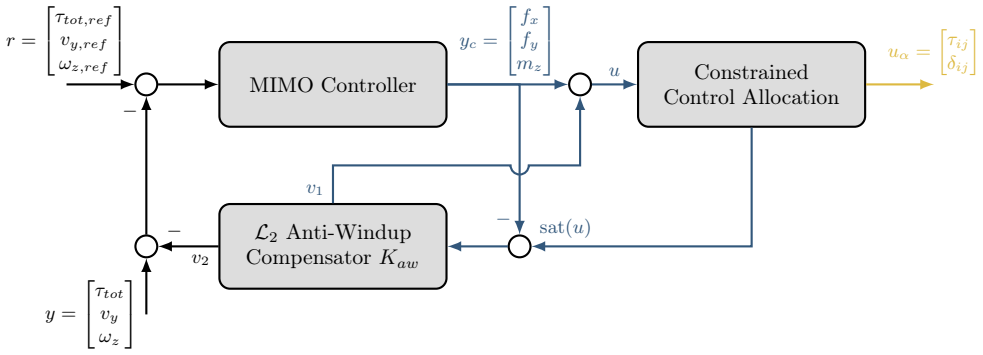

Figure 5.3: Youla Vehicle Motion Controller concept. Black signals (—) refer to regulated variables; blue signals (—) refer to generalized controls; and orange signals (—) refer to allocated controls.

$$m_z = l_F \sum_j f_{Fjyc} - l_R \sum_j f_{Rjyc} + w_R \sum_i f_{iRxc} - w_L \sum_i f_{iLxc} \tag{5.8}$$

Given the state $x = [v_x \quad v_y \quad \omega_z]$ and the wheel control $u_\alpha = [\tau_{ij} \quad \delta_{ij}]$, $g(x, u_\alpha)$ denotes Equations (5.3), (5.4) and (5.6) to (5.8) such that the chassis forces and moments $u = [f_x \quad f_y \quad m_z]$ can be written as $u = g(x, u_\alpha)$. Note that the model simplification reduces the state of the vehicle planar model, the wheel speed are no longer necessary after neglecting the wheel inertia.

5.2 MIMO High-Level Control With Control Allocation

Figure 5.3 shows the implementation of the vehicle motion controller block for this section. The framework developed in this section aims to solve the control problem by allocating longitudinal and lateral force targets and the yaw moment target to the different wheels. A linear multivariable controller sets the generalized forces. The control allocation is implemented as a constrained optimization problem. If the targets are not feasible, e.g., due to constraint violation, there will be a discrepancy between the total forces and moments requested by the MIMO controller and the outputs of the control allocation; an anti-windup controller is implemented to address this problem.

5.2.1 High-Level Controller and Anti-Windup Compensator

The goal of the controller is to define the total longitudinal and lateral forces and yaw moment to apply on the chassis to follow the driver's request. A model-based multivariable controller is

designed in this section based on the following planar vehicle model:

$$m(\dot{v}_x - v_y\omega_z) = f_x \tag{5.9}$$

$$m(\dot{v}_y + v_x\omega_z) = f_y \tag{5.10}$$

$$I_{zz}\dot{\omega}_z = m_z \tag{5.11}$$

This model is nonlinear, the first step to design a linear multivariable controller is to linearize the system around the operating point $(v_{x0}, v_{y0}, \omega_{z0})$. The linearized system is given by:

$$\begin{bmatrix} \dot{v}_x \\ \dot{v}_y \\ \dot{\omega}_z \end{bmatrix} = \begin{bmatrix} 0 & \omega_{z0} & v_{y0} \\ -\omega_{z0} & 0 & -v_{x0} \\ 0 & 0 & 0 \end{bmatrix} \begin{bmatrix} v_x \\ v_y \\ \omega_z \end{bmatrix} + \begin{bmatrix} \frac{1}{m} & 0 & 0 \\ 0 & \frac{1}{m} & 0 \\ 0 & 0 & \frac{1}{I_{zz}} \end{bmatrix} \begin{bmatrix} f_x \\ f_y \\ m_z \end{bmatrix} \tag{5.12}$$

$$\begin{bmatrix} \tau_{tot} \\ v_y \\ \omega_z \end{bmatrix} = \begin{bmatrix} 0 & 0 & 0 \\ 0 & 1 & 0 \\ 0 & 0 & 1 \end{bmatrix} \begin{bmatrix} v_x \\ v_y \\ \omega_z \end{bmatrix} + \begin{bmatrix} r_w & 0 & 0 \\ 0 & 0 & 0 \\ 0 & 0 & 0 \end{bmatrix} \begin{bmatrix} f_x \\ f_y \\ m_z \end{bmatrix} \tag{5.13}$$

From the state-space representation, we can deduct the transfer function from chassis forces and moment f_x, f_y, m_z, to the outputs τ_{tot}, v_y, ω_z:

$$G_p = \begin{bmatrix} r_w & 0 & 0 \\ -\frac{\omega_{z0}}{m(s^2+\omega_{z0}^2)} & \frac{s}{m(s^2+\omega_{z0}^2)} & -\frac{sv_{x0}+v_{y0}\omega_{z0}}{I_{zz}s(s^2+\omega_{z0}^2)} \\ 0 & 0 & \frac{1}{I_{zz}s} \end{bmatrix} \tag{5.14}$$

The transfer function mapping the total longitudinal force f_x to the total wheel torque τ_{tot} is modified to include the dynamic of the drivetrain and to remove the direct feed through term in G_p, this added dynamics is represented by a first-order transfer function with time constant τ. The transfer functions mapping the generalized forces f_x and f_y to the vehicle lateral velocity v_y are not stable and have a resonant frequency when $\omega = \omega_{z0}$ if $\omega_{z0} \neq 0$. The value of ω_{z0} is usually small, ranging from $-0.5\,\mathrm{rad\,s^{-1}}$ to $0.5\,\mathrm{rad\,s^{-1}}$. The linearization point is chosen such that $\omega_{z0} = 0$ which

reduces the plant to:

$$G_p = \begin{bmatrix} \frac{r_w}{\tau s+1} & 0 & 0 \\ 0 & \frac{1}{ms} & -\frac{v_{x0}}{I_{zz}s^2} \\ 0 & 0 & \frac{1}{I_{zz}s} \end{bmatrix} \tag{5.15}$$

In the previous model, the longitudinal dynamic is decoupled from the lateral and handling dynamics. Moreover, the vehicle model whose inputs are the chassis forces and moment and represented by Equations (5.9) to (5.11) is a more simplified model than the one described in Section 2.4.2, it neglects some dynamics in the vehicle yaw moment and lateral velocity. Indeed, with the linearized model from Section 2.4.2, the transfer functions mapping the yaw moment m_z to the lateral velocity v_y and yaw rate ω_z can be obtained by multiplying the transfer function mapping a left-to-right torque difference τ_{TV_i} to v_y and ω_z by $\frac{r_w}{w_L+w_R}$, yielding:

$$\begin{bmatrix} v_y \\ \omega_z \end{bmatrix} = \frac{r_w}{w_L+w_R} \begin{bmatrix} \frac{K_{\tau_{TV_F}m_z}(\tau_{\tau_{TV_F}m_z}s+1)}{s^2+2\zeta\omega_0 s+\omega_0^2} \\ \frac{K_{\tau_{TV_F}v_y}(\tau_{\tau_{TV_F}v_y}s+1)}{s^2+2\zeta\omega_0 s+\omega_0^2} \end{bmatrix} m_z \xrightarrow{K_U=0} \begin{bmatrix} -\frac{v_{x0}}{I_{zz}} \frac{1}{(s+\frac{C_{yF}+C_{yR}}{mv_{x0}})^2} \\ \frac{1}{I_{zz}} \frac{1}{s+\frac{C_{yF}+C_{yR}}{mv_{x0}}} \end{bmatrix} m_z \tag{5.16}$$

where parameters ζ, ω_0, $\tau_{\tau_{TV_F}v_y}$, $\tau_{\tau_{TV_F}m_z}$, $K_{\tau_{TV_F}v_y}$, $K_{\tau_{TV_F}m_z}$ are coefficients from the linearized planar vehicle (see Tables 2.1 and 2.2). The linearized planar vehicle model presented in Section 2.4.2 and the vehicle model used to design the high-level controller defined in Equations (5.9) to (5.11) only match at high-frequencies and for a neutral-steer vehicle (i.e., $K_U = 0$).

The high-level controller is designed via mixed-sensitivity $\mathcal{H}_\infty$-synthesis using the transfer function (5.15); this is a loop-shaping design method where the sensitivity and closed-loop transfer functions are shaped along with other transfer functions (e.g., Youla transfer function). In this section, the controller aims at minimizing the $\mathcal{H}_\infty$ norm of $[w_\Delta T \quad w_p S]^T$ where T is the closed-loop transfer function, S is the sensitivity transfer function, and w_Δ and w_p are filters chosen to obtain the desired transfer function shape. The filter w_p penalizes the error signal to enforce good tracking and allows the designer to shape the sensitivity S, w_Δ penalizes the output signal and shapes the closed-loop T. Such a problem can be solved by $\mathcal{H}_\infty$-synthesis, which aims at finding the controller

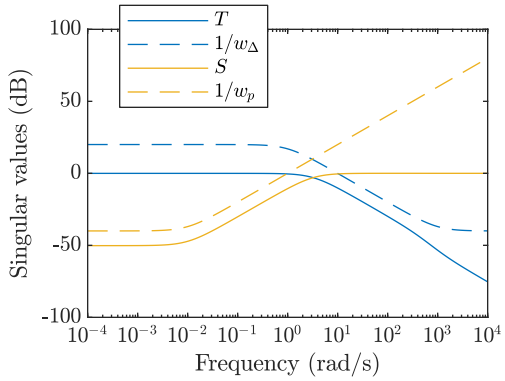

Figure 5.4: Singular values of the closed-loop system with an $\mathcal{H}_\infty$-controller

K minimizing $\|F_l(P,K)\|_\infty$. The augmented plant P is defined as:

$$P = \begin{bmatrix} w_p I & -w_p G_p \\ 0 & w_\Delta G_p \\ I & -G_p \end{bmatrix} \text{ such that } F_l(P_K) = \begin{bmatrix} w_p S \\ w_\Delta T \end{bmatrix} \tag{5.17}$$

The weighting filter w_Δ is chosen as a first-order low-pass filter with a high gain at frequencies below the closed-loop bandwidth to penalize the sensitivity function S and steady-state error. The filter w_p is designed similar to a lead-compensator to force the closed-loop transfer function T to be low-gain at frequencies beyond the bandwidth and improve noise rejection. Figure 5.4 shows the singular values of the sensitivity and closed-loop transfer functions and the weighing filters.

The controller output signals are fed to a constrained control allocation; because the allocation is constrained, it is not guaranteed that the allocated controls u_α will produce the requested high-level target y_c defined by the controller. The mismatch between high-level control target y_c and actual efforts $\text{sat}(u)$ might cause integral windup, deteriorate performance, and cause closed-loop instabilities.

Given a state-space representation (A, B, C, D) of the plant G_p, Teel and Kapoor [94], [95] propose

the following multivariable anti-windup compensator:

$$\dot{\zeta} = A\zeta + B(\text{sat}(u) - y_c) \tag{5.18}$$

$$v_1 = K\zeta \tag{5.19}$$

$$v_2 = C\zeta + D(\text{sat}(u) - y_c) \tag{5.20}$$

where $\text{sat}(u)$ is the saturated control input and y_c is the controller output signal, a precise value of $\text{sat}(u)$ is not necessary, in this work, the constrained control allocation will provide an estimate of $\text{sat}(u)$. The gain K must be chosen such that $K = -B^T P$ where P is a symmetric positive definite matrix solution of the Lyapunov inequality $A^T P + PA \leq 0$. Teel and Kapoor show that interconnecting the anti-windup compensator in the feedback loop such that the controller input is $u_c = r - (y - v_2)$ and the plant input is $u = \text{sat}(v_1 + y_c)$ provides appropriate anti-windup behavior for a marginally stable system;[1] i.e., when the controller outputs are within the saturation limits, the anti-windup compensator leaves the closed-loop behavior unchanged, and the anti-windup compensator quickly recovers back to the linear unconstrained behavior after the saturation limits have been exceeded.

This paragraph explains the derivation of the matrix P, necessary to derive the anti-windup compensator, for a marginally stable system [95]. Since the plant is marginally stable, its state-space matrix A can be decomposed into a matrix A_s which has all its eigenvalue in the left half plane and a matrix A_0 with all its eigenvalues on the $j\omega$-axis by using a similarity transformation T as follows, $T^{-1}AT = \text{blockdiag}(A_s, A_0)$. For the stable part of the system, we find the solution of the Lyapunov equation $A_s^T P_s + P_s A_s = -Q_s$ where Q_s is a symmetric positive definite matrix. Finally, the matrix P is chosen as $P = (T^{-1})^T \,\text{blockdiag}(P_s, P_0) T^{-1}$ where P_0 is a symmetric positive definite matrix. Building P accordingly guarantees that the matrix P is positive definite and $A^T P + PA$ is negative semi-definite.

Figure 5.5 shows the closed-loop system response to a step input $\tau_{tot} = 100\,\text{N m}$, $v_y = -3\,\text{m s}^{-1}$, and $\omega_z = 0.5\,\text{rad s}^{-1}$ with input saturation such that $|f_x| \leq 500\,\text{N}$, $|f_y| \leq 16\,000\,\text{N}$, and $|m_z| \leq 2000\,\text{N m}$. The closed-loop correspond to the interconnection of the nonlinear system described

[1] Anti-windup compensation for unstable systems is more involved than for marginally stable systems [96, p. 271]. In this dissertation, anti-windup compensation is used only for marginally stable plants.

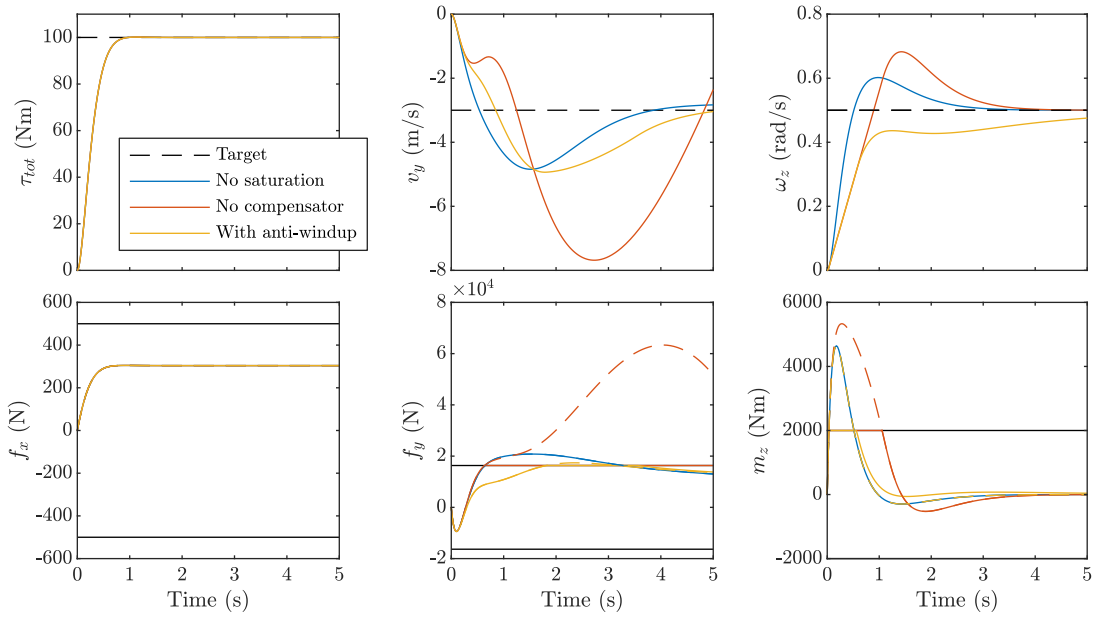

Figure 5.5: Step response of the MIMO controller with saturated inputs. In the control signal response, dashed lines are the (unsaturated) controller outputs y_c, and solid lines are the saturated plant input $u = \mathrm{sat}(v_1 + y_c)$.

in Equations (5.9) to (5.11) with $m = 1800\,\mathrm{kg}$ and $I_{zz} = 3515\,\mathrm{kg\,m^2}$, the $\mathcal{H}_\infty$-controller, and the anti-windup compensator. The blue curve shows the system's response without actuator saturation; the linear controller can stabilize the nonlinear system. The red curve shows the system's response without the anti-windup compensator, and the yellow curve shows the response with the anti-windup compensator. For all configurations, the longitudinal controller does not saturate and applies the same total longitudinal force, illustrating that the anti-windup compensator does not modify the system response when inputs are not saturating; moreover, the longitudinal and handling controller are decoupled. Without an anti-windup compensator, the controller attempts to apply excessive lateral force and produces large lateral velocities. Note that the nonlinear model (5.9)–(5.11) does not include a tire friction model; this effect combined with large lateral velocities would result in excessive slip angle on a vehicle, limiting the lateral force the vehicle can generate and further destabilizing the system. The closed-loop system with the anti-windup compensator tracks the targets well while maintaining actuator signals within their saturation limits.

5.2.2 Optimal Wheel Control Allocation from Generalized Forces

Once the high-level target $u^T = [f_x \quad f_y \quad m_z]$ have been defined, they must be distributed to the wheel controls $u_\alpha^T = [\tau_{ij} \quad \delta_i]$. This allocation is formulated as a constrained optimization problem. The cost function penalizes tracking error, power loss, and actuator rate of change; constraints enforce the feasibility of the controls u_α by respecting actuator saturation limits and preventing tire saturation by constraining the friction coefficients to stay within the friction circle.

Given the vehicle state $x^T = [v_x \quad v_y \quad \omega_z]$ and wheel controls u_α, the longitudinal, lateral forces and the yaw moment applied on the chassis is $g(x, u_\alpha)$, see Section 5.1.2. In the optimization problem, the tracking error is penalized in the cost function by the weighted nonlinear least square term $\|u - g(x, u_\alpha)\|_{Q_e}^2 = \frac{1}{2}(u - g(x, u_\alpha))^T Q_e (u - g(x, u_\alpha))$ where Q_e is a positive definite matrix.

The optimization penalizes the rate of change of the actuator to account for the bandwidth of the wheel controls. Instead of penalizing the rate of change of the individual wheel torques τ_{ij} and steering angles δ_{ij}, we choose to penalize the rate of change of the total torque applied on the chassis $\tau_{tot} = \sum_{ij} \tau_{ij}$, the left-to-right torque difference on each axle $\tau_{TV_i} = \frac{1}{2}(\tau_{iR} - \tau_{iL})$, the front-to-rear torque difference $\tau_{TV_{F/R}} = \frac{1}{2}(\tau_{FL} + \tau_{FR} - \tau_{RL} - \tau_{RR})$, and active steering angle at each axle δ_i. The penalty is represented by the term $\|\Delta u_\alpha\|_{R_\Delta}^2 = \frac{1}{2}\Delta u_\alpha^T R_\Delta \Delta u_\alpha$, the matrix R_Δ is positive definite and $\Delta u_\alpha = u_\alpha - u_\alpha^{prev}$ where u_α^{prev} is the wheel controls at the last timestep. This term also prevents obtaining a singular Hessian matrix of the cost function and helps to guarantee a unique, well-defined solution to the optimization problem.

Only penalizing the tracking of the chassis forces and moment and the bandwidth of the wheel controls might still result in inadequate allocation; for instance, nothing prevents the allocation from distributing a positive torque to the front axle and a negative torque of the same amplitude to the rear axle when tracking a zero longitudinal torque target. The optimization problem is set up to avoid using actuators, resulting in high-power usage. More precisely, the optimization penalizes the power loss $\mathcal{P}$ associated with the drivetrain electric motors and the power dissipated by the eLSD and friction brakes; drivetrain transmission losses and losses in active steering actuators are neglected. The exact power dissipated by the actuators depends on the actuator configuration, and the distribution of actuator signals, the design of the abstract layer of the vehicle motion controller is supposed to be independent of the actuator configuration; therefore, the exact value of

the power dissipated is not known; instead, we assume that the application layer (which is aware of the actuator configuration and actuator states) provides the Jacobian $p^T = \frac{\partial \mathcal{P}}{\partial \Delta u_\alpha}\Big|_{u_\alpha^{prev}}$ and the Hessian $P = \frac{\partial^2 \mathcal{P}}{\partial \Delta u_\alpha}\Big|_{u_\alpha^{prev}}$ of the power loss with respect to wheel controls u_α evaluated at u_α^{prev}. The power loss is indirectly penalized by the the second-order Taylor expansion of the power loss $\mathcal{P}(\Delta u_\alpha) = \mathcal{P}_0 + p^T \Delta u_\alpha + \frac{1}{2}\Delta u_\alpha^T P \Delta u_\alpha$, and the constant term $\mathcal{P}_0$ can be dropped.

The optimization problem must guarantee that the actuators can apply the requested wheel target, this is enforced by constraints on u_α. For instance, the quad-motor drivetrain with EHB allows to control the wheel torque independently at each wheel but the wheel torque must be constrained by the brake and motor actuator capabilities. The wheel torques and steering angles are dealt with independently; so the constraints can be separated in two parts: one for steering controls and one for wheel torque controls. In the general case, we assume a linear map between the steering actuator controls δ_{act} and the wheel steering angles δ_{ij} and a linear map between the drivetrain and brake actuator signals τ_{act} to wheel torques τ_{ij}, i.e. $\delta_{ij} = A_\delta \delta_{act}$ and $\tau_{ij} = A_\tau \tau_{act}$. Actuator constraints $\underline{\delta}_{act} \leq \delta_{act} \leq \overline{\delta}_{act}$ and $\underline{\tau}_{act} \leq \tau_{act} \leq \overline{\tau}_{act}$ can be expressed as constraints on the wheel controls by $A_\delta \underline{\delta}_{act} \leq \delta_{ij} \leq A_\delta \overline{\delta}_{act}$ and $A_\tau \underline{\tau}_{act} \leq \tau_{ij} \leq A_\tau \overline{\tau}_{act}$. This can be sum up by:

$$A u_\alpha \leq b \text{ where } A = \begin{bmatrix} I \\ -I \end{bmatrix}, \text{ and } b^T = \begin{bmatrix} (A_\tau \overline{\tau}_{act})^T & (A_\delta \overline{\delta}_{act})^T & (-A_\tau \underline{\tau}_{act})^T & (-A_\delta \underline{\delta}_{act})^T \end{bmatrix} \quad (5.21)$$

where the matrices A_τ and A_δ, and the vector b are provided by the application layer since they depend on the vehicle actuator configuration. For instance, for the quad-motor topology equipped with EHB without active steering, the drivetrain and brake actuator signals are the four electric motor torques τ_{mij} and the four friction braking torque τ_{bij} and there is no active steering actuator, thus:

$$\tau_{act}^T = \begin{bmatrix} \tau_{mFL} & \tau_{mFR} & \tau_{mRL} & \tau_{mRR} & \tau_{bFL} & \tau_{bFR} & \tau_{bRL} & \tau_{bRR} \end{bmatrix}^T, \text{ and } A_\tau = \begin{bmatrix} I & I \end{bmatrix} \quad (5.22)$$

Note that Equation (5.21) is a necessary condition to enforce actuator constraint but not sufficient. For instance, let's consider the dual motor topology and let $\overline{\tau}_m$ and $\underline{\tau}_m$ be the maximum and minimum torques the traction motor can applied at the wheel and $\overline{\tau}_{bk}$ and $\underline{\tau}_{bk}$ the maximum and minimum torques the friction brake can apply, Equation (5.21) yields $\frac{1}{2}\underline{\tau}_m + \underline{\tau}_{bk} \leq \tau_{ij} \leq \frac{1}{2}\overline{\tau}_m + \overline{\tau}_{bk}$

but it would not enforce $\tau_{iL} = \tau_{iR}$ if friction-based left-to-right TV is not authorized and $\underline{\tau}_{bk} - \overline{\tau}_{bk} \leq \frac{1}{2}(\tau_{iR} - \tau_{iL}) \leq \overline{\tau}_{bk} - \underline{\tau}_{bk}$ if it is authorized. If the actuators have such limitations, they are added to the polytopic constraints $Au_\alpha \leq b$ such that it becomes a necessary and sufficient condition for actuator constraints.

Recall that Equation (5.4) requires that the longitudinal friction coefficient is inside the friction circle, i.e. it must be lower-bounded by $\bar{\mu}_{ijx} - \Delta\mu_{ijx}$ and upper-bounded by $\bar{\mu}_{ijx} + \Delta\mu_{ijx}$. Since the value of the longitudinal friction coefficients is set by the wheel torque in $\tau_{ij} = r_w \mu_{ijx} f_{ijz}$, the wheel torque must be constrained as follows:

$$\bar{\mu}_{ijx} - \Delta\mu_{ijx} \leq \frac{\tau_{ij}}{r_w f_{ijz}} \leq \bar{\mu}_{ijx} + \Delta\mu_{ijx} \tag{5.23}$$

The upper and lower bounds of the previous inequality are a nonlinear function of the wheel controls u_α; therefore, this constraint is summarized as $g(u_\alpha) \leq 0$. Moreover, this constraint helps prevent tire saturation since it forces the tire to operate inside the tire friction circle, which is scaled down by the maximum friction coefficient.

To summarize, the control allocation problem is formulated as follows,

$$\arg\min_{u_\alpha} \|u - g(x, u_\alpha)\|^2_{Q_e} + q_p \mathcal{P}(\Delta u_\alpha) + \|\Delta u_\alpha\|^2_{R_\Delta} \tag{5.24a}$$

$$\text{subject to } Au_\alpha \leq b \tag{5.24b}$$

$$g(u_\alpha) \leq 0 \tag{5.24c}$$

u are the high-level targets, u_α are the wheel controls, $g(x, u_\alpha)$ represents the mapping from wheel controls to generalized ones, Δu_α is the wheel controls rate of change, Q_e, q_p, and R_Δ are tuning parameters. Equation (5.24b) represents the actuator magnitude saturation, and Equation (5.24c) represents the tire saturation constraint. The 'Constrained Control Allocation' block in Figure 5.3 is set up to output the optimal wheel control u_α and the chassis forces and moment applied by those controls $\text{sat}\,(u) = [f_x \quad f_y \quad m_z] = g(x, u_\alpha)$. It is implemented in MATLAB with the `fmincon` solver and executed in Simulink inside a MATLAB System object.

5.3 Model Predictive Control

Model Predictive Control (MPC) is a method that uses an internal model of the system to control the system predictively. The major advantage of MPC is that it allows enforcing constraints on the actuator limits and the system dynamics by solving an optimization problem and can therefore avoid violating the dynamics of the system and the limits of the actuator. The main drawback of this method is that it relies heavily on solvers, and finding a solution in real-time can be difficult. Explicit or multi-parametric MPC attempt to reduce the time complexity at the expense of space complexity by solving problems offline and implementing the MPC as a lookup table of controllers.

Another disadvantage of MPC is that, because of its time-window formulation, MPC makes it hard to analyze its robustness in the frequency domain as opposed to linear control. Instead, some other formulation aims at minimizing an objective function while considering a worst-case disturbance, i.e., minimizing a cost function, this is the minimax or robust MPC; however, these formulations further increase the computational burden of MPC [97], [98].

Because MPC is an optimization-based control strategy that assigns controls to be *optimal* while enforcing constraints, it is suited to control and allocate the torque and steering angle at each wheel. This section will present different types of MPC controllers to implement the 'Optimal Wheel Control Allocation' block of Figure 3.2 and replace the implementation with an $\mathcal{H}_\infty$-controller and control allocation presented in Section 5.2.

5.3.1 Implementations of Model Predictive Controller

A linear-quadratic MPC propagates a discrete-time linear state-space representation of the plant to control over an horizon of time from an initial state $x_{0|t} = \hat{x}(t)$ where $\hat{x}(t)$ is the measured or estimated state of the model at t and computes a sequence of inputs $(u_{k|t})$ to minimize a cost function subject to constraints on the states and on the input. The constraints are polytopic and represented by the inequality Equation (5.25d). The control law of the MPC implements the first iteration $u_{0|t}$ of the sequence $(u_{k|t})$ for a time period corresponding to the sampling time T_s of the model, at the next timestep, the MPC recomputes a solution $(u_{k|t+T_s})$ solution to the same optimization problem with the updated initial state $x_{0|t+T_s} = \hat{x}(t + T_s)$ over a horizon shifted in time by one timestep, hence the name receding window control. A linear-quadratic MPC problem solves the following

Optimal Control Problem (OCP):

$$\underset{(u_{k|t})_{k\in[\![0,N-1]\!]}}{\arg\min} \quad \mathcal{J} = \left\|x_{k|t}\right\|_P^2 + \sum_{k=0}^{N-1} \left\|x_{k|t}\right\|_Q^2 + \left\|u_{k|t}\right\|_R^2 \tag{5.25a}$$

$$\text{subject to } x_{0|t} = \hat{x}(t) \tag{5.25b}$$

$$x_{k+1|t} = Ax_{k|t} + Bu_{k|t} \tag{5.25c}$$

$$u_{min} \leq u_{k|t} \leq u_{max} \tag{5.25d}$$

$$A_x x_{k|t} + A_u u_{k|t} \leq b \tag{5.25e}$$

The term $\left\|x_{k|t}\right\|_P^2$ is the terminal cost and $\sum_{k=0}^{N-1} \left\|x_{k|t}\right\|_Q^2 + \left\|u_{k|t}\right\|_R^2$ is the incremental cost. The matrix Q must be positive definite and the matrix R positive semi-definite. Choosing a positive semi-definite matrix P solution to the discrete algebraic Riccati equation $P = Q + A^TPA - A^TPB(R + B^TPB)^{-1}B^TPA$ ensures the recursive feasibility of the problem, however, for more general formulations (e.g. nonlinear or with time-varying weighting matrix and bound) this term can be hard to defined and it is omitted in the next formulations. Equation (5.25b) initializes the state, Equation (5.25c) defines the dynamic of the system, and Equations (5.25d) and (5.25e) are bounds and polytopic constraints. For each variable, the subscript k indicates the timestep within the time window and the subscript t shows the time at which the receding horizon starts.

Applying the solution of the previous optimization problem results in a regulation controller making the state converge to zero [99]. The problem must be modified, or the model must be augmented to track the desired signal $y_{ref,k|t}$. A common approach is to augment the plant by adding an integrator at the input: instead of controlling the plant input directly, the MPC problem is formulated in terms of the rate of change of the actuator input $\Delta u_{k|t} = u_{k|t} - u_{k-1|t}$ such that in steady-state only the tracking error is penalized.

$$\underset{(\Delta u_{k|t})_{k\in[\![0,N-1]\!]}}{\arg\min} \quad \mathcal{J} = \sum_{k=0}^{N-1} \left\|y_{k|t} - y_{ref,k|t}\right\|_{Q_e}^2 + \left\|\Delta u_{k|t}\right\|_{R_\Delta}^2 \tag{5.26a}$$

$$\text{subject to } x_{0|t} = \hat{x}(t) \tag{5.26b}$$

$$x_{k+1|t} = Ax_{k|t} + Bu_{k|t} \tag{5.26c}$$

$$y_{k|t} = Cx_{k|t} + Du_{k|t} \tag{5.26d}$$

$$\Delta u_{k|t} = u_{k|t} - u_{k-1|t} \tag{5.26e}$$

$$u_{min} \leq u_{k|t} \leq u_{max} \tag{5.26f}$$

$$A_x x_{k|t} + A_u u_{k|t} \leq b \tag{5.26g}$$

Previous problem consider the implementation of an MPC for an LTI system. One possible strategy to implement a MPC controller for a nonlinear systems described by $x_{k+1} = f(x_k, u_k)$ and $y_k = g(x_k, u_k)$ is to approximate the internal model by a linearized state-space of the nonlinear model at the operating point $(x_{op,t}, u_{op,t}) = \big(\hat{x}(t), u(t - T_s)\big) = \big(x_{0|t}, u_{0|t-T_s}\big)$. Doing so yields the Linear Time-Varying MPC (LTVMPC) where the plant internal model is a linear state-space over the receding horizon and the state-space model is updated when the receding horizon is shifted, i.e. the model is LTI for setting up the optimization problem but Linear Time-Varying (LTV) over time. The perturbed variable of the linearized system are $\tilde{x}_{k|t} = x_{k|t} - x_{op,t}$, $\tilde{u}_{k|t} = u_{k|t} - u_{op,t}$, and $\tilde{y}_{k|t} = y_{k|t} - g(x_{op,t}, u_{op,t})$, and the state-space matrices are:

$$A_t = \frac{\partial f}{\partial x_k}\Big|_{(x_{op,t},u_{op,t})},\ B_t = \frac{\partial f}{\partial u_k}\Big|_{(x_{op,t},u_{op,t})},\ C_t = \frac{\partial g}{\partial x_k}\Big|_{(x_{op,t},u_{op,t})},\ D_t = \frac{\partial g}{\partial u_k}\Big|_{(x_{op,t},u_{op,t})} \tag{5.27}$$

The LTVMPC solves the following optimization problem. The optimization variables are the perturbed model input $\tilde{u}_{k|t}$, note that $\tilde{u}_{0|t} = \Delta u_{0|t}$ and $\Delta u_{k|t} = \tilde{u}_{k|t} - \tilde{u}_{k-1|t}$ for $k > 0$. The OCP can still be solved with the same computational complexity as for the problem (5.26), appendix B describes the transformation of the LTVMPC problem (5.28) into a QPP, a standard QP solver can then be used to obtain the solution.

$$\underset{(\tilde{u}_{k|t})_{k\in[\![0,N-1]\!]}}{\arg\min}\ \mathcal{J} = \sum_{k=0}^{N-1} \left\|y_{k|t} - y_{ref,k|t}\right\|_{Q_e}^2 + \left\|\Delta u_{k|t}\right\|_{R_\Delta}^2 \tag{5.28a}$$

$$\text{subject to } \tilde{x}_{0|t} = 0 \tag{5.28b}$$

$$\tilde{x}_{k+1|t} = A_t \tilde{x}_{k|t} + B_t \tilde{u}_{k|t} \tag{5.28c}$$

$$\tilde{y}_{k|t} = C_t \tilde{x}_{k|t} + D_t \tilde{u}_{k|t} \tag{5.28d}$$

$$x_{k|t} = x_{op,t} + \tilde{x}_{k|t},\ u_{k|t} = u_{op,t} + \tilde{u}_{k|t} \tag{5.28e}$$

$$y_{k|t} = g(x_{op,t}, u_{op,t}) + \tilde{y}_{k|t} \tag{5.28f}$$

$$\Delta u_k = u_k - u_{k-1} \tag{5.28g}$$

$$u_{min} \leq u_{k|t} \leq u_{max} \tag{5.28h}$$

$$A_x x_{k|t} + A_u u_{k|t} \leq b \tag{5.28i}$$

Nonlinear MPC (NMPC) directly tackles nonlinear constraints and nonlinear dynamics without resorting to linearization, instead it solves a nonlinear optimization problem defined by the following OCP:

$$\underset{(u_{k|t})_{k\in[\![0,N-1]\!]}}{\arg\min} \quad \mathcal{J} = m(x_{N|t}) + \sum_{k=0}^{N-1} l(x_{k|t}, u_{k|t}) \tag{5.29a}$$

$$\text{subject to } x_{0|t} = \hat{x}(t) \tag{5.29b}$$

$$x_{k+1|t} = f(x_{k|t}, u_{k|t}) \tag{5.29c}$$

$$h(x_{k|t}, u_{k|t}) \leq 0 \tag{5.29d}$$

The previous NMPC problem is a NLP optimization problem, such problems are not necessarily convex and can be extremely computationally intensive to solve. Various approaches exist to solve this kind of problem, one of the most popular option is SQP which was presented on page 63. SQP approximates the nonlinear optimization by a sequence of QP defined from the Jacobian and Hessian[2] matrices of the cost function, system dynamics, and inequality constraints evaluated at a guess solution $\boldsymbol{x}_{guess,t}^T = [x_{guess,0|t}^T \quad \cdots \quad x_{guess,N|t}^T]$ and $\boldsymbol{u}_{guess,t} = [u_{guess,0|t}^T \quad \cdots \quad u_{guess,N-1|t}^T]$. Given $\boldsymbol{x}_{guess,t}$ and $\boldsymbol{u}_{guess,t}$, the QP subproblem is defined as follows,

$$\underset{(\tilde{u}_{k|t})_{k\in[\![0,N-1]\!]}}{\arg\min} \quad \mathcal{J} = \tilde{x}_{N|t}^T P_{N|t} \tilde{x}_{N_t} + \sum_{k=0}^{N-1} \begin{bmatrix} \tilde{x}_{k|t} \\ \tilde{u}_{k|t} \end{bmatrix}^T H_{k|t} \begin{bmatrix} \tilde{x}_{k|t} \\ \tilde{u}_{k|t} \end{bmatrix} + J_{k|t}^T \begin{bmatrix} \tilde{x}_{k|t} \\ \tilde{u}_{k|t} \end{bmatrix} \tag{5.30a}$$

$$\text{subject to } \tilde{x}_{0|t} = \hat{x}(t) - x_{guess,0|t} \tag{5.30b}$$

$$\tilde{x}_{k+1|t} = A_{k|t}\tilde{x}_{k|t} + B_{k|t}\tilde{u}_{k|t} + f(x_{guess,k|t}, u_{guess,k|t}) - x_{guess,k+1|t} \tag{5.30c}$$

[2]The Hessian matrix is usually not computed exactly, instead a procedure approximates it, e.g. Gauss-Newton Hessian approximation.

$$C_{k|t}\tilde{x}_{k|t} + D_{k|t}\tilde{u}_{k|t} + h(x_{guess,k|t}, u_{guess,k|t}) \leq 0 \tag{5.30d}$$

where the matrices $A_{k|t}$, $B_{k|t}$, $C_{k|t}$, and $D_{k|t}$ are the Jacobian of the state and constraint equations evaluated at $(x_{guess,k|t}, u_{guess,k|t})$. Once the problem (5.30) has been solved and the search direction $(\tilde{x}_{k|t}, \tilde{u}_{k|t})$ is known, Newton's iterative method is used to update the guess solution: $(x_{guess,k|t}, u_{guess,k|t}) \leftarrow (x_{guess,k|t}, u_{guess,k|t}) + \alpha(\tilde{x}_{k|t}, \tilde{u}_{k|t})$ where $\alpha \in [0, 1]$ is computed to guarantee a better solution. Several QP iterations (i.e. transforming the NLP into a QP and using Newton's method to update the guess solution) may be necessary until a satisfying solution is found, thus requiring to solve several QPP to solve a single NMPC problem which can be very computationally intensive and time-consuming even though efficient QP solvers exist. Recent developments in algorithms promise to solve NMPC problem faster. The Real-Time Iteration (RTI) scheme implements a single QP iteration to compute the search direction and use a full Newton step (i.e. $\alpha = 1$) to update the solution [100]. RTI relies on assumption that NMPC problems with horizon starting at t and $t + T_s$ have similar solutions. With $(\boldsymbol{x}_{guess,t}, \boldsymbol{u}_{guess,t})$ the solution of the NMPC problem at time t, the shifting procedure set the guess solution of the problem starting at time $t + T_s$ as follows:

$$x_{guess,k|t+T_s} = x_{k+1|t} \ \forall k \in [\![0, N-1]\!], \tag{5.31a}$$

$$u_{guess,k|t+T_s} = u_{k+1|t} \ \forall k \in [\![0, N-2]\!], \tag{5.31b}$$

$$x_{guess,N|t+T_s} = f(x_{guess,N-1|t+T_s}, u_{guess,N-1|t+T_s}), \tag{5.31c}$$

$$u_{guess,N-1|t+T_s} = u_{guess,N-2|t+T_s} \tag{5.31d}$$

Therefore, RTI allows to solve NMPC problems with the computational cost close to the one of a linear MPC problem. In addition, the RTI scheme help reducing the feedback latency associated with solving the NMPC problem on real-life implementation. Indeed, the shifting procedure (5.31), the computation of the Jacobian and Hessian matrices $A_{k|t}$, $B_{k|t}$, $C_{k|t}$, $D_{k|t}$, $J_{k|t}$, $H_{k|t}$, and $P_{N|t}$ do not depend on the measurement $\hat{x}(t)$ and can thus be computed in advance. In general, the RTI algorithm is decomposed in two parts: a preparation part which is independent of and executed before the state measurement, a feedback phase which solves the QP problem. Under some conditions

provided in [100] and [101], the RTI scheme guarantees to follow the global solution of the NMPC problem.

5.3.2 Linear Time Varying Model Predictive Control

The goal of the abstract layer is to define controls at the wheel level so that the driver's requests are met while ensuring vehicle stability. Since actuators have saturation limits, the controller should also prevent them from exceeding those limits even though the abstract layer does not perform the allocation to the vehicle actuators. Constraints are used to maintain vehicle stability and to prevent actuator saturation.

The internal model used by the MPC is based on the planar vehicle model presented in Equations (2.81) to (2.83) where the tire lateral and longitudinal tire forces are computed as described in Equation (2.83). The vehicle model approximates the longitudinal and lateral load transfer by solving the system (2.89) and neglect the wheel dynamics, the states of the system are $x = [v_x \quad v_y \quad \omega_z]$ and its inputs are $u = u_\alpha = [\tau_{ij} \quad \delta_{ij}]$. Reducing the number of state of the system by neglecting the wheel inertia decreases the size of the QP problem and helps reducing the computational burden of the MPC.

The objective function is defined by the incremental cost $\|y - y_{ref}\|^2_{Q_e} + q_p\mathcal{P}(\Delta u_k) + \|\Delta u_k\|^2_{R_\Delta}$, where:

- The term $\|y - y_{ref}\|^2_{Q_e}$ is the error between the output $y^T = \begin{bmatrix}\tau_{tot} & v_y & \omega_z\end{bmatrix}$ and the reference signals $y^T_{ref} = \begin{bmatrix}\tau_{tot,ref} & v_{y,ref} & \omega_{z,ref}\end{bmatrix}$, the reference signals are kept constant over the prediction horizon since the driver's request is not known in advance. Contrary to the control strategy developed in Section 5.2, the MPC implementation directly defines controls to track the target without the need to define generalized forces.

- The term $q_p\mathcal{P}(\Delta u_k)$ penalizes the power loss associated with the torque distribution. This penalty should be smaller than the one associated with target following to avoid introducing significant steady-state tracking error in situations where large power loss cannot be avoided. Secondary penalties might be considered; for instance, one might penalize the covariance of the friction coefficients for reducing tire wear.

- The term $\|\Delta u_k\|^2_{R_\Delta}$ is the actuator rate of change, and it penalizes sudden change in wheel controls.

For the tire model simplification to be valid, the longitudinal friction coefficient must be bounded as described in (5.23), this constraint is a nonlinear constraint and it is linearized around $(x_{op,t}, u_{op,t}) = \big(\hat{x}(t), u(t - T_s)\big)$ to be formulated as a polytopic constraint. The bounds of this constraint are scaled by an estimate of the maximum friction coefficient to prevent traction forces from exceeding the surface limit. In addition, to prevent tire force saturation, state constraints on the yaw rate and lateral velocity enforce vehicle stability; the yaw rate is bounded by $|\omega_z| \leq \frac{\mu g}{|v_x|}$, and the lateral velocity is bounded by $|v_y| \leq 0.01|v_x|\mu g$ as suggested in [48]. The constraints on tire saturation, yaw rate, and lateral velocity are state constraints; they are therefore formulated as soft constraints to ensure the feasibility of the optimization problem. Finally, polytopic constraints on the actuators, see Equation (5.21), are enforced.

5.3.3 Nonlinear Model Predictive Control

The free and open-source software `acados` [102] compute solutions to OCP that typically have to be solved for NMPC and MHE, it implements a SQP solver with RTI and allows to solve the underlying QP problem using a variety of solver (HPIPM, qpOASES, qpDUNES...), Runge-Kutta integrators are available to discretize the continuous-time system, `acados` has interfaces for C/C++, Python, and MATLAB.

A NMPC is implemented using the `acados` solver, it implements the same cost function as the linear MPC designed in Section 5.3.2 and uses the same internal model, i.e. planar vehicle model with algebraic load distribution and with the tire model simplification. Contrary to the LTVMPC, the constraints on the tire saturation, vehicle yaw rate and lateral velocity are not linearized. Actuator constraints are formulated as polytopic constraints. The NMPC uses `acados` RTI-SQP solver.

5.3.4 Tuning of the Hyper-Parameters

The hyper-parameters of the MPC have a significant impact on the computational load required to implement the controller. In this section, we investigate the trade-off between computational burden and performance when applying MPC to the vehicle motion control problem. The computational

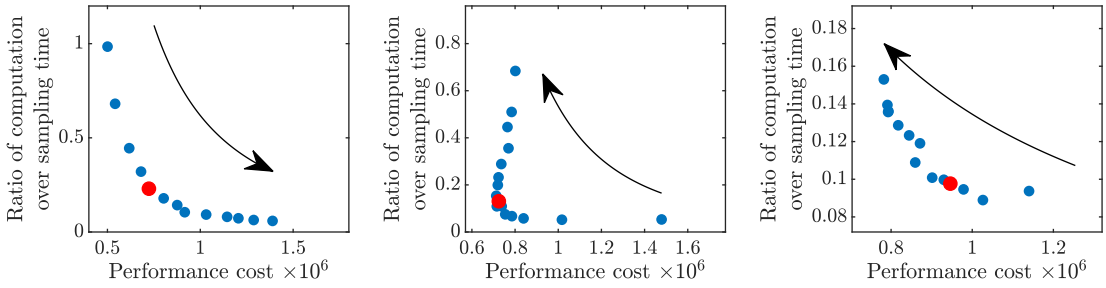

(a) Sampling time **(b)** Prediction horizon **(c)** Control horizon

Figure 5.6: Tuning of the LTVMPC hyper-parameters. The arrow indicates the direction of increasing sampling time, prediction and control horizons. The red dot highlights the chosen parameters ($T_s = 30\,\text{ms}$, $N_p = 25$, $N_t = 5$).

load is characterized by the ratio of the time needed to solve the MPC problem over the sampling time. The performance is quantified by the following metric, which uses the same penalty matrix as the one in the MPC problem.

$$\mathcal{J} = \int_0^{T_{sim}} \left(\|y(t) - y_{ref}(t)\|^2_{Q_e} + q_p \mathcal{P}(u(t)) + \|\Delta u(t)\|^2_{R_\Delta} \right) \mathrm{d}t \tag{5.32}$$

The metric represents a cost similar to the MPC cost function, both the metric and the MPC cost function compute the integral of the error, power loss, and input rate of change. Contrary to the MPC which integrates it over the prediction horizon, the metric integrates it over the duration of the benchmark simulation, which consists of a set of maneuvers. The sampling time, prediction horizon, and control horizon are tuned, Figure 5.6 shows the effect of varying the MPC hyper-parameters on the controller performance in term of controls and computational need and highlight the trade-off between computational load and control performance. First, the sampling time is tuned while using large prediction and control horizons (both are kept constant in duration, not in the number of steps); the computational load increases rapidly when the sampling time is smaller than 30 ms without a significant increase in performance (Figure 5.6a). Indeed, short sampling time and large prediction horizons result in a computationally complex optimization problem. Second, both the prediction and control horizons N_p and N_t are decreased such that $N_p = N_t$, a prediction horizon of 25 is selected, corresponding to a prediction window of 0.75 s (Figure 5.6b). Finally, the control horizon N_t is decreased (Figure 5.6c) to limit the number of decision variables and speed up the optimization problem. The MPC is set to use a control horizon $N_t = 5$.

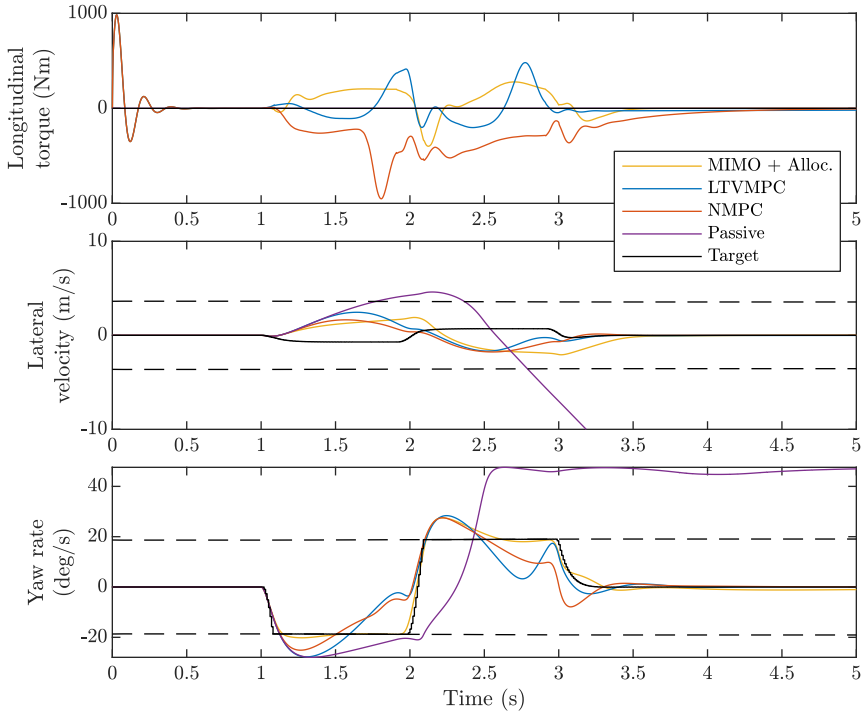

Figure 5.7: Generalized forces during double-step steer

5.4 Simulation Results

The controllers are tested on a 90° double-step-steer maneuver performed at $120\,\mathrm{km\,h^{-1}}$. During this maneuver, the driver holds the steering angle at $-90°$ for one second and 90° for another second; during the transition, the steering angle is changed linearly with a rate of $1000\,\mathrm{deg\,s^{-1}}$. The vehicle is equipped with 4WD and with AFS.

Figure 5.7 shows the target signals for the three different controllers and the passive vehicle. The driver's inputs cause the passive vehicle to become unstable; all controllers can stabilize the vehicle and track the target signals. Note that the yaw rate target is saturating, i.e. $|\omega_{z,ref}| = \frac{\mu_{max} g}{v_x}$. None of the controllers tracks the lateral velocity target well because the cost function is set up to prioritize the tracking of the yaw rate over the lateral velocity. The MIMO high-level controller with a control allocation achieves the best yaw rate target tracking. All the controllers use left-to-right torque-vectoring and active steering to apply a positive yaw moment on the vehicle between $t = 1\,\mathrm{s}$ and $t = 2\,\mathrm{s}$ to reduce the vehicle yaw rate, and a negative yaw moment between $t = 2\,\mathrm{s}$ and $t = 3\,\mathrm{s}$ (Figure 5.8).

Figure 5.9 shows the high-level force and moment requested by the multivariable controller with

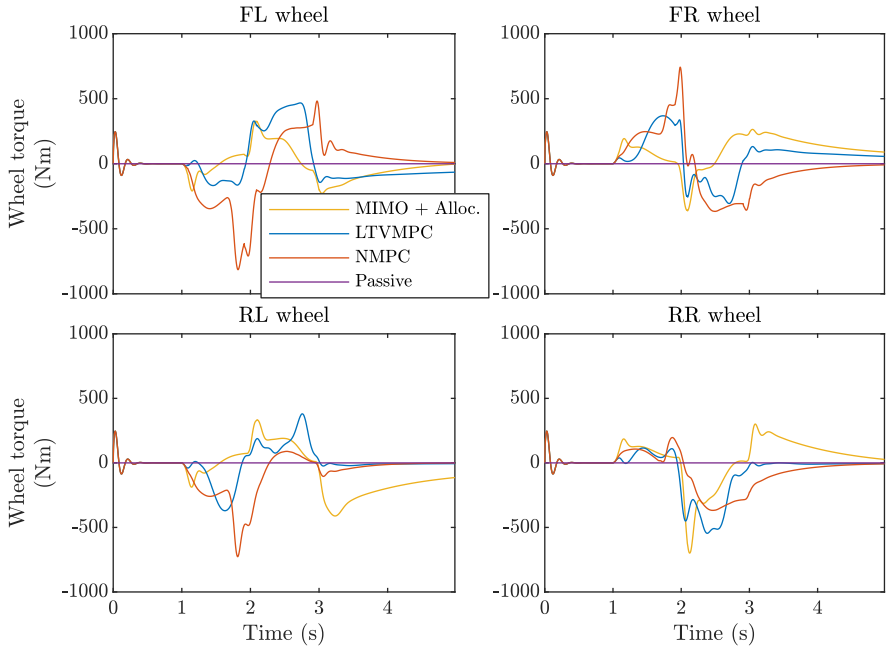

Figure 5.8: Wheel torques during double-step steer

anti-windup compensation, i.e. the input of the control allocation $u = y_c + v_1$ from Figure 5.3, and the allocated generalized forces reported by the control allocation, i.e. $\text{sat}(u)$, during a double step-steer maneuver. The control allocation tracks adequately the longitudinal and lateral tire forces and yaw moment, the tracking error at $t = 1\,\text{s}$, $t = 2\,\text{s}$, and $t = 3\,\text{s}$ are due to the rapid change in the driver steering input.

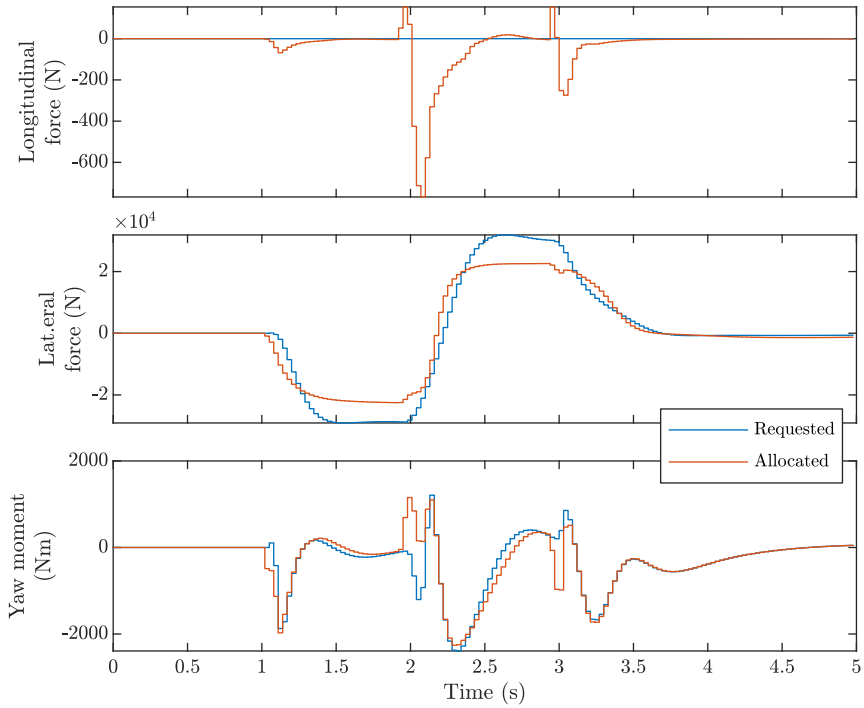

Figure 5.9: High-level request tracking with the MIMO and control allocation strategy

Chapter 6

Drivetrain and Brake Coordination

The drivetrain and the friction brakes control requests must be coordinated to apply the correct wheel torque. With the quad-motor drivetrain topology with independent EHB braking, the wheel motor and EHB torque requests must be coordinated to apply the desired wheel torque. With other drivetrain topologies or without independent braking, the coordination is more complex because of the coupling between the different actuators; for instance, a left-to-right torque vectoring request can be executed by applying a torque difference using the friction brakes or by using the TV motor or eLSD.

Several aspects must be considered when allocating the actuator signals to follow the desired wheel torque. Regenerative braking should be preferred over the use of friction brakes due to improved energy efficiency; however, friction brakes can provide larger wheel torque during braking and apply a larger left-to-right torque difference than the TV devices. During braking, different strategies exist to blend the wheel torque applied by electric motors and friction brakes [103], [104]. In series braking, the electric motor applies a braking torque up to a defined threshold; friction braking is only employed if the braking torque request is too large and the electric motor cannot meet the braking request. In parallel braking, regenerative braking and friction brakes are used simultaneously; thus, the ratio of regenerative braking torque over friction braking torque is independent of the braking wheel torque request. Series braking allows to maximize energy recovered during braking but is more complex to implement than parallel braking and requires a pedal feel simulator.

In addition to coordinating the actuator to follow the desired wheel torques, the coordination layer is also responsible for preventing excessive longitudinal slip ratio if the tire saturation constraint of

the 'Optimal Wheel Controls Allocation' block does not guarantee wheel stability (for instance, if the constraint is violated or if the maximum friction coefficient is over-estimated). Proper coordination between the different actuators must be ensured to guarantee reasonable slip control, especially during ABS events. Regenerative braking is usually deactivated during ABS event [105]; however, since electric motors promise faster and better control, many researchers have investigated integrated wheel slip control methods using both electric motors, especially IWEM, and friction brakes. Wang [106] designs a sliding mode controller for wheel slip and validates the algorithm in simulations; the controller is robust against uncertainties in vehicle parameters such as vehicle mass and effective wheel radius. De Castro et al. [107] replaces the sliding mode controller with a nonlinear controller obtained from input-output linearization; the allocation algorithm is formulated as a QPP with constraints on each actuator magnitude and rate saturation, the optimization cost is a weighted sum of torque and torque variation applied by the IWEM and EHB. In addition to the controller and allocation algorithm, De Castro provides a braking supervisor whose role is to define several operating modes (e.g., series or parallel braking, IWEM failure) by modifying the weights of the cost function.

6.1 Wheel Slip Stability Analysis

A simple model based on the single-wheel model is provided to understand the wheel slip dynamics; only the longitudinal dynamic is considered, and the lateral dynamic is ignored. The model has two states: the wheel speed ω and the vehicle speed v_x; the input is the torque applied on the wheel. Equations of motion are,

$$\dot{v_x} = \frac{f_x}{m} \tag{6.1}$$

$$\dot{\omega} = \frac{1}{J_{w,eq}}\Big(\tau - r_w f_x\Big) \tag{6.2}$$

where m is the quarter-car mass, $J_{w,eq}$ is the lumped wheel and motor inertia,[1] r_w is the wheel radius, and f_x is the tire longitudinal force. The longitudinal tire force is a nonlinear function of the

[1]The wheel, shaft, and motor inertias are lumped together to reduce the order of the controller derived from this model. For instance with the quad-motor drivetrain the equivalent inertia is $J_{w,eq} = J_w + J_{mot}G_{mot}^2$ with J_w the wheel inertia, J_{mot} the motor inertia, and G_{mot} the motor gearing ratio.

slip ratio s_x and it is assumed to be a linear function of the normal force f_z, i.e. $f_x = \mu(s_x) f_z$. The slip ratio is defined as,

$$s_x = \frac{r_w \omega - v_x}{\max(r_w \omega, v_x)} \tag{6.3}$$

When the vehicle is braking, $s_x \leq 0$ or $r_w \omega \leq v_x$. After differentiating the slip definition (6.3), the dynamics of the system can be formulated as a first-order system with the slip as the only state,

$$\dot{s}_x = \frac{r_w}{J_{w,eq} v_x} \Big[\tau - \Big(1 + \frac{J_{w,eq}}{m r_w^2} (1 + s_x) \Big) r_w f_x \Big] \tag{6.4}$$

When the vehicle is accelerating, $s_x \geq 0$ or $r_w \omega \geq v_x$, the slip dynamics is described by,

$$\dot{s}_x = \frac{r_w (1 - s_x)}{v_x} \Big[\frac{1}{J_{w,eq}} (1 - s_x)(\tau - r_w f_x) - \frac{f_x}{m r_w} \Big] \tag{6.5}$$

The time-derivative of the longitudinal slip is a nonlinear function of the wheel slip. A linear system analysis is conducted at the steady-state operating points (s_{x0}, τ_0), moreover, the dynamics associated with the longitudinal vehicle velocity v_x is assumed to be slower than the slip dynamics and the longitudinal velocity is treated as a constant parameter $v_x = v_{x0}$. For the system to be at steady-state with slip s_{x0}, the wheel torque τ_0 must be defined as follows,

$$\tau_0 = \begin{cases} r_w \mu(s_{x0}) f_z \Big(1 + \frac{J_{w,eq}}{m r_w^2} (1 + s_{x0}) \Big), & \text{if } s_{x0} \leq 0 \\ r_w \mu(s_{x0}) f_z \Big(1 + \frac{J_{w,eq}}{m r_w^2} \frac{1}{1 - s_{x0}} \Big), & \text{if } s_{x0} > 0 \end{cases} \tag{6.6}$$

After linearization, the slip equation of motion becomes $\dot{\tilde{s}}_x = A \tilde{s}_x + B \tilde{\tau}$, where $A = \frac{\partial \dot{s}_x}{\partial s_x}|_{(s_{x0}, \tau_0)}$ and $B = \frac{\partial \dot{s}_x}{\partial \tau}|_{(s_{x0}, \tau_0)}$ are the Jacobian matrices and where $\tilde{s}_x = s_x - s_{x0}$ and $\tilde{\tau} = \tau - \tau_0$ are the perturbed variables after linearization. The Jacobian matrices of the linearized slip model are given by:

$$A = \begin{cases} -\frac{r_w^2 f_z}{J_{w,eq} v_{x0}} \Big[\frac{J_{w,eq}}{m r_w^2} (\mu_0 + (1 + s_{x0}) \mu_0') + \mu_0' \Big], & \text{if } s_{x0} \leq 0 \\ -\frac{r_w^2 f_z}{J_{w,eq} v_{x0}} \Big[\frac{J_{w,eq}}{m r_w^2} (\mu_0 + (1 - s_{x0}) \mu_0') + (1 - s_{x0})^2 \mu_0' \Big], & \text{if } s_{x0} > 0 \end{cases} \tag{6.7}$$

$$B = \begin{cases} \frac{r_w}{J_{w,eq} v_{x0}} & \text{if } s_{x0} \leq 0 \\ \frac{r_w}{J_{w,eq} v_{x0}} (1 - s_{x0})^2 & \text{if } s_{x0} > 0 \end{cases} \tag{6.8}$$

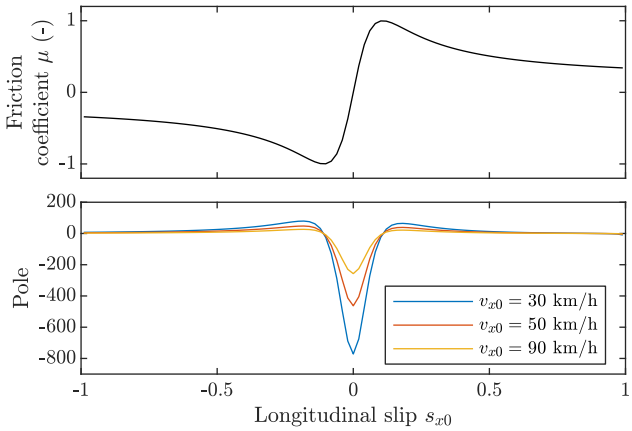

Figure 6.1: Road friction coefficient and pole of the single-wheel model versus the longitudinal slip operating point

where $\mu_0 = \mu(s_{x0})$ and $\mu'_0 = \frac{\partial \mu}{\partial s_x}|_{s_{x0}}$ are respectively the value of the friction coefficient and the slope of the friction coefficient evaluated at the operating point s_{x0}. Assuming that $s_{x0} \ll 1$ and given that $J_{w,eq} \ll m r_w^2$, for both braking and acceleration, the pole is given by $A \sim -\frac{r_w^2 f_z}{J_{w,eq} v_{x0}} \mu'_0$. Therefore, the system is locally asymptotically stable when $\mu'_0 > 0$, i.e. when the tire operates in the *linear region*. This is illustrated by Figure 6.1 which shows a friction curve and the pole of the linearized system.

6.2 Actuator Dynamics

The actuator dynamics are represented by the transfer function G_{act} such that the total wheel torque is $\tau = G_{act}\tau_{act}$ where τ_{act} are the actuator torques, this transfer function will be used to derive controllers. The electric motor is modeled by a first-order low-pass filter of cutoff frequency $\frac{1}{\tau_{EM}}$ and the hydraulic brakes are modeled by Equation (2.77). With the quad-motor drivetrain, the actuator dynamics is given in Equation (6.9).

$$\tau = G_{act}\tau_{act} = \begin{bmatrix} \frac{1}{\tau_{EM}s+1} & \frac{k_{cal}}{m_{p,eq}s^2+b_{p,eq}s+k_{cal}} \end{bmatrix} \begin{bmatrix} \tau_{mot} \\ \tau_{bk} \end{bmatrix} \tag{6.9}$$

where τ_{EM} is the electric motor time constant, $m_{p,eq} = m_p + S_p^2 I_l$ and $b_{p,eq} = b_p + S_p^2 I_l$ are the equivalent piston and fluid mass and damping coefficient, and k_{cal} is the caliper stiffness.

6.3 Drivetrain and Brake Coordination Control Architecture

Figure 6.2 shows the proposed control architecture for regulating the wheel slip and coordinating the drivetrain and brake actuators. Since the four wheels are decoupled with the quad-motor topology, this control structure is used independently at each wheel for this topology; for the dual-motor and eAWD topology, a coupling occurs between the left and right wheels, so this control structure can only be used independently at each axle.

Several controllers are designed to implement ABS, TCS, they define the wheel torque τ_w to apply in order to follow a wheel speed target ω_{ref}. The 'Wheel Slip Supervisor' block decides whether to use the ABS or TCS slip controller or the torque defined by the abstract layer based on the wheel slip and wheel torque applied. The 'Control Allocation' block maps the four wheel torques output by the 'Wheel Slip Supervisor' to actuator signals $\tau_{act}^T = [\tau_{mot}^T \quad \tau_{bk}^T]$ where τ_{mot} denotes drivetrain torques and τ_{bk} denotes the torque applied by the friction brakes; e.g., τ_{mot} denotes the four electric motor torque commands for the quad-motor topology, it corresponds to the two motor torque commands for the dual-motor drivetrain, and the two traction motor and the two torque vectoring device torque commands for the eAWD drivetrain; for all topologies, τ_{bk} denotes the four friction brake wheel torque requests. The 'Control Allocation' block considers the actuator dynamics and saturation. It implements a daisy-chain allocation represented by the 'Algebraic Allocation' block, which defines the desired actuator distribution τ_{des} based on the actuator saturation limits and the desired wheel torques. A Smith-McMillan-based nullspace allocator (see Section 3.3.1) is used to make sure that the dynamic allocation does not destabilize the feedback loop by making the control allocation invisible at the wheel torque level.

The ABS and TCS slip controllers are implemented with SISO Youla parameterized model-based controllers, both ABS and TCS controllers are implementing the same controllers, only their setpoints ω_{ref} are different. Since the tire model is nonlinear and the slip controllers are implementing linear controllers, it would be necessary to define several controllers–one for each operating point (i.e., wheel slip) at which the wheel-tire model is linearized–and switch between the different controllers. Moreover, anti-windup compensators would be needed to ensure bumpless transfer, and their design can be difficult if the model is not marginally stable (i.e., in the tire saturation region). Instead, the ABS and TCS slip controllers implements two controllers labeled 'First spin/dip' and 'Closed-loop'

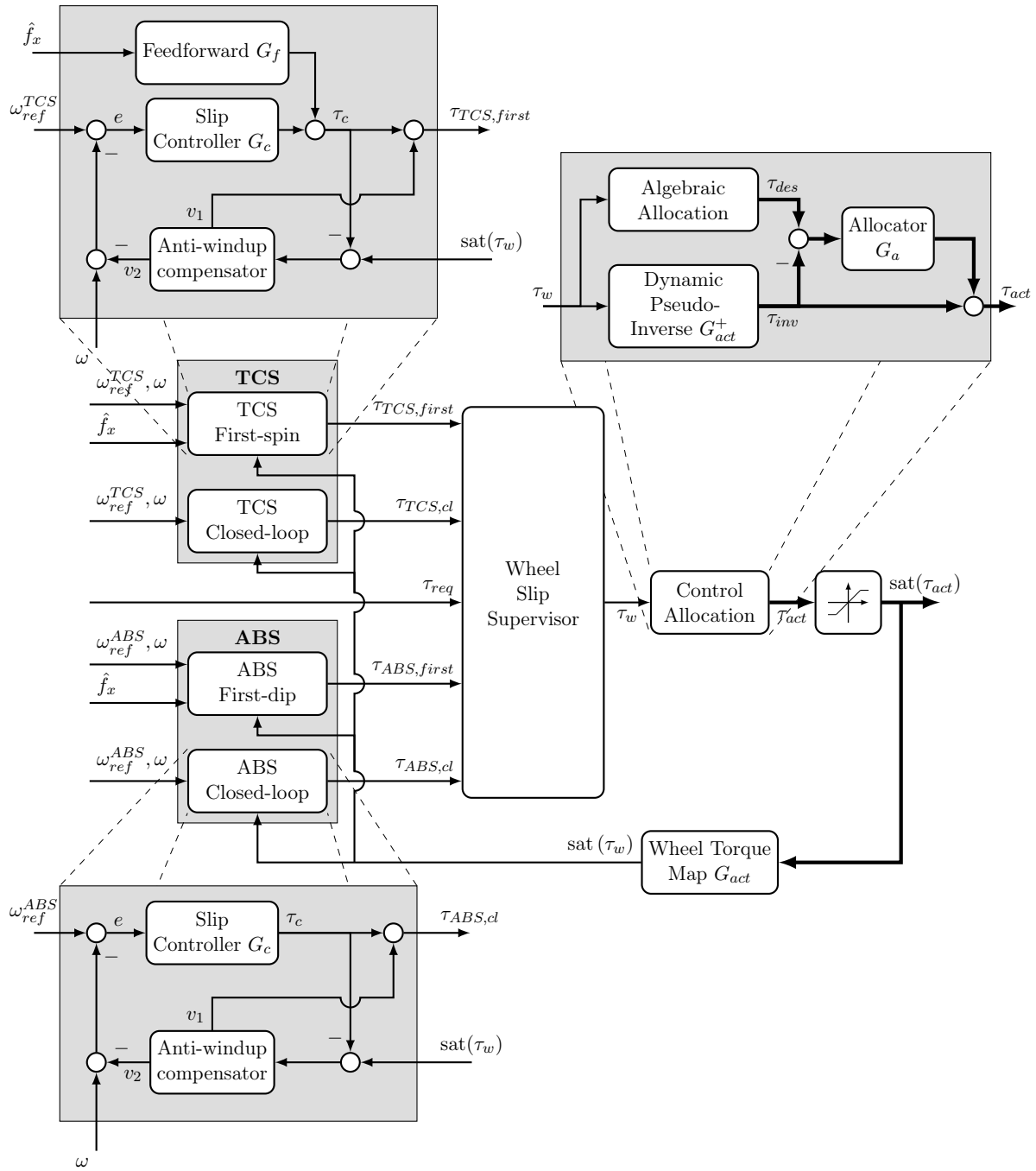

Figure 6.2: Control architecture for drivetrain and brake coordination and slip control of a single wheel. Thick lines represent actuator multichannel signals, thin lines represent wheel scalar signals. The architecture is illustrated for the quad-motor drivetrain. With the dual-motor and eAWD drivetrains, additional feedforward blocks should be inserted in the 'First spin/dip' and 'Closed-loop' ABS and TCS slip controllers to decouple the left and right wheel speeds (see Section 6.5.1 and Figure 6.5); the 'Control Allocation' should be given the left and right wheel torque requests τ_w.

controllers derived after two marginally stable models. The 'First dip/spin' controller design is based on a model where the longitudinal tire force is treated as a disturbance;[2] hence it does not use a tire model. Instead, the controller uses a disturbance rejection scheme and an estimate of the longitudinal tire force $\hat{f}_x$, which is computed using a YCOO developed in [55]. Because the estimate of the tire force may not be perfect, the 'First spin/dip' controller cannot ensure perfect tracking; its goal is only to bring the wheel slip back to the linear tire region. The 'Closed-loop' controller is based on a model that includes a tire map linearized in the stable region of the tire near the peak of friction.[3] It ensures perfect tracking of the wheel slip ratio as long as the wheel slip is near the controller linearization point. Thus, the strategy of the ABS and TCS slip controllers to regulate the wheel slip is: first, use the 'First dip/spin' controller to bring the wheel slip near the peak of friction independently of the initial wheel slip; second, switch to the 'Closed-loop' controller once the wheel slip is inside the controller's operating range to ensure good tracking. The design of the slip controllers and the anti-windup compensators is further explain in Sections 6.5.1 and 6.5.2.

The 'Wheel Slip Supervisor' block is shown in Figure 6.3, it is implemented as a finite-state machine. When the longitudinal slip ratio and wheel torque become smaller than the threshold $s_{x,ABS}$ and τ_{ABS}, the ABS slip controller becomes active. Similarly, if the slip ratio and wheel torque are too big, the TCS becomes active. The slip controllers are deactivated when the wheel torque request of the abstract layer becomes smaller than the torque applied by the slip controllers. To take the vehicle to a complete stop, the ABS controller must be deactivated below a threshold vehicle speed; the ABS slip controller cannot guarantee closed-loop stability at low speed due to poor velocity estimation at low speed and to a large unstable pole in the plant. Thus, the ABS makes a distinction between high-speed and low-speed.

When ABS or TCS are engaged, the slip control switch from the 'Off' state to the 'First dip/spin' mode for a predefined period before switching to the 'Closed-loop' state or reverting to the 'Off' state if the supervisor switches back to the torque control mode.

[2]The model used to design the 'First spin/dip' controller is marginally stable; thus, an anti-windup compensator can be easily designed.
[3]The model is asymptotically stable.

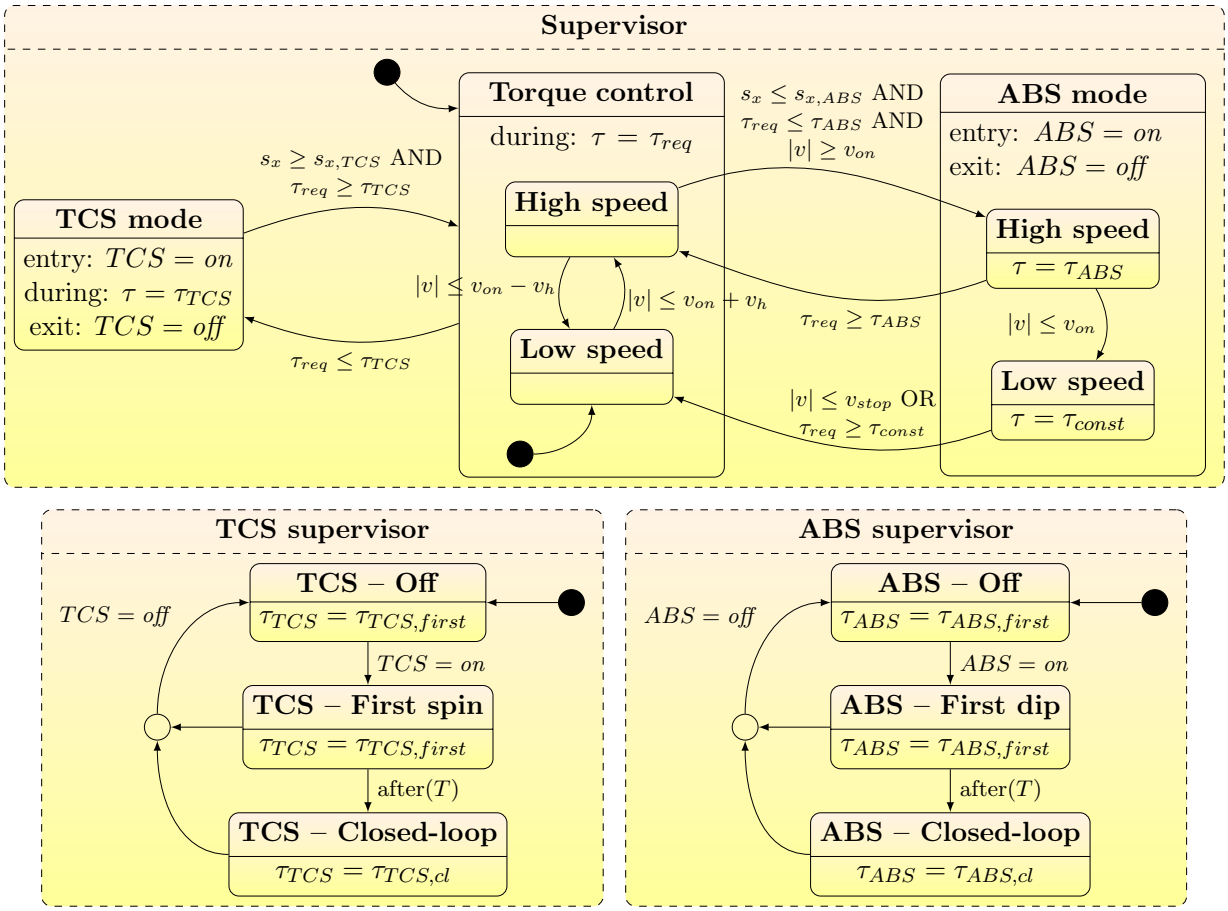

Figure 6.3: Finite state machine of the 'Wheel Slip Supervisor' block

6.4 Dynamic Control Allocation

6.4.1 Dynamic Pseudo-Inverse

The Smith-McMillan decomposition generalizes the concept of poles and zeros to multivariable systems; it also defines a basis for decoupling the system, which facilitates the controller design. Using the Smith-McMillan decomposition, the system is represented by $M_P = U_L G_{act} U_R$, and U_L and U_R are unimodular polynomial matrices. With the quad-motor drivetrain:

$$M_{P,act} = \begin{bmatrix} \frac{m_{p,eq}\tau_{EM}}{(\tau_{EM}s+1)(m_{p,eq}s^2+b_{p,eq}s+k_{cal})} & 0 \end{bmatrix}, \tag{6.10}$$

$$U_L = 1, \quad U_R = \begin{bmatrix} \frac{m_{p,eq}\tau_{EM}^3}{k_{cal}\tau_{EM}^2 - b_{p,eq}\tau_{EM} + m_{p,eq}} & s + \frac{1}{\tau_{EM}} \\ -\frac{m_{p,eq}\tau_{EM}(b_{p,eq}\tau_{EM} + m_{p,eq}(\tau_{EM}s-1))}{k_{cal}(k_{cal}\tau_{EM}^2 - b_{p,eq}\tau_{EM} + m_{p,eq})} & -\frac{m_{p,eq}s^2 + b_{p,eq}s + k_{cal}}{k_{cal}\tau_{EM}} \end{bmatrix} \tag{6.11}$$

Because the system is over-actuated, we define the matrix $\underline{M}_{P,act}$ as the full-rank square matrix

extracted from $M_{P,act}$ such that $M_{P,act} = [\underline{M}_{P,act} \quad 0]$. The 'Control Allocation' block maps the wheel torque to the actuator signals, it considers the actuator dynamics and uses a dynamic pseudo-inverse matrix defined from the Smith-McMillan decomposition of G_{act}:

$$G_{act}^{+} = U_R \begin{bmatrix} \underline{M}_{P,act}^{-1} \\ 0 \end{bmatrix} U_L \tag{6.12}$$

When G_{act} is strictly proper, G_{act}^{+} is not proper, and unstable zeros of G_{act} are unstable poles of G_{act}^{+}. If the system G_{act} is strictly proper or has unstable zeros, G_{act}^{+} is multiplied by a transfer function $w(s)$ of unit gain to make G_{act}^{+} proper and cancel its unstable poles. With the quad-motor, one can select the transfer function $w(s) = k_{cal}/((\tau_{EM}s+1)(m_{p,eq}s^2+b_{p,eq}s+k_{cal}))$. By construction, we have:

$$G_{act}G_{act}^{+} = w(s)I \text{ and } G_{act}^{+}G_{act} = w(s) \begin{bmatrix} I & 0 \\ 0 & 0 \end{bmatrix} \tag{6.13}$$

The dynamic pseudo-inverse is used to define a control distribution from the wheel torque τ_w requested by the 'Wheel Slip Supervisor': $\tau_{inv} = G_{act}^{+}\tau_w$.

6.4.2 Nullspace Allocator

The slip controllers define a control distribution to stabilize the wheel slip; the actuators have variable saturation levels: at high speed, the maximum torque the motor can apply depends on the motor speed, whereas at low speed, the maximum torque corresponds to the base torque; the friction brake can only apply negative wheel torque. Moreover, series braking is more efficient than parallel braking but requires modifying the ratio of regenerative braking torque over friction braking torque. Variable saturation levels, series braking, and deteriorated modes (e.g., if the electric motor becomes faulty) forces to use of a dynamic control allocation and to modify the actuator distribution defined by the controller, the Smith-McMillan-based nullspace allocator presented in Section 3.3.1 is used to modify the control distribution without affecting the closed-loop response.

The plant model can be written as G_wG_{act} where G_w is a scalar transfer function mapping the wheel torque τ to the wheel speed ω (see Section 6.1) and G_{act} is a non-square matrix mapping the actuator commands τ_{act} to the wheel torque τ (see Section 6.2). Since the matrix G_w is square

and has full rank, the nullspace allocator is designed based on the matrix G_{act} representing the actuator dynamics. With the quad-motor drivetrain, the right nullspace of the plant corresponds to the column space of the following matrix:

$$K_a = \begin{bmatrix} \tau_{EM}s + 1 \\ -\frac{m_{p,eq}s^2 + b_{p,eq}s + k_{cal}}{k_{cal}} \end{bmatrix} \tag{6.14}$$

The allocator is designed to follow the desired control distribution τ_{des} by minimizing the quadratic error $\|\tau_{act} - \tau_{des}\|_W^2$ with $W = I$, from Equation (3.9), the allocator is defined as:

$$G_a = \bar{G}_a w(s) = K_a (K_a^T W K_a)^{-1} K_a^T W w_a(s) \tag{6.15}$$

For the quad-motor drivetrain and with $w_a(s) = 1$, the nullspace allocator is defined as follows,

$$G_a = \begin{bmatrix} \frac{(\tau_{EM}s+1)^2}{(\tau_{EM}s+1)^2 + \left(\frac{m_{p,eq}s^2 + b_{peq,s} + k_{cal}}{k_{cal}}\right)^2} & -\frac{(\tau_{EM}s+1)\left(\frac{m_{p,eq}s^2 + b_{p,eq}s + k_{cal}}{k_{cal}}\right)}{(\tau_{EM}s+1)^2 + \left(\frac{m_{p,eq}s^2 + b_{peq,s} + k_{cal}}{k_{cal}}\right)^2} \\ -\frac{(\tau_{EM}s+1)\left(\frac{m_{p,eq}s^2 + b_{p,eq}s + k_{cal}}{k_{cal}}\right)}{(\tau_{EM}s+1)^2 + \left(\frac{m_{p,eq}s^2 + b_{peq,s} + k_{cal}}{k_{cal}}\right)^2} & \frac{\left(\frac{m_{p,eq}s^2 + b_{peq,s} + k_{cal}}{k_{cal}}\right)^2}{(\tau_{EM}s+1)^2 + \left(\frac{m_{p,eq}s^2 + b_{peq,s} + k_{cal}}{k_{cal}}\right)^2} \end{bmatrix} \tag{6.16}$$

6.4.3 Drivetrain and Brake Algebraic Allocation

Several actuators can be used to follow the wheel torque request from the abstract layer or slip controllers. The electric motors allow for faster, more power-efficient, and more accurate controls than the EHB and eLSD, but they cannot generate as much braking torque. Moreover, with the dual-motor drivetrain, electric motors cannot apply a left-to-right TV. However, with the eAWD drivetrain, a left-to-right TV can be generated either by the TV device (i.e., the TV motor on the front axle or eLSD on the rear axle) or by a brake-based torque difference. The additional DoF due to over-actuation are used to improve the power efficiency of the vehicle. The 'Algebraic Allocation' block defines the steady-state control distribution to apply for a given wheel torque, enforcing actuator saturation limits and neglecting the actuator dynamics. The Smith-McMillan allocator ensures the tracking of the control distribution in the ℓ_2 sense while maintaining internal stability and addressing actuator dynamics.

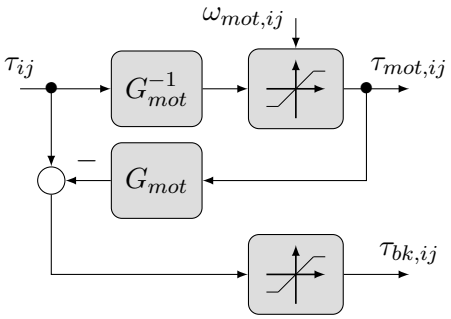

(a) Quad-motor drivetrain allocation at the ij wheel

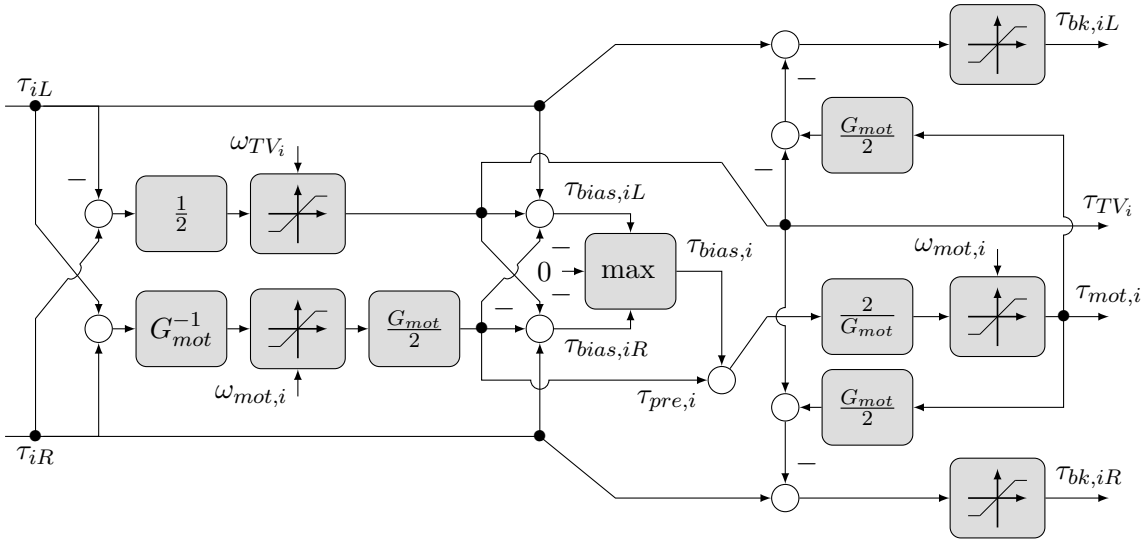

(b) Dual-motor and eAWD drivetrains allocation at the i axle

Figure 6.4: Daisy-chain control allocation coordinating the drivetrain and friction brakes

Quad-motor Drivetrain

With the quad-motor drivetrain, the wheel torque are decoupled at each wheel and depends on the torque generated by the wheel motor and the friction brake torque. In steady-state, the wheel torque is given by $\tau_{ij} = G_{mot}\tau_{mot,ij} + \tau_{bk,ij}$ where $\tau_{mot,ij}$ is the torque generated by the motor, $\tau_{bk,ij}$ is the torque applied by the friction brake, and G_{mot} is the electric motor gearing ratio. A daisy-chain allocation is employed (see Figure 6.4a) since the regenerative braking is more efficient than friction brakes, the electric motor are used up to their saturation limits, friction brakes assist the electric motor if necessary to provide additional braking torque. Given the wheel torque request τ_{ij}, the electric motor torque is defined as $\tau_{mot,ij} = \text{sat}_{mot,ij}(\tau_{ij})$ and the friction brake torque is $\tau_{bk,ij} = \text{sat}_{bk,ij}(\tau_{ij} - \tau_{mot,ij})$, where $\text{sat}_{mot,ij}$ is the speed dependent electric motor torque saturation and $\text{sat}_{bk,ij}$ denotes the EHB torque saturation. This control allocation is carried out at each wheel

independently.

Dual-motor and eAWD Drivetrains

With the dual-motor and eAWD drivetrains, the front and rear axles are decoupled but the torque applied on the left and right wheels of each axles are not independent, the wheel torque is $\tau_{ij} = \frac{G_{mot}}{2}\tau_{mot,i} \pm \tau_{TV_i} + \tau_{bk,ij}$. The control allocation tracks two targets: the left and right wheel torque τ_{iL} and τ_{iR}; the targets can be reformulated as an axle torque target $\tau_{tot,i} = \tau_{iL} + \tau_{iR}$ and the axle torque difference $\tau_{TV_i} = \frac{1}{2}(\tau_{iR} - \tau_{iL})$. The torque difference can be generated by the TV device or by applying different brake torque on each side of the vehicle, the latter option has the drawback of generating a negative axle torque bias while the TV device generates a torque difference without modifying the axle torque, this torque bias deteriorates the vehicle efficiency, hence the allocation prioritize the TV device to generate a torque difference τ_{TV_i} and electric traction motor to generate the axle torque.

The functions sat_{TV_i}, $\text{sat}_{mot,i}$, and $\text{sat}_{bk,ij}$ denote respectively the magnitude saturation of the TV device, electric traction motor, and friction brakes; note that the torque saturation of the electric motors and TV device are speed dependent. Variables τ_{iL} and τ_{iR} denote the left and right wheel torque request from the abstract layer. Since the electric traction motor and the torque vectoring device are more efficient than the friction brakes, the axle torque and the left-to-right TV torques should be respectively allocated first to the traction motor and to TV device up to their saturation limits. However, filling the remaining left and right torque requests using the friction brakes does not guarantee perfect tracking. Indeed, if the axle torque request is positive and the TV device is saturating, the request on the side with the highest torque cannot be met since the friction brakes can only apply negative torques. Moreover, the friction-based torque applied on the side with the lowest torque introduces an axle torque bias which decreases the total axle torque, deteriorating the tracking of the axle torque request. The traction motor must compensate the bias introduced by the friction-based axle torque to perfectly track both the TV and axle torques. Pre-compensation, the TV device torque is set as $\tau_{TV_i} = \text{sat}_{TV_i}(\frac{1}{2}(\tau_{iR} - \tau_{iL}))$; the axle torque is allocated only to the electric traction motor and $\tau_{pre,i} = \frac{G_{mot}}{2}\,\text{sat}_{mot,i}\,(G_{mot}^{-1}(\tau_{iL} + \tau_{iR}))$ corresponds to the wheel torque applied by the traction motor, the friction brakes need to generate $\tau_{bias,ij} = \tau_{ij} - (\tau_{pre} \pm \tau_{TV_i})$ to track the target which result in a torque bias $\tau_{bias,i} = \max(0, \tau_{bias,iL}, \tau_{bias,iR})$. Post-compensation, the bias is added

to the motor torque command $\tau_{mot,i} = \text{sat}_{mot,i}\left(\frac{2}{G_{mot}}(\tau_{pre,i} + \tau_{bias,i})\right)$, the TV torque command τ_{TV_i} is not modified, and the brake torque request are adjusted $\tau_{bk,ij} = \text{sat}_{bk,ij}\left(\tau_{ij} - (\frac{G_{mot}}{2}\tau_{mot,i} \pm \tau_{TV_i})\right)$.

The control allocation is depicted in Figure 6.4b, it uses the traction motor and the TV device up to their saturation limits, friction brakes assist if additional braking torque is required. The allocation is carried at each axle independently; both drivetrain topologies use the same daisy-chain control allocation; with the dual-motor drivetrain, the torque difference $\tau_{TV_i} = 0$.

6.5 Wheel Slip Controller

6.5.1 Slip Controller Design

In [108], a Youla parameterized controller design for slip control is compared to a first-order sliding mode controller. Although the sliding mode controller guarantees stability based on Lyapunov arguments, finite-time convergence, and robustness to parametric uncertainties, its design is more complex than the Youla controller; moreover, the Youla controller does not suffer from chattering and guarantees perfect tracking. $\mathcal{H}_\infty$ or μ-synthesis could also be used to derive a linear controller and optimize the controller's robust performance, but these methods usually yield a high-order controller; Youla parameterization is preferred for this application since it gives a lower order linear controller than $\mathcal{H}_\infty$ and μ-synthesis while showing good robustness properties.

Youla parameterization is a loop-shaping control design method, the controller G_c is defined from desired closed-loop transfer functions and a model of the system G_p. By selecting three transfer functions–the closed-loop transfer function T_y, the sensitivity function $S_y = I - T_y$, and the Youla transfer function $Y = G_c S_y$–one can ensure good disturbance and sensor noise rejection. When designing the controller, interpolation conditions on the rational functions T_y and S_y are enforced such that the transfer functions Y, S_y, T_y, and $S_y G_p$ are stable, guaranteeing internal stability. For any unstable pole p with multiplicity k_p and for any unstable zero z with multiplicity k_z, the interpolation conditions are:

$$T_y(s = p) = 1 \text{ and } \left.\frac{\mathrm{d}^k S_y}{\mathrm{d}s^k}\right|_{s=p} = 0 \quad \forall k \in [\![0, k_p - 1]\!] \tag{6.17}$$

$$S_y(s = z) = 1 \text{ and } \left.\frac{\mathrm{d}^k T_y}{\mathrm{d}s^k}\right|_{s=z} = 0 \quad \forall k \in [\![0, k_z - 1]\!] \tag{6.18}$$

If the transfer functions S_y and T_y respect the previous interpolation conditions, the feedback loop combining the controller G_c and the plant G_p is internally stable where G_c is defined as $G_c = YS_y^{-1}$.

First Spin and First Dip Slip Control

The 'First spin' and 'First dip' slip controllers are based on the wheel inertia (6.2) and consider the tire force as a disturbance, the wheel speed is $\omega = G_w\tau + G_d f_x$ where $G_w = \frac{1}{J_{w,eq}s}$ and $G_d = \frac{-r_w}{J_{w,eq}s}$. The 'Control Allocation' block inside the feedback loop add additional dynamics, the dynamic allocation is invisible thanks to the Smith-McMillan nullspace allocator, however, the pseudo-inverse block adds the dynamic $w(s)$ to the system. Indeed, the wheel torque applied at the wheel is $\tau = G_{act}\tau_{act}$ where $\tau_{act} = \tau_{inv} + G_a(\tau_{des} - \tau_{inv})$ is the sum outputs of the pseudo-inverse G_{act}^+ and the nullspace allocator (see Figure 6.2), so $\tau = G_{act}\tau_{act} = G_{act}G_{act}^+\tau_w$ since the nullspace allocator is designed such that $G_{act}G_a = 0$; finally, $\tau = w(s)\tau_w$ where τ_w is the controller output.

The plant model to design the controller is $G_p = G_w w(s)$, the plant G_p has an unstable pole at $p = 0$, the interpolation condition $S_y(0) = 0$, or equivalently $T_y(0) = 1$, guarantees internal stability. The closed-loop transfer function is selected to be a second-order Butterworth filter of unit gain and crossover frequency ω_0, additional poles τ_p are added to ensure the controller is proper.

$$T_{des} = \frac{\omega_0^2}{(s^2 + 2\zeta\omega_0 s + \omega_0^2)(\tau_p s + 1)^2} \tag{6.19}$$

To obtain $T_y = T_{des}$, the sensitivity function must be $S_y = 1 - T_{des}$ and the Youla transfer function Y must satisfy $YG_p = T_{des}$, one can obtain the controller transfer function from $G_c = YS_y^{-1}$. This yields the controller $G_c = U_R M_Y (I - M_P M_Y)^{-1} U_L$. For the quad-motor drivetrain, the controller is:

$$G_c = \frac{J_{w,eq}s\omega_0^2}{w(s)[(s^2 + 2\zeta\omega_0 s + \omega_0^2)(\tau_p s + 1)^2 - \omega_0^2]} \tag{6.20}$$

For a system with disturbance defined by $y = G_p u + G_d d$, modifying the control input by $u \leftarrow u - G_p^{-1}G_d d$ cancels the effects of the disturbance at the output. The first spin/dip controller implements this disturbance rejection scheme to cancel the effect of the tire force, the wheel torque is modified by $\tau \leftarrow \tau - G_w^{-1}G_d\hat{f}_x$. With the quad-motor drivetrain, this yields the following feedforward

transfer function, an extra pole τ_d is added to prevent inserting noise in the control loop:

$$G_f = -G_w^{-1} G_d = \frac{r_w}{\tau_d s + 1} \tag{6.21}$$

Closed-loop Slip Control

The 'First spin' and 'First dip' controllers are independent of the tire model; they can stabilize the system independently of the operating condition since the model does not need to be linearized. However, it relies on a disturbance rejection scheme (implemented as a feedforward control) and the tire force estimation; therefore, it cannot ensure perfect tracking. Once the 'First spin' and 'First dip' controllers bring the wheel slip ratio close to the operating point of the 'Closed-loop' controller, the 'Closed-loop' controller takes over the wheel slip control. This controller does not use an estimate of the tire force; instead, its design is based on a tire model linearized near the peak friction.

The wheel dynamics is defined by the linearized wheel model presented in Section 6.1, the wheel dynamics is represented by $G_w = \frac{B}{s-A}$ where A and B are given in Equations (6.7) and (6.8) and the plant model is defined as $G_p = G_w w(s)$. The system is linearized near the peak of friction but in the linear region, hence $A < 0$. The system has no unstable pole and zero so there is no interpolation condition needed to enforce internal stability, to obtain good tracking to step input, the closed-loop transfer function must satisfy $T_y(0) = 1$. The closed-loop transfer function is defined as Equation (6.19) which yields the following controller:

$$G_c = \frac{(s - A)\omega_0^2}{B w(s)[(s^2 + 2\zeta\omega_0 s + \omega_0^2)(\tau_p s + 1)^2 - \omega_0^2]} \tag{6.22}$$

Decoupling with Dual-Motor and eAWD Drivetrains

The slip controllers are SISO controllers; each filter is responsible for preventing excessive slip at a single wheel and assumes no coupling with other wheels; this is true for the quad-motor drivetrain but not for the dual-motor and eAWD topologies. For instance, after neglecting the shaft compliance

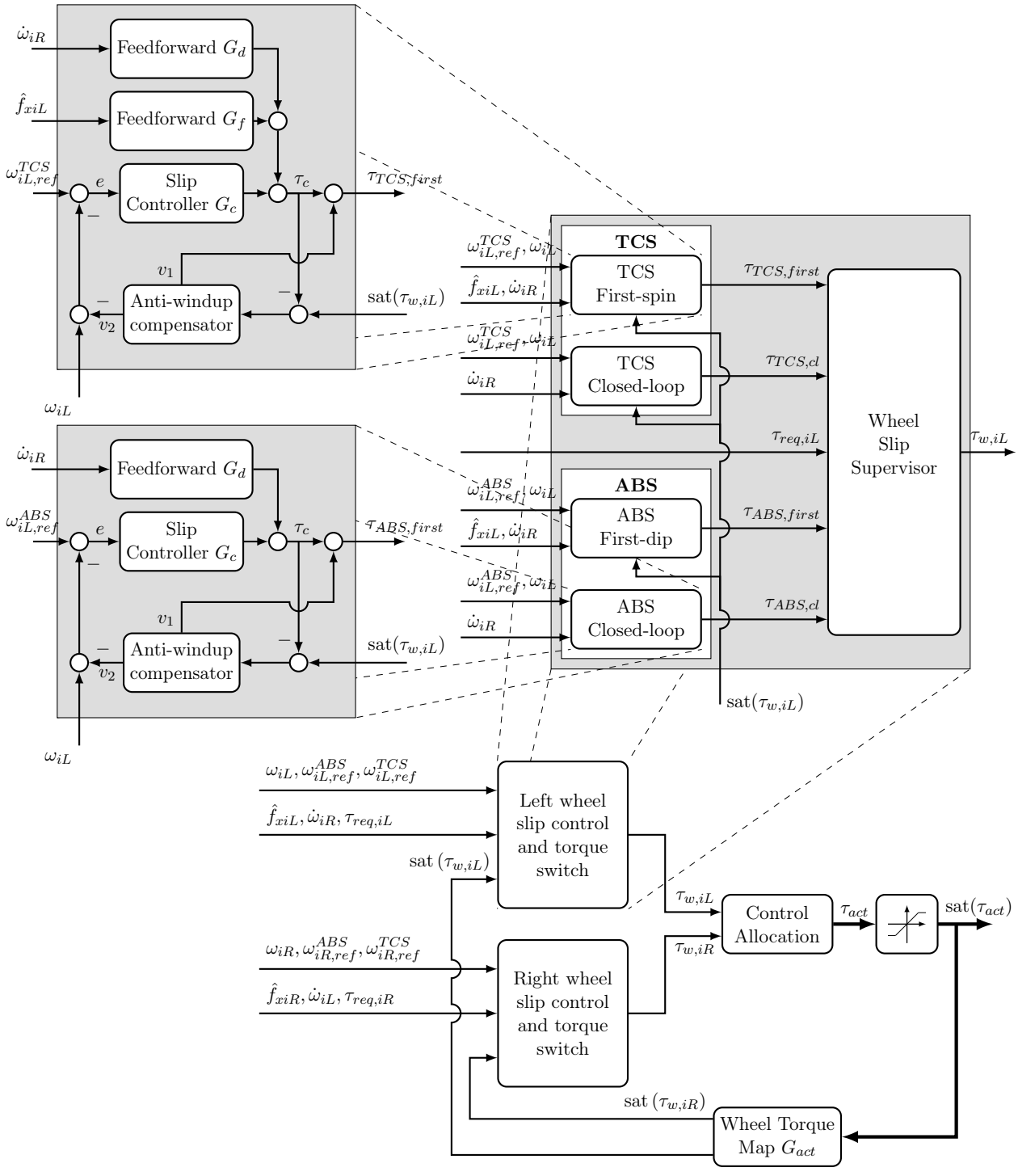

Figure 6.5: Control architecture for drivetrain and brake coordination and slip control of a single axle for the dual-motor and eAWD drivetrains. The structure of the 'Control Allocation' block remains the same as one in Figure 6.2; but it must assign the two wheel torques $\tau_{w,iL}$ and $\tau_{w,iR}$.

of the dual-motor drivetrain, one can obtain the following equation of motion:

$$\left(J_w + \frac{G_{mot}^2}{4} J_{mot}\right) \dot{\omega}_{iL} + \frac{G_{mot}^2}{4} J_{mot} \dot{\omega}_{iR} = \tau_{bk,iL} - r_w f_{xiL} + \frac{G_{mot}}{2} \tau_{mot} \tag{6.23a}$$

$$\frac{G_{mot}^2}{4} J_{mot} \dot{\omega}_{iL} + \left(J_w + \frac{G_{mot}^2}{4} J_{mot}\right) \dot{\omega}_{iR} = \tau_{bk,iR} - r_w f_{xiR} + \frac{G_{mot}}{2} \tau_{mot} \tag{6.23b}$$

The terms $\frac{G_{mot}^2}{4} J_{mot}$ are not negligible and create a coupling between the left and right wheel speeds. In practice, it would be necessary to design a MIMO slip controller regulating both left and right wheels; however, only one wheel may require active slip control while the other wheel does not have excessive slip (e.g., a split-μ scenario). To avoid the need for multiple MIMO controllers implementing all possible combination of torque and slip controls, we instead use a disturbance rejection scheme to respectively cancel the cross-terms $\frac{G_{mot}^2}{4} J_{mot} \dot{\omega}_{iR}$ and $\frac{G_{mot}^2}{4} J_{mot} \dot{\omega}_{iL}$ in the state equation of ω_{iL} and ω_{iR}; the disturbance rejection scheme allows to use SISO slip controllers while decoupling the left and right side. Figure 6.5 shows the wheel slip control architecture for the dual-motor and eAWD. As can be seen from the figure, the disturbance rejection scheme decouple the control of the left and right wheels, allowing to reuse a similar control architecture to the one used with the quad-motor drivetrain.

6.5.2 Anti-Windup and Bumpless Transfer

Anti-windup compensator are added to the feedback loop to address the actuator saturation and to ensure bumpless transfer between the different modes. Given (A, B, C, D) a state-space realization of the plant, Zaccarian [109] proposes the following anti-windup compensator:

$$\dot{\zeta} = A\zeta + B(\text{sat}(\tau_w) - \tau_c) \tag{6.24a}$$

$$v_1 = K\zeta + L(\text{sat}(\tau_w) - \tau_c) \tag{6.24b}$$

$$v_2 = C\zeta + D(\text{sat}(\tau_w) - \tau_c) \tag{6.24c}$$

where ζ are the anti-windup compensator states, K is the compensator gain, $\text{sat}(\tau_w)$ is the torque applied at the wheel, τ_c is the torque command of the feedforward and feedback controllers, the compensator must be connected such that the torque command send to the control allocation is $\tau_w = \tau_c + v_1$ and the feedback controller input is $e = \omega - v_2$ (see Figure 6.2).

The design of the anti-windup compensator for slip controllers differs from the design of the anti-windup compensator used with the MIMO high-level controller (Section 5.2.1) since the former uses a gain $L \neq 0$. The gain L improves the anti-windup performance but creates an algebraic loop around the saturation block. The design of the anti-windup compensator assumes a marginally stable plant (A, B, C, D), hence the choice of linearization point for the closed-loop controller in the linear tire region; with a marginally stable plant, the gains K and L must be chosen such that there exists a symmetric positive definite matrix $P = P^T > 0$ and a diagonal positive definite matrix W so that:

$$\begin{bmatrix} A^T P + PA & PB + K^T W \\ B^T P + WK & L^T W + WL - 2W \end{bmatrix} < 0 \tag{6.25}$$

If the plant (A, B, C, D) is stable, choosing K and L such that Equation (6.25) is true guarantees that the closed-loop system with the anti-windup compensator is well-posed and stable. Among all possible solutions of (6.25), the gains (K, L) which minimizes the cost function $J = \int_0^\infty (\zeta^T Q_P \zeta + v_1^T R_P v_1)\,\mathrm{d}t$ can be obtained by solving the following Linear Matrix Inequality (LMI) system in (γ, Q, U, X_1, X_2) [109]

$$\underset{(\gamma,Q,U,X_1,X_2)}{\arg\min} \quad \gamma \tag{6.26a}$$

$$\text{subject to} \quad \begin{bmatrix} QA^T + AQ & BU + X_1^T \\ UB^T + X_1 & X_2^T + X_2 - 2U \end{bmatrix} < 0 \tag{6.26b}$$

$$\begin{bmatrix} \gamma I & I \\ I & Q \end{bmatrix} > 0 \tag{6.26c}$$

$$\begin{bmatrix} QA^T + AQ + BX_1 + X_1^T B^T & Q & X_1^T \\ Q & -Q_P^{-1} & 0 \\ X_1 & 0 & -R_P^{-1} \end{bmatrix} < 0 \tag{6.26d}$$

$$Q = Q^T > 0 \text{ and } U > 0 \text{ diagonal} \tag{6.26e}$$

and the compensator gains are obtained from $K = X_1 Q^{-1}$ and $L = X_2 U^{-1}$.

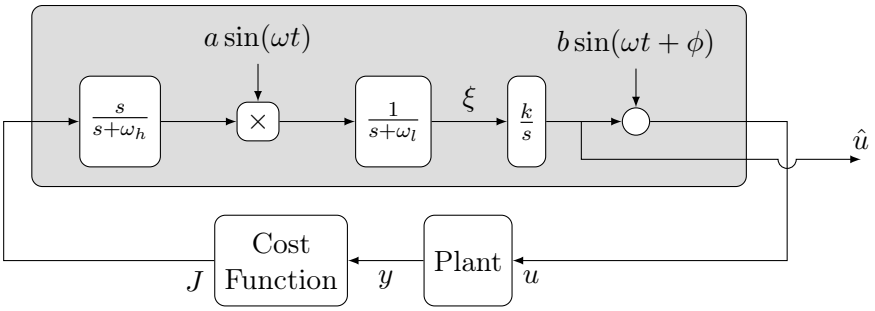

Figure 6.6: Extremum Seeking Control

6.5.3 Slip Reference Generation

The slip controllers rely on a target value for the wheel speed to maximize the longitudinal friction coefficient; unfortunately, the relation between wheel slip ratio to longitudinal friction coefficient is unknown and changes over time depending on the properties of the road and the tire. Extremum Seeking Control (ESC) is a model-free algorithm that tracks the maximum of a time-varying performance function. The algorithm is illustrated in Figure 6.6, the signal $b\sin(\omega t+\phi)$ is injected into the plant to probe the objective function; this is referred to as the modulation stage; if the change in the cost J is in-phase with the sine perturbation, the estimate of the extremum $\hat{u}$ should increase to track the extremum, if it is out-of-phase, it should decrease. The high-pass filter $\frac{s}{s+\omega_h}$ removes the low-frequency component of the cost J and keeps only the variation; the demodulation stage multiplies the variation of the cost by the sine wave such that the signal ζ is positive if both signals are in-phase and negative if they are out-of-phase. The integrator increases or decreases the estimate $\hat{u}$ based on the signal ζ to implement the desired update law. An optional low-pass filter $\frac{1}{s+\omega_l}$ is added to eliminate high-frequency measurement noise, and the gain of the integrator allows for tuning the rate of convergence.

ESC is used to find the longitudinal slip ratio $s_{ijx,ref}$ which yields the maximum friction coefficient, hence the cost $J=|\mu_{ijx}|$, the slip ratio is then converted to a wheel speed setpoint $\omega_{ij,ref}$ by modulating the wheel speed as follows $\omega_{ij,ref}=(1+s_{ijx,ref})\omega_{ij,0}$ where $\omega_{ij,0}$ is the wheel speed without slipping. The ESC strategy is running only when the slip controller is active; when slip controls are not active, the slip ratio yielding the maximum friction coefficient is not updated and kept at a constant guess value $s_{ijx,ref}=\pm 0.10$; when slip controls become active, the ESC integrator is initialized with the most recent slip ratio target.

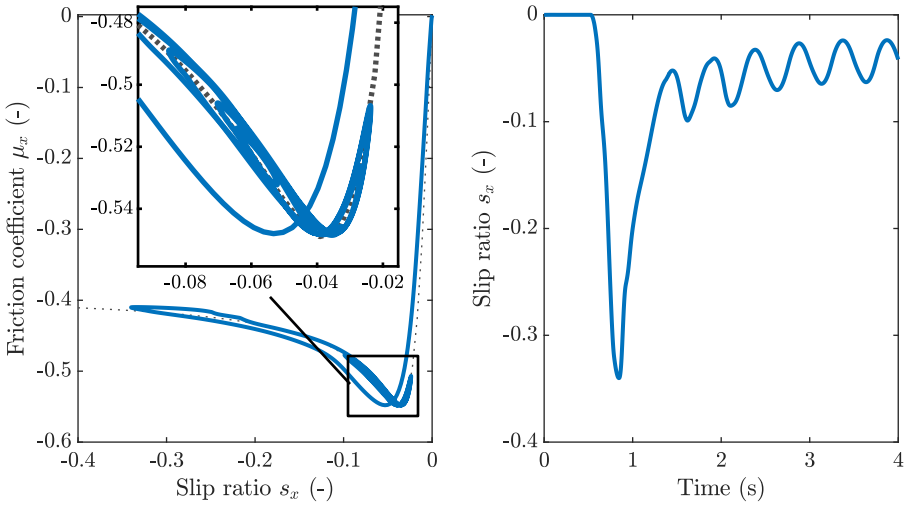

Figure 6.7: Longitudinal wheel slip and friction coefficient with slip controls. The dotted line shows the tire map.

6.6 Simulation Results

The performance of the slip controller is evaluated in a simulation in which the driver requests a braking step torque that exceeds the surface friction limit. The maximum friction coefficient estimation is disabled, and a wrong value of $\hat{\mu}_{max} = 1.0$ is provided such that the abstract layer applies excessive torque and the tire saturates, the actual maximum friction coefficient is $\mu_{max} = 0.55$.

Results are shown in Figures 6.7 and 6.8. The longitudinal slip ratio oscillates around the value yielding the maximum friction coefficient, approx. -0.05 when the initial guess is $s_{ijx,ref} = -0.10$. ABS is engaged when the slip becomes high, the 'First Dip' controller is able to stabilize the wheel slip and the 'Closed-loop' controller successfully tracks the desired wheel slip.

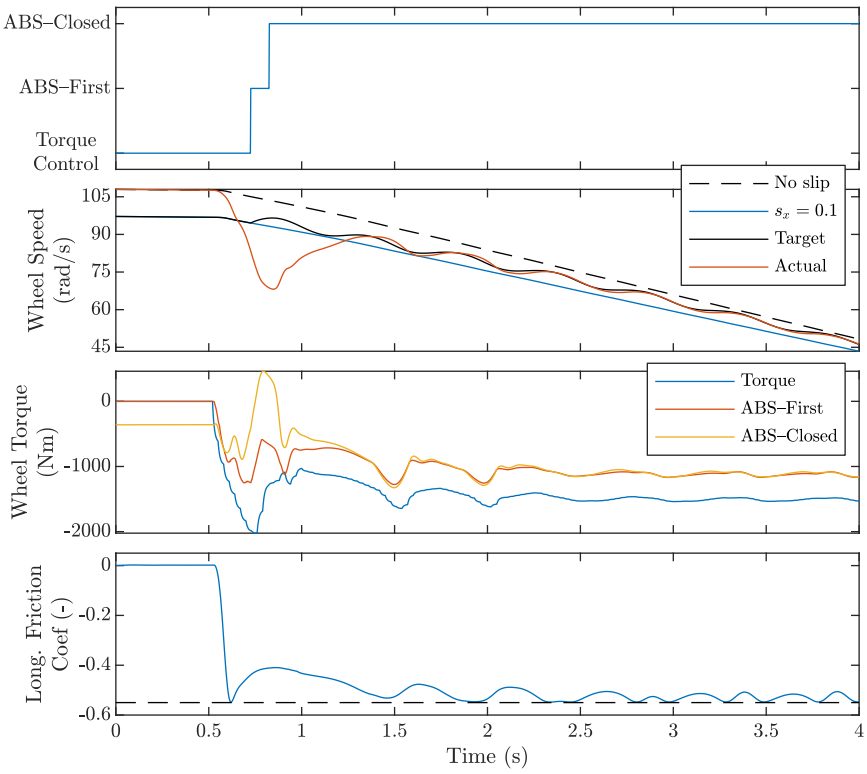

Figure 6.8: Simulation results of the slip controllers. Plots are for the front left wheel.

Chapter 7

Results and Analysis

The control framework developed in this dissertation is tested in simulation with a high-fidelity vehicle model for validation; the chassis model is the 18 DoF developed in Section 2.1 with the MF94 Pacejka tire model; the drivetrain, brake, and steering models are the bond graph models from Section 2.3. The control framework is evaluated in open-loop driving scenarios where the driver's input are functions of time and on closed-loop maneuvers where the driver's input depends on the environment (e.g., the car's position relative to a predefined trajectory).

7.1 Metrics

Several metrics are used to compare the performance of the different configurations. The Root Mean Square Error (RMSE) evaluates the Root Mean Square (RMS) of the error between a time signal $x(t)$ and a desired signal $x_d(t)$, the RMS value x_{RMS} of the signal $x(t)$ and the RMSE between $x(t)$ and $x_d(t)$ are defined as follows:

$$x_{RMS} = \sqrt{\frac{1}{T}\int_0^T x(t)^2 \,\mathrm{d}t}, \quad x_{RMSE} = \sqrt{\frac{1}{T}\int_0^T (x(t) - x_d(t))^2 \,\mathrm{d}t} \tag{7.1}$$

where T is the duration of the maneuver.

The RMSE between the vehicle and desired lateral velocity, yaw rate, and total torque quantify the tracking performance of the control system; it should be noted that the yaw rate target depends on the vehicle velocity; thus, the target might differ between simulations despite using the same user steering and throttle inputs. The energy dissipated by the brake actuators and by the drivetrain

(i.e., electric motors and eLSD) measures the energy efficiency of the vehicle and control strategy.

7.2 Open-Loop Maneuver: Sine with Dwell Steering Input

The open-loop sine with dwell maneuver is applied to the vehicle model. The vehicle is initially traveling at $120\,\mathrm{km\,h^{-1}}$. The steering input is a single sine period of amplitude 90° and of frequency, $f = 0.7\,\mathrm{Hz}$, when $t > \frac{3}{4f}$, the steering angle is maintained at $-90°$ for $0.5\,\mathrm{s}$ before applying the last quarter phase of sine input.

Figure 7.1 shows the vehicle yaw rate of the uncontrolled vehicle and with all configurations of drivetrain and active steering considered in this dissertation, Tables 7.1 and 7.2 list the RMSE of lateral velocity, yaw rate, and torque. The uncontrolled vehicle exhibits a large yaw rate and sideslip angle; the control framework can stabilize all tested configurations. The control strategy uses the more flexible capabilities of the quad-motor and eAWD drivetrain to better track the yaw rate target; similarly, active steering actuators are employed to improve further the tracking of the desired lateral velocity and yaw rate. The results show that AFS is employed in this scenario to improve the energy efficiency of the vehicle.

7.3 Closed-Loop Maneuvers

7.3.1 Driver Model

Closed-loop maneuvers where a driver model defines the vehicle's input based on the environment are necessary to evaluate how the vehicle would behave in real driving scenarios; this model represents the driver and defines the steering and throttle inputs given to the vehicle to follow the desired trajectory. The driver model is separated into two parts: a longitudinal and lateral controller: a PID controller defines the throttle input to follow the desired velocity profile, the lateral controller implements Sharp and Valtetsiotis's optimal steering controller, which consists of an Linear Quadratic Regulator (LQR) with preview outputting the steering wheel input to follow the desired trajectory [110].

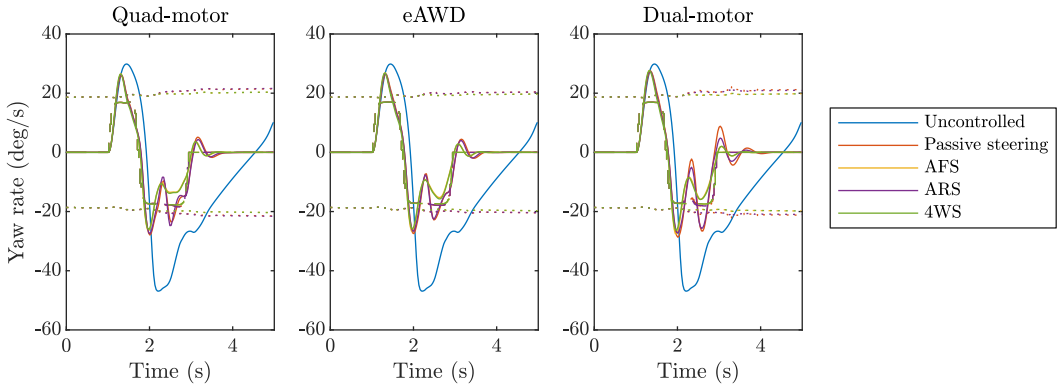

Figure 7.1: Sine with dwell maneuver. Dashed lines represent target signals, dotted lines represent bounds.

Table 7.1: Simulation results for several driving scenarios (no active steering and AFS)

	Base (Quad)	Passive steering			Active Front Steering		
		Quad	eAWD	Dual	Quad	eAWD	Dual
				90° sine with dwell at 120 km h^{-1}			
Lateral vel. RMSE (m s^{-1})	6.35	0.72	0.68	0.68	0.61	0.61	0.64
Yaw rate RMSE (deg s^{-1})	15.21	4.00	3.95	4.95	3.69	3.68	3.98
Torque RMSE (N m)	166.2	531.0	400.8	719.6	262.5	97.7	199.9
Total energy dissipated (kJ)	3.88	55.56	133.65	321.80	26.97	98.77	195.57
				High-speed double lane change			
Lateral vel. RMSE (m s^{-1})	13.52	1.19	1.12	1.08	1.11	1.06	1.06
Yaw rate RMSE (deg s^{-1})	40.15	5.78	6.21	6.44	5.54	5.10	5.70
Torque RMSE (N m)	6996.8	869.6	708.8	1690.0	566.7	310.3	756.9
Total energy dissipated (kJ)	442.20	382.46	474.86	746.28	352.76	487.72	701.40
Terminal vel. (km h^{-1})	73.09	129.84	129.98	130.35	129.69	129.86	129.90
Steer. angle θ_{dri} RMS (deg)	431.97	44.02	51.72	42.96	64.47	62.93	72.93
Max. wheel slip angle (deg)	80.78	8.70	9.37	7.99	9.05	8.91	8.89

Table 7.2: Simulation results for several driving scenarios (ARS and 4WS)

	Base (Quad)	Active Rear Steering			Four Wheel Steering		
		Quad	eAWD	Dual	Quad	eAWD	Dual
				90° sine with dwell at 120 km h^{-1}			
Lateral vel. RMSE (m s^{-1})	6.35	0.66	0.64	0.66	0.59	0.59	0.61
Yaw rate RMSE (deg s^{-1})	15.21	4.05	3.80	4.40	3.61	3.53	3.76
Torque RMSE (N m)	166.2	599.0	382.1	580.5	267.1	98.0	189.5
Total energy dissipated (kJ)	3.88	60.30	137.28	315.22	27.10	99.22	194.99
				High-speed double lane change			
Lateral vel. RMSE (m s^{-1})	13.52	0.93	0.99	0.94	1.06	1.03	1.10
Yaw rate RMSE (deg s^{-1})	40.15	6.00	6.12	5.29	5.27	4.86	5.31
Torque RMSE (N m)	6996.8	1097.9	672.8	1253.8	552.8	250.5	588.5
Total energy dissipated (kJ)	442.20	400.26	479.63	707.43	355.12	450.45	655.74
Terminal vel. (km h^{-1})	73.09	130.06	130.03	130.26	129.84	129.88	129.96
Steer. angle θ_{dri} RMS (deg)	431.97	44.96	50.27	44.27	61.09	59.90	67.45
Max. wheel slip angle (deg)	80.78	8.21	8.72	7.96	8.99	8.85	8.83

7.3.2 U-Turn

During this maneuver, the driver only controls the lateral vehicle dynamics to perform a U-turn of 45 m radius; the driver requests no acceleration or braking command. The vehicle's initial speed is 80 km h^{-1}. Figure 7.2 shows the vehicle trajectory, driver steering input, lateral acceleration, velocity, and yaw rate for the quad-motor drivetrain vehicle; no active steering actuators are equipped on the vehicle. The uncontrolled vehicle tracks a wider path during the first half of the turn than the controlled vehicle. The driver must apply large steering input and a sudden change at $t \approx 6$ s to stabilize the vehicle trajectory. The IVDC control strategy employed by the controlled vehicle allows for an easier turn with a faster exit speed, showing the effectiveness to maintain the vehicle yaw rate and lateral velocity within reasonable values. The controlled vehicle is more maneuverable and safer

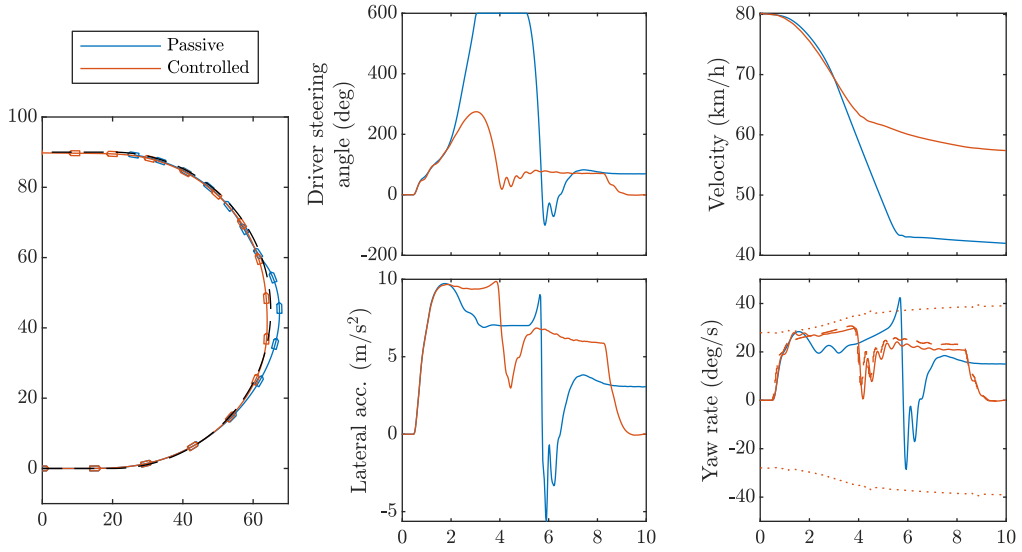

Figure 7.2: U-turn maneuver with the quad-motor drivetrain and no active steering. Dashed lines represent target signals, dotted lines represent bounds.

than the passive one.

7.3.3 High-speed Double Lane Change

The double lane change is a well-known test method to evaluate the vehicle dynamics under extreme cornering. In this maneuver, the vehicle must be driven through the tracks. The trajectory followed by the driver model corresponds to a straight segment, followed by a lane transition 3.5 m to the left and 20 m long, a 40 m long straight segment, a lane transition 20 m long to the original lane, and a final straight segment. The longitudinal controllers aim at maintaining the vehicle's original velocity.

Results are shown in Figures 7.3 to 7.6 and Tables 7.1 and 7.2. The base vehicle is unstable when the driver performs the double lane change maneuver; the driver applies large steering angle; without action to improve the vehicle's handling performance, the base vehicle sideslip and yaw rate become too large, and the driver loses control of the vehicle. The control framework can stabilize the vehicle for all configurations tested. The control framework reduces the driver load, indeed the RMS of the steering input signal with the base model is $\theta_{dri,RMS} = 430\,\text{deg}$, and $\theta_{dri,RMS} = 44\,\text{deg}$ with the quad-motor topology without active steering. The driver load is slightly higher when the vehicle is equipped with AFS or 4WS than when equipped with no active steering or ARS (see Figure 7.6 and Tables 7.1 and 7.2). This is not due to violation of tire saturation constraints since

for all configurations the wheel slip angle stays below the value yielding maximum lateral force (approx. 10°). Instead, this is due to the design of the driver evaluator which makes the car more understeer, hence more stable but also less maneuverable; AFS and ARS provide more actuation, allowing to improve the tracking of the reference signals ($\tau_{tot,ref}, v_{y,ref}, \omega_{z,ref}$), making the car less maneuverable and increasing the driver load.

When the vehicle is equipped with active steering, AFS is used to reduce the steering angle applied by the driver at the front wheels and to reduce the slip angle at the front wheels. Torque vectoring capabilities, either from TV device or brake-based torque vectoring, are employed to maintain the vehicle yaw rate within the bounds and follow the target. Tables 7.1 and 7.2 show the metrics used to compare the performance with the different configurations. The quad-motor and eAWD drivetrains usually provide better tracking for yaw rate than the dual-motor topology due to more flexible TV capabilities. Active steering improves the tracking of the lateral velocity and reduces the energy dissipated by the drivetrain and the friction brakes. Overall, the best-combined performance is obtained with the quad-motor or eAWD drivetrain and 4WS, showing that the control framework can use the different actuators to improve the system performance.

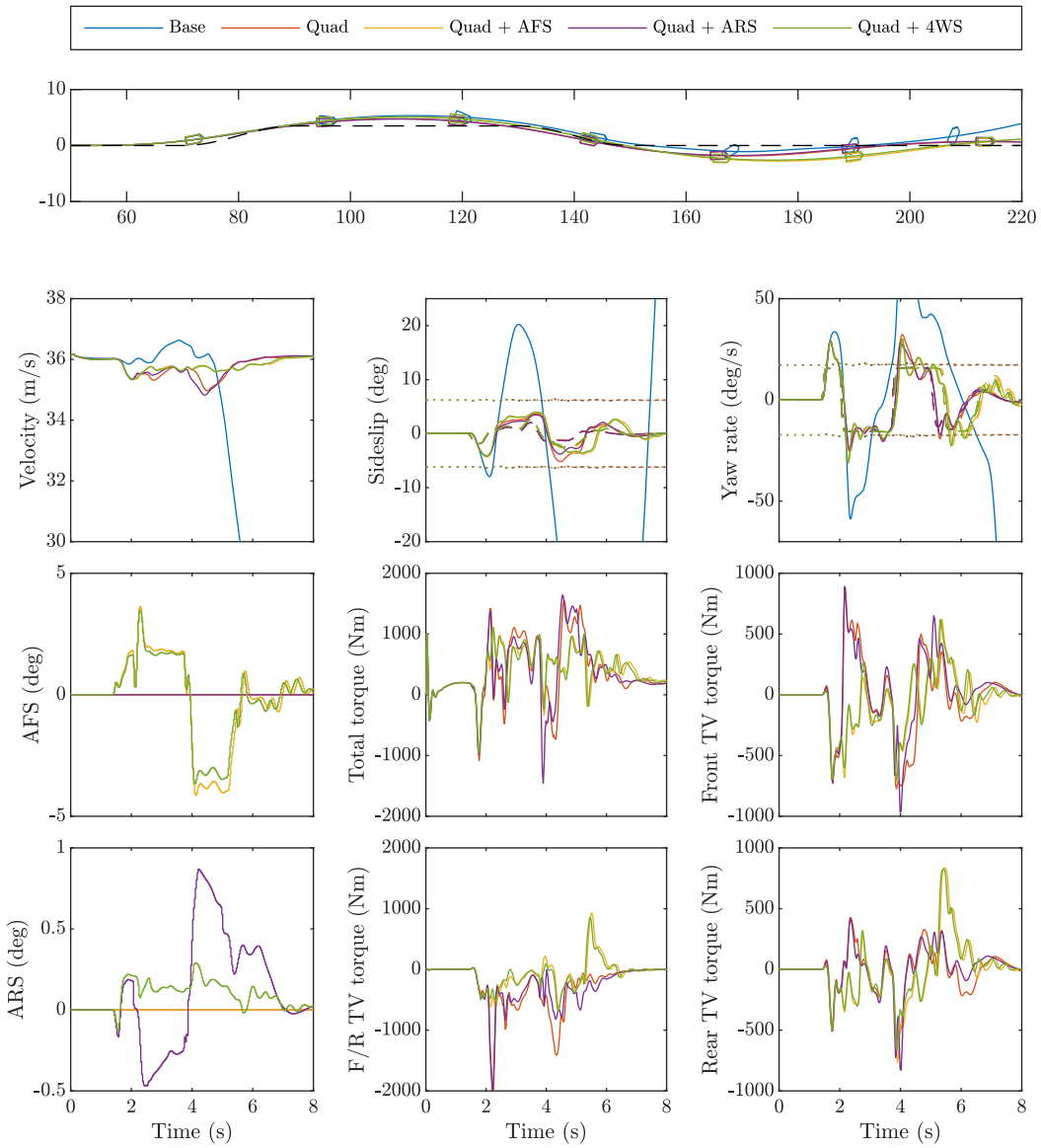

Figure 7.3: Double lane change maneuver with the quad-motor drivetrain. Dashed lines represent target signals, dotted lines represent bounds.

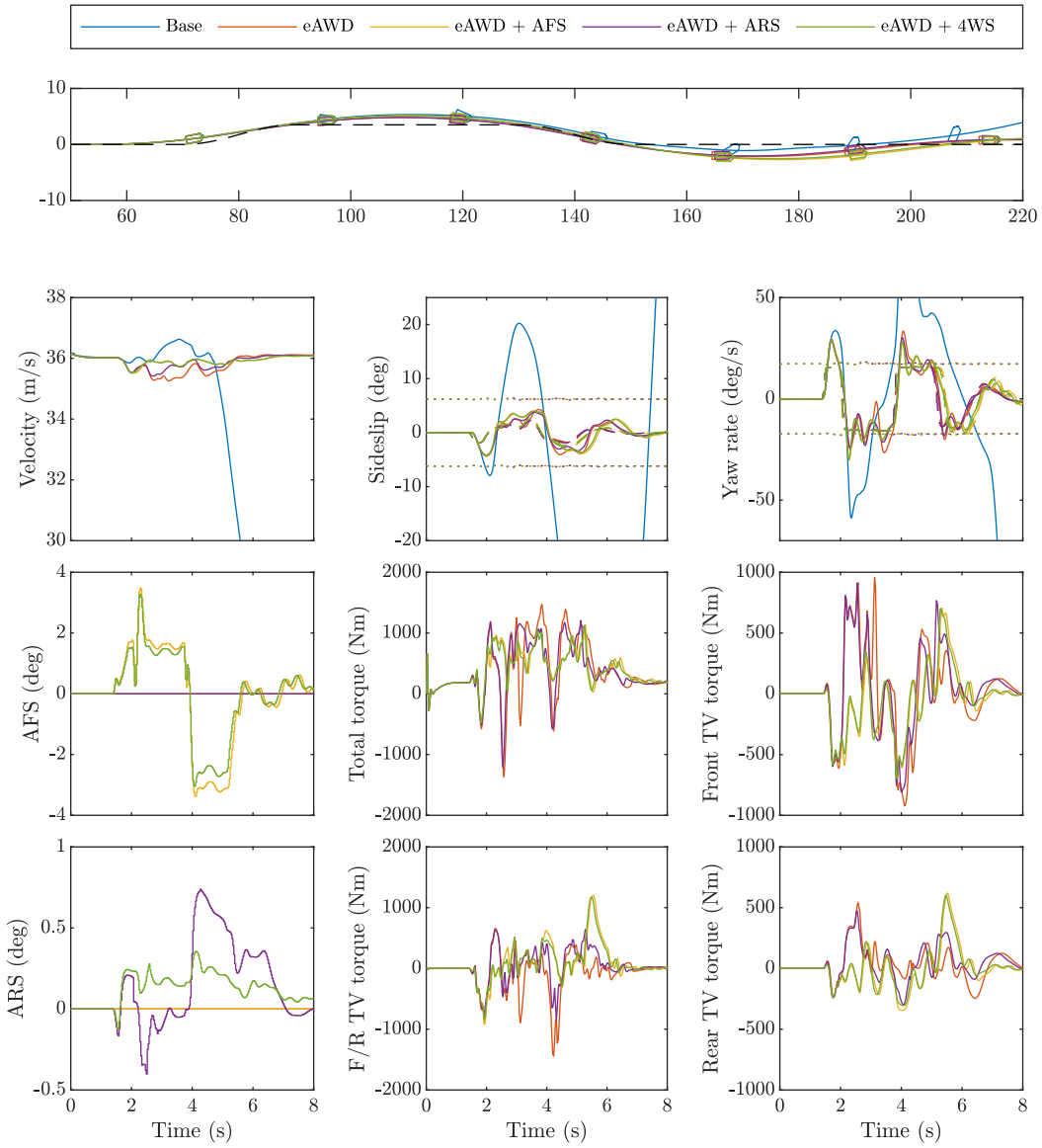

Figure 7.4: Double lane change maneuver with the eAWD drivetrain. Dashed lines represent target signals, dotted lines represent bounds.

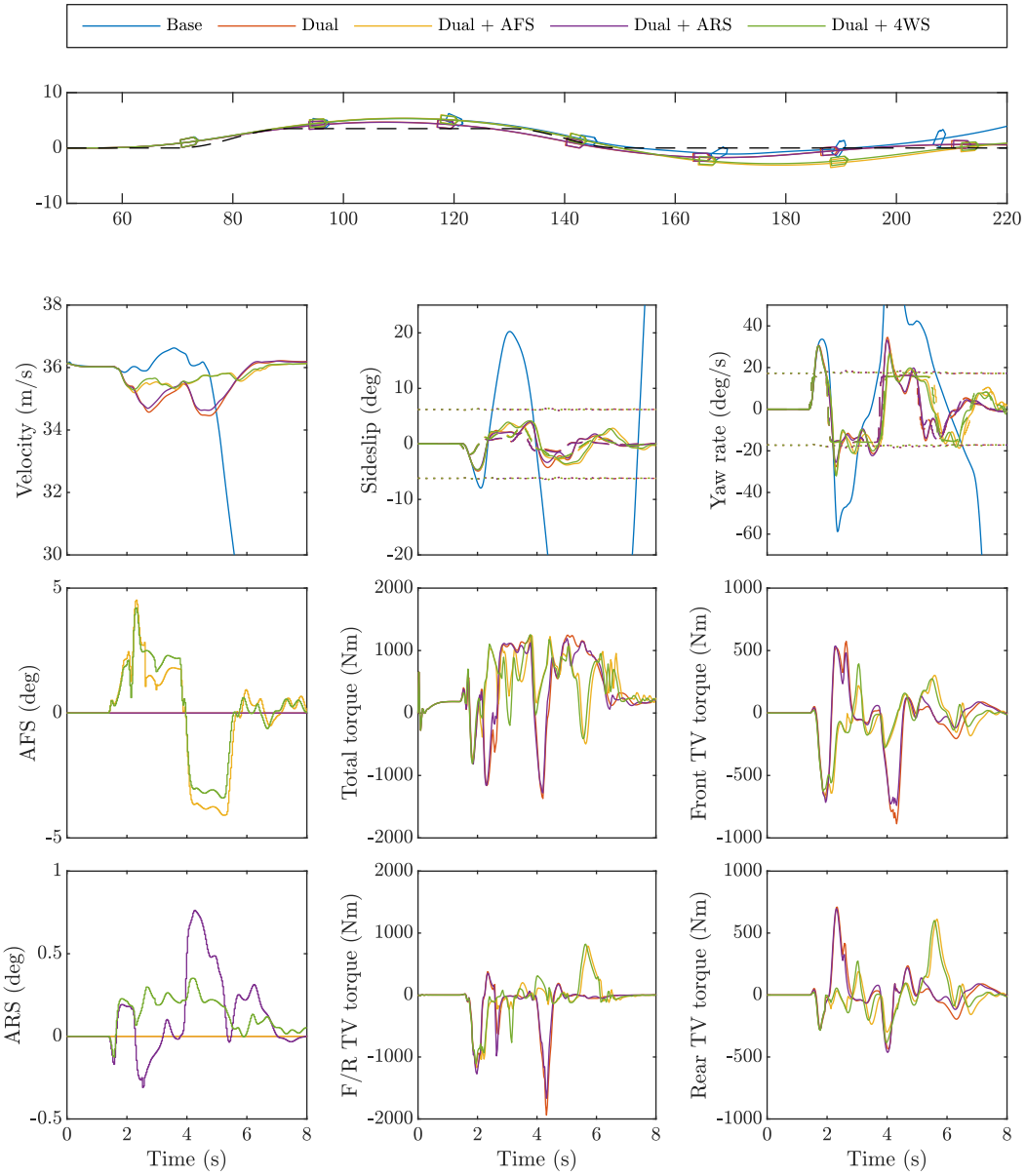

Figure 7.5: Double lane change maneuver with the dual-motor drivetrain. Dashed lines represent target signals, dotted lines represent bounds.

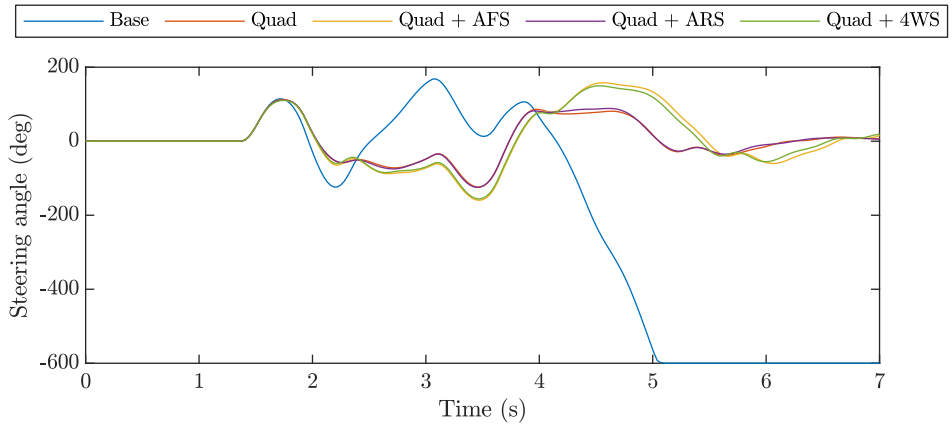

(a) Quad-motor drivetrain

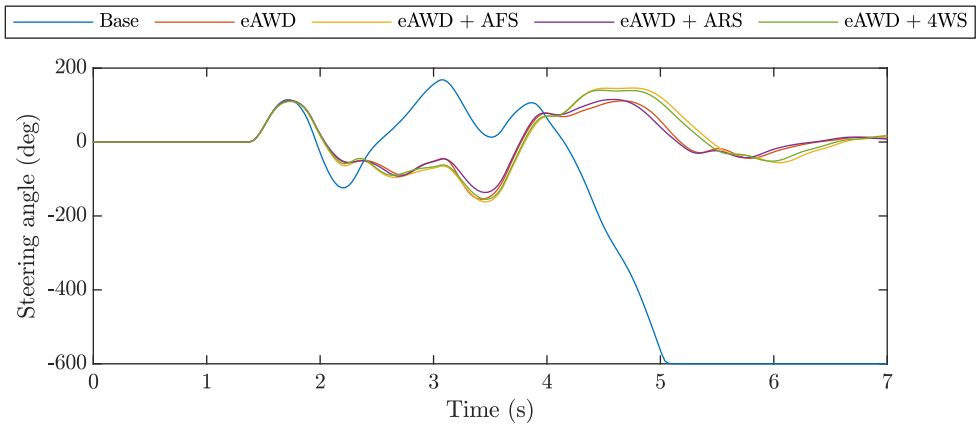

(b) eAWD drivetrain

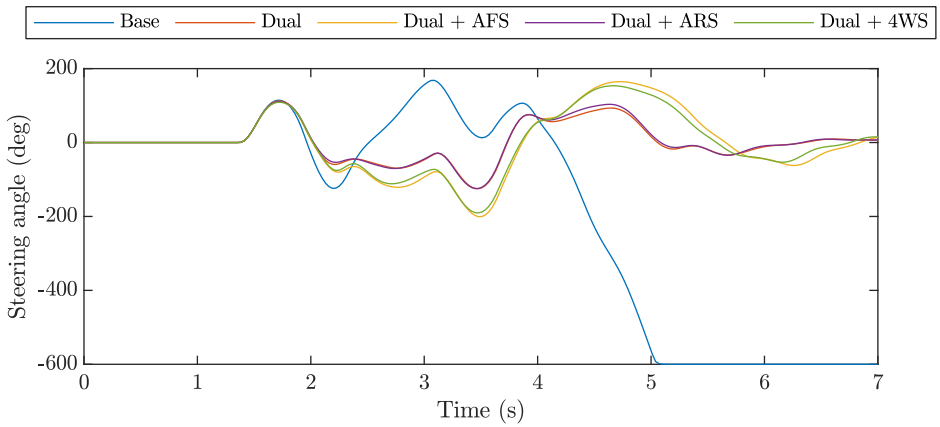

(c) Dual-motor drivetrain

Figure 7.6: Driver steering input during the double lane change maneuver

Chapter 8

Conclusions and Future Work

8.1 Conclusions

This research presents the development of vehicle dynamics control for electric vehicles. Vehicle models are provided to investigate and better understand the system dynamics, the effect of front-to-rear TV, left-to-right TV, and active steering on the vehicle handling have been presented. Several actuators have been modeled with the bond graph method to show the reusability of the architecture: three drivetrains and brake topologies with varying TV capabilities, namely the quad-motor, dual-motor, and eAWD drivetrain topologies equipped with EHB; possible steering configuration include passive steering, AFS, ARS, and 4WS. The actuators considered in this research include TV and active steering, other actuators such as active suspension or active roll control are outside the scope of this research.

The control framework proposed in this dissertation is based on a multi-layered control architecture. However, instead of using generalized forces as controls to follow the motion requests, we used controls at the wheel level, i.e., wheel torque and steering angle. The architecture is decomposed into two parts: upstream of the wheel controls is the abstract layer, and downstream is the application layer.

The abstract layer goal is to define wheel controls to follow the motion requests without precise knowledge of the actuators equipped on the vehicle; this is done to make the architecture more reusable when developing a vehicle with new actuators; only the application layer must be redefined. The abstract layer uses a simplified tire model to generate the wheel controls optimally while considering the coupling between the longitudinal and lateral tire force; the tire model approximates

the pairs of longitudinal and lateral friction coefficients given a slip angle by ellipses. The abstract layer is also responsible for ensuring vehicle stability and attempts to preemptively avoid tire saturation by relying on estimating the maximum road-tire friction coefficient. Observers for the tire normal force and maximum tire-road friction coefficients are developed and used by the control framework. Several control methodologies have been proposed to implement the abstract layer: a MIMO $\mathcal{H}_\infty$-controller with a nonlinear control allocation and anti-windup compensators; a LTVMPC; and a NMPC implemented with the `acados` library.

Once the wheel controls are defined, the abstract layer coordinates the actuators. A daisy-chain control allocation is proposed to blend the EHB and drivetrain torques. The control allocation is not directly connected to the plant inside the control loop; instead, it defines the desired control distribution, and the Smith-McMillan-based nullspace allocator is responsible for following the requested control distribution without modifying the plant output response. This control structure allows a more modular approach where the feedback controller design is independent of the control allocation. The stability and robustness properties associated with adding the Smith-McMillan-based allocator in the feedback loop have been investigated. Indeed, nominal stability is maintained after connecting the allocator to the feedback loop; the framework is not sensitive to multiplicative output uncertainties; bounds on the closed-loop structured singular value with the nullspace allocator under multiplicative input uncertainties are provided given some assumptions. In addition, the abstract layer pro-actively ensures wheel stability, ABS and TCS slip controllers are implemented to maintain the wheel slip in the tire's stable region. The slip controllers are implemented by several SISO Youla parameterized controllers, which track the desired wheel speed by controlling the wheel torque: when a slip event occurs, the 'first spin/dip' controllers bring the wheel slip in the 'closed-loop' controllers operating range, once this is done, the 'closed-loop' controller takes over and ensure good tracking of the wheel speed reference defined by an ESC.

8.2 Future Work

The performance of the slip controller might be improved by ensuring smoother transitions. Currently, a slip supervisor decides the control law to apply and switches between the different controllers. A smoother transition between the different modes could be implemented using fuzzy logic instead.

The abstract layer relies on a simplified tire model to model the coupling phenomenon between the longitudinal and lateral tire forces where the f_x–f_y curves for a given slip angle are approximated by ellipses. The coefficients defining the ellipse are chosen by selecting four points of the f_x–f_y curve to be on the ellipse. This method approximates the tire forces reasonably well at low slip values. This approach was chosen because of its simplicity and the ability to provide an analytical expression (instead of lookup tables) that can be used online to solve optimization problems efficiently. However, this method does not guarantee finding the best set of coefficients; more advanced regression methods could provide a better approximation. Moreover, this method relies on a static tire model; using a tire model with time-varying parameters and estimating these parameters could further improve system performance.

The control architecture developed in this dissertation focuses on a vehicle equipped with an electric drivetrain, independent braking, and active steering, with a major focus on the vehicle's longitudinal, lateral, and handling behavior; the control framework could be extended by considering additional actuators. More specifically, active or semi-active suspension via CDC or ARC via active roll-bar allows for modifying the vehicle's ride, roll, and pitch behavior by modifying the vehicle's normal tire forces. Additionally, several simplifications have been done when designing the proposed control architecture: the tire coupling phenomenon only considers the coupling between the longitudinal and lateral friction coefficient but neglects the nonlinear relation between the longitudinal or lateral friction coefficient and the tire normal force. The abstract layer could be modified to consider this coupling and define wheel normal load targets to the application layer; the application can then coordinate the actuators that impact the tire normal loads. Perhaps a comparison between a time-varying tire model and a dynamic one would also be beneficial for this work.

We proposed an implementation of the abstract layer using MPC where the driver's requests are kept constant during the prediction horizon since they cannot be known beforehand. Suppose the architecture was implemented on autonomous vehicles; in that case, the control architecture could make full use of the predictive power of MPC to stabilize the vehicle trajectory: the MPC in the abstract layer would need to be redesigned, the internal model should be augmented to allow defining a desired trajectory, and the cost function should be modified to penalize trajectory tracking error.

Bibliography

[1] V. Ivanov and D. Savitski, "Systematization of integrated motion control of ground vehicles," eng, *IEEE Access*, vol. 3, pp. 2080–2099, 2015, ISSN: 2169-3536.

[2] M. Kissai, B. Monsuez, and A. Tapus, "Current and future architectures for integrated vehicle dynamics control," Jun. 2017.

[3] C. Ebert and C. Jones, "Embedded software: Facts, figures, and future," *Computer*, vol. 42, no. 4, pp. 42–52, Apr. 2009, ISSN: 0018-9162. DOI: 10.1109/MC.2009.118. [Online]. Available: https://doi.org/10.1109/MC.2009.118.

[4] P. Koehn and M. Eckrich, "Active steering - the BMW approach towards modern steering technology," *SAE Technical Paper*, 2004. DOI: 10.4271/2004-01-1105.

[5] M. Gerard, "Global chassis control and braking control using tyre forces measurement," Ph.D. dissertation, Technische Universiteit Delft, 2011.

[6] W. Chen, *Integrated vehicle dynamics and control*, eng. 2016, ISBN: 9781118380024.

[7] S. Skogestad, *Multivariable feedback control: analysis and design*, eng, 2nd ed. Chichester, England; Hoboken, NJ: John Wiley, 2005, ISBN: 047001167X.

[8] T. Gordon, M. Howell, and F. Brandao, "Integrated control methodologies for road vehicles," eng, *Vehicle System Dynamics*, vol. 40, no. 1-3, pp. 157–190, 2003, ISSN: 0042-3114.

[9] M. Kissai, B. Monsuez, and A. Tapus, "Review of integrated vehicle dynamics control architectures," in *2017 European Conference on Mobile Robots (ECMR)*, Paris, France: IEEE,

Sep. 2017. DOI: 10.1109/ECMR.2017.8098687. [Online]. Available: https://hal.archives-ouvertes.fr/hal-01690788.

[10] T. A. Johansen and T. I. Fossen, "Control allocation—a survey," *Automatica*, vol. 49, no. 5, pp. 1087–1103, 2013, ISSN: 0005-1098. DOI: 10.1016/j.automatica.2013.01.035. [Online]. Available: http://www.sciencedirect.com/science/article/pii/S0005109813000368.

[11] A. Soltani, "Low cost integration of electric power-assisted steering (EPAS) with enhanced stability program (ESP)," Ph.D. dissertation, Cranfield University, 2014.

[12] C. A. Vivas-Lopez, J. C. Tudon-Martinez, D. Hernandez-Alcantara, and R. Morales-Menendez, "Global chassis control system using suspension, steering, and braking subsystems," *Mathematical Problems in Engineering*, vol. 2015, 2015, ISSN: 15635147. DOI: 10.1155/2015/263424.

[13] P. He, Y. Wang, Y. Zhang, Y. Liu, and Y. Xu, "Integrated control of semi-active suspension and vehicle dynamics control system," in *2010 International Conference on Computer Application and System Modeling*, vol. 5, 2010, pp. V5-63-V5–68. DOI: 10.1109/ICCASM.2010.5619352.

[14] P. Falcone, F. Borrelli, J. Asgariy, H. E. Tsengy, and D. Hrovat, "A model predictive control approach for combined braking and steering in autonomous vehicles," *2007 Mediterranean Conference on Control and Automation, MED*, 2007. DOI: 10.1109/MED.2007.4433694.

[15] P. Falcone, F. Borrelli, J. Asgari, H. E. Tseng, and D. Hrovat, "Predictive active steering control for autonomous vehicle systems," *IEEE Transactions on Control Systems Technology*, vol. 15, no. 3, pp. 566–580, 2007, ISSN: 10636536. DOI: 10.1109/TCST.2007.894653.

[16] P. Falcone, M. Tufo, F. Borrelli, J. Asgari, and H. E. Tseng, "A linear time varying model predictive control approach to the integrated vehicle dynamics control problem in autonomous systems," in *2007 46th IEEE Conference on Decision and Control*, 2007, pp. 2980–2985. DOI: 10.1109/CDC.2007.4434137.

[17] S. J. Varhagen, "Development of vehicle dynamics control for wheel-motored vehicles," Ph.D. dissertation, University of California Davis, 2014.

[18] J. Velazquez Alcantar and F. Assadian, "A robust stability control system for a hybrid electric vehicle equipped with electric rear axle drive," *SAE International Journal of Passenger Cars - Mechanical Systems*, vol. 9, no. 2, 2016, ISSN: 19464002. DOI: 10.4271/2016-01-1649.

[19] J. Velazquez Alcantar, "Investigation & development of vehicle dynamics control frameworks for an electric all-wheel-drive hybrid electric vehicle," Ph.D. dissertation, University of California Davis, 2017.

[20] M. Kissai, B. Monsuez, X. Mouton, D. Martinez, and A. Tapus, "Adaptive robust vehicle motion control for future over-actuated vehicles," *Machines*, vol. 7, no. 2, 2019, ISSN: 2075-1702. DOI: 10.3390/machines7020026. [Online]. Available: https://www.mdpi.com/2075-1702/7/2/26.

[21] M. Kissai, X. Mouton, B. Monsuez, and A. Tapus, "Optimization-based control allocation for driving braking torque vectoring in a race car," in *American Control Conference (ACC)*, Denver, United States, 2020. [Online]. Available: https://hal.archives-ouvertes.fr/hal-02447091.

[22] D. Nigicser, V. Turri, M. Jonas, M. A. Arat, and E. S. Silva, "Predictive vehicle motion control for post-crash scenarios," *Proceedings of the 14th International Symposium on Advanced Vehicle Control (AVEC' 18)*, 2018.

[23] E. Mousavinejad, Q.-L. Han, F. Yang, Y. Zhu, and L. Vlacic, "Integrated control of ground vehicles dynamics via advanced terminal sliding mode control," *Vehicle System Dynamics*, vol. 55, no. 2, pp. 268–294, 2017. DOI: 10.1080/00423114.2016.1256489. eprint: https://doi.org/10.1080/00423114.2016.1256489. [Online]. Available: https://doi.org/10.1080/00423114.2016.1256489.

[24] S. Yim and K. Yi, "Design of active roll control system and integrated chassis control for hybrid 4WD vehicles," *International IEEE Conference on Intelligent Transportation Systems*, vol. 9, pp. 1193–1198, 2011.

[25] B. Shyrokau, D. Wang, D. Savitski, K. Hoepping, and V. Ivanov, "Vehicle motion control with subsystem prioritization," *Mechatronics*, vol. 30, pp. 297–315, 2015, ISSN: 09574158. DOI: 10.1016/j.mechatronics.2014.11.004.

[26] H. Zengin, "Multiple-model robust adaptive vehicle motion control," Ph.D. dissertation, University of Waterloo, 2019.

[27] J. Andreasson and T. Bunte, "Global chassis control based on inverse vehicle dynamics models," *Vehicle System Dynamics*, vol. 44, no. SUPPL. 1, pp. 321–328, 2006, ISSN: 00423114. DOI: 10.1080/00423110600871459.

[28] H. Yin, Y. H. Chen, and D. Yu, "Vehicle motion control under equality and inequality constraints: A diffeomorphism approach," *Nonlinear Dynamics*, vol. 95, no. 1, pp. 175–194, 2019, ISSN: 1573269X. DOI: 10.1007/s11071-018-4558-6.

[29] D. C. Karnopp, D. L. Margolis, and R. C. Rosenberg, *System Dynamics: Modeling, Simulation, and Control of Mechatronic Systems: Fifth Edition*. 2012, ISBN: 9780470889084. DOI: 10.1002/9781118152812.

[30] T. Shim and C. Ghike, "Understanding the limitations of different vehicle models for roll dynamics studies," *Vehicle System Dynamics - Vehicle System Dynamics*, vol. 45, pp. 191–216, Mar. 2007. DOI: 10.1080/00423110600882449.

[31] P. Andrén, "Power spectral density approximations of longitudinal road profiles," *International Journal of Vehicle Design - INT J VEH DES*, vol. 40, Jan. 2006. DOI: 10.1504/IJVD.2006.008450.

[32] M. Acosta, S. Kanarachos, and M. Blundell, "Road friction virtual sensing: A review of estimation techniques with emphasis on low excitation approaches," *Applied Sciences (Switzerland)*, vol. 7, no. 12, 2017, ISSN: 20763417. DOI: 10.3390/app7121230.

[33] H. Pacejka, *Tire and Vehicle Dynamics*, third. Elsevier Ltd, 2012, pp. 187–190.

[34] P. R. Dahl, "A solid friction model," *Technical Report, The Aerospace Corporation, El Segundo,*, vol. 158, 1968.

[35] P. Tsiotras, E. Velenis, and M. Sorine, "A lugre tire friction model with exact aggregate dynamics," *Vehicle System Dynamics*, vol. 42, pp. 195–210, Dec. 2004. DOI: 10.1080/00423110412331289835.

[36] L. De Novellis, A. Sorniotti, and P. Gruber, "Design and comparison of the handling performance of different electric vehicle layouts," *Proceedings of the Institution of Mechanical Engineers, Part D: Journal of Automobile Engineering*, vol. 228, no. 0, pp. 218–232, 2013, ISSN: 0954-4070. DOI: 10.1177/0954407013506569.

[37] D. Hrovat and W. E. Tobler, "Bond graph modeling of automotive power trains," *Journal of The Franklin Institute-engineering and Applied Mathematics*, vol. 328, pp. 623–662, 1991.

[38] D. Karnopp, "Computer simulation of stick-slip friction in mechanical dynamic systems," *Journal of Dynamic Systems, Measurement and Control, Transactions of the ASME*, vol. 107, no. 1, pp. 100–103, Mar. 1985, ISSN: 00220434.

[39] A. Mahmoudi, W. L. Soong, G. Pellegrino, and E. Armando, "Efficiency maps of electrical machines," in *2015 IEEE Energy Conversion Congress and Exposition (ECCE)*, 2015, pp. 2791–2799. DOI: 10.1109/ECCE.2015.7310051.

[40] E. Arasteh and F. Assadian, "A comparative analysis of brake-by-wire smart actuators using optimization strategies," *Energies*, vol. 15, no. 2, 2022, ISSN: 1996-1073. DOI: 10.3390/en15020634.

[41] A. Soltani and F. Assadian, "New slip control system considering actuator dynamics," en, *SAE International Journal of Passenger Cars - Mechanical Systems*, vol. 8, no. 2, pp. 512–520, Apr. 2015, ISSN: 1946-4002. DOI: 10.4271/2015-01-0656. [Online]. Available: https://www.sae.org/content/2015-01-0656/ (visited on 05/25/2021).

[42] J. Loyola and F. Assadian, "An investigation into new ABS control strategies," en, *SAE International Journal of Passenger Cars - Mechanical Systems*, vol. 9, no. 2, pp. 869–876, Apr. 2016, ISSN: 1946-4002. DOI: 10.4271/2016-01-1639. [Online]. Available: https://www.sae.org/content/2016-01-1639/ (visited on 04/11/2020).

[43] M. Kuang, M. Fodor, D. Hrovat, and M. N. Tran, "Hydraulic brake system modeling and control for active control of vehicle dynamics," *Proceedings of the 1999 American Control Conference (Cat. No. 99CH36251)*, vol. 6, 4538–4542 vol.6, 1999.

[44] D. Peng, Y. Zhang, C.-L. Yin, and J.-W. Zhang, "Combined control of a regenerative braking and antilock braking system for hybrid electric vehicles," *International Journal of Automotive Technology*, vol. 9, 2008. DOI: 10.1007/s12239-008-0089-3.

[45] J. Zhao, D. Song, B. Zhu, Z. Chen, and Y. Sun, "Nonlinear backstepping control of electro-hydraulic brake system based on bond graph model," *IEEE Access*, vol. 8, pp. 19 100–19 112, 2020. DOI: 10.1109/ACCESS.2020.2968513.

[46] L. Filipozzi, E. Velenis, and F. Assadian, "Minimization of steering corruption during front axle torque vectoring," in *European Control Conference (ECC)*, Limasol, Cyprus, Jun. 2018, pp. 673–678. DOI: 10.23919/ECC.2018.8550603.

[47] D. R. Diez, "Front to rear torque vectoring," M.S. thesis, Cranfield University, 2015.

[48] R. Rajamani, *Vehicle Dynamics and Control*, second. London: Springer, 2012, ISBN: 9780387263960. DOI: 10.1007/b22134.

[49] K. Jiang, A. Pavelescu, A. Charara, and A. Victorino, "Estimation of vehicle's vertical and lateral tire forces considering road angle and road irregularity," *2014 17th IEEE International Conference on Intelligent Transportation Systems, ITSC 2014*, Oct. 2014. DOI: 10.1109/ITSC.2014.6957714.

[50] B. Ozkan, D. Margolis, and M. Pengov, "The controller output observer: Estimation of vehicle tire cornering and normal forces," *Journal of Dynamic Systems Measurement and Control-transactions of The Asme*, vol. 130, Nov. 2008. DOI: 10.1115/1.2957627.

[51] F. Gustafsson, "Monitoring tire-road friction using the wheel slip," *IEEE Control Systems*, 1998, ISSN: 1066033X. DOI: 10.1109/37.710877.

[52] A. Andrieux, P. O. Vandanjon, R. Lengelle, and C. Chabanon, "New results on the relation between tyre-road longitudinal stiffness and maximum available grip for motor car," *Vehicle System Dynamics*, vol. 48, no. 12, pp. 1511–1533, 2010, ISSN: 00423114. DOI: 10.1080/00423111003770421.

[53] L. R. Ray, "Nonlinear tire force estimation and road friction identification: Simulation and experiments," *Automatica*, vol. 33, no. 10, pp. 1819–1833, 1997, ISSN: 00051098. DOI: 10.1016/S0005-1098(97)00093-9.

[54] J. Velazquez Alcantar, F. Assadian, and M. Kuang, "Vehicle velocity state estimation using youla controller output observer," in *2018 Annual American Control Conference (ACC)*, 2018, pp. 2587–2592. DOI: 10.23919/ACC.2018.8431594.

[55] J. Velazquez Alcantar and F. Assadian, "Longitudinal tire force estimation using youla controller output observer," *IEEE Control Systems Letters*, vol. 2, no. 1, pp. 31–36, 2018. DOI: 10.1109/LCSYS.2017.2722405.

[56] L. Zaccarian, "Dynamic allocation for input redundant control systems," *Automatica*, vol. 45, no. 6, pp. 1431–1438, 2009, ISSN: 00051098. DOI: 10.1016/j.automatica.2009.01.013.

[57] L. Zaccarian, "On dynamic control allocation for input-redundant control systems," *Proceedings of the IEEE Conference on Decision and Control*, no. 4, pp. 1192–1197, 2007, ISSN: 01912216. DOI: 10.1109/CDC.2007.4434679.

[58] P. Kolaric, V. G. Lopez, and F. L. Lewis, "Optimal dynamic control allocation with guaranteed constraints and online reinforcement learning," *Automatica*, vol. 122, p. 109 265, 2020, ISSN: 0005-1098. DOI: https://doi.org/10.1016/j.automatica.2020.109265. [Online]. Available: https://www.sciencedirect.com/science/article/pii/S0005109820304635.

[59] A. Cristofaro and S. Galeani, "Output invisible control allocation with steady-state input optimization for weakly redundant plants," in *53rd IEEE Conference on Decision and Control*, 2014, pp. 4246–4253. DOI: 10.1109/CDC.2014.7040051.

[60] A. Serrani, "Output regulation for over-actuated linear systems via inverse model allocation," in *2012 IEEE 51st IEEE Conference on Decision and Control (CDC)*, 2012, pp. 4871–4876. DOI: 10.1109/CDC.2012.6426209.

[61] M. Cocetti, A. Serrani, and L. Zaccarian, "Linear output regulation with dynamic optimization for uncertain linear over-actuated systems," *Automatica*, vol. 97, pp. 214–225, 2018, ISSN: 0005-1098. DOI: 10.1016/j.automatica.2018.08.002.

[62] C.-T. Chen, *Linear System Theory and Design*, 3rd. USA: Oxford University Press, Inc., 1998, ISBN: 0195117778.

[63] F. Assadian and K. Mallon, *Robust Control: Youla Parameterization Approach*. Hoboken, New Jersey, USA: John Wiley & Sons, Inc., 2021.

[64] M. Doumiati, A. Victorino, A. Charara, G. Baffet, and D. Lechner, "An estimation process for vehicle wheel-ground contact normal forces," *IFAC Proc. Vol.*, 2008. DOI: 10.3182/20080706-5-KR-1001.01205.

[65] M. Doumiati, A. Victorino, A. Charara, and D. Lechner, "Virtual sensors, application to vehicle-tire road normal forces for road safety," in *American Control Conference*, San Diego, CA, USA, Jun. 2009, pp. 3337–3343. DOI: 10.1109/ACC.2009.5159866.

[66] R. Jazar, *Vehicle Dynamics: Theory and Application*. Boston,MA, USA: Springer, 2008.

[67] S. Gillijns and B. De Moor, "Unbiased minimum-variance input and state estimation for linear discrete-time systems," *Automatica*, vol. 43, no. 1, pp. 111–116, 2007, ISSN: 0005-1098. DOI: https://doi.org/10.1016/j.automatica.2006.08.002. [Online]. Available: https://www.sciencedirect.com/science/article/pii/S0005109806003189.

[68] W. Kratz, "Characterization of strong observability and construction of an observer," *Linear Algebra and its Applications*, vol. 221, pp. 31–40, 1995, ISSN: 0024-3795. DOI: https://doi.org/10.1016/0024-3795(93)00221-K. [Online]. Available: https://www.sciencedirect.com/science/article/pii/002437959300221K.

[69] P. Krauze, J. Kasprzyk, A. Kozyra, and J. Rzepecki, "Experimental analysis of vibration control algorithms applied for an off-road vehicle with magnetorheological dampers," *Journal of Low Frequency Noise, Vibration and Active Control*, vol. 37, no. 3, pp. 619–639, 2018. DOI: 10.1177/1461348418756018.

[70] H. J. Palanthandalam-Madapusi and D. S. Bernstein, "Unbiased minimum-variance filtering for input reconstruction," in *2007 American Control Conference*, 2007, pp. 5712–5717. DOI: 10.1109/ACC.2007.4282834.

[71] W. F. Milliken, *Race car vehicle dynamics*, eng. Warrendale, PA, U.S.A.: SAE International, 1995, ISBN: 1560915269.

[72] M. A. Arat and S. Taheri, "Identification of road surface friction for vehicle safety systems," *SAE Technical Papers*, vol. 1, 2014, ISSN: 26883627. DOI: 10.4271/2014-01-0885.

[73] K. B. Singh and S. Taheri, "Estimation of tire–road friction coefficient and its application in chassis control systems," *Systems Science and Control Engineering*, vol. 3, no. 1, pp. 39–61, 2015, ISSN: 21642583. DOI: 10.1080/21642583.2014.985804. [Online]. Available: https://doi.org/10.1080/21642583.2014.985804.

[74] K. B. Singh, M. A. Arat, and S. Taheri, "Enhancement of collision mitigation braking system performance through real-time estimation of tire-road friction coefficient by means of smart tires," *SAE International Journal of Passenger Cars - Electronic and Electrical Systems*, vol. 5, no. 2, pp. 607–624, 2012, ISSN: 19464622. DOI: 10.4271/2012-01-2014.

[75] F. Holzwarth and U. Eichhorn, "Non-contact sensors for road conditions," *Sensors and Actuators: A. Physical*, vol. 37-38, no. C, pp. 121–127, 1993, ISSN: 09244247. DOI: 10.1016/0924-4247(93)80023-A.

[76] U. Sandberg, "Influence of road surface texture on traffic characteristics related to environment, economy and safety. a state-of-the-art study regarding measures and measuring methods," p. 93, 1997.

[77] A. J. Tuononen, "Optical position detection to measure tyre carcass deflections," *Vehicle System Dynamics*, vol. 46, no. 6, pp. 471–481, 2008, ISSN: 00423114. DOI: 10.1080/00423110701485043.

[78] A. J. Tuononen, "Laser triangulation to measure the carcass deflections of a rolling tire," *Measurement Science and Technology*, vol. 22, no. 12, 2011, ISSN: 13616501. DOI: 10.1088/0957-0233/22/12/125304.

[79] S. Roychowdhury, M. Zhao, A. Wallin, N. Ohlsson, and M. Jonasson, "Machine learning models for road surface and friction estimation using front-camera images," *Proceedings of the International Joint Conference on Neural Networks*, vol. 2018-July, pp. 1–8, 2018. DOI: 10.1109/IJCNN.2018.8489188.

[80] T. Dieckmann, "Assessment of road grip by way of measured wheel variables," in *Proceedings of FISITA*, 1992.

[81] M. Ito, K. Yoshioka, and T. Saji, "Estimation of road surface conditions using wheel speed behavior," English, *JSAE Review*, vol. 16, no. 2, pp. 221–222, 1995.

[82] J. Deur, "Modeling and analysis of longitudinal tire dynamics based on the Lugre friction model," *IFAC Proceedings Volumes*, vol. 34, no. 1, pp. 91–96, 2001, ISSN: 14746670. DOI: 10.1016/s1474-6670(17)34383-5.

[83] T. Dieckmann, "Der reifenschlupf als indikator für das kraftschlusspotential," Ph.D. dissertation, TU Hannnover, 1992.

[84] F. Gustafsson, "Slip-based tire-road friction estimation," *Automatica*, 1997, ISSN: 00051098. DOI: 10.1016/s0005-1098(97)00003-4.

[85] S. Müller, M. Uchanski, and K. Hedrick, "Slip-based tire-road friction estimation during braking," vol. 2, pp. 1165–1172, Jan. 2001.

[86] M. Uchanski, "Road friction estimation for automobiles using digital signal processing methods," *Dissertation*, 2001.

[87] S. L. Miller, B. Youngberg, A. Millie, P. Schweizer, and J. C. Gerdes, "Calculating longitudinal wheel slip and tire parameters using GPS velocity," in *Proceedings of the 2001 American Control Conference. (Cat. No.01CH37148)*, vol. 3, 2001, 1800–1805 vol.3.

[88] T. Umeno, E. Ono, and K. Asano, "Estimation of tire-road friction using tire vibration model," *Society*, vol. 2002, no. 724, 2002.

[89] E. Ono, K. Asano, M. Sugai, *et al.*, "Estimation of automotive tire force characteristics using wheel velocity," *Control Engineering Practice*, vol. 11, no. 12, pp. 1361–1370, 2003, ISSN: 09670661. DOI: 10.1016/S0967-0661(03)00073-X.

[90] M. Zanon, J. V. Frasch, and M. Diehl, "Nonlinear moving horizon estimation for combined state and friction coefficient estimation in autonomous driving," *2013 European Control Conference, ECC 2013*, pp. 4130–4135, 2013. DOI: 10.23919/ecc.2013.6669832.

[91] M. Wielitzka, M. Dagen, and T. Ortmaier, "Sensitivity-based road friction estimation in vehicle dynamics using the unscented kalman filter," eng, in *2018 Annual American Control Conference (ACC)*, vol. 2018-, AACC, 2018, pp. 2593–2598, ISBN: 9781538654286.

[92] A. Albinsson, F. Bruzelius, T. Gustafsson, M. Jonasson, and B. Jacobson, "Identification of tyre characteristics using active force excitation," Aug. 2015, ISBN: 978-1-138-02885-2. DOI: 10.1201/b21185-55.

[93] E. Siampis, E. Velenis, and S. Longo, "Rear wheel torque vectoring model predictive control with velocity regulation for electric vehicles," *Vehicle System Dynamics*, vol. 53, no. 11, pp. 1555–1579, 2015. DOI: 10.1080/00423114.2015.1064972.

[94] A. R. Teel and N. Kapoor, "The L2 anti-winup problem: Its definition and solution," eng, in *1997 European Control Conference (ECC)*, IEEE, 1997, pp. 1897–1902, ISBN: 9783952426906.

[95] L. Zaccarian, Y. Li, E. Weyer, M. Cantoni, and A. Teel, "Anti-windup for marginally stable plants applied to open water channels," in *2004 5th Asian Control Conference (IEEE Cat. No.04EX904)*, vol. 3, 2004.

[96] S. Tarbouriech, *Stability and Stabilization of Linear Systems with Saturating Actuators*, eng, 1st ed. 2011. London: Springer London, 2011, ISBN: 0-85729-941-7.

[97] P. O. M. Scokaert and D. Q. Mayne, "Min-max feedback model predictive control for constrained linear systems," *IEEE Transactions on Automatic Control*, vol. 43, no. 8, pp. 1136–1142, Aug. 1998, ISSN: 0018-9286. DOI: 10.1109/9.704989.

[98] D. Munoz de La Pena, T. Alamo, D. R. Ramirez, and E. F. Camacho, "Min-max model predictive control as a quadratic program," *IET Control Theory Applications*, vol. 1, no. 1, pp. 328–333, Jan. 2007, ISSN: 1751-8644. DOI: 10.1049/iet-cta:20060016.

[99] D. D. Ruscio, "Model Predictive Control with Integral Action: A simple MPC algorithm," *Modeling, Identification and Control*, vol. 34, no. 3, pp. 119–129, 2013, ISSN: 03327353. DOI: 10.4173/mic.2013.3.2.

[100] S. Gros, M. Zanon, R. Quirynen, A. Bemporad, and M. Diehl, "From linear to nonlinear MPC: Bridging the gap via the real-time iteration," *International Journal of Control*, vol. 93, no. 1, pp. 62–80, 2020. DOI: 10.1080/00207179.2016.1222553. [Online]. Available: https://doi.org/10.1080/00207179.2016.1222553.

[101] M. Diehl, "Real-time optimization for large scale nonlinear processes," Ph.D. dissertation, Universität Heidelberg, 2001.

[102] R. Verschueren, G. Frison, D. Kouzoupis, *et al.*, *Acados: A modular open-source framework for fast embedded optimal control*, 2020. arXiv: 1910.13753 [math.OC].

[103] S. Oleksowicz, K. Burnham, and A. Gajek, "On the legal, safety and control aspects of regenerative braking in hybrid/electric vehicles," Sep. 2012.

[104] C. N. Kumar and S. C. Subramanian, "Cooperative control of regenerative braking and friction braking for a hybrid electric vehicle," *Proceedings of the Institution of Mechanical Engineers, Part D: Journal of Automobile Engineering*, vol. 230, no. 1, pp. 103–116, 2016. DOI: 10.1177/0954407015581082.

[105] L. Zhang, L. Yu, N. Pan, Y. Zhang, and J. Song, "Cooperative control of regenerative braking and friction braking in the transient process of anti-lock braking activation in electric vehicles," *Proceedings of the Institution of Mechanical Engineers, Part D: Journal of Automobile Engineering*, vol. 230, no. 11, pp. 1459–1476, 2016. DOI: 10.1177/0954407015613193.

[106] B. Wang, X. Huang, J. Wang, X. Guo, and X. Zhu, "A robust wheel slip ratio control design combining hydraulic and regenerative braking systems for in-wheel-motors-driven electric vehicles," *Journal of the Franklin Institute*, vol. 352, no. 2, pp. 577–602, 2015, Special Issue on Control and Estimation of Electrified vehicles, ISSN: 0016-0032. DOI: https://doi.org/10.1016/j.jfranklin.2014.06.004. [Online]. Available: https://www.sciencedirect.com/science/article/pii/S0016003214001756.

[107] R. De Castro, R. E. Araújo, M. Tanelli, S. M. Savaresi, and D. Freitas, "Torque blending and wheel slip control in EVs with in-wheel motors," *Vehicle System Dynamics*, vol. 50, no. SUPPL. 1, pp. 71–94, 2012, ISSN: 00423114. DOI: 10.1080/00423114.2012.666357.

[108] L. Filipozzi, F. Assadian, M. Kuang, R. Johri, and J. Velazquez Alcantar, "An investigation into the traction and anti-lock braking system control design," in *SAE Technical Paper*, SAE International, Apr. 2020. DOI: 10.4271/2020-01-0997. [Online]. Available: https://doi.org/10.4271/2020-01-0997.

[109] L. Zaccarian and A. R. Teel, "A common framework for anti-windup, bumpless transfer and reliable designs," eng, *Automatica*, vol. 38, no. 10, pp. 1735–1744, 2002, ISSN: 0005-1098.

[110] R. S. Sharp and V. Valtetsiotis, "Optimal preview car steering control," *Vehicle System Dynamics Supplement*, vol. 35, pp. 101–117, 2001.

[111] *MATLAB robust control toolbox*, The MathWorks, Natick, MA, USA, 2019.

[112] C. Scherer, "Mixed H2/H-infinity control," *Trends in Control: A European Perspective*, pp. 173–216, 1995.

[113] H. Ferreau, A. Potschka, and C. Kirches, *qpOASES webpage*, http://www.qpOASES.org/, 2017.

[114] H. Ferreau, H. Bock, and M. Diehl, "An online active set strategy to overcome the limitations of explicit mpc," *International Journal of Robust and Nonlinear Control*, vol. 18, no. 8, pp. 816–830, 2008.

[115] H. Ferreau, C. Kirches, A. Potschka, H. Bock, and M. Diehl, "qpOASES: A parametric active-set algorithm for quadratic programming," *Mathematical Programming Computation*, vol. 6, no. 4, pp. 327–363, 2014.

Appendix A

Robust Dynamic Control Allocation Synthesis

From Equations (3.25) and (3.26), if bounds on the structured singular values are not enough to guarantee robust performance and stability, or if the uncertainties cannot be represented by Equation (3.20) with invertible filters W_u and W_y, another approach must be conducted to design a robust feedback loop with dynamic control allocation. This chapter proposes a general solution to this problem by modifying the DK-iteration algorithm used for μ-synthesis.

Using the LFT framework, μ-synthesis is a method that aims at finding a controller that minimizes the maximum μ-value of an uncertain system over a frequency range to maximize the robust performance of the closed-loop system. There is no direct way to compute such a controller directly; therefore, μ-synthesized controllers are usually computed with the DK-iteration algorithm, which is motivated by the following upper-bound on the μ value:

$$\mu_{\bar{\Delta}}(N(j\omega)) \leq \overline{\sigma}(D_R N D_L^{-1}(j\omega)),\ (D_L, D_R) \in \mathcal{S}_{\bar{\Delta}} \tag{A.1}$$

$$\text{where } \mathcal{S}_{\bar{\Delta}} = \{(D_L, D_R) \in \mathbb{R}^{n_{u_{\bar{\Delta}}} \times n_{u_{\bar{\Delta}}}} \times \mathbb{R}^{n_{y_{\bar{\Delta}}} \times n_{y_{\bar{\Delta}}}} \mid D_L \bar{\Delta} = \bar{\Delta} D_R\} \tag{A.2}$$

The DK-iteration algorithm, described in Algorithm 1, works in two steps. In the D-step, the two scaling filters D_L and D_R are computed in order to minimize the upper-bound $\left\| D_R F_l(P, K) D_L^{-1} \right\|_\infty$ given a controller K. In the K-step, a controller is computed by solving an H_∞-synthesis problem that minimizes the ∞-norm of the scaled closed-loop $D_R F_l(P, K) D_L^{-1}$ given the scaling filters (D_L, D_R). By successively iterating between the K and D steps, the DK-iteration algorithm tries to minimize the upper-bound (A.1), which in turn minimizes the μ-value of the closed-loop. Nevertheless, the

Algorithm 1 DK-iteration algorithm

Input: Augmented plant P
Parameters: Signal size n_{u_K}, n_{y_K}
Output: Robust controller K_μ

$\mu \leftarrow \infty$, $P_D \leftarrow P$
while termination condition not reached **do**
  Solve the $\mathcal{H}_\infty$-optimization problem in K: *// K-step*

$$K = \arg\min_K \|F_l(P_D, K)\|_\infty$$

  if $\|F_l(P_D, K)\|_\infty = \infty$ **then**
    break
  end if
  Solve the optimization problem for several frequencies ω: *// D-step*

$$(D_L, D_R) = \arg\min_{(D_L, D_R) \in \mathcal{S}_{\bar{\Delta}}} \bar{\sigma}(D_R F_l(P, K) D_L^{-1}(j\omega))$$

  Fit stable minimum-phase filters $D_L(s)$ over $(\omega, D_L(j\omega))$ and $D_R(s)$ over $(\omega, D_R(j\omega))$.
  Compute the scaled augmented system P_D as follows

$$P_D \leftarrow \begin{bmatrix} D_R & 0 \\ 0 & I_{n_{y_K}} \end{bmatrix} P \begin{bmatrix} D_L^{-1} & 0 \\ 0 & I_{n_{u_K}} \end{bmatrix}$$

  if $\max_\omega \mu_{\bar{\Delta}}(F_l(P, K)(j\omega)) < \mu$ **then** *// Select the best controller*
    $K_\mu \leftarrow K$ and $\mu \leftarrow \max_\omega \mu_{\bar{\Delta}}(F_l(P, K)(j\omega))$
  end if
end while
return K_μ

DK-iteration algorithm does not guarantee finding the optimal controller and may converge to a local optimum.

We propose to modify the DK-iteration algorithm to modify the K-step to solve an H_∞-optimization problem subject to an H_2 constraint. This optimization problem can be achieved by a mixed $\mathcal{H}_2/\mathcal{H}_\infty$-synthesis. For mixed $\mathcal{H}_2/\mathcal{H}_\infty$ optimization, the regulated outputs z are divided into two parts $z^T = [z_\infty^T \quad z_2^T]$ to define two augmented plants P^2 and P^∞; the optimization minimizes a weighted sum of the $\mathcal{H}_2$-norm of P^2 and the $\mathcal{H}_\infty$-norms of P^∞ subject to constraints on each norm [111], [112].

$$\arg\min_K \alpha \|F_l(P^\infty, K)\|_\infty^2 + \beta \left\|F_l(P^2, K)\right\|_2^2 \tag{A.3a}$$

$$\text{s.t. } \|F_l(P^\infty, K)\|_\infty \leq \gamma_0 \tag{A.3b}$$

$$\left\|F_l(P^2, K)\right\|_2 \leq \nu_0 \tag{A.3c}$$

By setting $\alpha = 1$, $\beta = 0$, and $\gamma_0 = \infty$, it is possible to minimize an $\mathcal{H}_\infty$-norm subject to a

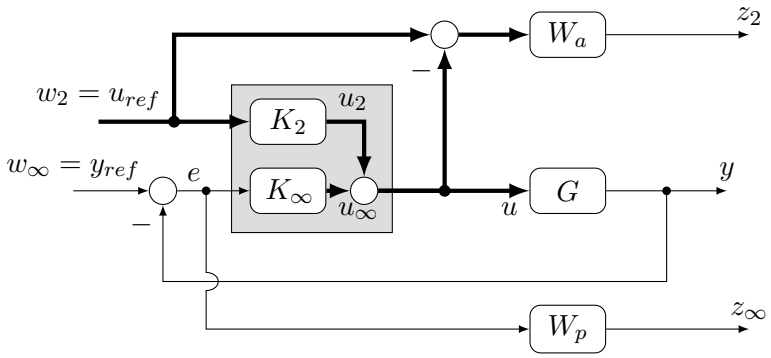

Figure A.1: Augmented system for the controller/allocator synthesis

constraint on the $\mathcal{H}_2$-norm. In this section, the control allocation performance is expressed as a $\mathcal{H}_2$-norm on the plant mapping exogenous inputs to the signal $z_2 = W_a(u_{ref} - u)$. If the objective is that u tracks a constant signal u_{ref} during steady-state, the weight $W_a(s)$ should be big at low-frequencies and small at high-frequencies.

Robust performance specifications are set by the filter W_p which defines a signal $z_\infty = W_p(y_{ref} - y)$, see Figure A.1. Modifying the K-step to minimize the $\mathcal{H}_\infty$-norm of the plant P^∞ mapping exogenous inputs w to $z_\infty = W_p(y_{ref} - y)$ with a constraints on the $\mathcal{H}_2$-norm of the plant P^2 mapping w to z_2 will aim at finding the most robust controller able to achieve a desired control allocation performance.

For an over-actuated system, the number of secondary objectives that can be achieved while providing output tracking during steady-state is given by $n_u - r$, where n_u is the number of actuators and r is the rank of the system; therefore, the signal z_2 should have at most $n_a = n_u - r$ elements. We showed that connecting the Smith-McMillan-based allocator to the control loop is equivalent to modifying the feedback controller and adding a feedforward term from the desired control distribution u_{ref} to the applied input u; the same structure will be used to synthesize a robust controller for the over-actuated system. Figure A.1 shows the controller K is decomposed into two parts, a feed-forward term K_2 and a feedback controller K_∞. One major drawback of the method presented compared to the Smith-McMillan-based allocator is that the design of the allocator and the controller are not independent; instead, a unique controller K will achieve both roles.

The modified DK-iteration algorithm, which computes a robust controller while enforcing an $\mathcal{H}_2$ constraint, is shown in Algorithm 2. Its inputs are the upper bound on the $\mathcal{H}_2$ constraint and an augmented plant P mapping the output of the uncertainty block u_Δ, the exogenous output w, the

Algorithm 2 Modified DK-iteration algorithm subject to an $\mathcal{H}_2$-constraint

Input: Augmented plant P, upper-bound ν_0
Parameters: Signals size n_{u_K}, n_{y_K}, n_{w_2}, n_{z_2}, n_{y_Δ}, n_{z_∞}
Output: Robust controller K_μ

$\mu \leftarrow \infty$, $P^2 \leftarrow \begin{bmatrix} 0 & I_{n_{z_2}+n_{y_K}} \end{bmatrix} P$, $P^\infty \leftarrow \begin{bmatrix} I_{n_{y_\Delta}+n_{z_\infty}} & 0 & 0 \\ 0 & 0 & I_{n_{y_K}} \end{bmatrix} P$, $P_D^\infty \leftarrow P^\infty$
while termination condition not reached **do**
  Solve the mixed $\mathcal{H}_2/\mathcal{H}_\infty$-optimization problem: *// K-step*

$$\begin{aligned} \arg\min_K \quad & \|F_l(P_D^\infty, K)\|_\infty \\ \text{s.t.} \quad & \left\|F_l(P^2, K)\right\|_2 \leq \nu_0 \end{aligned}$$

  if no solution K **or** $\|F_l(P_D, K)\|_\infty = \infty$ **then**
    break
  end if
  Solve the optimization problem for several frequencies ω: *// D-step*

$$(D_L, D_R) = \arg\min_{(D_L, D_R) \in \mathcal{S}_{\bar{\Delta}}} \bar{\sigma}(D_R F_l(P^\infty, K) D_L^{-1}(j\omega))$$

  Fit stable minimum-phase filters $D_L(s)$ over $(\omega, D_L(j\omega))$ and $D_R(s)$ over $(\omega, D_R(j\omega))$.
  Compute the scaled augmented system P_D^∞ with exogenous output z_∞ as follows

$$P_D^\infty \leftarrow \begin{bmatrix} D_R & 0 & 0 \\ 0 & 0 & I_{n_{y_K}} \end{bmatrix} P \begin{bmatrix} D_L^{-1} & 0 \\ 0 & I_{n_{w_2}+n_{u_K}} \end{bmatrix}$$

  if $\max_\omega \mu_{\bar{\Delta}}(F_l(P^\infty, K)(j\omega)) < \mu$ **then** *// Select the best controller*
    $K_\mu \leftarrow K$ and $\mu \leftarrow \max_\omega \mu_{\bar{\Delta}}(F_l(P^\infty, K)(j\omega))$
  end if
end while
return K_μ

controller output u_K to the input of the uncertainty block y_Δ, regulated output z, and controller input y_K. As is has been said, the regulated outputs are decomposed into two parts, the same applies to the exogenous inputs w, they are decomposed into w_2 and w_∞ such that $w^T = [w_\infty^T \quad w_2^T]$. We assume that there is no coupling in the mapping from w_∞ to z_2 and from w_2 to z_∞; this assumption is necessary to avoid scaling $\mathcal{H}_2$ constraint by the D_L and D_R filters used in the D-step.

Like to the original DK-iteration algorithm, the D-step computes the filters D_L and D_R to scale the augmented plant P^∞. The K-step has been modified to minimize the H_∞-norm of the scaled closed-loop $F_l(P_D^\infty, K)$ subject to an H_2 constraint on the closed-loop $F_l(P^2, K)$.

Example with an Ill-Conditioned System The plant describes an over-actuated system. Although the plant defined in Equation (A.4) has maximum rank, it is ill-conditioned and its condition number is $\kappa(G_p) = 40$. The plant is assumed to have multiplicative input and output uncertainties as defined in Equation (3.20). In this example, only the second actuator suffers from uncertainties.

The weighting filters on the uncertainty blocks are:

$$G_p = \frac{1}{75s+1}\begin{bmatrix} 85 & 80 & 75 \\ 100 & 100 & 100 \end{bmatrix} \tag{A.4}$$

$$W_u = \mathrm{diag}(0, w_\Delta, 0),\ W_y = w_\Delta I_2,\ w_\Delta = \frac{3s+0.42}{s+42} \tag{A.5}$$

The filter W_u is not invertible, thus Equations (3.25) and (3.26) do not apply. The objective of the control allocation is to minimize a tracking error between a target value and the actual value of the first actuator as defined by the following filter

$$W_p^T = \frac{3.16\times10^{-3}s+3.16}{s+3.16\times10^{-6}},\quad W_a^T = \begin{bmatrix} \frac{100}{10s+1} & 0 & 0 \end{bmatrix} \tag{A.6}$$

The uncertainty block of the input and output multiplicative uncertainty are stacked in a single uncertainty block Δ. With the LFT framework, the controller input are $y_K^T = [u_ref^T \quad (y_{ref}-y)^T]$ and its output is $u_K = u$. The exogenous inputs are $w^T = [w_\infty^T \quad w_2^T] = [y_{ref}^T \quad u_{ref}^T]$ and the regulated outputs are $z^T = [z_\infty^T \quad z_2^T]$. The augmented system mapping $[u_\Delta^T \quad w^T \quad u_K^T]$ to $[y_\Delta^T \quad z^T \quad y_K^T]$ is given by:

$$P = \mathrm{diag}(W_u, W_y, W_p, W_a, I) \times \left[\begin{array}{cc:cc:c} 0 & 0 & 0 & 0 & I \\ G_p & 0 & 0 & 0 & G_p \\ \hdashline -G_p & -I & I & 0 & -G_p \\ 0 & 0 & 0 & I & -I \\ \hdashline 0 & 0 & 0 & I & 0 \\ -G_p & -I & I & 0 & -G_p \end{array}\right] \tag{A.7}$$

The Smith-McMillan-based allocator G_a does not provide combined robustness with control allocation for such a system. Indeed, with a controller K_G designed via μ-synthesis,[1] connecting the allocator substantially degrades the robustness of the feedback loop. Table A.1 shows that the μ-value for robust performance is 0.58 without allocator, and 2.05 with allocator. Designing a controller $K_{G(I-G_a)}$ based on an augmented system that includes the allocator improves the robustness while

[1]The controller K_G ignores the presence of the allocator G_a in its design, contrary to the controller $K_{G(I-G_a)}$; this is used to show that the flexibility offered by designing the allocator and controller independently comes at the expense of robustness.

Table A.1: Trade-off between robust performance (quantified by $\max_\omega \mu_{\bar{\Delta}}(N^\infty(j\omega))$) and dynamic control allocation (quantified by $\left\|N^2\right\|_2$) for an ill-conditioned system.

Feedback Controller	Feedforward controller	$\max_\omega \mu_{\bar{\Delta}}(N^\infty(j\omega))$	$\left\|N^2\right\|_2$
K_G	0	0.58	340
$(I - G_a)K_G$	G_a	2.05	0
$(I - G_a)K_{G(I-G_a)}$	G_a	1.45	0

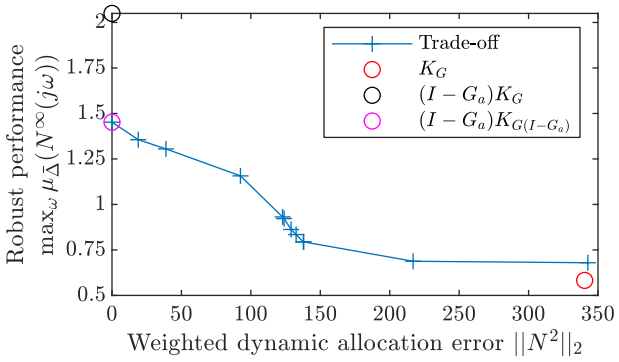

Figure A.2: Trade-off between robust performance and dynamic control allocation

providing reasonable control allocation. This result suggests that there is a trade-off between control allocation and robust performance for this ill-conditioned plant.

Figure A.2 shows the structured singular value for robust performance and the control allocation metric of the closed-loop with several controllers designed using Algorithm 2; note that the algorithm is initialized with the feedforward controller $K_2 = G_a$ and the feedback controller $K_\infty = (I - G_a)K_{G(I-G_a)}$. Relaxing the $\mathcal{H}_2$ constraint allows the algorithm to find a controller which provides better robustness at the expense of control allocation; this further illustrates the trade-off between control allocation and robust performance that this ill-conditioned system exhibits. Figure A.3 shows the output and input responses with several controllers. On the one hand, controllers which track the desired input u_1 do not have good robust performance; on the other hand, controllers with robust performance do not have good control allocation performance.

Like the original DK-iteration algorithm, the modified algorithm is not guaranteed to find the optimal solution. This is illustrated by the controller obtained using the modified DK-iteration algorithm which yield the point $\max_\omega \mu_{\bar{\Delta}}(N^\infty(j\omega)) = 0.68$ and $\left\|N^2\right\|_2 = 342$, this controller is less optimal than K_G both in terms of robustness and control allocation since K_G yields $\max_\omega \mu_{\bar{\Delta}}(N^\infty(j\omega)) = 0.58$ and $\left\|N^2\right\|_2 = 340$.

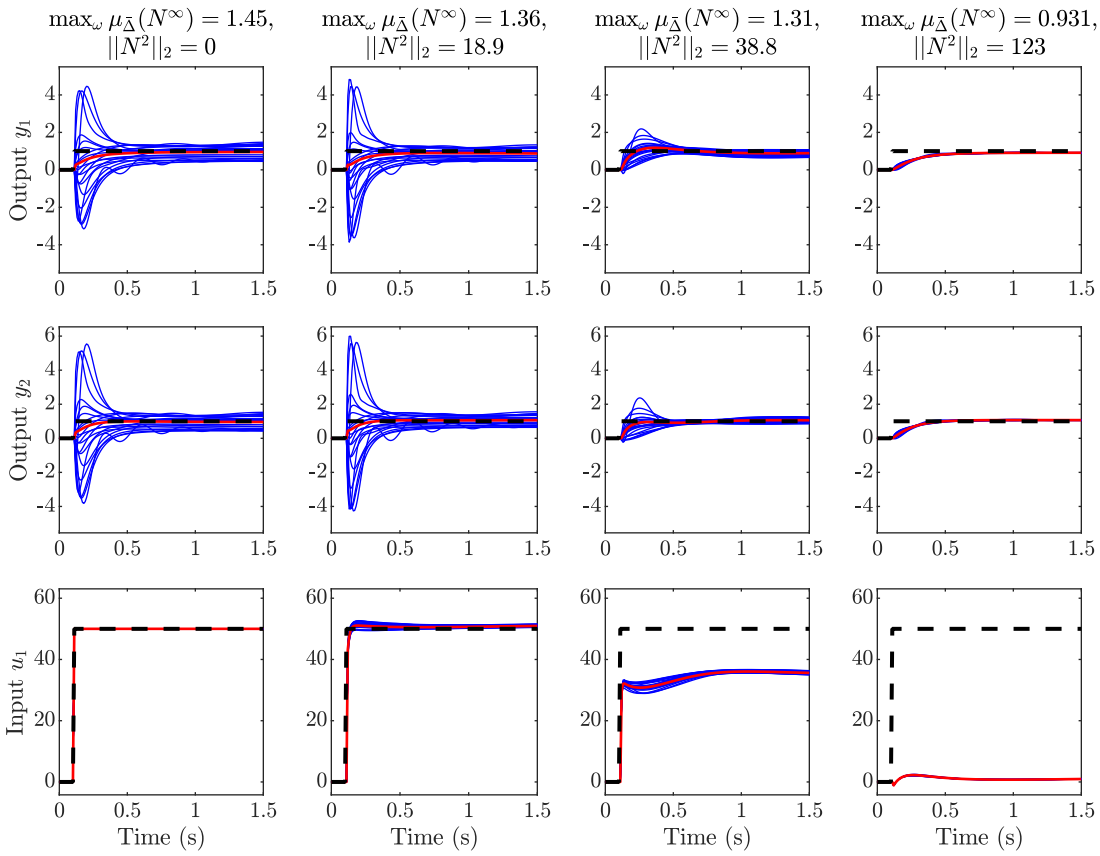

Figure A.3: Closed-loop response of several controllers designed with the modified DK-iteration algorithm. Blue curve show the response with a sampled uncertain system, the red curve correspond to the nominal system.

Appendix B

Solving a Model Predictive Control Problem

MPC is a control method that uses an internal representation of the system it controls to define command by minimizing a control function and enforcing constraints. The internal model is used to propagate or simulate the model over a finite horizon in the future: at time t, the internal model will generate a sequence of inputs to apply to the system and enforce constraints over a time window $[t, t+T]$ called prediction horizon, only the first element of this sequence of input will actually be used by the plant; at the next timestep $t+T_s$, this process will be repeated over the time window $[t+T_s, t+T_s+T]$. Note that the time window over which the controller generates a sequence of input is not always the same as the one used to enforce constraints; in this case, the controller uses different control and prediction horizons.

The MPC shown in this chapter uses a nonlinear system as its internal model, its outputs are computed by optimization methods and model is linearized during each timestep at the current state x_0 and the previous input u_{-1}, if the model is defined by the state function $\dot{x} = f(x,u)$ and output function $y = g(x,u)$, the linearized state-space is defined from the Jacobian matrices:

$$A_c = \frac{\partial f}{\partial x}\Big|_{(x_0,u_{-1})},\ B_c = \frac{\partial f}{\partial u}\Big|_{(x_0,u_{-1})},\ C = \frac{\partial g}{\partial x}\Big|_{(x_0,u_{-1})},\ D = \frac{\partial g}{\partial u}\Big|_{(x_0,u_{-1})} \tag{B.1}$$

Variables $\tilde{x}_k = x_k - x_0$, $\tilde{u}_k = u_k - u_{-1}$ and $\tilde{y}_k$ denote the perturbed variables obtained after linearization; x_0, u_{-1}, and $y_0 = g(x_0, u_{-1})$ are the linearization points. Moreover, $\tilde{y}_{ref}$ is defined as $\tilde{y}_{ref} = y_{ref} - y_0$. The MPC is a discrete-time controller and the model it is designed upon needs to be discrete-time. The continuous-time state-space (A_c, B_c, C, D) can be discretized into the discrete-time state-space system (A, B, C, D). Assuming a sampling time T_s and that the control

input u_k is kept constant over the sampling time, the discrete-time state space can be obtained from the following transformation:

$$A = e^{A_c T_s},\ B = \int_0^{T_s} B_c e^{A_c \tau}\, \mathrm{d}\tau \tag{B.2}$$

The following equation describes the MPC control problem, penalizes the tracking error, actuator use, and actuator rate of change and is subject to actuator bounds constraints and polytopic constraints on the states x_k and inputs u_k. Variables N_t and N_p refers to the control and prediction horizon and $N_t \leq N_p$. After the control horizon, the control input are kept constant, possibly at a non-zero value, i.e. $\forall k \geq N_t,\ u_k = u_{N_t-1}$ or equivalently $\tilde{u}_k = \tilde{u}_{N_t-1}$. To simplify the notations, only the timestep within the receding horizon is indicated, the time at which the horizon starts is not shown, all variable refers to the timestep within the receding horizon starting at time t with the exception of u_{-1} which refers to the value of u at the first timestep of the previous receding horizon starting at $t - T_s$. The timestep at which the receding horizon starts is not indicated. The MPC problem is written as follows,

$$\underset{(\tilde{u}_k)_{k\in[\![0,N-1]\!]}}{\arg\min} \sum_{k=0}^{N_p-1} ||y_k - y_{ref}||^2_{Q_e} + \sum_{k=0}^{N_p-1} ||u_k||^2_{R_u} + \sum_{k=0}^{N_t-1} ||\Delta u_k||^2_{R_{\Delta u}} \tag{B.3}$$

$$\text{subject to: } \tilde{x}_0 = 0 \tag{B.4}$$

$$\tilde{x}_k = x_k - x_0,\ \tilde{u}_k = u_k - u_{-1},\ \tilde{y}_k = y_k - y_0 \quad \forall k \in [\![0, N_p - 1]\!] \tag{B.5}$$

$$\tilde{x}_{k+1} = A\tilde{x}_k + B\tilde{u}_k \quad \forall k \in [\![0, N_p - 1]\!] \tag{B.6}$$

$$\tilde{y}_k = C\tilde{x}_k + D\tilde{u}_k \quad \forall k \in [\![0, N_p - 1]\!] \tag{B.7}$$

$$\Delta u_k = u_k - u_{k-1} \quad \forall k \in [\![0, N_p - 1]\!] \tag{B.8}$$

$$u_{min} \leq u_{-1} + \tilde{u}_k \leq u_{max} \quad \forall k \in [\![0, N_p - 1]\!] \tag{B.9}$$

$$A_x(x_0 + \tilde{x}_k) + A_u(u_{-1} + \tilde{u}_k) \leq b \quad \forall k \in [\![0, N_p - 1]\!] \tag{B.10}$$

$$u_k = u_{N_t-1} \quad \forall k \geq N_t \tag{B.11}$$

To solve the MPC problem, it is reformulated as a standard quadratic programming problem using the batch approach whose decision variables are the control inputs u_k over the control horizon. The problem can then be solved using a QP solver. In this work, the solver qpOASES is used [113], [114],

it is based on the online active set strategy [115]. The following paragraphs show how to express the cost function and the constraints as a function of the initial state $\tilde{x}_0$ and the sequence of control inputs over the control horizon $\tilde{\mathbf{u}}$.

It is convenient to stack the sequence of states, inputs and inputs rate of change over the control and prediction horizons to define the following vectors:

$$\tilde{\mathbf{x}}^T = \begin{bmatrix} \tilde{x}_0^T & \dots & \tilde{x}_{N_p-1}^T \end{bmatrix}, \quad \tilde{\mathbf{u}}_\mathbf{p}^T = \begin{bmatrix} \tilde{u}_0^T & \dots & \tilde{u}_{N_p-1}^T \end{bmatrix}, \tag{B.12}$$

$$\tilde{\mathbf{u}}^T = \begin{bmatrix} \tilde{u}_0^T & \dots & \tilde{u}_{N_t-1}^T \end{bmatrix}, \quad \boldsymbol{\Delta}\mathbf{u}^T = \begin{bmatrix} \Delta u_0^T & \dots & \Delta u_{N_t-1}^T \end{bmatrix} \tag{B.13}$$

The input rate of change $\Delta u_k = u_k - u_{k-1}$ can be rewritten in terms of the perturbed variables $\Delta u_k = \tilde{u}_k - \tilde{u}_{k-1}$ since the linerization point does not change. Moreover, the controls are constrained to be constant after the control horizon. Thus, the sequence of control signals over the prediction horizon $\tilde{\mathbf{u}}_\mathbf{p}$ and the sequence of input rate of change $\boldsymbol{\Delta}\mathbf{u}$ can be expressed as function of the sequence of control signals over the control horizon $\tilde{\mathbf{u}}_\mathbf{p}$ as follows,

$$\tilde{\mathbf{u}}_\mathbf{p} = \underbrace{\begin{bmatrix} I_{N_u} & 0 & \cdots & 0 \\ 0 & \ddots & \ddots & \vdots \\ \vdots & \ddots & \ddots & 0 \\ \vdots & & 0 & I_{N_u} \\ \vdots & & 0 & \vdots \\ 0 & \cdots & 0 & I_{N_u} \end{bmatrix}}_{S_{\tilde{u}_p}} \tilde{\mathbf{u}}, \quad \boldsymbol{\Delta}\mathbf{u} = \underbrace{\begin{bmatrix} I_{N_u} & 0 & \cdots & 0 \\ -I_{N_u} & \ddots & \ddots & \vdots \\ 0 & \ddots & \ddots & 0 \\ \vdots & \ddots & -I_{N_u} & I_{N_u} \\ \vdots & & 0 & 0 \\ \vdots & & \vdots & \vdots \\ 0 & \cdots & 0 & 0 \end{bmatrix}}_{S_{\Delta u}} \tilde{\mathbf{u}} \tag{B.14}$$

The sequence of states over the prediction horizon can be computed from the initial state and

sequence of input over the prediction horizon from the state update equation (B.6).

$$\tilde{\mathbf{x}} = \underbrace{\begin{bmatrix} I_{N_x} \\ A \\ \vdots \\ A^{N_p-1} \end{bmatrix}}_{S_x} \tilde{x}_0 + \underbrace{\begin{bmatrix} 0 & \cdots & \cdots & 0 \\ B & \ddots & & \vdots \\ AB & \ddots & \ddots & \vdots \\ \vdots & \ddots & \ddots & 0 \\ A^{N_p-1}B & \cdots & AB & B \end{bmatrix}}_{S_u} \tilde{\mathbf{u}}_\mathbf{p} \tag{B.15}$$

$S_{\tilde{u}_p}$ is $N_u N_p \times N_u N_t$, $S_{\Delta u}$ is $N_u N_p \times N_u N_t$, S_x is $N_x N_t \times N_x$ and S_u is $N_x N_p \times N_u N_p$. Using (B.14) to express $\tilde{\mathbf{u}}_\mathbf{p}$ as function of $\tilde{\mathbf{u}}$, the above equation can be rewritten as $\tilde{\mathbf{x}} = S_x \tilde{x}_0 + \bar{S}_u \tilde{\mathbf{u}}$ where $\bar{S}_u = S_u S_{\tilde{u}_p}$.

Plugging (B.7) in the cost function and substituting u_k by $\tilde{u}_k + u_{-1}$ leads allows to reformulate the cost function $\mathcal{J}$ as follows,

$$\begin{aligned} \mathcal{J} = & \sum_{k=0}^{N_p-1} \begin{bmatrix} \tilde{x}_k^T & \tilde{u}_k^T \end{bmatrix} \begin{bmatrix} C^T Q_e C & C^T Q_e D \\ D^T Q_e C & D^T Q_e D + R_u \end{bmatrix} \begin{bmatrix} \tilde{x}_k \\ \tilde{u}_k \end{bmatrix} \\ & + \sum_{k=0}^{N_p-1} \begin{bmatrix} -2\tilde{y}_{ref}^T Q_e C & -2\tilde{y}_{ref}^T Q_e D + 2u_{-1}^T R_u \end{bmatrix} \begin{bmatrix} \tilde{x}_k \\ \tilde{u}_k \end{bmatrix} \\ & + \sum_{k=0}^{N_t-1} \Delta u_k^T R_{\Delta u} \Delta u_k + \sum_{k=0}^{N_p-1} u_{-1}^T R_u u_{-1} \end{aligned} \tag{B.16}$$

The last term of the cost function is constant and can be ignored. Introducing the following matrices,

$$\begin{aligned} \bar{Q} &= \text{blockdiag}(C^T Q_e C, \ldots, C^T Q_e C) \\ \bar{R}_u &= \text{blockdiag}(D^T Q_e D + R_u, \ldots, D^T Q_e D + R_u) \\ \bar{R}_{\Delta u} &= \text{blockdiag}(R_{\Delta u}, \ldots, R_{\Delta u}) \\ \bar{T} &= \text{blockdiag}(C^T Q_e D, \ldots, C^T Q_e D) \\ F_x^T &= \begin{bmatrix} -2\tilde{y}_{ref}^T Q_e C & \ldots & -2\tilde{y}_{ref}^T Q_e C \end{bmatrix} \end{aligned}$$

$$F_u^T = \begin{bmatrix} -2\tilde{y}_{ref}^T Q_e D + 2u_{-1}^T R_u & \dots & -2\tilde{y}_{ref}^T Q_e D + 2u_{-1}^T R_u \end{bmatrix}$$

where $\bar{Q}$ is $N_x N_p \times N_x N_p$, $\bar{R}_u$ is $N_u N_p \times N_u N_p$, $\bar{R}_{\Delta u}$ is $N_u N_p \times N_u N_p$, $\bar{T}$ is $N_x N_p \times N_u N_p$, F_x is $N_x N_p \times 1$, and F_u is $N_u N_p \times 1$, the cost function can be reformulated as follows,

$$\mathcal{J} = \begin{bmatrix} \tilde{\mathbf{x}}^T & \tilde{\mathbf{u}}_\mathbf{p}^T \end{bmatrix} \begin{bmatrix} \bar{Q} & \bar{T} \\ \bar{T}^T & \bar{R}_u \end{bmatrix} \begin{bmatrix} \tilde{\mathbf{x}} \\ \tilde{\mathbf{u}}_\mathbf{p} \end{bmatrix} + \begin{bmatrix} F_x^T & F_u^T \end{bmatrix} \begin{bmatrix} \tilde{\mathbf{x}} \\ \tilde{\mathbf{u}}_\mathbf{p} \end{bmatrix} + \mathbf{\Delta u}^T \bar{R}_{\Delta u} \mathbf{\Delta u} \tag{B.17}$$

Using $\tilde{\mathbf{u}}_\mathbf{p} = S_{\tilde{u}_p} \tilde{\mathbf{u}}$, $\mathbf{\Delta u} = S_{\Delta u} \tilde{\mathbf{u}}$, and $\tilde{\mathbf{x}} = S_x \tilde{x}_0 + S_u \tilde{\mathbf{u}}_\mathbf{p}$ from (B.14) and (B.15) to substitute $\tilde{\mathbf{x}}$, $\tilde{\mathbf{u}}_\mathbf{p}$, and $\mathbf{\Delta u}$ in the cost function (B.17) allows to express it only as a function of the initial state and of the sequence of control inputs.

$$\begin{aligned} \mathcal{J} = & \begin{bmatrix} \tilde{x}_0 \\ \tilde{\mathbf{u}} \end{bmatrix}^T \begin{bmatrix} S_x^T \bar{Q} S_x & S_x^T (\bar{Q} \bar{S}_u + \bar{T} S_{\Delta u}) \\ (\bar{Q} \bar{S}_u + \bar{T} S_{\Delta u})^T S_x & \bar{S}_u^T \bar{Q} \bar{S}_u + S_{\tilde{u}_p}^T \bar{T}^T \bar{S}_u + \bar{S}_u^T \bar{T} S_{\tilde{u}_p} + \bar{R} \end{bmatrix} \begin{bmatrix} \tilde{x}_0 \\ \tilde{\mathbf{u}} \end{bmatrix} \\ & + \begin{bmatrix} F_x^T S_x & F_x^T \bar{S}_u + F_u^T S_{\tilde{u}_p} \end{bmatrix} \begin{bmatrix} \tilde{x}_0 \\ \tilde{\mathbf{u}} \end{bmatrix} \end{aligned} \tag{B.18}$$

where $\bar{R} = S_{\tilde{u}_p}^T \bar{R}_u S_{\tilde{u}_p} + S_{\Delta u}^T \bar{R}_{\Delta u} S_{\Delta u}$.

Moreover, inequality and equality constraints can also be reformulated as constraints on $\tilde{\mathbf{u}}$ using the matrices S_x and S_u. Indeed, inequalities constraints are written as $\forall k \in [\![0, N-1]\!],\ A_x \tilde{x}_k + A_u \tilde{u}_k \leq \tilde{b} = b - A_x x_0 - A_u u_{-1}$. Defining the following matrices

$$\bar{A}_x = \text{blockdiag}(A_x, \dots, A_x) \tag{B.19}$$

$$\bar{A}_u = \text{blockdiag}(A_u, \dots, A_u) \tag{B.20}$$

$$\bar{b}^T = \begin{bmatrix} \tilde{b}^T & \dots & \tilde{b}^T \end{bmatrix} \tag{B.21}$$

where $\bar{A}_x$ is $N_{ineq} N_p \times N_x N_p$, $\bar{A}_u$ is $N_{ineq} N_p \times N_u N_p$, and $\bar{b}$ is $N_{ineq} N_p \times 1$ with N_{ineq} the number of polytopic constraints.

The polytopic constraints over the prediction horizon can be written as $\bar{A}_x \tilde{\mathbf{x}} + \bar{A}_u \tilde{\mathbf{u}} \leq \bar{b}$. This yields:

$$(\bar{A}_x \bar{S}_u + \bar{A}_u S_{\tilde{u}_p}) \tilde{\mathbf{u}} \leq \bar{b} - \bar{A}_x S_x \tilde{x}_0 \tag{B.22}$$

Finally, since the MPC problem sets the perturbed initial state $\tilde{x}_0$ to 0, its formulation as a QP problem can be simplified as follows,

$$\arg\min_{\tilde{\mathbf{u}}} \frac{1}{2}\tilde{\mathbf{u}}\bar{H}\tilde{\mathbf{u}} + \bar{F}^T\tilde{\mathbf{u}} \tag{B.23}$$

$$\text{subject to: } \tilde{\mathbf{u}}_{\mathbf{min}} \leq \tilde{\mathbf{u}} \leq \tilde{\mathbf{u}}_{\mathbf{max}} \tag{B.24}$$

$$\bar{A}\tilde{\mathbf{u}} \leq \bar{b} \tag{B.25}$$

where

$$\bar{H} = 2(\bar{S}_u^T\bar{Q}\bar{S}_u + S_{\tilde{u}_p}^T\bar{T}^T\bar{S}_u + \bar{S}_u^T\bar{T}S_{\tilde{u}_p} + \bar{R}) \tag{B.26}$$

$$\bar{F} = \bar{S}_u^T F_x + S_{\tilde{u}_p^T F_u} \tag{B.27}$$

$$\bar{A} = \bar{A}_x\bar{S}_u + \bar{A}_u S_{\tilde{u}_p} \tag{B.28}$$

$$\tilde{\mathbf{u}}_{\mathbf{min}} = \begin{bmatrix} u_{min} - u_{-1} \\ \vdots \\ u_{min} - u_{-1} \end{bmatrix} \text{ and } \tilde{\mathbf{u}}_{\mathbf{max}} = \begin{bmatrix} u_{max} - u_{-1} \\ \vdots \\ u_{max} - u_{-1} \end{bmatrix} \tag{B.29}$$

The previous QP problem has $N_u N_t$ optimization variables which are the controls inputs over the control horizon and is subject to $N_u N_t$ bound constraints on the control inputs in addition to $N_{ineq}N_p$ polytopic constraints on the control inputs.

B.1 Soft Constraints and Slack Variables

Soft constraints are implemented by using slack variables denoted as ϵ, which will be considered as additional optimization variables.

In order to implement soft constraints, two steps are required:

- The inequality constraints $A_x\tilde{x}_k + A_u\tilde{u}_k \leq b$ is replace by $A_x\tilde{x}_k + A_u\tilde{u}_k - A_s\epsilon \leq b$.
- The slack variables are highly penalized in the cost function: $\mathcal{J} \leftarrow \mathcal{J} + \rho\epsilon^2$ where ρ is a positive constant.
- Optionally, the value of the slack variables can be lower bounded by 0.

Using the batch approach, the first condition can be enforced by modifying the inequality constraints of the optimization problem:

$$\bar{A}\tilde{\mathbf{u}} - \bar{A}_s\boldsymbol{\epsilon} \leq \bar{b} \tag{B.30}$$

where $\bar{A}_s$ is a matrix of 1 and 0 used to add the slack variables on the desired inequalities.

Finally, the cost function need to be modified to add the slack variables. The modified optimization problem becomes

$$\arg\min_{\tilde{\mathbf{u}}} \begin{bmatrix} \tilde{\mathbf{u}} & \boldsymbol{\epsilon} \end{bmatrix} \begin{bmatrix} \bar{H} & 0 \\ 0 & \rho I \end{bmatrix} \begin{bmatrix} \tilde{\mathbf{u}} \\ \boldsymbol{\epsilon} \end{bmatrix} + \begin{bmatrix} \bar{F} \\ 0 \end{bmatrix}^T \begin{bmatrix} \tilde{\mathbf{u}} \\ \boldsymbol{\epsilon} \end{bmatrix} \tag{B.31}$$

$$\text{subject to: } \begin{bmatrix} \tilde{\mathbf{u}}_{\mathbf{min}} \\ 0 \end{bmatrix} \leq \begin{bmatrix} \tilde{\mathbf{u}} \\ \boldsymbol{\epsilon} \end{bmatrix} \leq \begin{bmatrix} \tilde{\mathbf{u}}_{\mathbf{max}} \\ \infty \end{bmatrix} \tag{B.32}$$

$$\begin{bmatrix} \bar{A} & \bar{A}_s \end{bmatrix} \begin{bmatrix} \tilde{\mathbf{u}} \\ \boldsymbol{\epsilon} \end{bmatrix} \leq \bar{b} \tag{B.33}$$

B.2 Slew Rate Constraints

Slew rate constraints are formulated as $\forall k \in [\![0, N_t - 1]\!],\ \Delta_{min} \leq \Delta u_k \leq \Delta_{max}$ where $\Delta u_k = u_k - u_{k-1} = \tilde{u}_k - \tilde{u}_{k-1}$. In a matrix form, it gives

$$\begin{bmatrix} I_{N_u} & & & 0 \\ -I_{N_u} & \ddots & & \\ & \ddots & \ddots & \\ 0 & & -I_{N_u} & I_{N_u} \\ -I_{N_u} & & & 0 \\ I_{N_u} & \ddots & & \\ & \ddots & \ddots & \\ 0 & & I_{N_u} & -I_{N_u} \end{bmatrix} \tilde{\mathbf{u}} \leq \begin{bmatrix} \Delta_{max} \\ \vdots \\ \Delta_{max} \\ -\Delta_{min} \\ \vdots \\ -\Delta_{min} \end{bmatrix} \tag{B.34}$$